Design and Characterisation of a High Energy-Density Inductor

Rasha Saeed

Thesis submitted to the University of Nottingham for the degree of Doctor of Philosophy

July 2017

I dedicate this achievement to my beautiful mother Laila.

Also to the memory of my mother in law Luisa Pinzin.

Abstract

Power electronics is an enabler for the low-carbon economy, delivering flexible and efficient control and conversion of electrical energy in support of renewable energy technologies, transport electrification and smart grids. Reduced costs, increased efficiency and high power densities are the main drivers for future power electronic systems, demanding innovation in materials, component technologies, converter architectures and control. Power electronic systems utilise semiconductor switches and energy storage devices, such as capacitors and inductors to realise their primary function of energy conversion. Presently, roughly 50% of the volume of a typical power electronic converter is taken up by the energy storage components, so reducing their weight and volume can help to reduce overall costs and increase power densities. In addition, the energy storage densities of inductors are typically much lower than those of capacitors, providing a compelling incentive to investigate techniques for improvement.

The main goal of this research was to improve the design of an inductor in order to achieve higher energy densities by combining significantly increased current densities in the inductor windings with the ability to limit the temperature increase of the inductor through a highly effective cooling system. Through careful optimisation of the magnetic, electrical and thermal design a current density of 46 A/mm2 was shown to be sustainable, yielding an energy storage density of 0.537 J/ kg. A principal target for this enhanced inductor technology was to achieve a high enough energy density to enable it to be readily integrated within a power module and so take a step towards a fully-integrated “converter in package” concept. The research included the influence

of the operating dc current, current ripple, airgap location and operating frequency on the inductor design and its resulting characteristics. High frequency analysis was performed using an improved equivalent circuit, allowing the physical structure of the inductor to be directly related to the circuit parameters. These studies were validated by detailed small-signal ac measurements. The large signal characteristics of the inductor were determined under conditions of triangular, high-frequency current as a function of frequency, current (flux) ripple amplitude and dc bias current (flux) and a model developed allowing the inductor losses to be predicted under typical power electronic operating conditions.

Acknowledgements

I owe an enormous debt of gratitude to my supervisors Prof C. Mark Johnson, Prof Lee Empringham and Dr Liliana De Lillo for their guidance and support throughout my PhD study. Their advice, encouragement and feedback is invaluable for me and I shall be forever grateful.

I must thank Dr Behzad Ahmadi for his numerous help and support. I want to express my sincere appreciation to him for his instruction, time, and patience. I am so grateful for everything I learned from him through my PhD time.

I would like also to express my thanks to the following people:

Engineering and Physical Sciences Research Council (EPSRC) for their financial support of this study.

The great team of the PEMC group in the Electrical and Electronic Engineering (both Researchers and PhD students), for their support and friendship. I appreciate each help and the wonderful time that we worked and spent together. Also to the technicians in the PEMC group support for all their technical help.

My loving mother Laila and brother Maias for their encouragement, support and belief in me.

To my friends Dr Manuela Pacella and Dr Amir Badiee for their unlimited support and priceless friendship. To my friends the tutors in Willoughby Hall, Siavash, Njahira, Alberto & Miriam, Ibrahim, Rino, Tracy & Guan, Jess, Navin and Dr Gareth Stockey for all their support and the great happy times together.

To my amazing husband Simone for his endless love and support, without whom I could not have completed this work.

Publication

R. Saeed, C. M. Johnson, L. Empringham and L. De Lillo, "High current density air cored Inductors for direct power module integration," *2014 16th European Conference on Power Electronics and Applications*, Lappeenranta, 2014, pp. 1-6.

Contents

List of Contents

List of Figures

List of Tables

Table of Nomenclature

A	Ampere
A_c	Cross section of the core
A_{coil}	Cross section of the coil
A_w	Cross-sectional area of the winding conductor
α_1, α_2	Constants for core loss as a function of (W,mT)
B	Flux density
β_1, β_2	Constants for core loss as a function of (W,kHz)
B_i	Biot number
B_{max}	Maximum Flux density
B_{sat}	Flux density saturation
ΔB	Flux density ripple
C	Capacitance
c	Specific heat capacity
C°	Degree centigrade
CF	Confidence Factor
C_m	Capacitance between two adjacent turns, one in each half-winding
CO_2	Carbon dioxide
C_S	Stray capacitance or self-capacitance
C_{tt}	Turn to turn capacitance
C_{ts}	Capacitance between the bottom copper substrate and the inductor
DBC	Direct Bonding Copper
E	Stored Energy
EMI	Electromagnetic Interferences
FF	Fringing Factor
FEA	Finite Elements Analysis
FEM	Finite Elements Methods
F_R	AC-to-DC resistance ratio or AC resistance factor
f_r	Self-resonant frequency
f_0	First resonant frequency
Φ	Magnetic flux
φ	Phase

H	Magnetic field
h	Thermal conductivity
H_{dc}	Magnetic field DC bias
Hz	Hertz
I_{mn}	Amplitude of the n^{th} harmonic of the inductor current
iGSE	Improved method of the Generalised Steinmetz Equation
J	Current density
j	Joules
K	Kelvin
k	Thermal conductivity
kHz	Kilo Hertz
KW^{-1}	Kalvin per watt
L	Inductance
l_c	Length of the coil
l_g	Air gap length
l_m	Magnetic length in the core
L_t	Turn inductance
l_w	Winding conductor length
N	Number of turns of the winding
m	Mass
m	Meter
mm	Millimeter
MMF	Magneto-motive force
μ	Permeability
μ_0	Permeability of free space
μ_r	Relative permeability of magnetic material
μ_{re}	Effective permeability of magnetic material
μH	microhenry
OSC	Oscilloscope
Ω	Ohm
P	Rate of heat energy per total surface
P_{AC}	AC losses
P_{DC}	DC losses
PCB	Printed Circuit Board
P_{core}	Core loss

P_{tot}	Total loss
P_w	winding power loss
P_{wDC}	DC winding power loss
pF	picofarad
$\dot{Q}$	Rate of change of heat energy per total surface
q''	Heat flux per unit area
q'''	Volumetric heat source
R	Resistance
R_c	Reluctance of the core
R_g	Reluctance of the air gap
R_L	Resistance of the inductor
$R_{remnant}$	Resistance at number of turns N equal to zero
R_{sh}	Shunt resistance
R_t	Turn Resistance
R_{th}	Thermal resistance
$r_{th,sp}$	Specific thermal resistance
R_{wAC}	AC winding resistance
R_{wDC}	DC resistance of the winding
ρ	Density
ρ_E	Energy storage density
ρ_w	Winding conductor resistivity
s	seconds
SiC	Silicon Carbide
SPG	Steinmetz pre-magnetization graph
T	Temperature
T	Tesla
V	Volts
W	Watts
$Wm^{-1}K^{-1}$	Watt per meter per Kalvin
$Wm^{-2}K^{-1}$	Watt per square meter per Kalvin
Y	Admittance
ε_0	Di-electric constant
ε_r	Relative static permittivity
Z	Impedance

1 Chapter 1- Introduction

Climate change is one of the greatest global challenges due to its potential negative impact on mankind, thus governments and industries around the world are encouraging technological innovation towards reducing the release of green-house gases such as CO_2 into the atmosphere and preventing a further worsening of the environment to protect the health of current and future generations. Transport, which depends heavily upon fossil fuels contributes a significant proportion of greenhouse gas emissions which is responsible for global climatic change [1]. To avoid such problems and protect the environment, clean electric vehicles such as hybrid electric vehicles are being developed and their use is encouraged. Thus, the increased use of hybrid and electric vehicles for ground transportation has resulted in an increased demand for more power dense electrical systems.

Power electronics is an enabler for the low-carbon economy, delivering flexible and efficient control and conversion of electrical energy in support of renewable energy technologies, transport electrification and smart grids. Reduced costs, increased efficiency and high power densities are the main drivers for future power electronic systems, demanding innovation in materials, component technologies, converter architectures and control. Power electronic systems utilise semiconductor switches and energy storage devices, such as capacitors and inductors to realise their primary function of energy conversion. Presently, roughly 50% of the volume of a typical power electronic converter is taken up by the energy storage components, so reducing their weight and volume can help to reduce overall costs and increase power densities. In addition, the energy storage densities of inductors are typically much lower than those of capacitors, providing a compelling incentive to investigate techniques for improvement.

1.1 High power density converter

Many of the recent studies [2] [3] into power electronic integrated systems have focused their attention on improving their performance in order to achieve higher power densities, reduced size, increased efficiency and reliability. In automotive and aerospace applications where mass and space are at a premium it is desirable to

minimise the system mass and consequently enhance power density W per kg [4][5]. As weight has a dramatic impact on energy savings, CO_2 emissions and operational costs [6], topologies which satisfy these demands are needed.

Benefits such as improved efficiency, improved thermal performance, and high power density can be obtained on different ways. One method involves the interleaving technique. For high power applications, interleaving multi-channel converters is considered a good solution in order to meet certain system requirement, especially considering any limitation on performance of the available power devices. One such example can be found in the application of a Superconducting Magnetic Energy Storage System (SMES) [7]. Other studies have presented interleaved boost converters with coupled inductors [8] [9] where, higher frequency operation can be achieved for capacitive components by using interleaved technique. The effective ripple frequency the capacitive elements see is increased due to the interleaved structure. In general, the frequency is doubled with two interleaved cells and tripled for three etc. Researches have managed to achieve a power density up to 142.9 $W.in^{-3}$ [8720 $kW.m^{-3}$] using a 2 kW inverter with an interleaving technique [10]. Another study [11] has presented a DC-DC converter with power density 4.3 $kW.kg^{-1}$. The converter uses a water cooled cold-plate and magnetic components potted in aluminium heat-sinks to achieve the power density.

In general, a power converter typically consists of switching devices such as Silicon MOSFETs or IGBT's, control circuits and passive components such as capacitors, inductors and resistors. The passive components, particularly the inductors, are often bulky and typically the largest components within a converter as they represent around half the mass of a packaged power converter, in some cases their contribution is up to 70 %.Thus, they becomes the obstacle to further reduce the size of DC-DC converters [12] [13]. One solution for downsizing passive components is to increase the switching frequency of the power devices [14]. However, the disadvantage of this technique is that it leads to additional problems such as increased Electro-Magnetic Interference (EMI), thermal stress in active/passive devices and increased cooling requirements. Therefore, further solutions and considerations are required in order to achieve high power density [15].

The new generation of Silicon Carbide (SiC) and Gallium Nitride (GaN) power devices have the ability to operate at higher temperatures and higher switching frequencies than the typical Silicon (Si) power devices [16] [17]. With higher current density chips compared to their silicon counterparts, smaller packages could be obtained. Also, if operating frequencies are increased, the physical size of the passive components can be reduced, while maintaining or improving the efficiency [14]. In a previous study [18], a comparison of an all silicon matrix converter switching at 8kHz showed the same efficiency as a hybrid SiC-Si (SiC Schottky barrier diodes used instead of Si PN diodes) matrix converter operating at 19kHz. Thus, the inclusion of Silicon Carbide (SiC) devices can have a dramatic effect on the converter as it has a significant impact on the size and weight of the passive filter components. However, the advantageous features of these new devices cannot be presently fully utilised due to limitations in the packaging technologies being presently employed and there are a significant number of issues which require consideration including the inter-component interactions of the power converter [19].

In another study [20] a technology which can fulfil the requirements of achieving high-power-density and high-efficiency in DC/DC converters has been proposed. In this study the passive components have been downsized without the need for high-switching frequency of the power devices by using interleaved multi-phase circuits with integrated magnetic components. However, extra attention to the DC-biased magnetization of integrated magnetic components is needed when using this method and inductor average current control needs to be implemented in interleaved multi-phase DC/DC converters so that current sharing between the individual modules can be achieved.

In general, increasing the operating frequency and by fully utilising the core and conductor materials to the limit of their magnetic flux density and current density respectively alongside the choice of magnetic core structures and materials will lead to a reduction in volume and weight of inductors and will enable significant improvements in the energy density, hence, the power density of the converter can be increased. [21] [22].

1.2 Classical Approaches to high Energy density Inductors

The inductor is one of the most important parts in a variety of switched mode power converters ranging from buck converter, boost converter to full bridge or half bridge converters, among others [23]-[29]. In a boost DC-DC power converter, power inductors store energy in the form of magnetic field during the time interval when the control switch is turned on and they discharge the stored energy to support the current flow to the load during the time interval when the synchronous output switch (or output diode) is on. The desired inductance value for a power converter is normally determined based on the switching frequency, maximum inductor current ripple, input voltage and output voltage [30]. Power converters with higher switching frequency and similar ripple, require a lower value of inductance and hence smaller size [14]. However, switching frequency is limited by switching power losses and temperature rise [31], moreover, the size of an inductor may be determined by the desire to prevent the core from saturation at high current [30] [32].

Different approaches have been taken over the years in order to achieve larger inductance including the increases in permeability, higher saturation magnetization, higher frequency and lower loss magnetic materials for inductor cores [33] [34]. Also, improving the magnetic core structure such as in the use of multi-permeability cores which improves the utilization of the magnetic core material [35]-[39]. In addition to improving the winding structure to reduce the winding losses and increase the inductor power density [40] [41].

Magnetic material selection is one of the main issues in the inductor design which also depends on the system requirements and the trade-offs between the efficiency, specific power loss, weight, geometric dimensions and operating temperature [42][43] it is a challenge to find an ideal balance between these aspects and it can be accomplished through coupled electromagnetic, loss and thermal analyses [21],[44]. Hilal and Cougo [43] have presented an optimization of power inductors with the minimum weight for three-phase high-power-density inverters (540V-DC) of variable current ripple (10% to 200%) and switching frequency (10 kHz to 100 kHz) to be used in aircraft applications. Results showed that the highest inverter power densities and efficiency were achieved using Ferrite core material. The highest power density was achieved for a current ripple of 100%. Since the switching frequency must be high in

order to decrease the filter size and the current ripple high to decrease switching losses, only the use of low loss materials will result in high efficiency and power density of this inverter. Although other materials such as amorphous, Nanocrystalline, FeSi, and iron powder, have high saturation flux densities, a high ripple current induces high magnetic losses in these cores and consequently prevents these cores from operating at high flux densities where it is difficult to get the heat out of the material. Accordingly, these materials result then in cores having greater cross sectional areas than ferrite.

Nevertheless, when magnetic components (inductors and core materials) in high power density converters are designed it is important to calculate their losses as the temperature of the components tends to be high because loss density is also increased by the high power density. It has been suggested in previous studies [45] - [48] that there are practical effects of frequency, DC bias, airgap fringing and duty cycle on core power loss, all materials can experience increased core losses due to these effects.

Therefore, adequate cooling is required to evacuate the loss and maintain an operating temperature below the thermal limit of the materials. Thus, it is important to predict the thermal behaviour of the inductor, some studies have presented analyses of the inductor temperature caused by the losses with the help of both FEA (Finite Elements Analysis) and measurements [22] [49]. As a result, further size reduction and the possibility of applying a higher current through the inductor and hence a higher energy density can be achieved by using improved cooling methods [48]-[50].

1.3 Research Objective

The main goal of this research is to improve the design of an inductor in order to achieve higher energy densities by applying higher current densities, with the ability to limit the temperature increase of the inductor with the usage of an efficient cooling system. A principal target for this enhanced inductor technology was to achieve a high enough energy density to enable it to be readily integrated within a power module and so take a step towards a fully-integrated “converter in package” concept. The analysis of this structure at high frequencies will also be done in order to determine the high frequency performance and their suitability to be included in the high frequency EMI filter.

In addition, the choice of magnetic material for the design is not straightforward as the operating DC current, current ripple, airgap length, number of air gaps and operating frequency, all have a strong influence on the inductor size and high frequency behaviour. Thus, the following step will be done, in order to achieve high energy density by applying high current density and high switching frequency, considering these consequential aspects:

1- The compact inductor needs to be operated with a high current of up to 80A-DC as a part of a power converter using wide band-gap devices, in order to filter the high frequency harmonics where long feeder lines or stringent power quality requirements are in place, with a desired inductance of around 25 µH. These values have been chosen in consideration with the existing project requirements [51].
2- Following the structure proposed in the study [51] in order to accomplish the maximum energy density whilst utilizing the minimum space, integration of the passive components with the thermal management sub-system, substantially increases the potential power density of a typical high power system. Figure 1.1 shows the design constraint perspective with the available space for a single unit of a standard basic power cell with every part including the inductor and the magnetic core on the substrate.

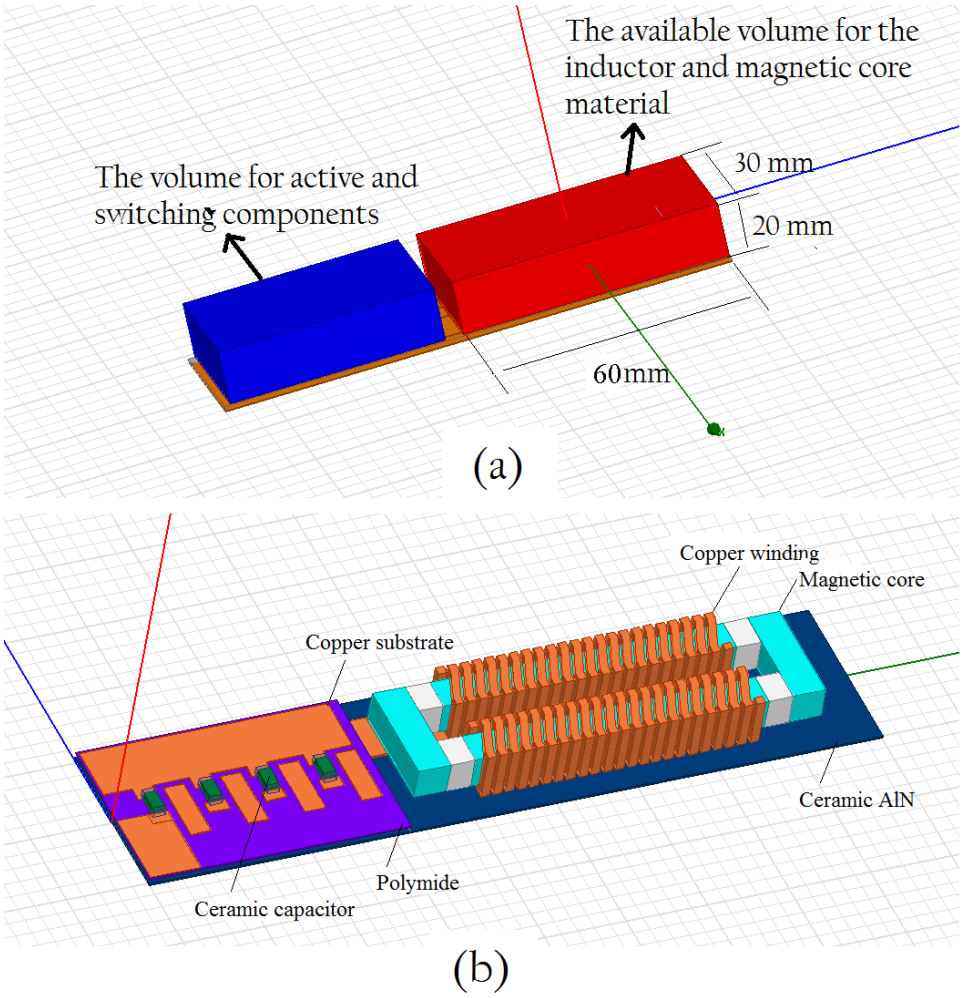

Figure 1.1- Design constraint perspective; (a) A schematic of available space for the inductor and the magnetic core on the substrate. (b)The illustrated schematic a converter topology with proposed cored inductors soldered on the copper substrate next to other active components [51].

3- The coil shape with a rectangular cross section, as shown in Figure 1.2-(a), was predefined to suit the volume available within the package on the substrate on one hand, and in order to enhance heat conduction by increasing the cross sectional area, which also increases the inductance per unit volume.

4- The coil has been soldered to the DBC (Direct Bonding Copper), with the turns positioned carefully on the strands, as shown in Figure 1.2-(b)&(c), avoiding short circuits by separating the gaps between the strands with high temperature paper strips, filling the solder paste then fixing the inductor on the substrate with each turn in the exact position.

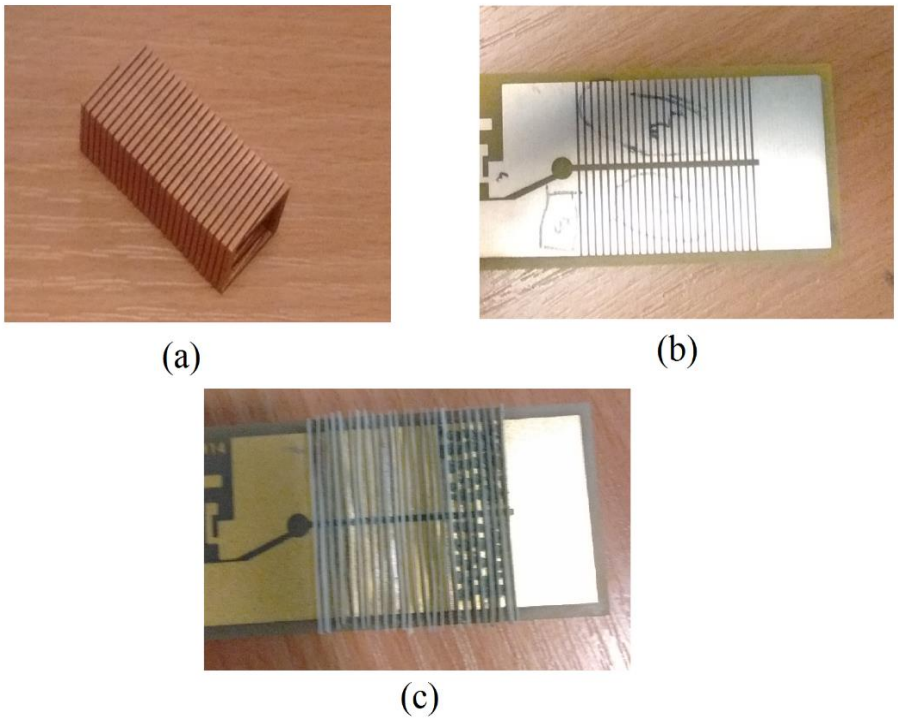

Figure 1.2- (a) A Rectangular cross section solenoid inductor with rectangular cross section copper winding.(b) DBC with the strands where the inductor winding will be soldered. (c) DBC with the strands and high temperature separating paper strips.

5- The magnetic material geometry design will be improved to achieve the desired inductance in the available volume when operated at the maximum current. A distributed air gap system will be introduced in order to avoid core saturation at high current.

6- A direct liquid cooling technology will be used in order to reduce the high temperature which may result high current through the inductor. Having the inductor on the same substrate level with the other power module components gives the chance of cooling both the passive and active components using the most advance direct liquid cooling. Although the size of the inductor and the cooling substrate is reduced, there is a trade- off because of the need for the other part of the liquid cooling system (the pump and the pipe) as a part of the improved direct liquid cooling system which increases the total size of the system.

- The magnetic components will be characterized in order to predict their resonant frequency and parasitic capacitance when operating at high switching frequencies. A Novel lumped model in order to find the equivalent electric circuit of the winding for fast determination of the resonance frequency of the inductor is proposed.

7- To study the losses produced in this components and identification different sources of losses will be accomplished by taking into account the performance of the component under the large signal ripple and an instantaneous DC bias (part of a low frequency AC component). The challenging contribution is in separating and measuring the losses of the air gapped core under AC current and DC bias. a new analytical approach is introduced to describe core loss calculation under DC bias conditions

Figure 1.3 shows the flow chart of the thesis.

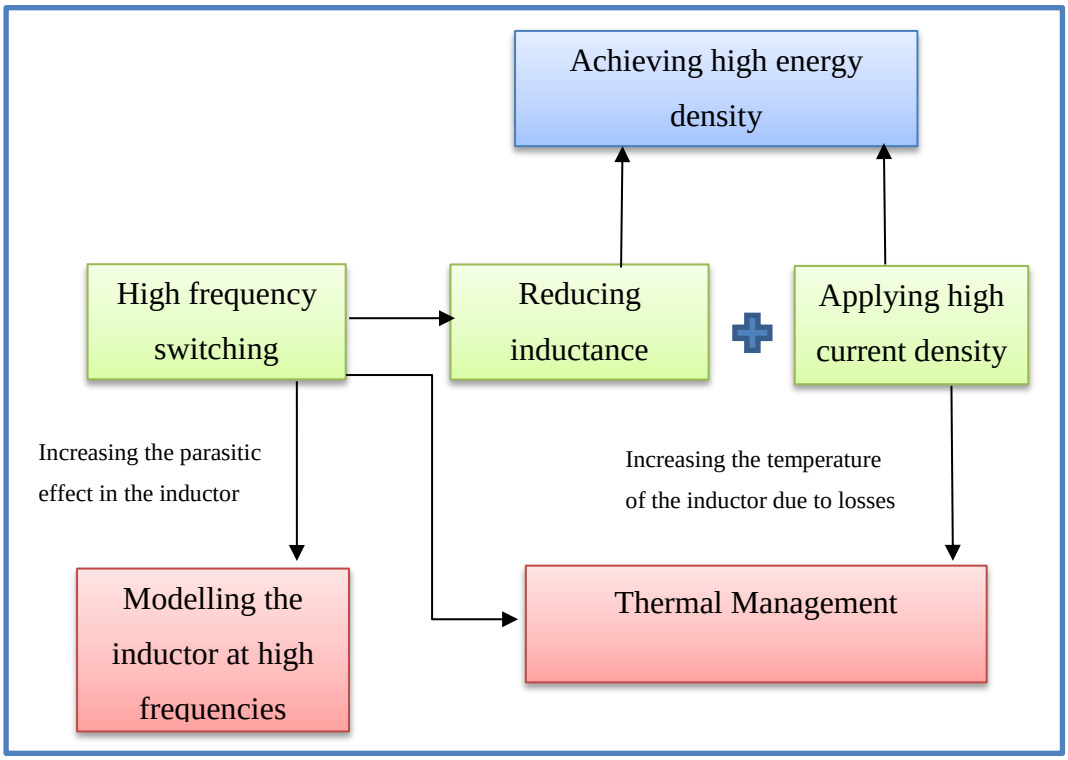

Figure 1.3- The flow chart of the thesis.

1.4 Outline of this Dissertation

The rest of this dissertation will be organized as in the following chapters with a literature review for each chapter:

Chapter 1 is the introduction of the thesis will highlight the classical approach to the high energy density inductors, introduce the research objective and outline the dissertation.

Chapter 2 will introduce a solution for the structural integration of high energy density inductors into power electronic modules at the substrate level. The design will be improved for minimum volume and maximum current in order to achieve a high current density and hence, a high energy density. Considering the design constraints, the available volume and the fact that air cored inductor's energy storage densities are generally too low, a magnetic core will be added to obtain the maximum inductance. In order to avoid core saturation at high current, a distributed air gap system will be introduced in order to achieve the desired inductance in the available volume when operated at the maximum current.

Chapter 3 aims to build on thermal simulation, theoretical analysis and experimental results and focuses on achieving high current density by applying high current up to 80 A through the inductor. A single cooling method will be applied on the bottom copper substrate of the DBC on to which the inductors are soldered. The thermal aspect of the proposed package (inductors and DBC) will be analysed in order to understand the heat flow through it and determine the performance of the individual parts.

Chapter 4 will characterize the magnetic components and model the inductor at high frequency and predict their resonant frequency and parasitic capacitance at high frequencies. An equivalent electric circuit of the inductor will be proposed and solved in LTSPICE. Then the method will be validated experimentally.

Chapter 5 will investigate in the performance of the designed inductor, under realistic operating conditions, where the magnetic component can be used as the output filter in a PWM inverter or a DC/DC converter, taking into account the performance of the component under the large signal AC ripple and an instantaneous DC bias (part of a low frequency AC component).The magnetic losses and their dependency on the

frequency and flux density will be examined in detail within this chapter, as large signal characterisation, unlike the small signal analysis, is limited to lower frequencies (some 250 kHz). However, they provide conditions which are closer to those in the real applications and therefore one can rely on the characterisation results to estimate the performance of the magnetic component. Operating within these conditions will produce different level of losses in the core compared to losses that are given by the datasheet values and this will be presented.

Chapter 6 is the conclusion of the thesis will highlight the main contributions and the summery of the chapter. It will also discuss the suggested further work.

1.5 Conclusion

In this chapter the classical approch to high energy density undector is highlighted , the reasearche objective is explained with the referingto the main contribution and novoloty of the thesis and the study is outlined.

2 Chapter 2- Design of Inductor and Core Geometry

2.1 Introduction

This chapter introduces a solution for the structural integration of a high energy density inductor into power electronic modules in order to achieve high power density converters. This is done by considering the issues relating to the integration of inductors, specifically due to their relatively large volume, their winding losses and parasitic capacitance. Also, due to the fact that in general, an air cored inductor's energy storage density is too low, a magnetic core is added to obtain the maximum inductance L for the available volume. As the main key to achieve a high energy density will be by applying a high current since energy density is proportional to the square of the current through the inductor, a design of cored inductor based on a solenoid geometry without the use of multiple layered windings is proposed in order to facilitate heat removal from the windings. The design was improved for minimum volume and maximum current density in order to achieve a per unit energy density with highest inductance L. In order to avoid core saturation at high current, a distributed air gap system is introduced and analysed in order to achieve the maximum inductance while minimising the losses for the available volume when operated at the maximum current. Ferrite N95 [52] was used as the core material.

The influence of the core material geometry and airgap will be determined by investigating the change in its inductance against an increasing DC current and the saturation effect will be examined with the usage of Maxwell16.0 3D software (Magneto-static solver) and then validated experimentally together with the proximity effect of the air-gap to the windings and its effect on the losses.

2.1.1 High Current Density Inductor Design

Most of the recent studies [2] [3] into integrated power electronic systems have focused their attention on improving their performance in order to achieve higher power densities, reduced size and increased efficiency. Passive components, mainly inductors, transformers and capacitors, are often the largest parts of a converter and consume the largest amount of manufacturing raw materials. Furthermore, inductors are often responsible for the much of the power loss and volume of the converter [12].

Researchers in a previous study [53] have optimised the trade-off between applying high current, reducing the inductor size, introducing air gap to the core in order to avoid the saturation at high current values, and thermal management. In this study they used a silicon-carbide MOSFET with a switching frequency up to 60 kHz in order to increase the power density and by maintaining a high current (72.5 A RMS) and increasing the switching frequency, the inverter side inductance has been reduced and core size has also been decreased in size.

The concept of integrating inductance structures into power module substrates was introduced by the author during the work carried out for this thesis [49], where, the feasibility of using high current density and thus high energy density inductors by providing an efficient path for the heat to the thermal management system has been investigated.

With the aim of designing a compact and efficient inductor, material selection is one of the main issues in the inductor design depending on the system requirements and the trade-offs between the efficiency, specific power loss, weight, and operating temperature. Thus, the inductor's design optimisation should take into account the inductor's geometric parameters, magnetic properties, core material selection, losses and temperature. The following section discusses the basics of the design of an inductor.

2.2 Basic Design of Inductor

An inductor is able to create a magnetic field and store magnetic energy in this field. A coil is generally formed by winding a wire (conductor) on a cylindrical former, called a bobbin [54]. One of the most basic forms used for an inductor is the solenoid which could have either a rectangular or circular cross section using either square cross sectional copper windings or a rounded cross section copper winding, as shown in Figure 2.1.

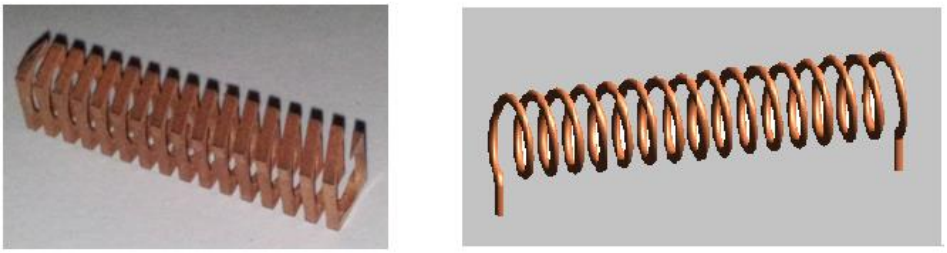

(a) (b)

Figure 2.1-(a) Rectangular cross section solenoid inductor with square cross section copper winding. (b) Rounded cross section inductor with rounded cross section copper winding.

In general, any conductor has an inductance, and this inductance depends on:

1. Winding geometry.
2. Core and bobbin geometry (for instance a solenoid geometry).
3. Permeability of the core material.
4. Frequency.

There are several general methods to determine the inductance depending on the kind of inductor and these discussed in the following sections.

2.2.1 Air cored solenoid Inductor

In an air-cored solenoid, the magnetic field is concentrated into a nearly uniform field in the centre of a long solenoid, as shown in Figure 2.2.

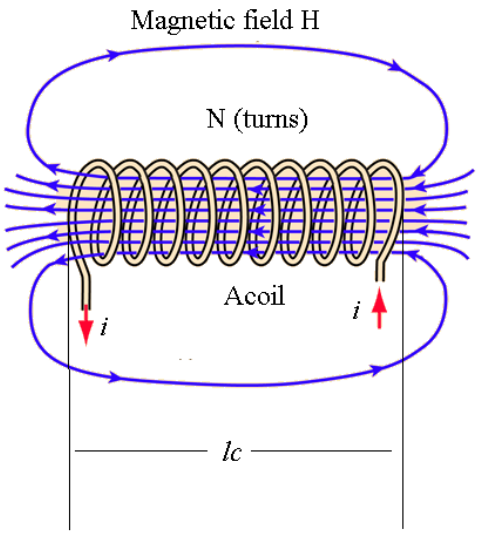

Figure 2.2- Air cored solenoid inductor (coil) with N turns of winding.

By using the standard derivations [54], the magnetic flux density B (T) within the coil is practically constant and given by:

$$B = \mu_0 H : H = \frac{Ni}{l_c} \qquad \text{EQ 2.1}$$

Where $\mu_0 = 4\pi \times 10^{-7}$ $(H.m^{-1})$ is the permeability of free space, N is the number of turns, i is the current, l_c is the length of the coil and H is the magnetic field (A.turn). Ignoring end effects, the total magnetic flux through the coil is obtained by multiplying the flux density B by the cross-section area A_{coil}:

$$\Phi = \mu_0 \frac{NiA_{coil}}{l_c} \qquad \text{EQ 2.2}$$

Combining this with the definition of inductance:

$$L = \frac{N\Phi}{i} \qquad \text{EQ 2.3}$$

and the inductance of a solenoid L [Henry]follows as:

$$L = \mu_0 \frac{N^2 A_{coil}}{i} \qquad \text{EQ 2.4}$$

Where A_{coil} is the cross section of the coil, l_c is the coil's length and N is the number of turns carrying the current i.

2.2.2 Inductor with Magnetic Core

Ferromagnetic materials have a relative permeability $\mu_r \gg \mu_0$ which depends on the magnetic flux B. For air-cored inductors, μ_0 creates a straight line slope when comparing B and H for all values of H thus the relationship between the magnetic field H and the flux density B is linear. While for ferromagnetic cored inductors the B-H relationship is a nonlinear and it is described by EQ 2.9. Figure 2.3 shows simplified plots of the magnetic flux density B as a function of the magnetic field intensity H (large signal DC) for both air-cored and cored inductors.

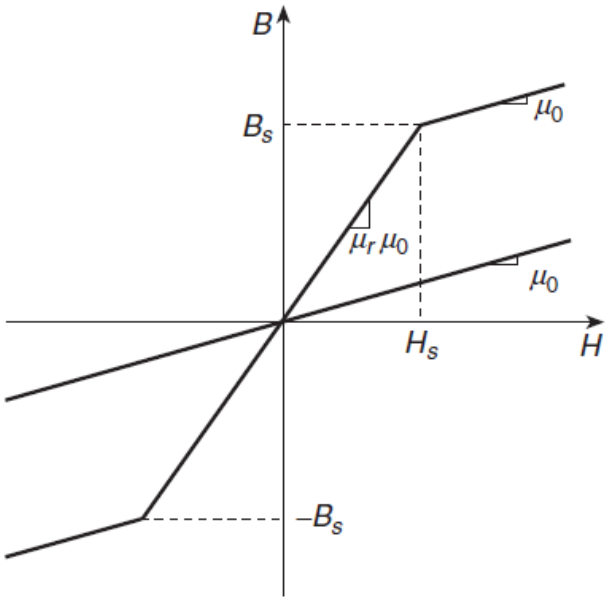

Figure 2.3-Simplified plots of magnetic flux density B as a function of magnetic field intensity H (large signal DC) for air-core inductors (straight line) and ferromagnetic core inductors (piecewise linear approximation)[54]

At low values of the magnetic flux density $B < B_S$ (where B_S is the saturation point of B), the relative permeability μ_r is high and the slope of the B-H curve $\mu_r \mu_0$ is also high. For $B > B_S$, the core saturates and $\mu_r = 1$, reducing the slope of the B-H curve to μ_0.

Figure 2.4-(a) shows an inductor composed of a core and a winding, while Figure 2.4-(b) shows the equivalent magnetic circuit.

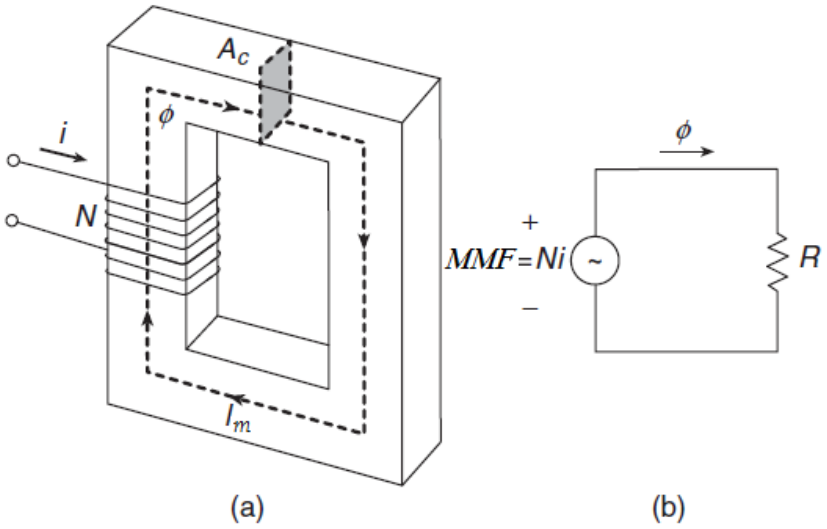

Figure 2.4- (a) An inductor composed of a core and a winding with number of turns N. (b) Equivalent magnetic circuit [54].

An inductor with N turns carrying a current i produces the MMF (A.turn) (also called the magneto-motive force which forces a magnetic flux ϕ to flow)[54].

By using the standard derivations [54], the MMF is given by:

$$\mathrm{MMF} = \mathrm{Ni} \qquad \text{EQ 2.5}$$

For a uniform magnetic field and parallel to path l_m, the MMF is also given by

$$\mathrm{MMF} = \mathrm{H}\, l_m \qquad \text{EQ 2.6}$$

The magnetic field intensity H ($A.turn.m^{-1}$) is defined as the MMF per unit length:

$$\mathrm{H} = \mathrm{Ni}/l_m \qquad \text{EQ 2.7}$$

l_m is the magnetic length in the core (Figure 2.4), N is the number of turns carrying the current i.

The magnetic flux ϕ per unit area $\mathrm{A_c}$ creates the magnetic flux density B (T) which is given by:

$$\mathrm{B} = \frac{\Phi}{\mathrm{A_c}} \qquad \text{EQ 2.8}$$

These two quantities, magnetic field and magnetic flux density, are associated to each other by:

$$B = \mu_0 \times \mu_r \times H \qquad \text{EQ 2.9}$$

Where $\mu_0 = 4\pi \times 10^{-7}$ $(H.m^{-1})$ is the permeability of free space, μ_r is the relative permeability of the core material and $\mu = \mu_0 \times \mu_r$ is the permeability.

Finally, the inductance L (H) of an inductor with a core with a permeability μ (Figure 2.4) can be obtained by:

$$L = \mu_0 \times \mu \times \frac{N^2 A_c}{l_m} \qquad \text{EQ 2.10}$$

Where A_c is the cross section of the core, l_m is the magnetic length and N is the number of turns carrying the current.

Applying a DC current will increase the magnetic field intensity H. Since H increases, the flux density B will also increase according to EQ 2.9. Further increase of DC bias will push the inductor operating point to the saturation region (Figure 2.3) where the relative permeability (μr) is decreased and the value of inductance will drop according to EQ 2.10 where the inductance L is proportional to the permeability μ.

The saturation of the magnetic core at high currents can be prevented by using two approaches. One is selecting low permeability materials, and the second is to reduce the effective permeability of the material by inserting low permeability areas or more typically an airgap in the material. The air gap is described as a reluctance to the magnetic flux density and it changes the effective B-H characteristics of the core as will be explained in the following sections.

2.2.3 Inductor with Air Gapped Core

In order to avoid core saturation at high current, an air gap can be introduced into the core. Implementation of air-gap influences the shape of the B-H curve of a magnetic circuit, decreasing the effective inductance and increasing the saturation current of an inductor. Additionally, implementation of an air-gap increases the fringing flux phenomenon which must be taken into account because of electromagnetic interferences (EMI) aspects, due to the fact that fringing flux causes higher propagation of electromagnetic disturbances.

The result of adding an airgap on the B-H curve is shown in Figure 2.5 where the steep slope (high permeability) is for a core without an air gap and the more gradual slope for the same core with a small air gap.

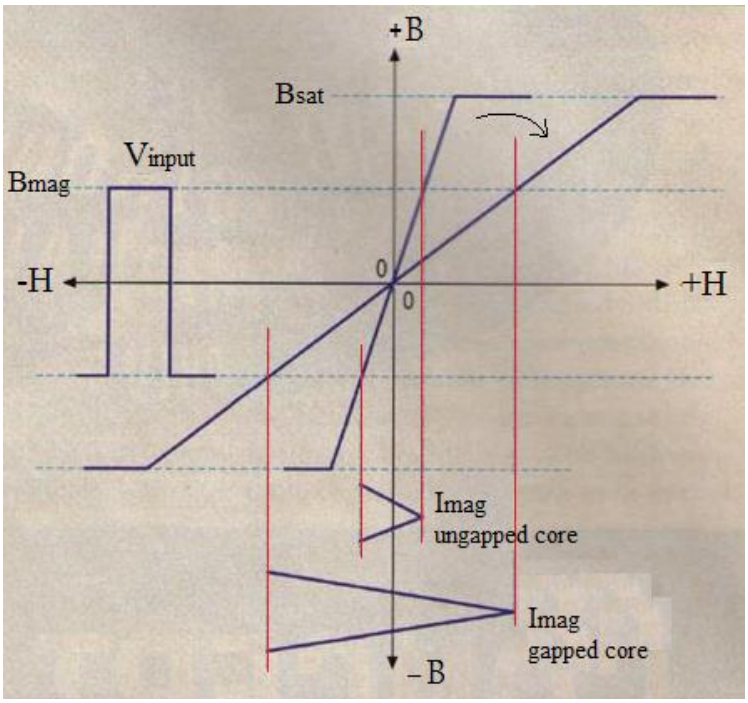

Figure 2.5- An idealised BH curves of Ferrite core, with and without air gaps [54].

Introducing an air gap into the core of an inductor will decrease the magnetic flux density B (T), it will also cause a considerable reduction in the inductance due to the decreasing permeability (as in EQ 2.9)

Figure 2.6 illustrates an inductor with air gapped core and the equivalent magnetic circuit of the core and the air gap. Air gaps can be bulk or distributed throughout the magnetic structure. The same magnetic flux ϕ flows in both the core and in the gap. Adding an air gap in a core is the equivalent to adding a large reluctance in series with the core reluctance as shown in Figure 2.6-(b).

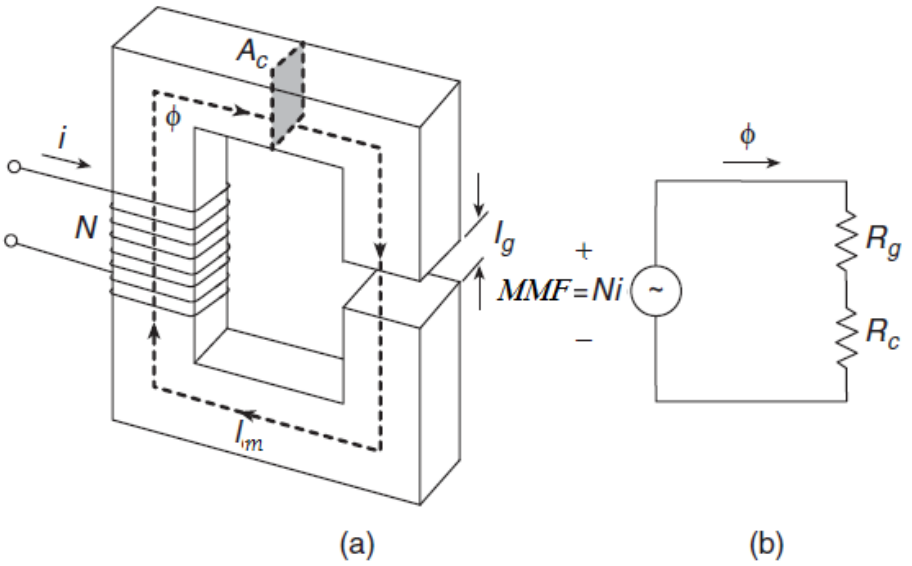

Figure 2.6- (a) An inductor composed of a core with an air gap and a winding with number of turns N. (b) Equivalent magnetic circuit [54].

As a result, the magnitude of the magnetic flux ϕ at a fixed value of Nl_m is reduced. This effect is analogous to an electric circuit where the adding of a series resistor reduces the magnitude of the current at a fixed source voltage.

By using the standard derivations [54] and solving the equivalent magnetic circuit in Figure 2.6-(b):

The reluctance of the air gap is

$$R_g = \frac{l_g}{\mu_0 \times A_c} \qquad \text{EQ 2.11}$$

The reluctance of the core is

$$R_c = \frac{l_m - l_g}{\mu_r \mu_0 \times Ac} \approx \frac{l_m}{\mu_r \mu_0 \times A_c} \qquad \text{EQ 2.12}$$

And the overall reluctance of the core with the air gap is

$$R = R_g + R_c = \frac{l_g}{\mu_0 \times A_c} + \frac{l_m}{\mu_r \mu_0 \times Ac} = \frac{l_m}{\mu_r \mu_0 \times A_c}\left(1 + \frac{\mu_r l_g}{l_m}\right) = F_g R_c \qquad \text{EQ 2.13}$$

Where the air gap factor is $F_g = \left(1 + \frac{\mu_r l_g}{l_m}\right)$.

The inductance of a coil with a magnetic core having an air gap at low frequencies is expressed as

$$L = \frac{N^2}{R} = \frac{N^2}{R_g + R_c} = \frac{\mu_r \mu_0 A_c N^2}{l_m(1+\frac{\mu_r l_g}{l_m})} = \frac{\mu_r \mu_0 A_c N^2}{l_m F_g} \qquad \text{EQ 2.14}$$

Where $\mu_0 = 4\pi \times 10^{-7}\ (H/m)$ is the permeability of free space, μ_r is the relative permeability of the core material, A_c is the magnetic cross section of the core, l_m is the magnetic length, l_g is the airgap length and N is the number of the winding's turns.

The effective permeability of a core with an air gap is

$$\mu_{re} = \frac{\mu r}{(1+\frac{\mu_r l_g}{l_m})} = \frac{\mu_r}{F_g} \qquad \text{EQ 2.15}$$

for high permeability cores $\frac{\mu_r\, l_g}{l_m} \gg 1$

$$\mu_{re} = \frac{l_m}{l_g} \qquad \text{EQ 2.16}$$

Thus,

$$L \approx \frac{N^2}{R_g} = \frac{\mu_0 A_c N^2}{l_g} \text{ [Henrys]} \qquad \text{EQ 2.17}$$

Thus, for high-permeability cores, the inductance is dominated by the air gap.

Maximum Flux density B_{max} :

$$B_{max} = \mu_r\, \mu_0\, \mathrm{H_{max}} = \frac{\mu_r\, \mu_0}{l_g} \mathrm{Ni_{max}} \approx \frac{\mu_0}{l_g} \mathrm{Ni_{max}} \qquad \text{EQ 2.18}$$

Stored energy E in the inductor:

$$E = \frac{1}{2} \mathrm{Li^2} \qquad \text{EQ 2.19}$$

Higher energy density (E) needs higher flux density (B) which needs a higher magnetic field intensity (H), thus there is a need for higher current (i), number of turns (N) and less reluctance (R).

However, introducing an air gap to the core will also lead to an interaction of the magnetic fringing flux with the windings around the airgap. Bearing this in mind, EQ 2.11 is only considered to be accurate when the fringing flux is small compared to the total flux, as it is when the air gap length is very small compared to the dimension of the air gap cross-sectional area. The fringing effect in the air gap will be explained in the following section.

2.2.4 Fringing Effect in the Air Gap

Introducing an air gap to the core will lead to an interaction of the magnetic flux fringing with the windings around the airgap as shown in Figure 2.7.

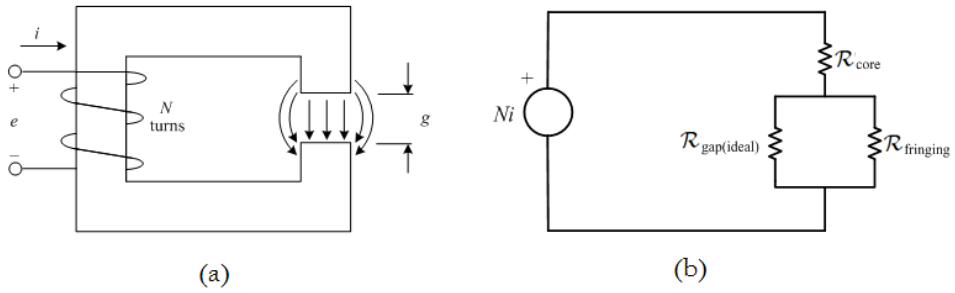

Figure 2.7-(a)-flux fringing at air gap. (b)- Equivalent magnetic circuit for fringing effects in an air-gap.

Different approaches have been devised in order to take the fringing flux into consideration. One method uses the Conformal Schwarz-Christoffel Transformation for calculating the air gap reluctance and an increase of the Air Gap Cross-Sectional Area [54][55]. However, using this method the cross-sectional area should be increased as a function of the air gap length l_g and the exact value by which the cross-sectional area has to be increased is difficult to determine and hence this method is restrictive in which geometries can be used.

In order to study the fringing effect in the presented model it is useful to talk first about the magnetic circuit and magnetic material's effects. The inductance change is directly proportional to the permeability change, if a small air gap with length l_g is inserted into the magnetic path; this will lower and stabilize the effective permeability μ_e. A very small air gap significantly modifies the parameters of magnetic devices by increasing the saturation current and linearizes B-H curve of a magnetic circuit, as explained before in Figure 2.3. An air gap reduces the effective permeability of the magnetic core, thus a high permeability material such as ferrite that are cut in E shape cores, has only about 80 percent of the permeability, than that of a toroid of the same material and this is because of the gap [56]. Although the air gap causes decreasing of the inductance, that inductance is predicted to be higher compared to the basic

analysis due to fringing flux which affects the perception of the size of A_e (the effective cross section) as shown in Figure 2.8. William T. McLyman in his exemplary equations for an idealized magnetic circuit has added a fringing factor (FF) to the basic inductor equation as shown in EQ 2.22& EQ 2.23 [56].

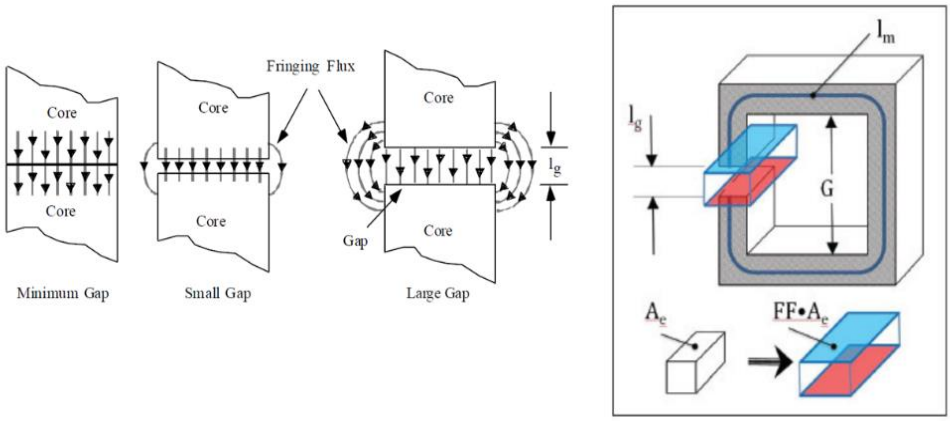

Figure 2.8- Fringing Flux (under large signal DC) at the Gap and it is effect on the air gap's cross section area Ae [56].

Thus according to the McLyman equations [56], the inductance of an inductor using the core with air gap as shown in Figure 2.8 is from EQ 2.14 and EQ 2.15 :

$$L=\frac{\mu_0\mu_{re}N^2A_c}{lm} \qquad \text{EQ 2.20}$$

Where A_c is the core's cross section, lm is the magnetic length in the core, μ_{re} is the effective permeability and N is the number of winding's turns.

McLyman has suggested a fringing factor FF which increase the cross section of the core to an effective cross section considering the fringing flux effect around the air gap.

$$A_{eff} = FF.A_c \qquad \text{EQ 2.21}$$

The fringing factor FF is given with the formula:

$$FF = 1 + \frac{l_g}{\sqrt{A_e}}\ln\left(\frac{2G}{l_g}\right) \qquad \text{EQ 2.22}$$

G is the internal length of the core, as shown in Figure 2.8.

Thus the inductance after the consideration of the fringing effect becomes:

$$L=FF(\frac{\mu_0\mu_{re}N^2A_c}{lm}) \quad \text{EQ 2.23}$$

For high permeability cores $\frac{\mu_r\, l_g}{l_m} \gg 1$ thus

$$L = FF(\frac{\mu_0 N^2 A_C}{l_g}) \quad \text{EQ 2.24}$$

These formulas are very helpful in generating an approximate estimation of an inductor's parameters but they can be difficult to implement in some advanced solutions with non-standard layouts, thus, the implementation of numerical methods (e.g. FEM methods) allows the preparation of an effective design and optimization of magnetic inductors.

2.2.5 Magnetic Core Materials

A magnetic core is a piece of magnetic material with a permeability μ used to guide magnetic fields in electrical, electromechanical and magnetic devices such as electromagnets, transformers, electric motors, generators and inductors.

Having no magnetically active core material, such as in an air cored component, provides very low inductance in most situations, so a wide range of high-permeability materials are used to concentrate the field.

The ideal choice for the magnetic material is one with high magnetization saturation and low magnetic loss, however one typically needs to find a trade-off with the available materials [57]. (The properties of some magnetic materials are listed in Figure 7.2 Appendix A)

2.2.5.1 Low Permeability Core Material

In applications with very high switching frequencies (10-100 MHz) magnetic components operating at high frequencies, and often under large flux swings are preferred [58]. Some low-permeability materials (relative permeability in the range of 4-40) can be used effectively at moderate flux swings at frequencies up to many tens of megahertz [59]. However, working with such low-permeability materials, especially with the un-gapped core structures which they are typically available in, presents somewhat different constraints and challenges than with typical high-permeability low-frequency materials [60].

Y. Han and D. J. Perreault in their previous study [61] have raised some concerns due to the lack of suitable design procedures for selecting low-permeability magnetic materials and available core sizes. Thus, they proposed a procedure and methods to help to design a magnetic-core inductor with low permeability core materials [61]. However, because of very high frequency operation and low-permeability characteristics of such materials, the operating flux density is limited by core loss rather than saturation. Without an air gap, the core loss begins to dominate the total loss and copper loss can be ignored in many cases [60].

One of the available low permeability core materials is 'Sendust' which is also known as KoolMu [62]. This material has a low permeability, from 26 to 125, a high saturation flux density and significantly low losses. Sendust cores also exhibit very low magnetostriction coefficient, and it is therefore suitable for applications requiring low audible noise such as Phase control circuits (low audible noise) for light dimmers [63]. However, although of it shows good temperature stability at up to 125 °C, as the temperature decreases to 65 °C, its inductance decreases by approximately 15%.

2.2.5.2 High Permeability Core Material with Air Gaps

High-permeability magnetic materials enhance the inductance of an inductor, however, some of these materials exhibit high losses at high frequencies such as Permalloy materials.

In most magnetic materials there is a slight decrease in permeability with time after the material is demagnetized. This effect is noticeable in low permeability materials and is negligible for high permeability materials. In some applications such as low flux level circuits, where a constant inductance is required, the effect must be considered. However, the effect can be minimized greatly by reduction of the effective permeability by insertion of an air gap. In general, introducing an air gap to the magnetic core causes a considerable decrease in the effective relative permeability. However, it produces a more stable effective permeability and reluctance, resulting in a more predictable and stable inductance with respect to an increasing current [54]. Inductors used in specific applications, such as resonant circuits and LC filters, should be designed to have predictable and stable inductances.

Ferrite, which is basically mixtures of iron oxide and other magnetic elements, has quite a large electrical resistivity but rather low saturation flux densities; typically about 0.45 T. Ferrites have only hysteresis loss as no significant eddy current loss occurs because of the high electrical resistivity, thus, Ferrite is a preferred material for cores that operate at high frequencies (greater than 10 kHz) because of the low eddy current loss [64]. Ferrite is used in applications such as signal transformers, which are of small size and higher frequencies, and power transformers, which are of large size and lower frequencies. Also some of its main applications are EMI Suppression, Automotive power electronics, Switch Mode Power Supplies and DC-DC converters [64]. Some application considerations-Ferrite advantages and disadvantages are shown in Figure 7.1 Appendix A.

In this thesis, the characterised inductor is aimed to be used as a part of an LC filter in the output of a DC-DC converter. The switching frequency is >100 kHz. Thus, magnetic core Ferrite N95 [52], with flux density $B_{max} = 0.45\,T$, is chosen for the following reasons:

1- For its high permeability and low losses (especially eddy current losses), (Refer to Figure 7.2 Appendix A).
2- Ferrite cores can be made in a various shapes such as toroid, E-I cores, U-I cores, Tube and EER cores, as shown in Figure 2.9.

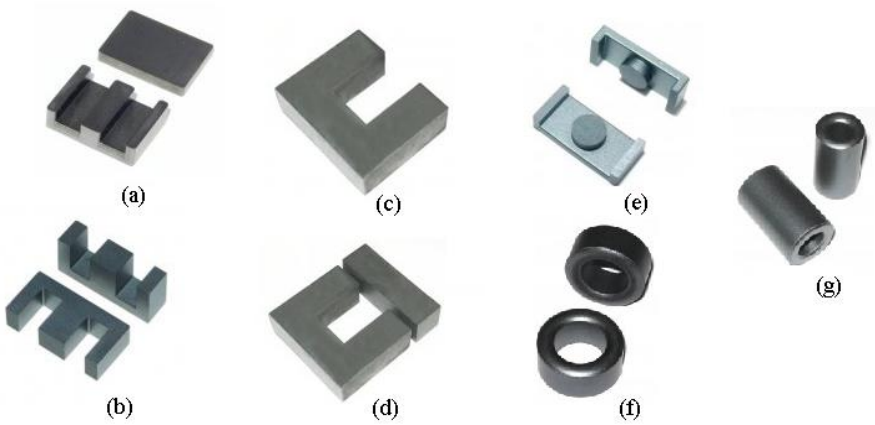

Figure 2.9- Different shapes of Ferrites cores. (a)E-I core. (b) E-E core. (c) U core. (d) U-I core. (e)EER core. (f) Toroid core. (g) Tube core [65]..

3- A ferrite pot core is inherently self-shielding by nature of the enclosed magnetic circuit.
4- Ferrites core operate at high frequencies up to 1MHz.

2.3 Proposed Design of the Inductor and Core

One of the aims of the work reported in this thesis is to increase the energy density of an inductor to facilitate its integration into power module packages by applying high current density to the windings. Thus, a high energy density inductor is designed using a specific design of the magnetic material, within the available volume, in order to achieve the desired inductance value with a small geometry and distributed air gap. The inductor is interfaced to a ceramic substrate material and as such, will allow a direct conduction path from the winding to the outer surface and on to the thermal management system. The total approach is explained as shown in Figure 2.10.

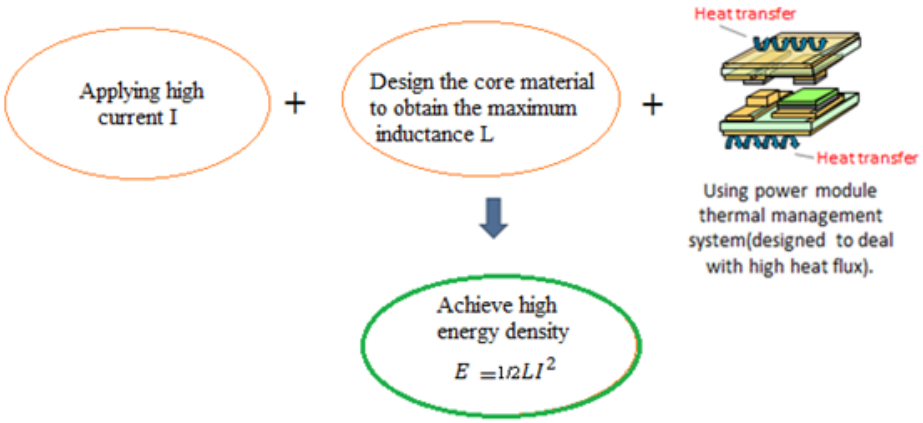

Figure 2.10- The procedure of achieving high energy storage density.

Figure 2.10 shows the procedure of increasing the energy of the inductor by applying a high current, as explained in EQ 2.25, whilst providing an effective cooling method in order to limit the temperature increase due to the losses accrued.

$$E = \frac{1}{2}Li^2 \qquad \text{EQ 2.25}$$

where,

E is the energy (Joule), L is the inductance in (H) and i is the current (A)

The copper winding geometry is designed with square cross section in order to provide sufficient contact with the substrate and the cooling system. This will allow a high current to be applied through the inductor.

The magnetic circuit analysis, both analytically and with the use of development software, Maxwell 16.0 will be presented. A ferrite magnetic core material with distributed air gaps is proposed and its effect on the energy density and inductance stability will be investigated. The magnetic flux distribution will be checked by using Maxwell (Magneto-static) simulation. The stability of the inductance against an increase in the DC bias will be validated experimentally. Such an approach will help to understand the real performance of the inductor and the core with distributed air gaps under high DC current.

2.3.1 Winding Geometry

In order to increase the energy density the current density is increased and thus the copper surface should also be increased in order to enhance heat conduction whilst choosing the winding geometry in order to increase the cross sectional area. A rectangular cross section, as shown in Figure 1.2-(a) was chosen. This winding shape is as suitable for the volume available within the package on the substrate, as shown in Figure 1.1. The Inductor geometry and dimensions details can be found in Figure 7.3-(a) Appendix A.

Some different aspects of the proposed inductor geometry have been considered as following:

1. The rectangular cross section winding provides a full connection between the inductor outer surface and the substrate of the cooling system which ensures greater heat conduction from the inductor, comparing to a rounded cross section winding which provides reduced connection area between the surfaces as shown in Figure 2.11.

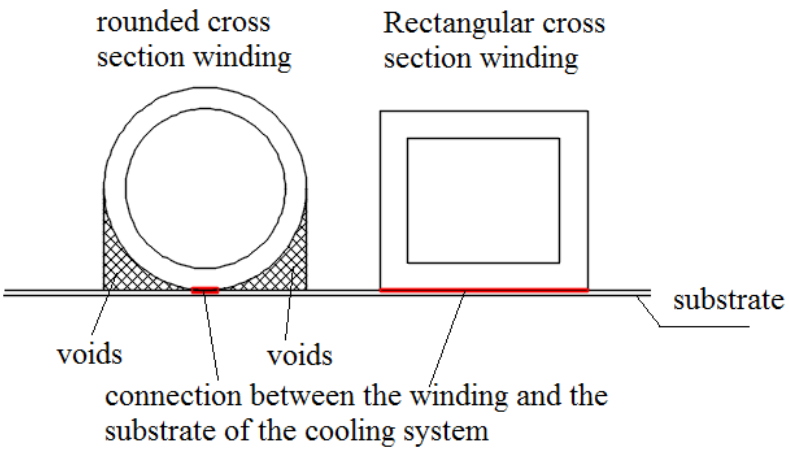

Figure 2.11- Comparison of the connection between the winding and the substrate for rectangular and rounded cross section winding.

2. The inductor is manufactured from the same material as the top layer of the substrate.
3. The inductor geometry is single layer solenoid which means reduced parasitic capacitance as there are no layers as in a typical inductor construction. However, the gap between the turns is very small thus the parasitic capacitance between the turns needs to be considered and investigated.

The sharp corner of the conductor however will show an increased resistance to the flow of the current through it. Still, this issue has no impact on the inductor performance as the current density in the corner of the winding shown a drop in a small area of $a\sqrt{2}$, as it was examined by simulations (Maxwell) and shown in Figure 7.4 Appendix A.

2.3.2 Design of Magnetic Core

Considering the design constrain and the selected winding geometry, the total magnetic length and cross section available for this inductor is limited. A schematic of available space for the inductor and the magnetic core on the substrate is shown in Figure 1.1.

A Ferrite N95 core with a shape, as shown in Figure 2.12-(a), has been chosen to suit both available volume on the substrate and the inductor geometry. N95 Ferrite was chosen due to its low loss/characteristics at high frequencies and flux saturation $B_{sat} = 0.5\,T\ at\ 25\,°C\ \ and\ B_{sat} = 0.41\,T\ at\ 100\,°C$. This material is used as a magnetic flux guide and in order to prevent core saturation at high current, a significantly long air gap needs to be inserted. Different ways of achieving the air gap are shown in Figure 2.12.

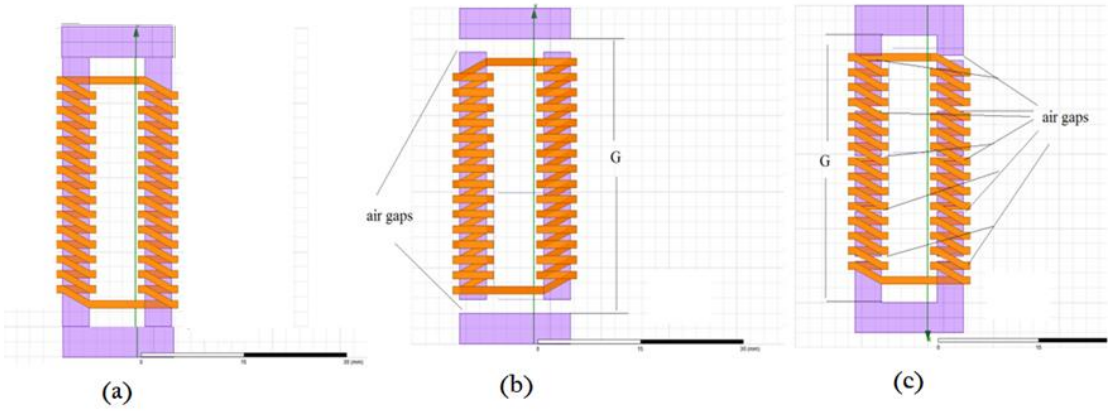

Figure 2.12- Inductors with N95 core (a) without air gap. (b) With 4 distributed air gaps. (c) With 10 distributed air gaps.

In the following section the effect of the presence of an air core, length, position and the number of air gaps on the magnetic path, inductance stability and the saturation of the core will be examined. The stability of the inductance against the increasing DC current and saturation effect will be examined with the usage of Maxwell16.0 3D software (Magneto-static solver) and validated experimentally. A schematic of dimensions details of the core with the distributed air gaps is shown in Figure 7.3 Appendix A.

2.4 The Design Specification

The effect of the presence of an air core, length, position and the number of the air gaps on the magnetic path, inductance stability and the saturation of the core will be examined. First the total length of the required air gap due to the system specification will be found as follows.

The compact inductor needs to be operated with a high current of up to 80A-DC, with a desired inductance L of around 25 μH. These values have been chosen in consideration with an existing project requirements [51], as it has been mentioned in chapter 1.

Due to both manufacturing and thermal management limitations, the cross section of the winding cannot be smaller than 1 mm^2 and since the aim is to achieve a current density of $J = 50\ A/mm^2$ with an average current up to 80 A, the cross section of the winding will be around 1.5 mm^2. Considering the volume constraint on the substrate and by assuming the minimum possible gap, which it is possible to be manufactured, between the turns of the inductor around 0.4 mm, a, this allows the insertion of two inductors each with 26 turns (dimensions of the inductor's winding are shown in Figure 7.3 Appendix A).

Consequently, the total number of turns will be N=52, cross section of the winding is $1.7mm \times 0.9\ mm$ and the available cross section of a core $A_c = 10mm \times 10\ mm$. The flux density saturation of the N95 ferrite is $B_{sat} = 0.41\ T\ at\ 100°C$, thus a maximum value of flux density B_{max} in the air gap is chosen $B_{max} < B_{sat} = 0.3\ T$. By using EQ 2.18 the total air gap length required to avoid the core saturation when applying a current up to 80 A is:

$l_g = \frac{Ni\mu_0}{B_{max}} \approx 18\ mm \quad : \mu_0 = 4\pi \times 10^{-7}\ (H/m)$.

As the total air gap length is too large to be used as one air gap, it will be distributed locally into a larger number of smaller air gaps along the length of the core. The number and the length of distributed airgaps and their effect on the inductor performance of inductance stability and saturation will be examined in the following section

2.4.1 Simulation Results

The effect of the presence of an air core, length, position and the number of the air gaps on the magnetic path will be examined. The calculated air gap's length will be divided into different arrangements. 4 distributed air gaps of 4.5 mm each, 6 distributed air gaps of 3 mm and10 distributed air gaps of 1.8 mm each as it is shown in Figure 2.13. In general, the magnetic field will choose the path with the smaller

reluctance, thus from EQ 2.11 the reluctance in the air gaps with l_g and d (the distance between the two long legs of the core, as shown in Figure 2.13) length will be respectively:

$$R_g = \frac{l_g}{\mu_0 A_g} \text{ and } R_d = \frac{d}{\mu_0 A_g}$$

thus,

$$\frac{R_g}{R_d} = \frac{l_g}{d} \qquad \text{EQ 2.26}$$

$R_g < R_d$ when $l_g < d$

if $l_g > d$ then the magnetic flux will fringe between the long leg of the core choosing the shortest path.

In the case of 4 air gaps each air gap's length $l_g = 4.5\ mm \leq d = 6\ mm$, in the case of 6 air gaps each air gap's length $l_g = 3\ mm < d = 6\ mm$ and in the case of 10 air gaps each air gap's length $l_g = 1.8\ mm < d = 6\ mm$. (d) is the distance between the two legs of the core.

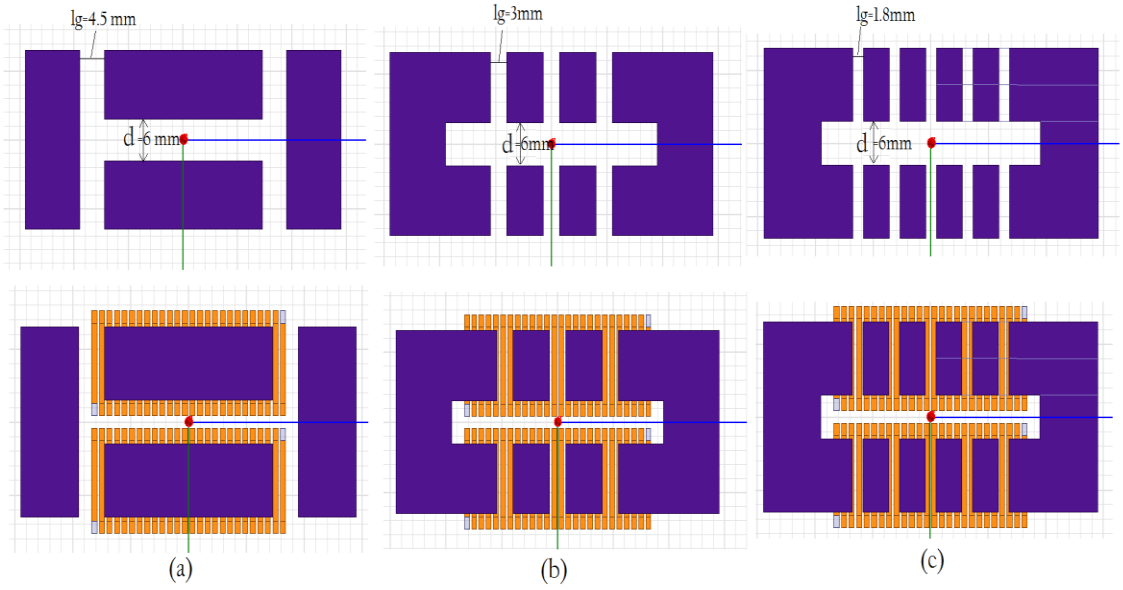

Figure 2.13- The presence of an air core, length, position and the number of the air gaps along the core. (a) 4 air gaps. (b) 6 air gaps. (c) 10 air gaps.

2.4.1.1 The effect of the air gap on the magnetic path and saturation

The inductor with core (a), (b) & (c), as in Figure 2.13, have been simulated in Maxwell (Magneto- Static solver) and a current of 80A DC has been applied to the inductors. The flux density inside the core for the three cases at 80A have been plotted as shown in Figure 2.14.

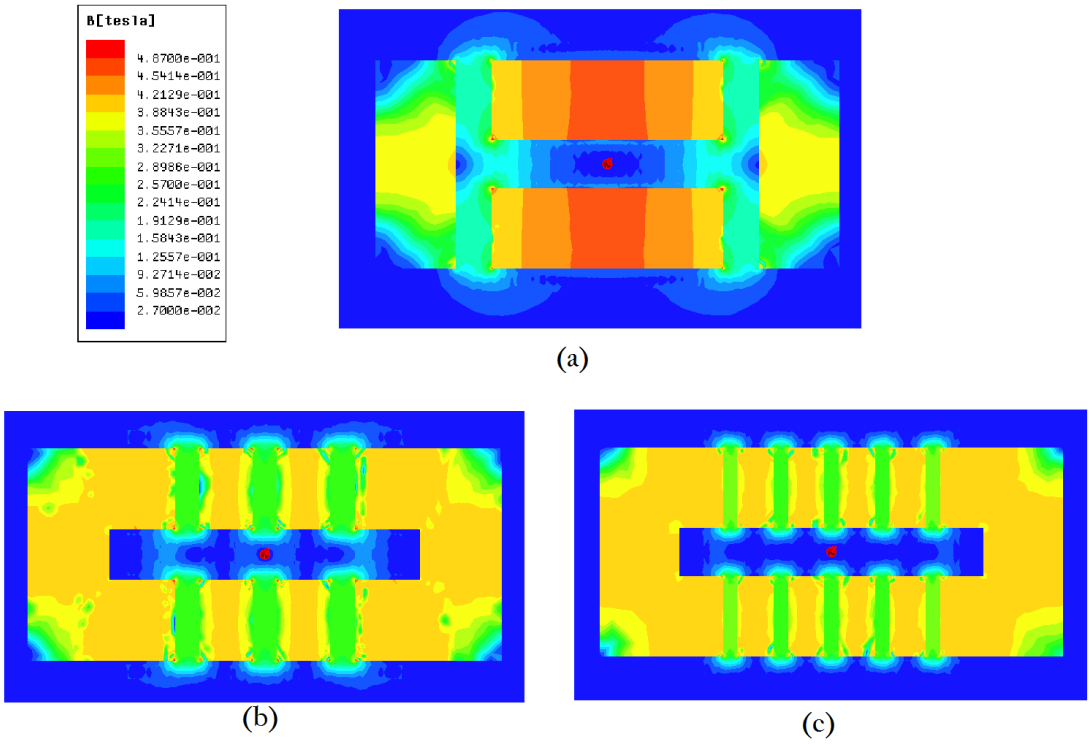

Figure 2.14- The flux density inside the core at current 80A. (a) 4 air gaps. (b) 6 air gaps. (c) 10 air gaps.

Simulation shows the flux density in inductor with core (a), (b) and (c). By applying the same current of 80 A, with distributed air gaps the flux density is spread homogeneously inside the core and the air gaps and the magnetic fringing is equal inside the airgaps, as shown in Figure 2.14-(b)&(c) and is even more homogeneous in core (c) than it is in core (b). While with four air gaps as in Figure 2.14- (a) the flux density is not equal and a significant leakage of the magnetic flux between the two legs of the core can be seen. One of the main issues is that the air gap length l_g should be significantly smaller than the distance between the two legs of the core d as explained in EQ 2.26, otherwise, the magnetic field will chose the shortest available

path, where the reluctance is smaller. Thus, the magnetic path will be as in Figure 2.15. It is also clear that the core with the least number of distributed air gaps will saturate before reaching the maximum flux density in the air gap comparing to the other cores with more distributed air gaps.

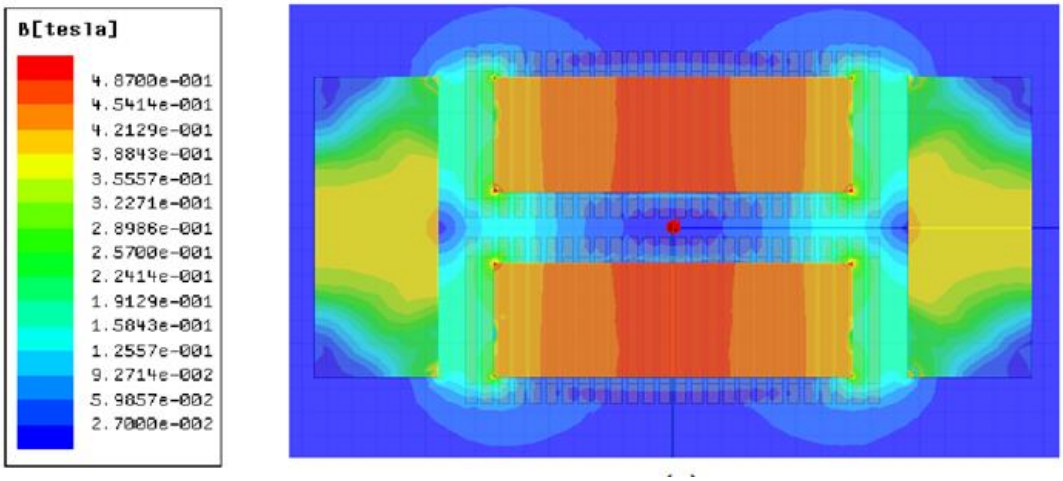

Figure 2.15- Magnetic flux density in the core with four air gaps at 80A.

Furthermore, it can be seen that the choice of the air gap position can directly determine the proximity losses at the high frequencies, as the magnetic flux leakage increases due to the interaction between the magnetic field and the winding [66]. In this design, as there is a tiny distance between air gap and winding, selecting a significantly long air gap will lead to more losses at high frequencies where magnetic field leakage will interfere with copper. Figure 2.16 shows the interference between the magnetic leakage and the copper winding for two cores with different numbers of air gaps. Thus, distributing the total airgap along the core into smaller air gaps, as in Figure 2.16-(b), has been chosen in order to reduce this effect.

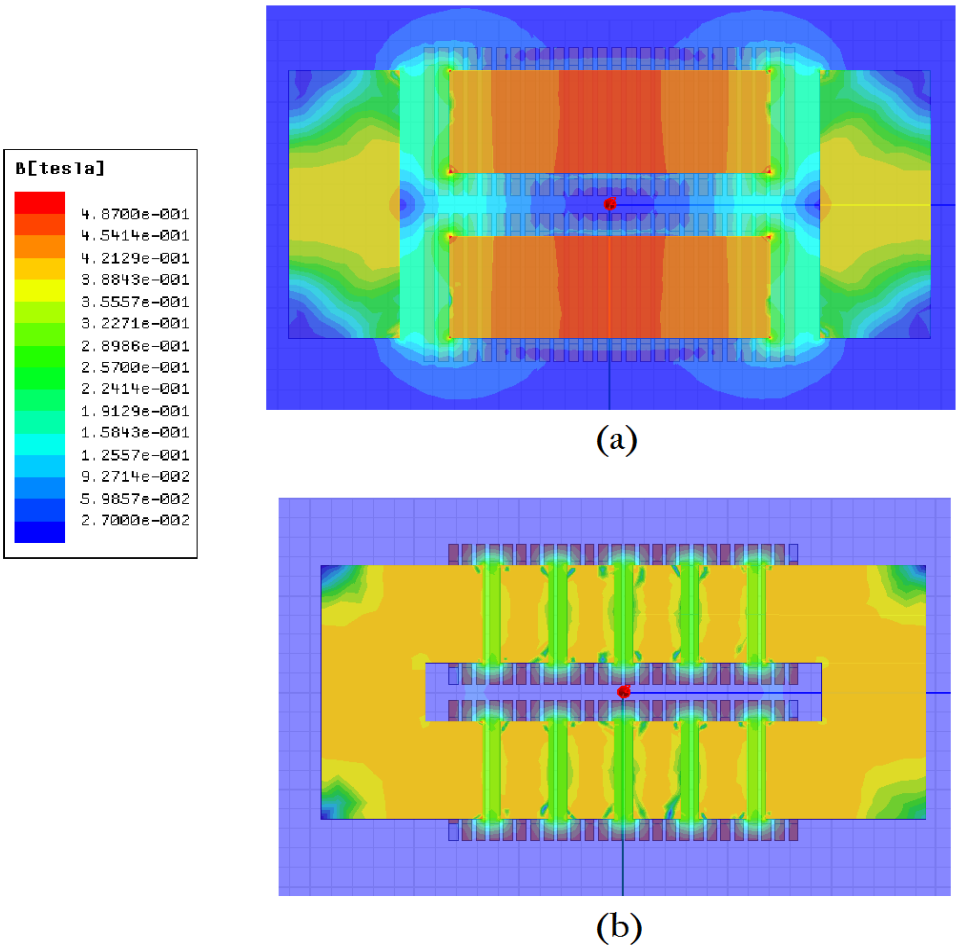

Figure 2.16- The interfering between the magnetic leakage and the copper winding-80A. (a) The core with 4 air gaps. (b) The core with 10 air gaps.

The inductors with core (a) (b) and (c) (Figure 2.14) have been simulated in Maxwell (Magneto-static), the current has been increased from 5 A to 100 A. the inductance's values L against I_{dc} have been plotted and are shown in Figure 2.17.

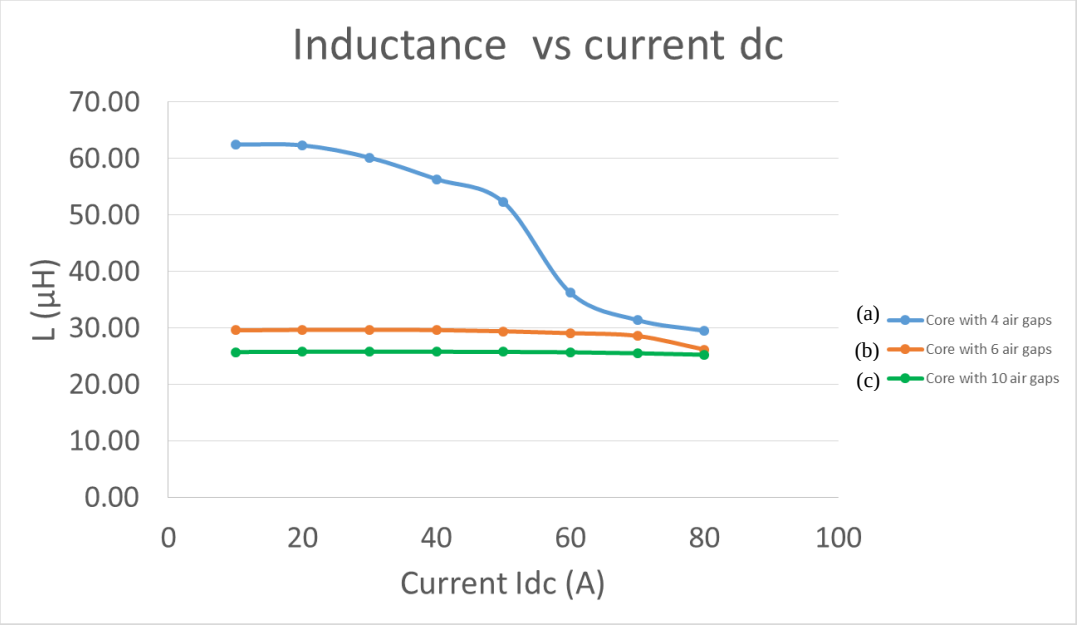

Figure 2.17- Inductance L vs current I_{dc}. (a) 4 air gaps. (b) 6 air gaps. (c) 10 air gaps.

It can be seen that having a larger air gap will cause the inductance to drop sharply as the current increases. This is due to the saturation inside the core, while distributing the total air gap into a larger number of smaller air gaps will avoid the saturation of the core till a higher current value and thus inductance is more stable against the increasing current as for core (b) and (c).When the reluctance of the core R_c is smaller than the reluctance of the air gap R_g, as in the case with long air gaps, the magnetic flux will prefer to stay in the core material and fringe around it causing an exchange in between the two legs as shown in Figure 2.14.

This effect will dominate until the increasing current starts to drive the core to saturation, then $R_c >> R_g$ and the magnetic flux will fringe outside the core. The method used by Maxwell to find the inductance matrix is explained later in chapter 4.

The core with 10 airgaps is offering a fixed value of inductance around 25 µH $\pm$ 20% which is important in the specification.

2.4.1.2 The effect of number and position of the air gaps on the volume and stored energy

The effect of the presence of an air core, length and position of the air gap on the energy density of the inductor have been examined. The inductors with cores (a), (c), as in Figure 2.13, have been simulated in Maxwell (Magneto- Static solver) whilst applying a current of 80A to the inductors. The stored energy in the air gaps has been found for the both cases and has been plotted in Figure 2.18.

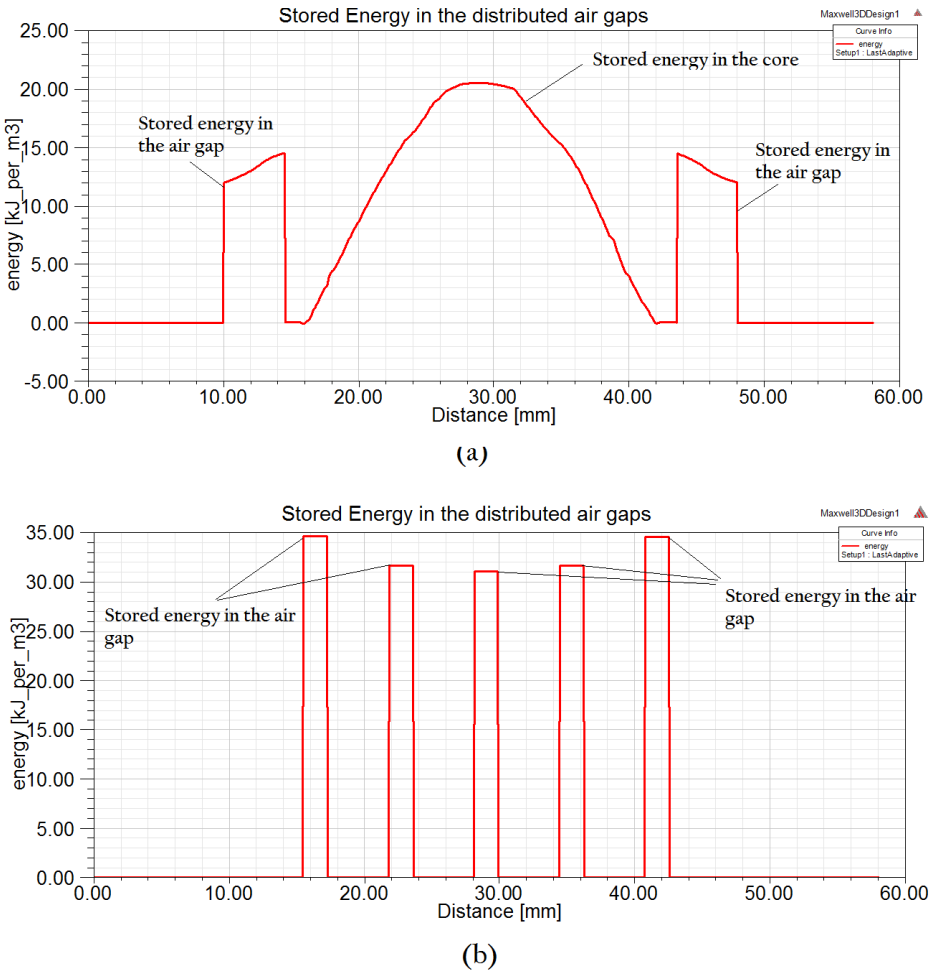

Figure 2.18- The stored energy in the air gaps in one leg of the core at 80A. (a) The core with 4 air gaps. (b) The core with 10 air gaps.

By distributing the air gap along the core the energy stored inside the gaps increases, as it is shown in Figure 2.18, the energy stored in the air gaps of core (b), as in

Figure 2.16-(b), is showing an average of 33 (kJ/m^3) in each air gap which means a total of 330 (kJ/m^3) in the total air gap.in both legs. While, core (a), as in Figure 2.16- (a), shows an average of 12 (kJ/m^3) in each air gap and 10 (kJ/m^3) inside the core, and a total of around 68 (kJ/m^3) in both airgap and core material in both legs.

It can be seen from the results that the most improved design with the desired inductance value considering the design volume constraint and under high current up to 80A is the inductor with the core and ten distributed air gaps (Figure 2.14-(c)). It offers an inductance of around 25 µH and a total stored energy of 330 kJ/m^3 at 80A.

2.4.2 Inductance vs DC Bias Experimental Validation

The saturation of the core has been investigated by verifying the inductance L against an increasing current experimentally. By having the inductors with both cores (a) & (c), as in Figure 2.13-(a)&(c), the input of a dc-dc converter was created (the experiment bench will explain in details in chapter 5) and with a switching frequency of 100 kHz different current values have been obtained and the inductance L has been measured from the current and voltage waveforms (taking an average over the undistorted section of the waveform) for each current level, as shown in Figure 2.19, and with the usage of EQ 2.27.

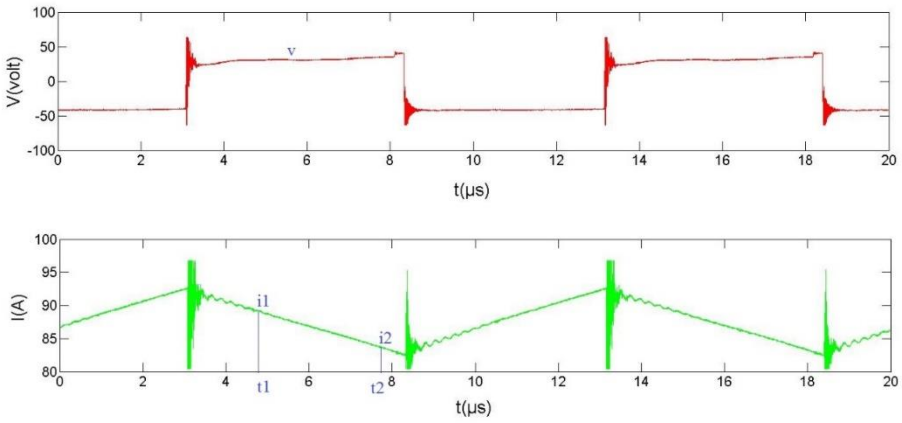

Figure 2.19- Current and voltage waveforms for current level 88 A

$$L = V \times \frac{t_1 - t_2}{i_2 - i_1} \qquad \text{EQ 2.27}$$

Inductance values against the increasing of the dc current are plotted for both cores and compared as can be seen in Figure 2.20 (a) & (b).

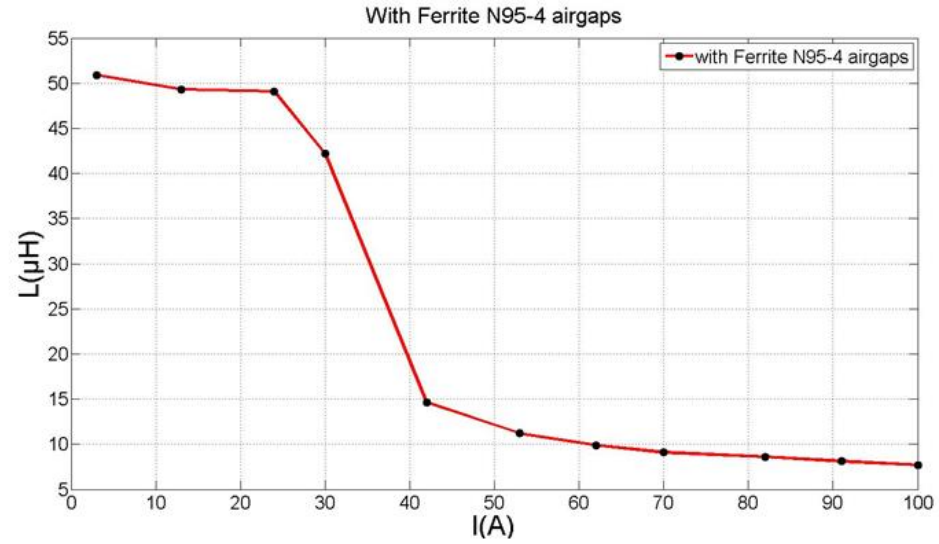

(a)

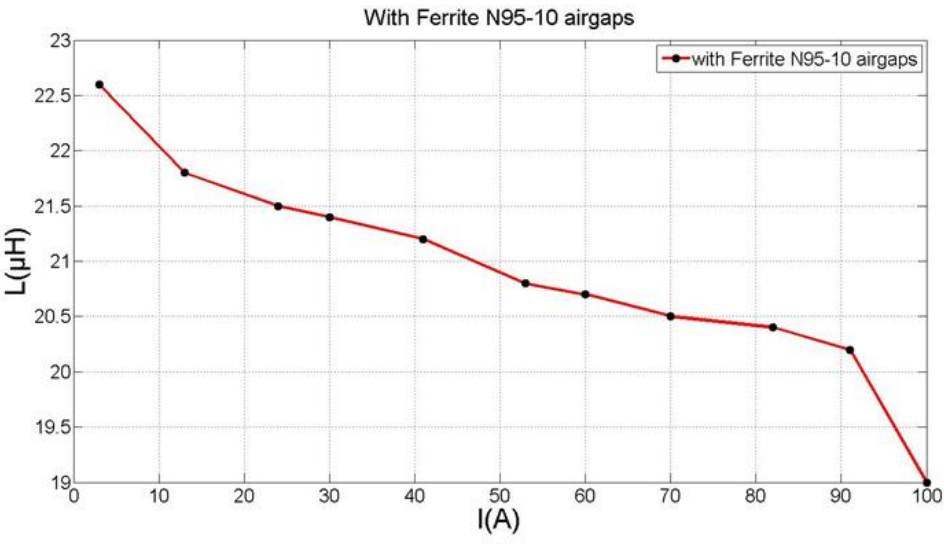

(b)

Figure 2.20- Verifying the inductance of the cored inductors against the increasing current. (a) The core is with 4 air gaps. (b) The core is with 10 air gaps.

The inductance L of the core with 4 air gaps has been found against the increase in DC current as shown in Figure 2.20-(a), and it is verified to be equal to 7 μH at 80A

and this is much less than 80% percent of its value at zero dc current ($0.8 \times L$ at 0 A) which is a maximum inductance of 52 µH.

The inductance L of the core with 10 distributed air gaps has been found against DC current and is shown in Figure 2.20-(b), and it is verified to be equal to 20.4 µH at 80A and this is higher than 80% percent of its value at zero dc current ($0.8 \times L$ at 0 A) which is equal to 22.7 µH. This is considered to be a sufficient value from a design perspective and indicates that the core will not saturate fully at the desirable current of 80 A.

2.4.3 Comparison with Commercial Inductors

A comparison between the design inductor and a high current helical inductor-30uH-180A [67] from the saturation perspective has been done. For the commercial inductor dimensions and details please refer to Figure 7.5 in Appendix A.

Figure 2.21 shows the inductance against the increasing of the current for both the designed and the commercial inductor.

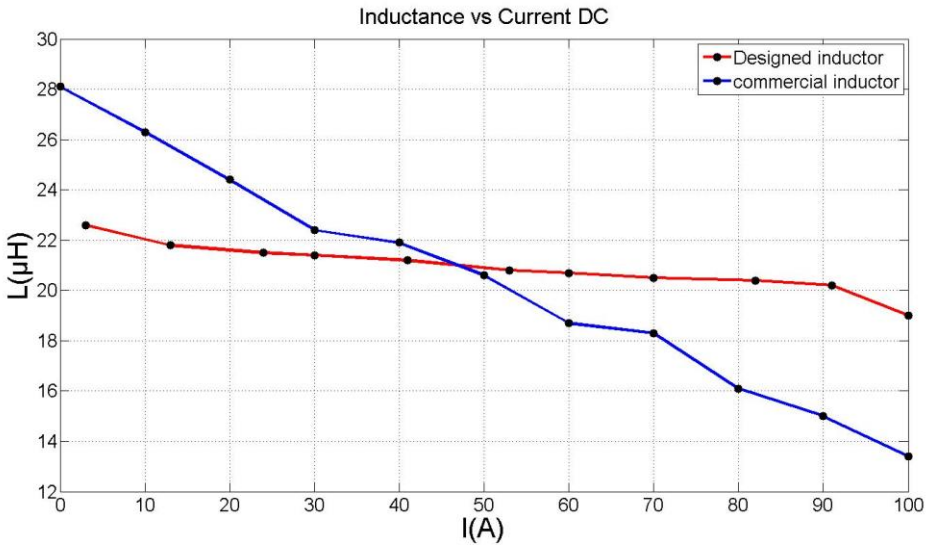

Figure 2.21- Verifying the inductance against the increasing of the current for both the designed and the commercial inductor.

It can be seen from both curves, which have a linear relationship with the DC current, that the commercial inductor's saturation current Isat at which its inductance value drops to 80% below the measured value with no DC current is about 30 A. Actually

this value is much than 180 A which is the rated current of the commercial inductor. Thus, the designed inductor shows more inductance stability against the increase in current which means it has a higher saturation current level.

By basic fitting the inductance curve of the commercial inductor (L = - 0.14*i + 28) thus at 180 A L= 1.8 uH.

2.5 Conclusion.

This chapter has described the design of a cored inductor based on a solenoid geometry. The design was tailored to be integrated in a minimum existed volume on the substrate, with a current up to 80A DC applied across the inductor in order to achieve a high current density and with a desired inductance around 25 µH. With the aim of preventing saturation of the magnetic material, a distributed air gap system is introduced in order to achieve the desired inductance value in the available volume when operated at the maximum current. Ferrite N95 was used as a core material.

The influence of the core material geometry and airgap has been determined by investigating the stability of its inductance against an increasing DC current. Also, the saturation effect has been examined with the use of Maxwell16.0 3D software (Magneto-static solver) and validated experimentally. The results have shown that it is possible to ensure a stable inductance under high DC bias current, allowing successful avoidance of the saturation of the core by distributing the air gaps along the core.

On the one hand the core material has increased the inductance of the inductor but on the other hand the total losses will also increase due to an increase in magnetic losses caused by the core. The losses in the ferrite and how the fringing flux will affect the AC loss will be investigated later in chapter 5.

3 Chapter 3- Thermal Management

3.1 Introduction

The cooling of passive components, especially inductors, is always challenging as the thermal management system needs to be designed to remove heat from the windings and core, which are often buried or inaccessible. The advantage to having the inductors integrated into the power module is that the conductors could be constructed, in whole or in part, from the substrate materials, allowing a direct conduction path from the winding to the substrate outer surface and on to the thermal management system. This means that very good heat transfer will be possible from the inductor winding.

This chapter aims to build on simulation, theoretical and experimental results and focuses on achieving a sustainable high current density of more than 50A/mm^2, in the inductor. The inductor windings are soldered on a DBC (Direct Bonding Copper) ceramic substrate, as shown in Figure 3.1 . A single-sided cooling method applied on the bottom copper layer of the substrate is proposed. Direct substrate cooling with water is used in order to realise a high film heat transfer coefficient at the cooled surface and so minimise the overall thermal resistance between the windings and the coolant. The thermal design of the proposed package (inductors and DBC) will be analysed in order to understand the heat conduction through it.

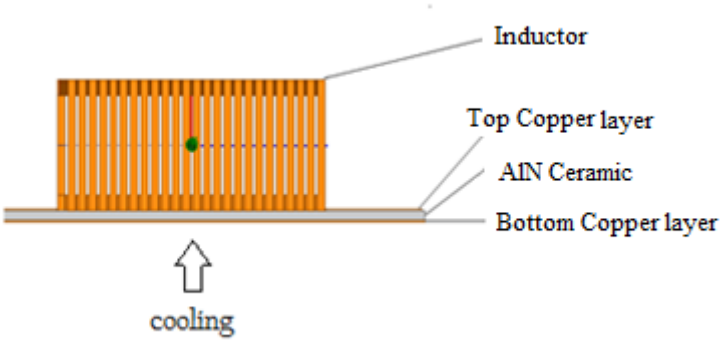

Figure 3.1- The proposed package; inductor is soldered on a DBC ceramic substrate with a direct cooling is applied on the bottom copper substrate.

A key factor in the design of a high energy inductor is on one hand increasing the current density in the windings and on the other hand using an integrated thermal management system to better manage the temperature increase of the inductor [49]. Thus the energy storage density ρ_E of the inductor, which is proportional to the current squared, $\left(\rho_E = \frac{1}{2} LI^2/Volume\right)$ will increase and hence the power density of the converter can be increased.

The magnetic component is designed in a way to increase the area of the windings which are in contact with the cooling system in order to increase the heat exchange surface. The windings are cut from bulk copper with a geometry and dimensions as shown before in Figure 7.3 Appendix A.
Integration of local passive components at the substrate reduces the lengths of interconnections and the related parasitic elements and greatly improves the EMI filter performance, especially at high frequency [69].

Furthermore, having both active and passive components on the same substrate will allow the reduction in the total power module package size and admits the possibility of cooling the components with the use of direct liquid cooling methods on the bottom of the substrate.

A schematic representation of integrating passive and active devices on the same base plate, considering the proposed cooling system is shown in Figure 3.2.

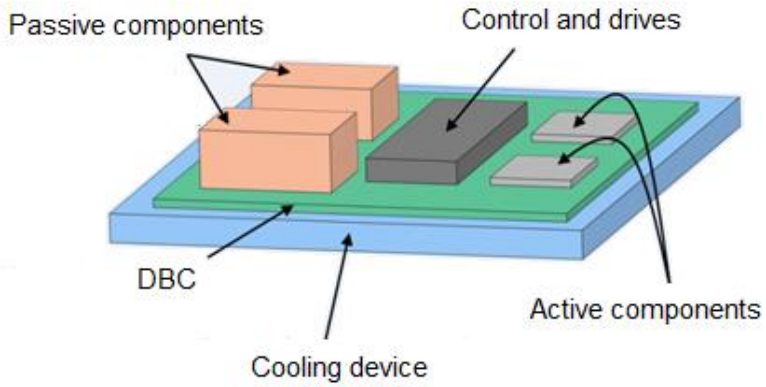

Figure 3.2- A Schematic representation module showing Integration of passive, active devices and other circuitry's components on the same base plate/DBC, considering the cooling system.

3.1.1 The Need for Improved Cooling

Thermal management is a crucial step in packaging power electronic components, as heat generated due to losses in the devices must be conducted away from the power devices into the environment using a low loss method in order to prevent any overheating and consequently any failure of the power electronic devices. Besides certain parts of the power module, such as the solder layer, have a higher probability to cause a failure with thermal cycling [70] [71] [72][11]. if a proper cooling system is not considered .

In the context of high power density, smaller power module packaging would be preferable. However the losses generated by the devices implemented in smaller volumes need to be considered, thus several approaches have been implemented trying to achieve high power density with regards to thermal cycling [3][73][74]. Bryan and Forsyth [11] have introduced a DC-DC converter with power density of 4.3 $kW.kg^{-1}$ using a water cooled cold-plate and magnetic components potted in aluminium heat-sinks to achieve this power density . As power density is increased, the surface area available for cooling is reduced. So, an improved cooling method such as direct liquid cooling was found to be more effective at cooling the power module compared to a traditional heatsink and cold plate [75][76].

3.1.2 Theoretical Background

The three main aspects in the design of a cooling system, from a theoretical point of view [82], can be summarised as follows:

1- Conduction of heat through materials, thus it is important to choose materials with small thermal resistanceR_{th}, such as copper for instance.
2- Heat flux *Q* flows across interfaces between different materials.
3- Heat transfer *h* to the coolant fluid by convection.

In general conduction is much more dominant than convection.

The performance of the heat spreader is a function of the size of the heat source, the thermal properties of the spreader itself and the heat transfer coefficient generated by the cooler as described in EQ 3.1[82] and shown in Figure 3.3. If the thickness of the heat spreader is increased, the thermal resistance will increase also, whereas if the

thermal conductivity of the heat spreader is increased the thermal resistance will be lower.

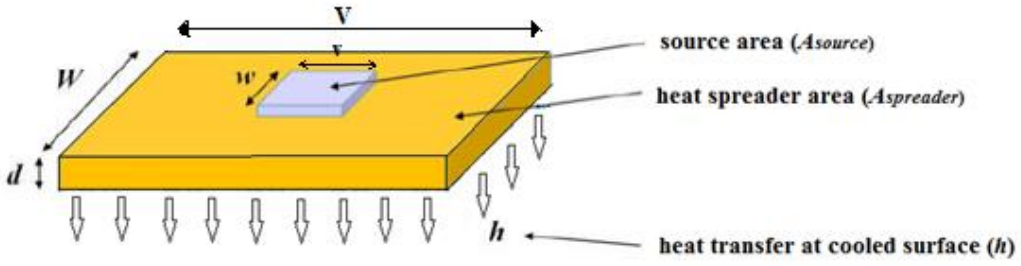

Figure 3.3- Schematic diagram of a small heat source of width (w) on larger heat spreader plate of thickness (d) and width (W)[82].

With no heat spreader, the source temperature would be determined solely by the heat transfer coefficient, *h*. A higher *h* would result in a lower source temperature.

$$r_{th,sp} = \frac{1}{h_{eff}} = \frac{A_{source}}{A_{spreader}}\left(\frac{1}{h} + \frac{d}{k}(1+F)\right) \qquad \text{EQ 3.1}$$

Where $r_{th,sp}$ $(K.m^2W^{-1})$ is the specific thermal resistance, k $(W.m^{-1}K^{-1})$ is the conductivity of the heat spreader material, h is heat transfer at the cooled surface $(W.m^{-2}K^{-1})$ and F is a geometrical factor which depends on the shape of the source, it is a function of following $F\left(\frac{W}{w}, \frac{d}{w}, \frac{k}{hw}, \frac{v}{w}, \frac{V}{v}\right)$, (F>0).

Where:

W is the width of the heat spreader (*m*).

w is the width of the source (*m*).

d the thickness of the heat spreader (*m*).

V is the length of the heat spreader (*m*).

v is the length of the source (*m*).

h is heat transfer at the cooled surface $(W.m^{-2}K^{-1})$.

k is the thermal conductivity is the thermal conductivity of the heat spreader $(W.m^{-1}K^{-1})$.

$$R_{th} = \frac{r_{th,sp}}{A}$$ EQ 3.2

R_{th} is the thermal resistance of an object (KW^{-1}), A is the area of the object (m^2).

3.1.2.1 Heat Transfer by Conduction

In general, the heat generated inside a package should be conducted out, from the heat source to the ambient, to avoid any overheating. When there is a temperature difference across a material, as it is shown in Figure 3.4, the energy (per unit time expressing power) flows from the higher temperature end to the lower temperature end. It is given by the standard formula:

$$P_{cond} = \frac{\mathrm{kA\Delta T}}{\mathrm{d}}$$ EQ 3.3

Where ΔT = T2 – T1 degrees centigrade (*ºC*), A is the cross-sectional area in square meters, d is the length in meters, and k is the thermal conductivity in watts per meter degrees centigrade or kelvin ($W.m^{-1}K^{-1}$)[77].

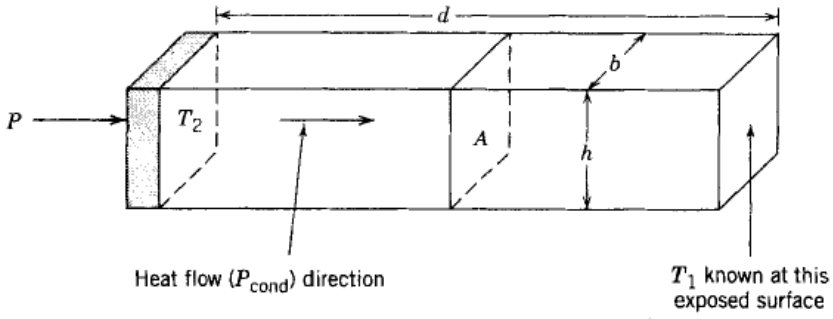

Figure 3.4- The conduction of P watts of heat energy per unit time [77].

From EQ 3.3, it can be understood that the larger the area of the surface is, the higher is the conductivity. Moreover, a package should be made of a materials with a high thermal conductivity such as copper and aluminium nitride AlN which is an insulating ceramic used as the electrical insulator in the DBC. These materials have a high thermal conductivity (70-285 $W.m^{-1}K^{-1}$) for AlN and (400 $W.m^{-1}K^{-1}$) for copper. Another material would be Aluminium oxide Al_2O_3 with thermal conductivity (28-35 $W.m^{-1}K^{-1}$) at ambient temperature [78].

The thermal resistance R_{th} is defined [77]:

$$R_{th} = \frac{d}{\mathrm{kA}} \qquad \text{EQ 3.4}$$

The thermal resistance has units of degrees Kelvin per watt ($K.W^{-1}$).

3.2 Improved Cooling Methods for Power Electronics

This section highlights some of the different thermal management and improved cooling methods which are available to the design engineer when designing a system. Recent studies suggested integrating the design of the cooler as part of the module in order to increase the efficiency of its associated cooling system [3] [79] [80].

In general the performance of a solid heat spreader is determined by the thermal conductivity of the coolant material *k* ($W.m^{-1}K^{-1}$), the cooling mechanism which is characterised by an effective heat transfer coefficient *h* ($W.m^{-2}K^{-1}$) and the physical size of the heat source L (m) which is the volume of the body divided by the surface area of the body. For cuboidal spreaders, the heat transfer behaviour is determined by the Biot number [79]:

$$B_i = \frac{hL}{k} \qquad \text{EQ 3.5}$$

A value of the Biot number smaller than 0.1 implies that the heat conduction inside the body is much faster than the heat convection away from its surface [79].

Thus, a heat source with relatively big physical size will cause a high increase in the temperature but its big surface area will provide sufficient contacting with the coolant in the cooling procedure. Using a proper cooling mechanism which offers the required heat transfer coefficient is a key factor in thermal management.

Some typical heat transfer coefficients are given in Table 7.1 in Appendix B. For instance air convection cooling has low thermal conductivity of 3- 25 ($W.m^{-2}K^{-1}$) which makes it a poor cooler medium and in order to improve the performance of a cooler which uses the air as a coolant, heat spreaders and finned surfaces are used [3] [81]. Liquids offers a higher heat transfer coefficients, for example, water has a thermal conductivity of 15-1000 ($W.m^{-2}K^{-1}$). The following subsections describe different cooling approaches and implementations.

3.2.1 Integrated Baseplate Coolers

Direct cooling of the electronic package can reduce the number of bonded layers and interfaces in the package resulting in a more compact and lightweight system. Improved design and integration of material choices and cooling can greatly improve the performance of power modules. In this method, the baseplate of the power module can be used as part of the cooler itself, when liquid coolant is in direct contact with the baseplate material.

It has been suggested in previous studies [76][79] that a heat spreader is not needed if a direct water cooling technique, with high heat transfer coefficient ,typically 20 ($kW/m^2.K$), is used. By removing the base plate, the thermal resistance, mass and volume of the combined electronic package and cooler is reduced. Figure 3.5-(a) shows a typical power electronic module where the heat generated by the devices is removed by means of a conduction path through the substrate tile followed by the copper baseplate to the final fluid swept surface at which convection occurs.

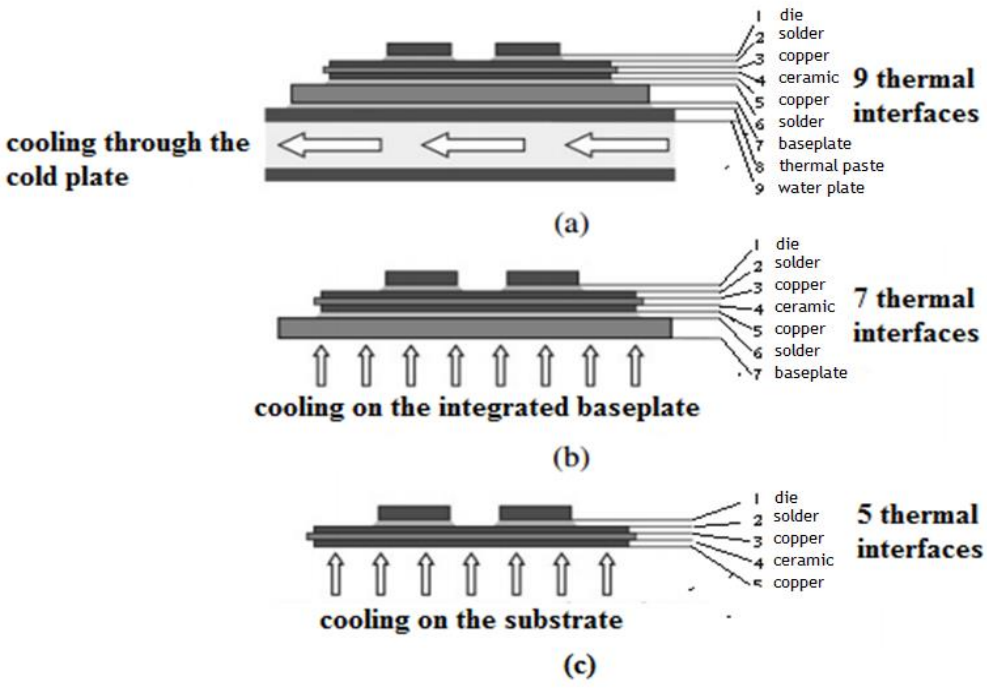

Figure 3.5- Cross-sections of the power module structure in various assemblies. (a) Substrate tiles on copper baseplate which is mounted onto a cold plate with a layer of thermal paste. (b) Direct cooling of the baseplate with liquid coolant. (c) Direct cooling of the substrate tiles [76].

The baseplate is mounted onto a cooler in the form of a cold plate. There are nine thermal interfaces between the die junction (where heat is generated) and the coolant fluid, as illustrated in Figure 3.5-(a) and they are:

1. Die / Solder
2. Solder / Copper
3. Copper / Ceramic
4. Ceramic / Copper
5. Copper / Solder
6. Solder / Baseplate
7. Baseplate / Thermal Paste
8. Thermal Paste / Water Plate
9. Water Plate / Water Coolant.

In order to sufficiently cool the electronic devices it is desirable for there to be as little thermal resistance between the hot die and the surface where heat transfers by convection to the cooling fluid [76]. This can be achieved in a number of ways: by using high conductivity materials, by thinning each layer, or by reducing the number of layers in the package. By cooling the baseplate of the power module directly with liquid (shown schematically in as in Figure 3.5-(b)). Two thermal interfaces can be removed, namely the layer of thermal paste and the thermal interface between the baseplate and the cooler, which highly contribute to the total thermal resistance of the module [82]. Thus, it goes from method (a) to (b) with 7 layers.

Furthermore, if a cooling method generating a sufficiently high heat transfer coefficient is used a heat spreading baseplate may not be necessary. The number of thermal interfaces can be further reduced by not including the baseplate in the assembly. Thus, two further layers (the copper baseplate and the layer of solder) can be removed reducing the number to five, as shown in Figure 3.5-(c), assuming that the bond between the ceramic and the copper is perfect. The geometry of the cooling arrangements were beyond the scope of the project.

3.2.2 Double sided cooling

Cooling a module on both its top and bottom side provides increasing amount of cooling to the devices compared to being cooled on one side. The power electronic devices can be soldered between two DBC’s, as illustrated in Figure 3.6, resulting in what is often referred to as a 'sandwich module' [80]. Cooling methods with sufficient heat transfer coefficient can be used to directly cool the substrates as illustrated.

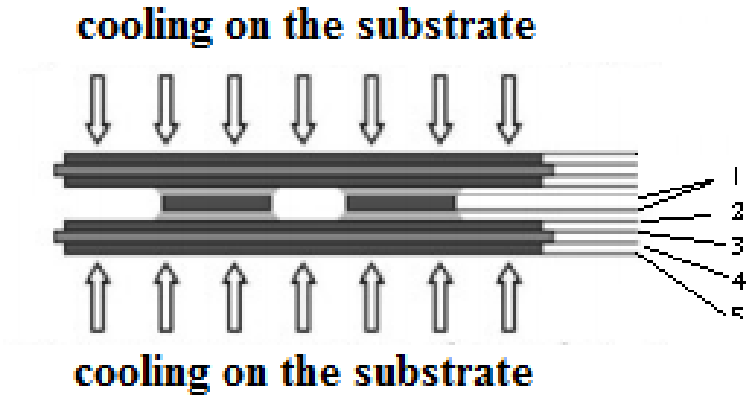

Figure 3.6 – Double side direct cooling of the substrate tiles. 1. Die / Solder 2. Solder / Copper 3. Copper / Ceramic 4. Ceramic / Copper 5. Copper [80].

Recent studies [80][83] [84] have proposed double-sided liquid cooling with embedded power packaging technology which allows double-sided thermal interface of a high heat transfer cooling.

A light-weight and compact module can be realised using a sandwich assembly where the DBC substrate tiles are cooled directly resulting in a very low thermal mass. Direct cooling method such as jet impingement with high heat transfer coefficient can be employed to provide the double-side cooling of the module which minimises the temperature rise of the devices during operation.

As with other liquid cooling methods there are potential issues including high-pressure leaks and electrical insulation which need to be considered.

3.2.3 Liquid Jet impingement cooling

Recent studies [82][80][85] confirmed that liquid jet impingement can be used to generate high heat transfer coefficients over 30 kW/m^2K at the heat transfer surface for an efficient cooling of power modules. Results from experimental tests [82] showed that directly cooling the substrate tile with jet impingement methods resulted in the devices being cooled more effectively and with lower pumping power compared to the commonly used cold plate. It was suggested that more efficient cooling can be achieved by targeting the hotspots on the substrate beneath each device with a

carefully designed impingement array. A layout of a simple liquid jet impingement cooling system is shown in Figure 3.7.

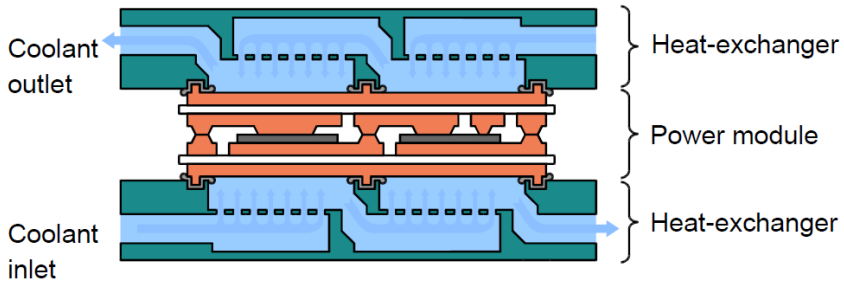

Figure 3.7 - A schematic diagram of two DBC are double side cooled using the jet impingement [82].

3.3 Proposed Thermal Management Strategy

This chapter aims to build on Electro-Thermal simulation, theoretical analysis and experimental results and focuses on achieving high current density in the inductor winding. A direct substrate cooling with water is used in order to reduce the thermal resistance between the winding and the coolant. Sources of heat include ohmic and magnetic losses which will be characterised and explained later in chapter 5.

3.3.1 Double Side Cooling

The inductor is soldered in between the two DBC ceramic substrates forming a sandwich structure, as shown in Figure 3.8. A double cooling system, with water as coolant liquid, is applied on both sides of the DBC providing cooling to the top and the bottom surface of the inductor.

The inductor has been thermally investigated by applying high current density up to $100A/mm^2$ and monitoring the rise in the temperature of the inductor at different current level with the existing cooling method. For the full paper and details please refer to Appendix B (section 7.2.1).

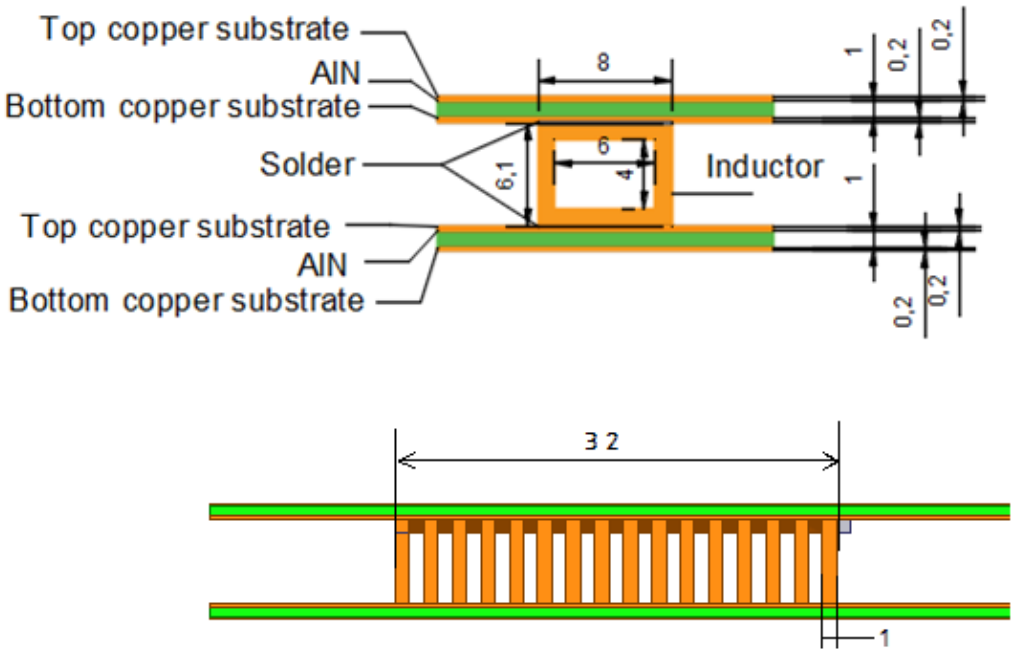

Figure 3.8- Inductor with double side cooling structure (all dimensions are in mm).

ANSYS R15.0 (Electro-Thermal simulation) has been used to design the package (the inductor on the DBC) and analyse the thermal characteristics then the results has been validated experimentally [49] using the thermal camera FLUKE , refer to Figure 7 and Table I in Appendix B (section 7.2.1) . Figure 5 in the paper shows the experiment in the lab which consists of the sandwich structure with top and bottom coolers, flow rate meter and thermal measurements for pre and post liquid temperature in order to calculate the calorimetric losses. Refer to Appendix B (section 7.2.1)

The experiment was carried out at ambient temperature of 25 C. A current was applied through the inductor, and was increased from 0 up to 100 A; the maximum temperature of the inductor was measured using a thermal camera. The temperature of both input and output water of the cooler was also measured together with the coolant flow rate. All experimental results have been organized in Table I in Appendix B (section 7.2.1). Both the ANSYS simulation results and measurements results are in agreement and can be seen in Figure 6 in Appendix B (section 7.2.1).

These results show, a current density of up to 90 A/mm^2 was achieved with only a 42 degree rise in temperature. Actually this is a much better results in comparison to some commercial high current inductors, such as high current helical inductor-30uH-180A and high current helical inductor-60uH-90A [67] which offer a current density of 9 A/mm^2 and 8 A/mm^2respectivly at their rated current when they both operated at their maximum rated current with the usage of a heatsink.

This was the initial proposed idea. This method of integrating inductors into the substrate and with an effective path for the heat to the thermal management system works well. Because of the power module structure, where the inductor will be integrated on the DBC, there are difficulties in creating a double side cooled module where on one side the output inductors and the power devices will need cooling and on the other side of the power module only the inductor will need cooling as shown in Figure 3.9.

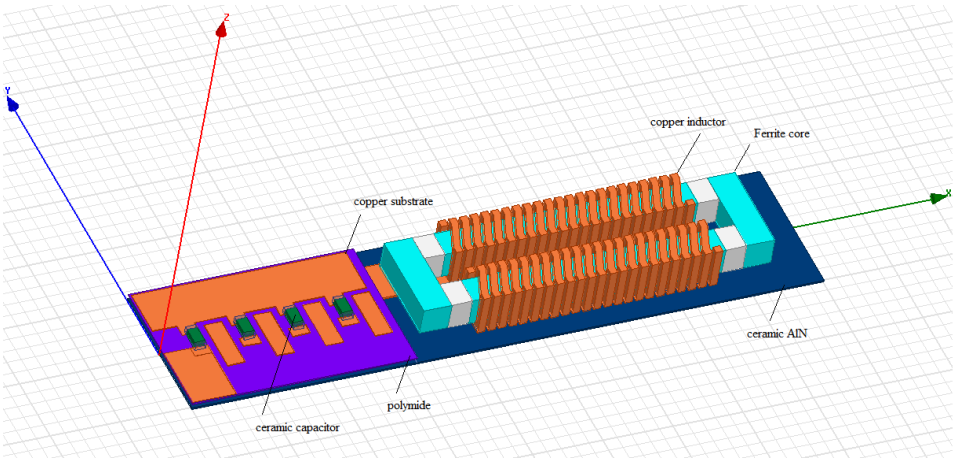

Figure 3.9–Inductors soldered on the substrate level.

Thus, a single cooling method on one side of the DBC is proposed in the following sub-section.

3.3.2 Single side cooling

Since in many cases the power devices are cooled on one side only, an investigation in single side cooling for the output inductors was performed. The inductors have been soldered on the DBC substrate tiles each measuring 105mm x 30mm. The tiles consists of a 1000μm thick Aluminium Nitride substrate with a 200μm layer of copper bonded

on both sides with a layer of solder with a thickness of approximately 200µm, as shown in Figure 3.10 (the solder layer is not shown in the illustrated figure). A single cooling method applied on the bottom of the substrate is proposed and it will be explained in the following section. A cooling system, with water as coolant liquid, is designed to be installed under the substrate and to be in direct contact with it. If a sufficient heat coefficient is provided on the bottom of the substrate it will secure a sufficient heat conduction even with one side cooling [82] [86].

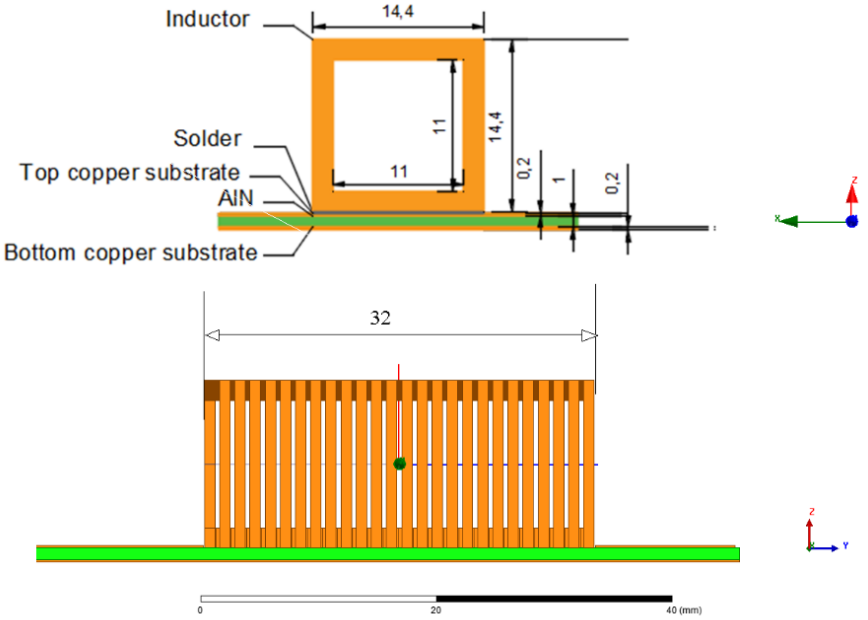

Figure 3.10- Inductor with one side cooling structure.

The inductor has been thermally investigated by applying high current and monitoring the rise in the temperature of the inductor at different current levels with the usage of a single direct cooling method.

3.3.3 Analyses of the Single Side proposed cooling method

The temperature will increase due to the losses in the inductor, such as winding and magnetic losses, which are primarily increased with the high current and high frequency. Thus, in order to maintain a good performance of the inductor, the

temperature of the core and windings must be kept at or below some allowable value. In practice the maximum temperature in power electronics is usually limited to 100-125 °C;

Heat will be transferred between components through conduction and convection [87] and it is important to analyse the thermal aspect of the proposed package in order to understand the heat conduction through it as shown in Figure 3.11.

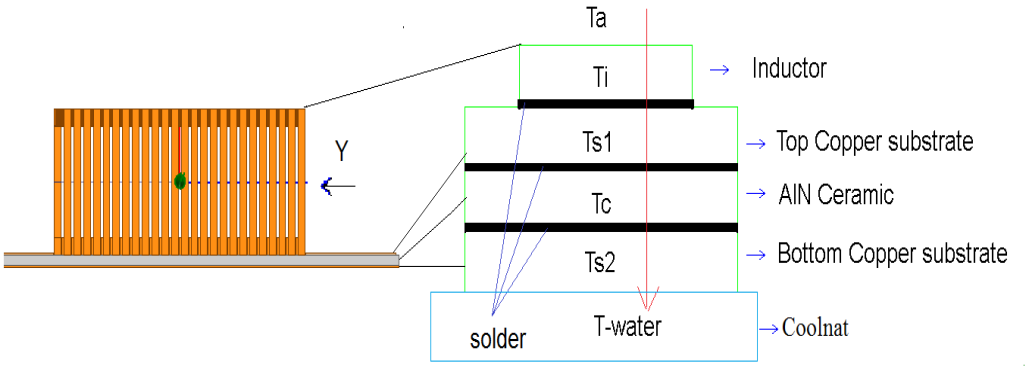

Figure 3.11 -Heat induction through the inductor and the substrate.

In order to analyse the thermal aspect in one turn, as shown in Figure 3.12, the Fourier law of thermodynamics is used in the following subsection. The heat flux q'' between a-b is calculated after applying boundary conditions between a-b as it will be explained later. The one turn is considered, as shown in Figure 3.12, by looking through the cross section of the inductor at the direction Y in Figure 3.11

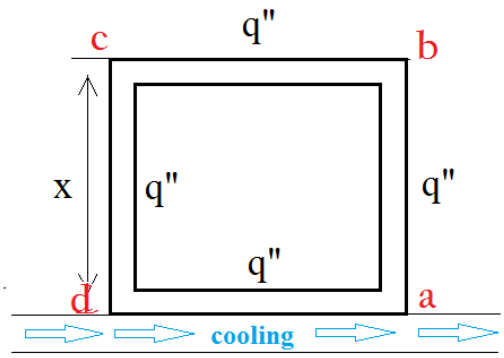

Figure 3.12- A cross section of the inductor showing the heat flux and the temperature dependence of each quarter of one turn Q1, Q2, Q3 and Q4.

3.3.3.1 Fourier Law in Thermodynamics

Heat energy Q transferred through a given surface per unit time forms the heat flux per unit area (q") and according to the Fourier law in thermodynamics [88], the heat flux per unit area $q''(Wm^{-2})$ is proportional to the gradient of temperature or temperature profile ∇T (*K*) in a material of thermal conductivity k (*W/m.K*).

$$q"(x,y,z) = -k(x,y,z).\vec{\nabla}T(x,y,z) \quad \text{EQ 3.6}$$

In one dimension *x:*

$$q" = -k.\vec{\nabla}T = -k\frac{\partial T}{\partial x} \quad \text{EQ 3.7}$$

Heat transfer equation:

Now, in order to find the heat energy equation, by using standard derivation [88], the rate of change of heat energy on total surface $\dot{Q}$ (W) is obtained by calculating the variation of the energy of that system:

$$P = \frac{dE}{dt} = \dot{Q} \quad \text{EQ 3.8}$$

E: The energy of the system.

$$E = \int_0^v \rho c\, \nabla T.dv \quad \text{EQ 3.9}$$

The sum of *E* as energies of small volume elements (dv) within the system can be expressed as an integral, which is equal to energy on total surface:

$$\dot{Q} = \frac{dE}{dt} = \int_0^v \rho c \frac{\partial T}{\partial t} dv \quad \text{EQ 3.10}$$

(ρ) is the density, (c) is the specific heat capacity (volumetric) and the integral is over the volume of the system.

The energy on total surface can also be written in integral form as:

$$\dot{Q} = -\int_0^A \overrightarrow{q"}.\hat{n}.dA + \int_0^v q'''.dv \quad \text{EQ 3.11}$$

n is the normal outward vector at the surface element (*dA)* (which is why the minus sign is present) and the integral is taken over the area of the system. The second integral represents the generation of heat within the system which is described by a volumetric heat source function q$'''$ (Wm^{-3}).

Writing all the terms in the energy equation in the form of volume integrals, and from EQ 3.10 & EQ 3.11, energy conservation gives:

$$\int_v (\rho c \frac{\partial T}{\partial t} + \nabla . \dot{q}^{"} - \dot{q}''') dv = 0 \quad \text{EQ 3.12}$$

The Law of conservation of energy must apply to any volume so must also apply to an infinitesimal volume dv over which all quantities can be considered to be constant thus:

$$\rho c \frac{\partial T}{\partial t} + \nabla . \dot{q}^{"} - \dot{q}''' = 0 \quad \text{EQ 3.13}$$

From EQ 3.7 & EQ 3.13

$$\rho c \frac{\partial T}{\partial t} = k . \overrightarrow{\nabla^2} T + \dot{q}''' \quad \text{EQ 3.14}$$

In steady state $\frac{\partial T}{\partial t}$=0, thus the conduction equation of the system can be written as:

$$k(x,y,z) . \overrightarrow{\nabla^2} T(x,y,z) + \dot{q}'''(x,y,z) = 0 \quad \text{EQ 3.15}$$

$$\begin{cases} k_x \frac{\partial^2 T(x,y,z)}{\partial x^2} + \dot{q}'''_x(x,y,z) = 0 \\ k_y \frac{\partial^2 T(x,y,z)}{\partial x^2} + \dot{q}'''_y(x,y,z) = 0 \\ k_z \frac{\partial^2 T(x,y,z)}{\partial x^2} + \dot{q}'''_z(x,y,z) = 0 \end{cases} \quad \text{EQ 3.16}$$

Simplify to one dimension x:

$$k(x) . \frac{\partial^2 T(x)}{\partial x^2} + \dot{q}'''(x) = 0 \quad \text{EQ 3.17}$$

For a specific conductor, the power generated P is proportional to the square of the current $I^2\ (A)$ applied through the conductor and the resistance R (Ω) for one-dimensional current flow only:

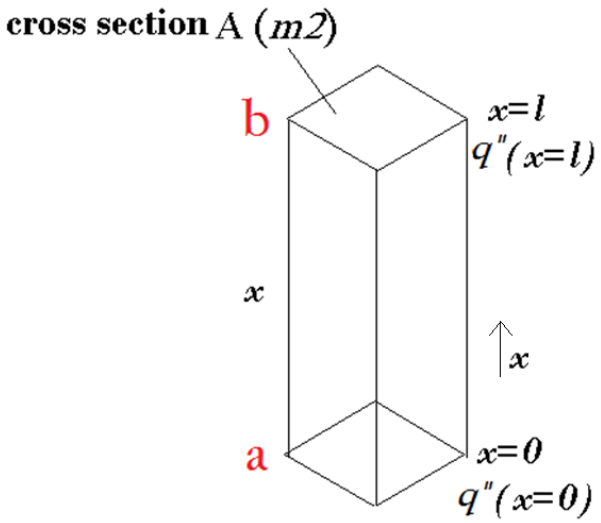

Figure 3.13- Applying a boundary condition between the part a-b in Figure 3.12 .

$$P = I^2.R : R = \frac{r.x}{A} \ , dR = r\frac{dx}{A} \qquad \text{EQ 3.18}$$

r is the electrical resistivity of the conductor ($\Omega.m$), A is cross section (m^2) and x is the length (m).

Also

$$P = \int q'''.dv \qquad \text{EQ 3.19}$$

Thus

$$\int q'''.dv = I^2R \ \rightarrow \ q''' = \frac{I^2 dR}{Adx} = \frac{I^2 r}{A^2} \qquad \text{EQ 3.20}$$

From EQ 3.17&EQ 3.20:

$$k.\frac{d^2T_{(X)}}{dx^2} + \frac{I^2 r}{A^2} = 0 \ \rightarrow \ \frac{dT_{(X)}}{dx} = -\frac{I^2 r}{kA^2}x + C_1 \qquad \text{EQ 3.21}$$

$$T_{(X)} = -\frac{I^2 r}{2kA^2}x^2 + C_1 x + C_2 \qquad \text{EQ 3.22}$$

From Fourier law EQ 3.7 &EQ 3.21, the heat flux per unit area in one direction x is calculated:

$$q" = \frac{I^2 r}{A^2} x - kC_1 \text{ (watt/m2)} \qquad \text{EQ 3.23}$$

3.3.3.2 Applying a boundary condition

In order to calculate the heat flux $q"$ between a-b (Figure 3.12) boundary conditions are applied as shown in Figure 3.13.

The solution to EQ 3.22 & EQ 3.23 is obtained by applying the boundary conditions $\begin{Bmatrix} T_{x=0} = t_0 \\ T_{x=l} = t_l \end{Bmatrix}$ assuming a given current value I. $T_{x=0}$ and $T_{x=l}$ are the temperatures on the surface "a" and "b" at x=0 and x= l respectively.

From EQ 3.22

$$T_{(x=0)} = -\frac{I^2 r}{2kA^2}(0)^2 + C_1(0) + C_2 = t_0 \quad \text{thus} \quad \boxed{C_2 = t_0}$$

Thus

$$T_{(x=l)} = -\frac{I^2 r}{2kA^2}(l)^2 + C_1(l) + t_0 = t_l$$

Thus,

$$C_1 = (t_l - t_0 + \frac{I^2 r}{2kA^2}(l)^2)/l \qquad \text{EQ 3.24}$$

Thus the temperature as a function of the height x is

$$T_{(X)} = -\frac{I^2 r}{2kA^2}x^2 + ((t_l - t_0 + \frac{I^2 r}{2kA^2}(l)^2)/l)x + t_0 \qquad \text{EQ 3.25}$$

From EQ 3.23 the heat flux as a function of the height x is

$$q" = \frac{I^2 r}{A^2} x - k((t_l - t_0 + \frac{I^2 r}{2kA^2}(l)^2)/l) \qquad \text{EQ 3.26}$$

It is indicated from EQ 3.25 & EQ 3.26 that the temperature is a function of the square of the current I^2 and the second degree of the height x^2. The heat flux is a function of the square of the current I^2 and the height x .If both temperature t_0 and t_l are known the temperature along l height can be obtained.

3.4 Electro-Thermal Simulation

Both the temperature of the inductor after applying a high current through it and the direct liquid cooling effect have been checked by simulating the inductor on the DBC, as shown in Figure 3.14, with the usage of ANSYS R15.0 (Electro-Thermal simulation).

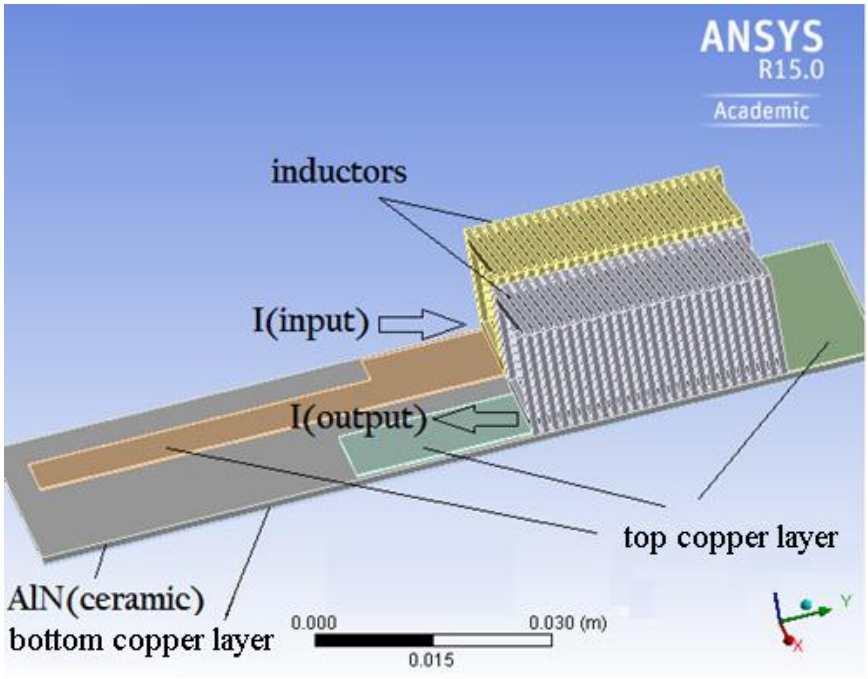

Figure 3.14- The inductors on the DBC-simulation in ANSYS.

The materials of the inductor, the top layer and the bottom layer of the DBC where set to copper while aluminium nitride AlN was chosen for the middle layer of the DBC.

First the simulation has been done by applying a current of 5A through the inductor considering only the exchange of the heat energy of both inductor and DBC with the surrounding environment. Thus, a convection of natural air (stagnant air convection of 5 $W.m^{-2}K^{-1}$) has been applied on the whole copper surface of the inductor and the substrate. The temperature of the inductor was captured, as shown in Figure 3.15. It shows an average temperature of 64 °C of the inductor. Thus, more efficient cooling will be required if a higher current is applied through the inductor.

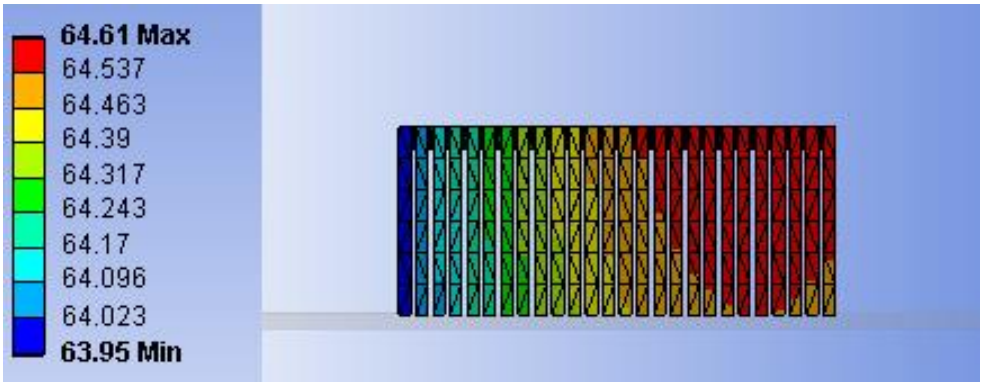

Figure 3.15-ANSYS simulation at 5 A with poor cooling.

In order to check the effect of the heat coefficient *h* on limiting the increase in the inductor's temperature a current of 60 A dc has been applied through the inductors. Various values of heat coefficient *h* were used by applying a convection which is presenting the direct cooling on the bottom of the substrate [1.2, 6, and 10] $kW.m^{-2}K^{-1}$ with fixed ambient temperature of 24 °C in order to show the effect of an appropriate cooling method on limiting the rise of the temperature when a high current is applied through the inductor. A stagnant air convection of 5 ($W.m^{-2}K^{-1}$) has been applied on the whole outer surface of the inductor representing the exchange in heat between the inductor and the surrounding environment, in addition to the direct substrate cooling but it doesn't significantly change the results.

The captured temperatures of the inductor at 60A and different values of heat coefficient *h* are shown in Figure 3.16.

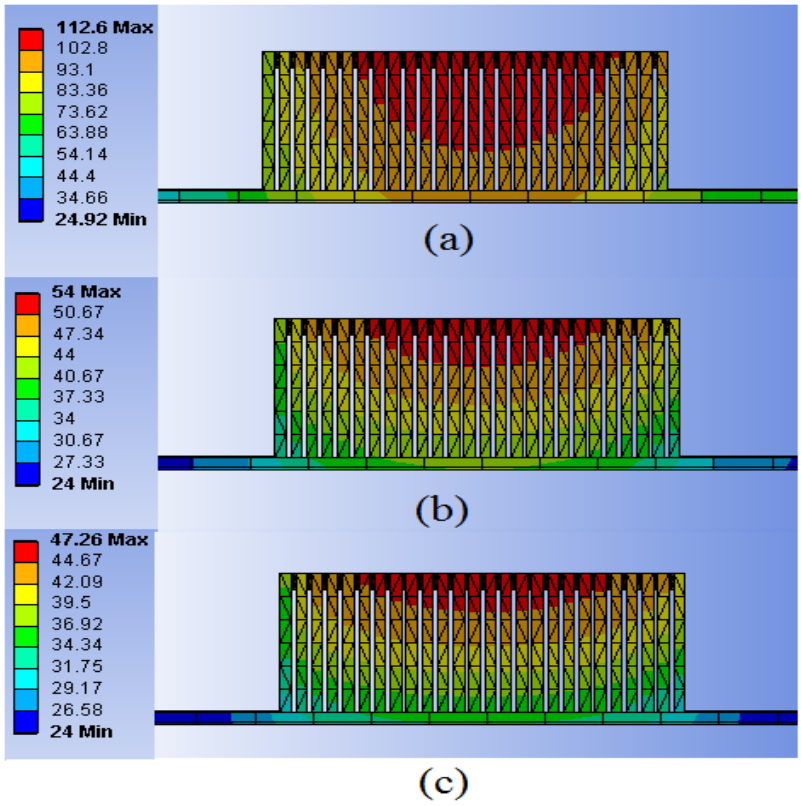

Figure 3.16- ANSYS simulation at 60 A, one side direct liquid cooling with (a) h= 1.2 kW/m^2K. (b) h=6 kW/m^2K. (c) h=10 kW/m^2K.

Figure 3.16 shows the temperature of the inductor at different heat transfer coefficients h when applying 60A DC. It is shown that at the higher heat coefficient of 10 kW/m^2K an average temperature of around 40 °C occurs in the inductor, while it is around 44 °C and 90 °C when the heat coefficient is 6 kW/m^2K and 1.2 kW/m^2K respectively. Thus the usage of an efficient direct liquid cooling method ensures a limits of the temperature increase in the inductor. A value of heat coefficient is chosen to simulate the inductor in order to provide close enough values of temperature at the points a & b to those obtained from measurements in the following section. The heat flux (q") and the temperature (T) were plotted against height (x) and compared to the measurements in the following section.

3.5 Experimental Validation

The possibility of obtaining a high energy density by applying a high current through the inductor with the ability to restrict the inductor's temperature, by using an efficient direct cooling method, is validated in this section. The DC current will be increased between [20A-80A] and it will be applied through the inductors as in Figure 3.17 . The temperature of the inductor will be captured with the usage of a thermal camera and will be compared to the ones from the analytical model and ANSYS simulations.

3.5.1 Experiment Setup

The experimental setup is shown in Figure 3.17 and the block diagram including the pump and the pips is shown in Figure 3.18, where a direct liquid cooling system was attached to the bottom of the DBC. Temperature sensors have been attached to the pipes which supplies the input and output water to the package. A DC current was applied at currents between [20A-80A] to provide a source of heat in the inductor winding.

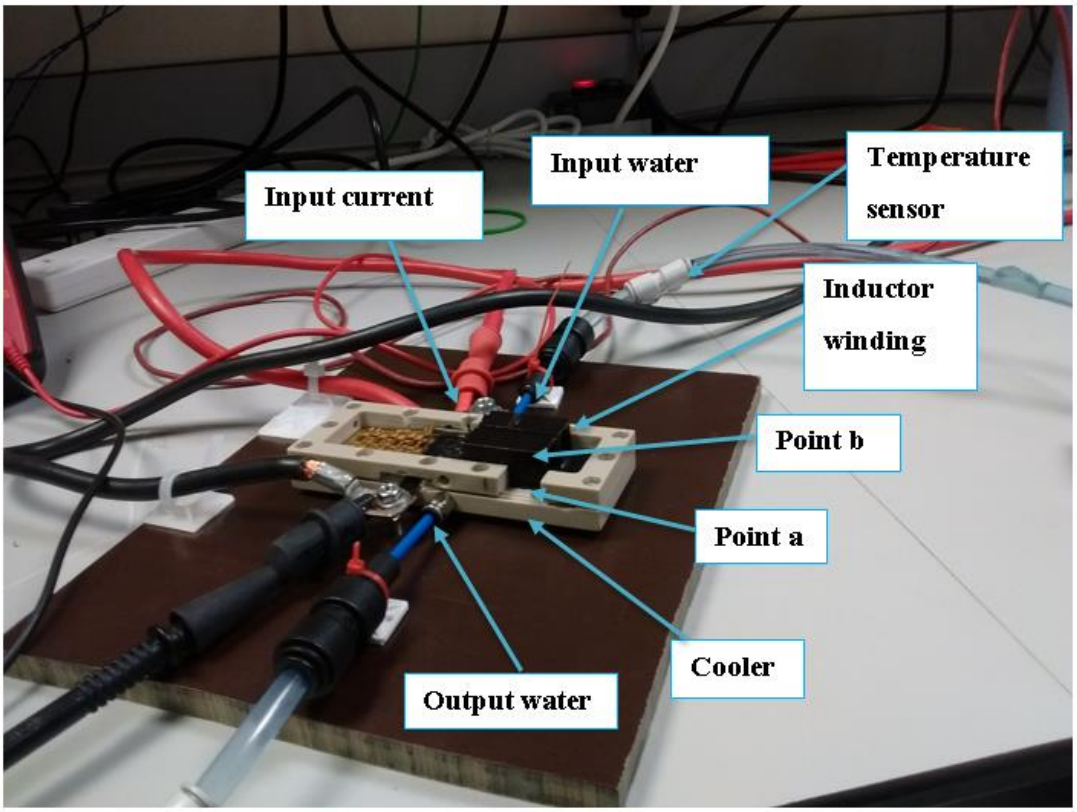

Figure 3.17- The experiment setup.

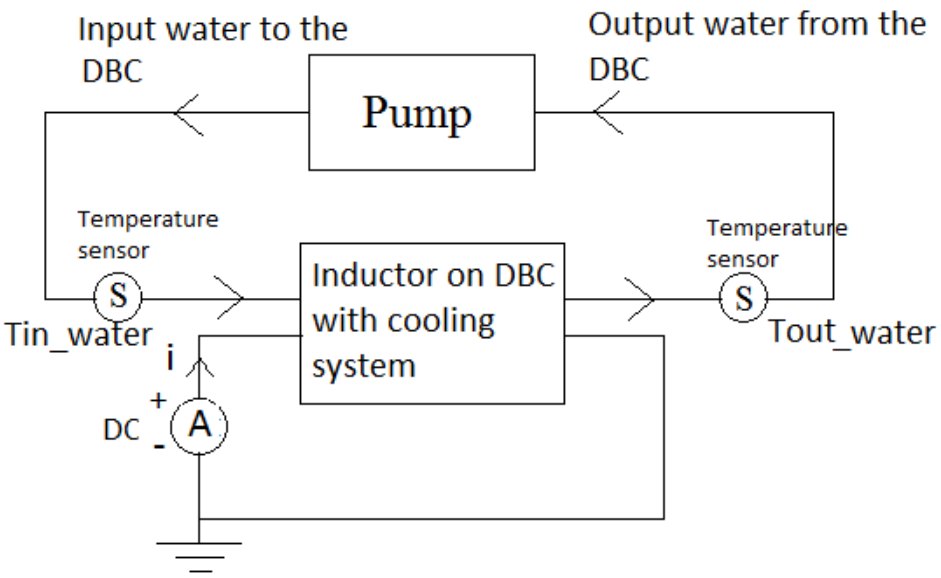

Figure 3.18- The experiment setup diagram.

The cooler used in the test has been chosen in cooperation with an existing project, it was designed to create as far as possible a uniform heat transfer coefficient under the inductor winding. The geometry of the cooling arrangements were beyond the scope of the project.

3.5.1.1 The Pre-Test Considerations

1- A DC current supplier (TDK-Lambda, 0-120 A) has been used in order to apply up to 80A (DC) across the inductor.

2- In order to avoid any possible high-pressure leak of the coolant liquid the package (the inductor on the DBC) has been fixed on the top of the cooler using a non-corrosive silicon rubber RS 494-118 [89]. A further fixing, using a two plastic parts attached to each other with screws as it is shown in Figure 3.19, in order to fix the cooler and the package firmly.

3- Because of the fact that the copper is a thermally reflective metal, all copper surfaces were coated in black paint to enhance the emissivity of the surface of the inductor.

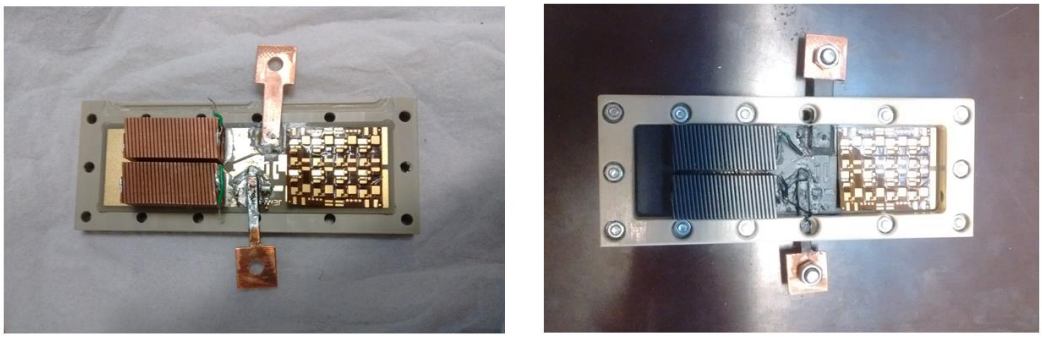

(a) (b)

Figure 3.19- Assembling the cooler system and the DBC with the inductors. (a) Before painting the inductor and attach the top cover. (b) After painting the copper surfaces and attaching the cover.

4- De-ionised Water [90] was used as a liquid coolant, in the pump (Thermo SCIENTIFIC), with temperature 24.9 °C at the ambient. The flow rate of the coolant inside the package was measured showing a value of 0.013 $kg.s^{-1}$. the test has been done under the same conditions as the flow rate was measured, where the pipe with the return water was left unattached with the device and the water was running directly inside the tank.

5- The Cedip Infrared System Thermal Camera (TITANIUM Series) has been used in order to capture the temperature in the inductor. The camera was calibrated (auto calibration) and the ambient temperature was set to the room temperature 24.9 °C. The position of the camera was fixed in order to capture the side face of the package as shown in Figure 3.17, thus the temperature along the line between the points (a-b) top-to bottom of the side of one turn of the inductor (refer to Figure 3.17), can be captured.

6- A KEITHLEY 2700 Multi-meter [92] and two temperature sensor, which is compatible with the PT100 Resistance Table (Resistance vs Temperature), refer to Figure 7.7 Appendix B, is used in order to register the inlet and outlet Temperature of the water. Results have been obtained and organised in Table 7.4- Appendix B. The inlet/outlet temperature was measured after a period of time when the readings of the multi meter are stable, refer to the temperature vs time at 60A Figure 7.6 Appendix B as an example.

Another issue to be considered is the way that the inductor has been soldered on the substrate. Actually the bottom turns of the coil were expected to be connected fully in order to provide the maximum conduction of heat through them. The package has been scanned using a 3-D X-Ray Computed Tomography System. A cross section in the inductor and the substrate, as shown in Figure 3.20, indicates that the solder between the inductor and the substrate is not filling all the area and it is with more or less 40 % voids. Actually this is due to the difficulties in soldering this type of inductor on the substrate without shorting the turns of the inductor. Thus only a relatively small amount of the solder paste was applied. The existence of the voids in the solder layer which connects the inductor and the substrate will affect the conduction of the heat out of the inductor's winding due to the increased thermal resistance. Thus, a difference in the temperature values between simulation and experiment is expected.

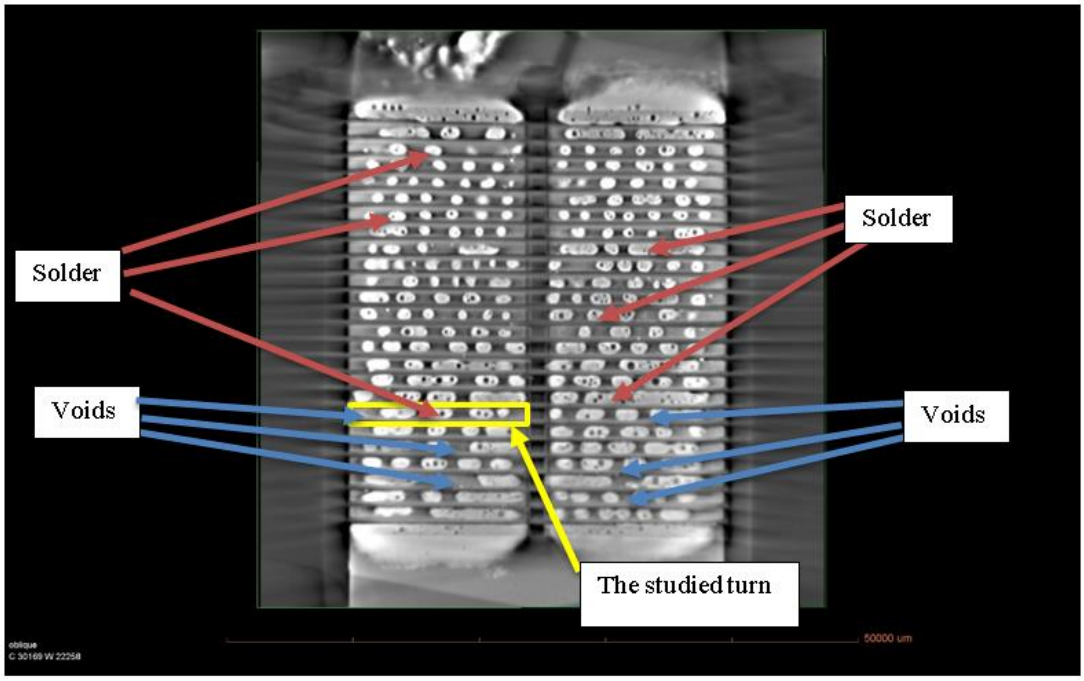

Figure 3.20- A cross section of the package, obtained by 3-D X-Ray, showing the situation of the solder's density between the inductor and the substrate.

3.5.2 Experimental Results

The test has been done by applying different DC current values between [20-80A] on the inductor. The temperature at each different current has been captured through the thermal camera. Figure 3.21 shows a comparison between the temperature at currents 60 and 80 A. The rise in temperature at higher current is noticeable. Also the captured temperature at the top surface of the inductor far from the direct cooling is higher than the bottom one. This is in agreement with the analysis. The inconsistent temperature gradient between turns, as shown in Figure 3.21, is due to the inconsistent thermal contact between the inductor and the DBC as explained previously.

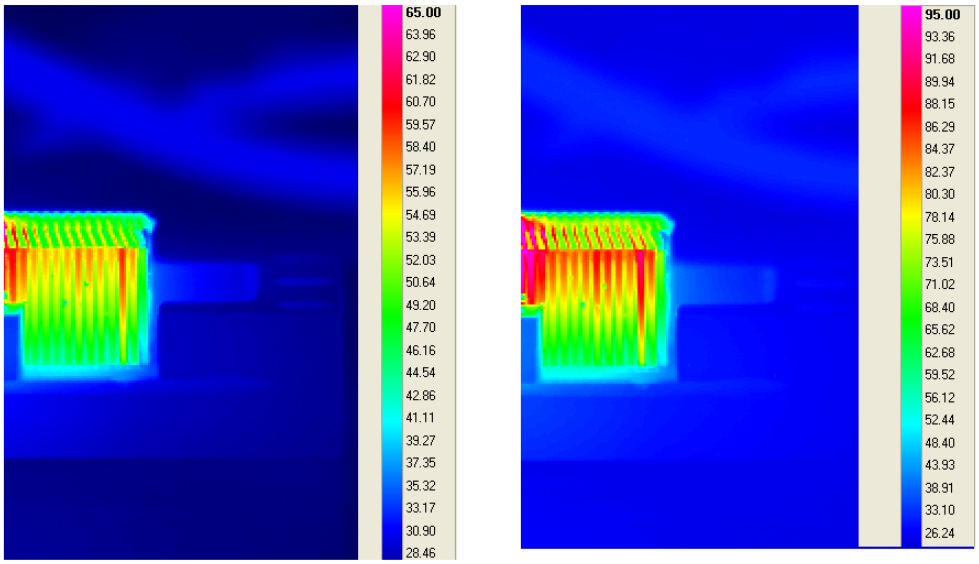

Figure 3.21– Thermal camera image for one side cooling (a) at 60A. (b) At 80A.

Figure 3.22 shows the temperature at each different current along one turn (as shown in Figure 3.20- the studied turn is defined by a yellow rectangular) between the bottom and the top of the inductor side face (a-b) (refer to Figure 3.17), with the usage of the direct liquid cooling.

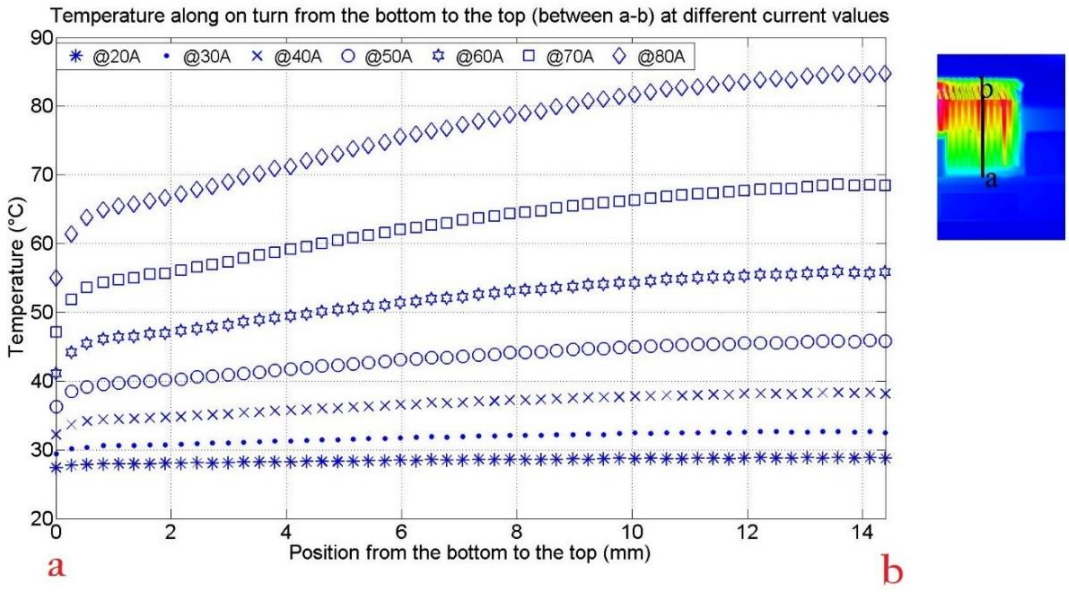

Figure 3.22- Temperature vs Current on one turn between two points from the bottom till the top (a-b).

Figure 3.23 shows the temperature difference ΔT1 between point a (which is at the level of the connection between the winding and the DBC) and the ambient water temperature. It also shows the temperature difference ΔT2 between points a & b (which is at the level of the top surface of the winding).

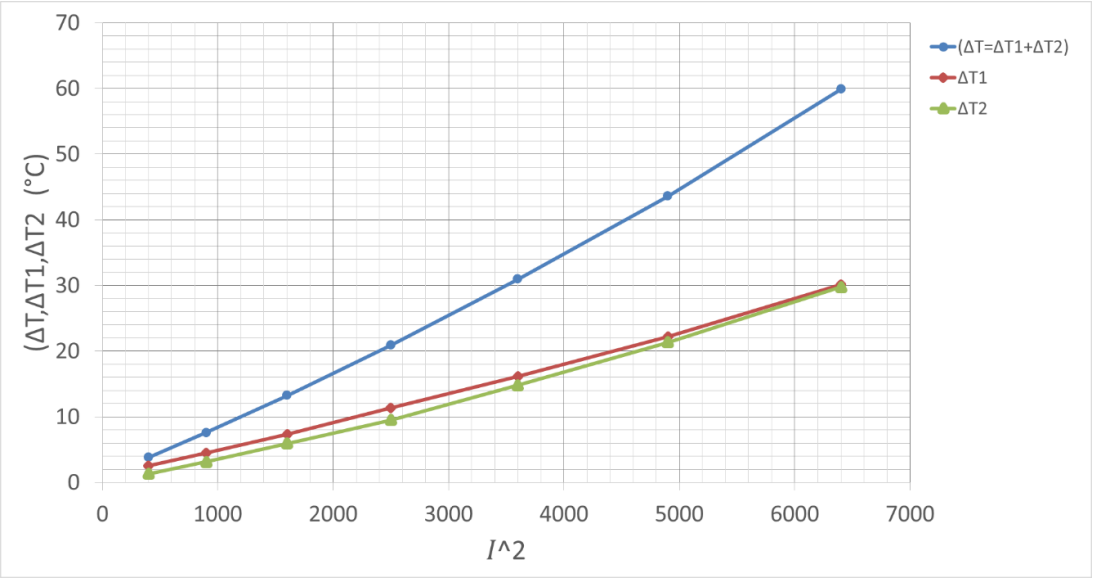

Figure 3.23- The temperature rise at both points a & b vs I^2.

It is apparent from both Figure 3.22 and Figure 3.23 that the increase of the temperature against the increase of I^2 at point "a" is equal to the increase of the temperature at point "b" for a certain current value. In other words the drop of temperature in the winding is nearly equal to the drop of temperature between the water and DBC top layer. This for the case of this specific design.

In order to understand the efficiency of the suggested cooling method the thermal resistance of the cooling system (as shown in Figure 3.24) has been calculated, for a specific flow rate (0.013 kg/sec) as following:

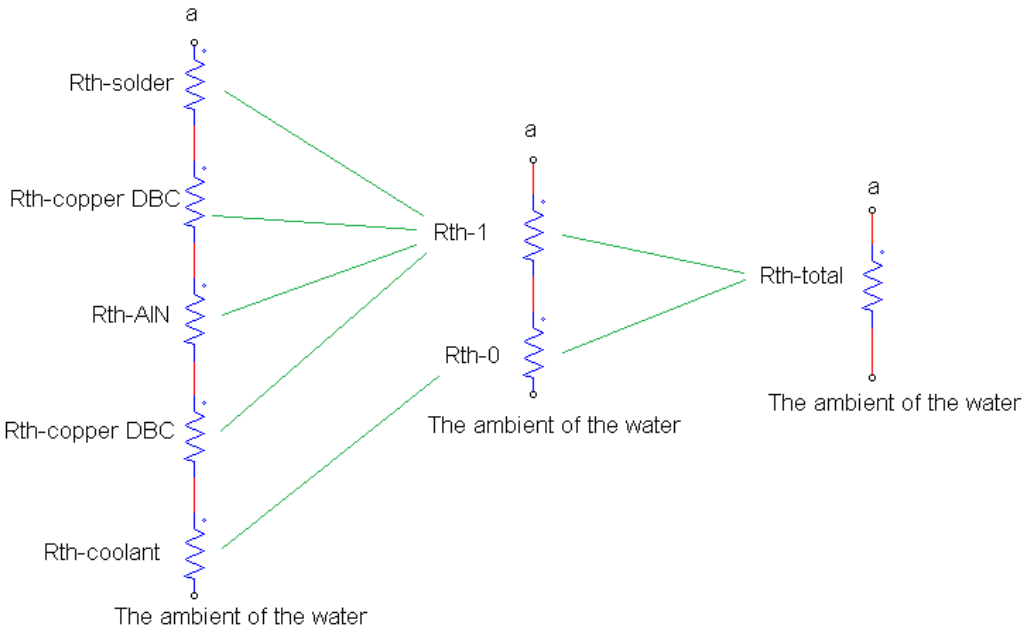

Figure 3.24- Total thermal resistance between the cooling level and point a (the bottom of the copper winding).

The rate of change of heat energy on total surface in watts is

$$\dot{Q} = \frac{dm}{dt} \times c \times \Delta t \qquad \text{EQ 3.27}$$

Where

1. $\frac{dm}{dt}$ is the flow rate in $kg.s^{-1}$.
2. c is the specific heat ($Kj.kg^{-1}K^{-1}$).
3. Δt is the change of temperature.

By using EQ 3.27. The heat transfer for the water at 60A is $\dot{Q} = 98.34\,W$

Where

- Δt is the difference of the inlet and outlet temperature of the water at 60A is 1.79 K from Table 7.4 in Appendix B.
- $\frac{dm}{dt}$ The flow rate of the water in the cooling system is 0.013 kg from Table 7.4 in Appendix B.
- Thermodynamic properties of water are from Table 7.2 in Appendix B.

The thermal resistance between the cooling level and point "a" is explained in Figure 3.24.

Total thermal resistance is found from EQ 3.28, $R_{th-total} = 0.164\,K.W^{-1}$

$$\Delta T = \dot{Q} \times R_{th} \qquad \text{EQ 3.28}$$

ΔT is the temperature difference between the cooler and point "a" at 60A , $\Delta T = 16.18$ K as in Figure 3.23.

The total thermal resistance in the DBC and the solder has been calculated for each layer using EQ 3.29, $R_{th-1} = 0.039\,K.W^{-1}$.

$$R_{th} = \frac{d}{k \times A} \qquad \text{EQ 3.29}$$

Where;

d is the thickness of the layer in meter (refer to Table 7.3 in Appendix B).

K is the thermal conductivity of the material (refer to Table 7.3 in Appendix B).

A is the cross section of the heat transfer area. For the DBC A= 404.4 mm^2 is the total bottom surface area of the copper winding considering only 60% of this area is in contact with the DBC as it was explained before in Figure 3.20. For the solder layer A= 269.6 mm^2 is the total bottom surface area of the copper winding considering only 40% of this area is presenting the solder surface area as was explained before in Figure 3.20.

As a result, the thermal resistance of the cooler as in Figure 3.24:

$R_{th-0} = R_{th-total} - R_{th-1} = 0.164 - 0.039 = 0.125\ K.W^{-1}$.

Comparing this value to the thermal resistance of some commercial heatsink, it is found that a heat sink with a similar thermal resistance value of $0.177\ K.W^{-1}$.[91] has a volume of ($151.5\ mm \times 181.5\ mm \times 89\ mm$) and a weight of 535g, while the cooling structure used in this test has a volume of ($50\ mm \times 70\ mm \times 10mm$) and a weight < 50 g.

It is indicated from Figure 3.23 that at a current of 70 A the temperature increase from the ambient is around 43 °C. Thus this current value will be considered the rated I_{rms} of the inductor which is the current that causes a temperature rise of 40°C in the inductor.

Figure 3.25 shows a comparison between analysis, simulation and measurement for the temperature vs height at different points between "a" and "b" when applying 60A through the conductor.

For the simulation, the purpose was to predict the heat coefficient of the used cooling system, thus a heat coefficient of 5 $\mathrm{kW.m^{-2}K^{-1}}$ has been found to give the closest temperature values comparing to those obtained from the measurements. The only convection of temperature applied in the simulation was on the bottom of the substrate, thus no further exchange of temperature between the inductor and the surrounded space has been considered.

For the analysis, EQ 3.25 has been used at 60A the both t_0 and t_l were taken from the measurements results at $x = 0\ mm$ and $x = l = 14.4\ mm$ respectively. The cross section of the turn $A = 1.53\ mm^2$, the thermal conductivity of the copper (at 56 °C) $K = 400\ \mathrm{W/mK}$ and the resistivity of the copper (at 56 °C) $r = 1.91\ \Omega.\mathrm{m}$ have been used in order to obtain the curve of the temperature against the height.

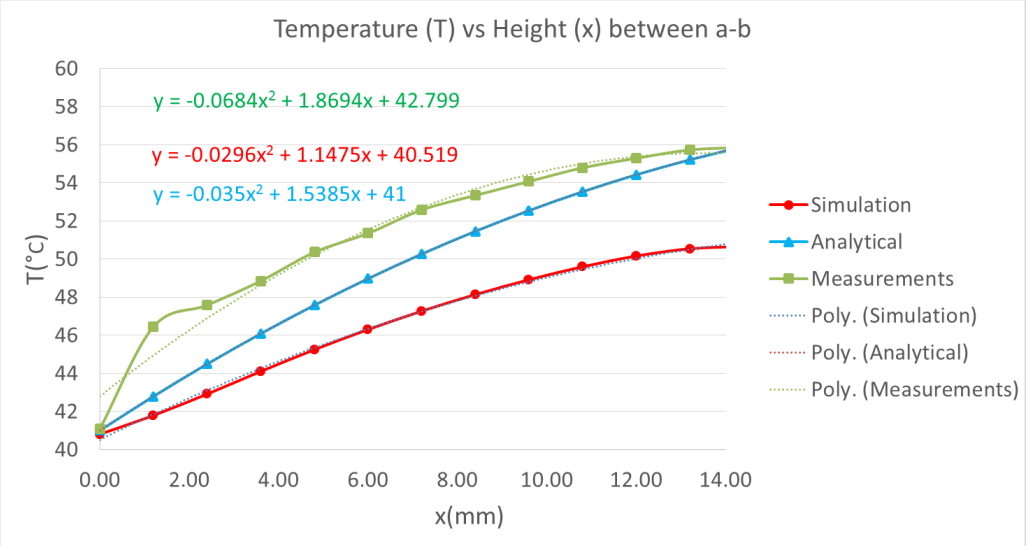

Figure 3.25- A comparison between analysis, simulation and measurement for the Temperature (T) vs Height (x) between the part a-b with boundary condition at 60A.

Figure 3.25 shows a good agreement in the temperature curve shape between analytical analyses, simulation and measurement with less than a 5°C error in experimental testing. It is noticed from Figure 3.25 that the temperature's values obtained from the measurements are higher comparing to the analytical and simulation results especially at the second point close to the substrate where there is an increase in temperature about 5 °C. Actually this difference is probably due to two facts:

1- The poor thermal contact between the windings and the substrate in reality as it is shown in Figure 3.20.
2- Fixed values for thermal conductivity and resistivity of the copper were used in the analytical analysis in order to simplify the formulas. While in reality both thermal conductivity and resistivity of the copper conductor are temperature dependent. Resistivity increases or decreases significantly as temperature changes. The relationship between resistivity and temperature is:

$$\Delta\rho = \alpha \times \Delta T \times \rho_0 \qquad \text{EQ 3.30}$$

Where,

$\Delta\rho$: Change of the resistivity.

α : Resistivity, temperature coefficient.

ΔT : Change of temperature.

ρ_0 : Original resistivity.

While the thermal conductivity K is defined in EQ 3.31 as the quantity of heat transmitted, Q, due to unit temperature gradient ∂T, in unit time under steady conditions in a direction normal to a surface of unit area ∂n [92].

$$K = -Q/\frac{\partial T}{\partial n} \qquad \text{EQ 3.31}$$

3- Another error here to be considered could be inaccuracies in the measurement technique as the line from a to b has been drawn manually and proximity along the turn as it shown in Figure 3.22, thus the points compared along the line a-b between the analytical analysis , simulation and measurements are not quite the same.

4- In the theory one isolated turn was considered and it was assumed that the heat is going in one direction and the calculations have been done for one direction. While in reality the heat is going in 3 direction as it is shown in Figure 3.16 where the temperature of the middle turns seems higher.

Actually, the modelling of the heat transfer along the conductor was useful in order to evaluate the efficiency of the cooling system as it shows a lower temperature at the point (a) near the applied cooling comparing to the temperature at the furthest point from the cooling (b) with a difference around 40%. The simulation has been done by matching the temperature values from the experiments in order to predict the heat transfer coefficient of the used cooling system, which it was around 6 $/m^2K$. This value is within the typical heat transfer values of the cooling method used (forced liquid cooling) which is up to 10 kW/m^2K (refer to Table 7.1 [94]). In general if the specific heat transfer coefficient of the cooling system is known the ANSYS simulation might be useful to predict a temperature value close to reality.

3.5.3 Comparison with Commercial Inductors

In order to determine the effectivity of the thermal performance of the designed inductor at high currents it is compared to a standard inductor off-the-shelf. Table 3.1 shows a comparison between the design inductor and a high current helical inductor-

30µH-180A [67], as shown in Figure 3.26, at their rated I_{rms} current has been done from the energy density perspective.

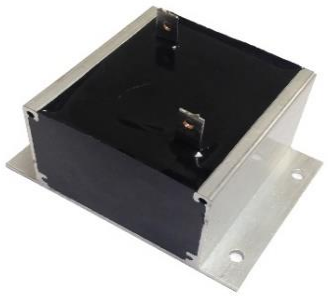

Figure 3.26- High Current Helical Inductor-30uH-180A.

This comparison considers the fact that the commercial inductor is without any heat sink or direct cooling and its heat is conducted naturally to the outer environment through its Aluminium enclosure while the designed inductor has a liquid direct cooling applied at the bottom of the substrate. Refer to Figure 7.8 Appendix B for the thermal camera measurements of the commercial inductor at different current values. The commercial inductor shows a larger weight and volume (0.5 kg) and $207.4 \times 10^3\ mm^3$ respectively comparing to the designed inductor's which has a 0.0935 Kg of weight and a $25.05 \times 10^3\ mm^3$ of volume.

A comparison between the energy density of both inductors for their maximum operated current (not including the cooling system for the commercial inductor nor the pump for the cooling system of the designed inductor) is shown in Table 3.1

Table 3.1 A comparison between the energy density of both inductors at their maximum operated current

	Commercial inductor	Designed inductor
Maximum operated current I(A)	100	70
Inductance value at the operated current (µH)	13.4	20.5
Stored energy E (J)	0.067	0.05
Volumetric Energy density (J/mm3)	0.32×10^{-6}	2×10^{-6}
Gravimetric Energy density (J/Kg)	0.134	0.537

The higher value of energy density of the designed inductor makes it more suitable solution for this kind of integration and energy density requirement. For all dimension and schematics for both inductors please refer to Appendix A (Figure 7.3 and Figure 7.5).

3.6 Conclusion

The work in this chapter has investigated the cooling design of high energy density inductors. The inductor design has been exported into ANSYS R15.0 where it has been analysed under the effect of high DC current. The thermal management method has been validated by experiment and results have been achieved and analysed. This work has obtained a high energy density inductor by applying a high current density, with the use of an efficient cooling system. It has been found that increasing the current up to 70 A, a current density of around 46A/mm^2 will increase the temperature of the inductor from the ambient temperature by 40 °C, This current is defined by the I_{rms} of the inductor.

This temperature rise is for the DC winding losses $I^2 R$. For the increase of the temperature due to the extra losses under ripples and DC bias a cooling with higher heat coefficient might be needed. These losses will be investigated in Chapter 5

Actually the obtained I_{rms} in this section has a significant value of 70 A. However, this value can be increased by improving the contact between the windings and the substrates, as explained in Figure 3.20. This will lead to less voids in the solder layer and thus a better conduction of the temperature out of the inductors. Then the applied current can be increased.

A comparison between a commercial inductor (high current helical inductor-30uH-180A) and the designed inductor from an energy density perspective has shown that although it is possible to find an inductor off-the-shelf which can operate at a high current level, the proposed inductor with its light weight and smaller volume is more suitable for the purpose of the integration on the same substrate of the active components than the bulky commercial inductor such as this,.

4 Chapter 4- High Frequency Modelling of the Inductor, Electro-Magnetic Approach

4.1 Introduction

The design of passive filtering components is one of the important issues in the conception of power converters [95][96] as smaller size passive components are preferred. Some of the applications of these components include input/output ripple reduction filters, common mode and differential mode filters. At high frequency the passive components with their stray elements, such as equivalent series inductance of capacitors and equivalent parallel capacitance of inductors, have a major impact on filter efficiency [97]. Thus, in order to design and improve the performance of the filter a high-frequency model including parasitic elements, must be used, particularly, in the case of wide band gap devices which operate at frequencies where the inductor doesn't behave as an inductor.

Two distinct methods are recognized to model these components:

1. Physical based models which represent device characteristics through physical equations and associated equivalent circuits. This method will require some knowledge of the material properties, structure, and operating mechanism. Thus it is often not easy to use [98] [99] [100].

   Researchers have proposed a method to identify the model parameters by fitting an equivalent circuit model of the passive components [101]. In their study [101] an equivalent circuit model of coupled inductors is proposed and validated experimentally using the open and short circuit measurements. Their results show a very good agreement between simulation results and experimental data up to 30 MHz.
2. Behavioural modelling which is widely used in the literature for noise modelling and prediction process [102][103][104]. The behavioural model represents the noise source with an equivalent circuit, typically a current or voltage source or an ideal switch, together with some equivalent impedances representing parasitic impedances. A new frequency-domain modular-terminal-behavioural (MTB) modelling approach for characterizing conducted

(EMI) noise sources in a converter is proposed by researchers [104] where the equivalent current source and source impedance are established through a test and characterization procedure for a given device under the specified operating conditions.

It is clear from the comparison between the methods above that the physical-based model is more challenging to realise as a design tool due to its modelling and application complexity. On the other hand, behavioural modelling, although simpler than the physical based model, may have compromised accuracy because no knowledge of internal material is required and the parasitic impedance is simplified and sometimes totally omitted.

In this chapter, because it is very important to characterize the magnetic components and predict their resonance frequency and parasitic capacitance at high frequencies. An equivalent electric circuit of the inductor based on a physical model is proposed and solved in LTSPICE, and the impedance curve is obtained. The method is validated experimentally using the Impedance Analyser KEYSIGHT E4990A by means of impedance measurements between the input and output of the inductor. Both inductance and capacitance matrices are obtained using MAXWELL 16 software (Magneto-static and Electrostatic solvers). An equivalent electrical circuit of the inductor is proposed.

Most existing passive filtering components response test procedures are based on 50 ohm insertion loss measurements. Which can result in unanticipated responses which can lead to serious system degradation problems [105]. The two port network measurements have been recommended by J.E. Bridges & W. Emberson [105]. Two- port measurements can be used to provide sufficient information to completely characterize the performance of passive components over a wide variety of source and load impedance conditions.

Other studies have presented methods of obtaining an impedance matrix and the transfer function matrix, for example, Snowdon [106] who derived the relations for the four-port parameters of a passive system and Doige [107] who extended this to a general symmetric system, but both studies lacked mathematical rigour. In another study [108] the general relationships between these matrices were derived by

investigating the properties of the impedance matrix and the transfer matrix of symmetrical, reciprocal and conservative system.

4.1.1 Equivalent Circuit of the Inductor

In order to characterize the inductor and predict its resonance frequency and parasitic capacitance at high frequencies, it is important to propose an equivalent electric circuit of it. Ideally A simplified equivalent circuit consists of inductance and the self-capacitance with no resistive part, they both form a parallel resonant circuit, which has self-resonance frequency f_r [54].

$$f_r = \frac{1}{2\pi\sqrt{LC}} \qquad \text{EQ 4.1}$$

Figure 4.1 shows the plots of the susceptances $B_C = \omega C$, $B_L = -1/(\omega L)$,and $B = B_C + B_L = \omega C - 1/(\omega L)$ as functions of frequency for inductance L = 1μH and C = 1nF. At f_r , the total susceptance of an inductor is zero. Below f_r , the inductor reactance is inductive. Above f_r , the inductor reactance is capacitive. Therefore, the operating frequency range of an inductor is usually from DC to 0.9 f_r [54].

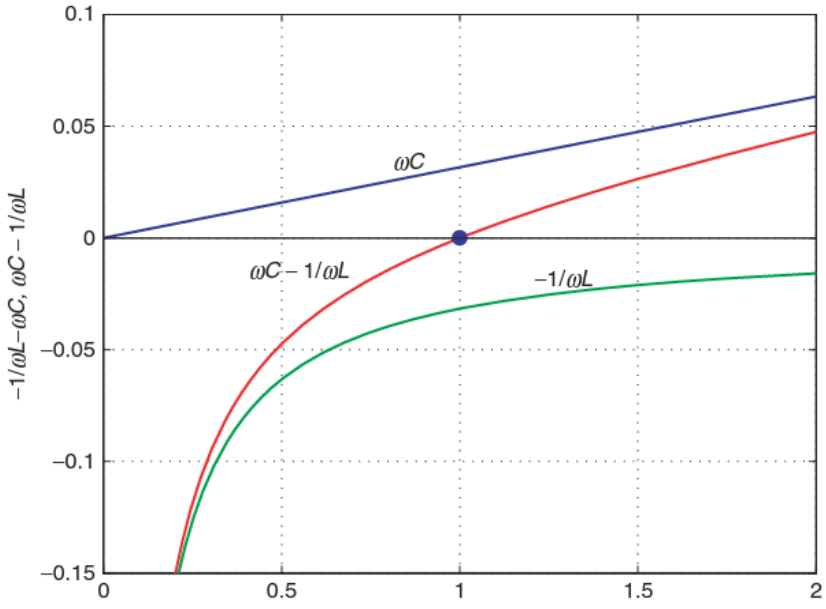

Figure 4.1- the plots of the susceptances $B_C = \omega C$, $B_L = -1/(\omega L)$,and $B = B_C + B_L = \omega C - 1/(\omega L)$ as functions of frequency for inductance L = 1 μ H and C = 1nF [54].

In practice, an inductor has a resistive part and it can be modelled by an equivalent circuit at high frequency as shown in Figure 4.2-(a), whereR_L, $L_L$and C_S are, respectively, the equivalent resistance, inductance and lumped capacitance of the inductor [109]. The resistive effect R_L is mainly caused by winding, eddy current and hysteresis losses, and C_S ,which is called stray capacitance or self-capacitance, represents the distributed capacitance, between the winding turns, acts like a shunt capacitance, passing a high-frequency displacement current. While, the classic lumped model of an inductor is as shown in Figure 4.2-(b), where C_{tt} is the turn to turn capacitance, R_t is the turn resistance and L_t is the turn inductance [110][111]. It depends on the winding geometry, the proximity of turns, core, and shield, and the permittivity of the dielectric insulator, in which the winding wire is coated. If the core is a conductive material then it should be insulated to increase the distance between the turns and the core, and therefore reduce the capacitance between the winding and the core. The coil-to-ground stray capacitance is negligible which means that there are no grounded conductors nearby. Otherwise, a different circuit model for the stray capacitance has to be used [54].

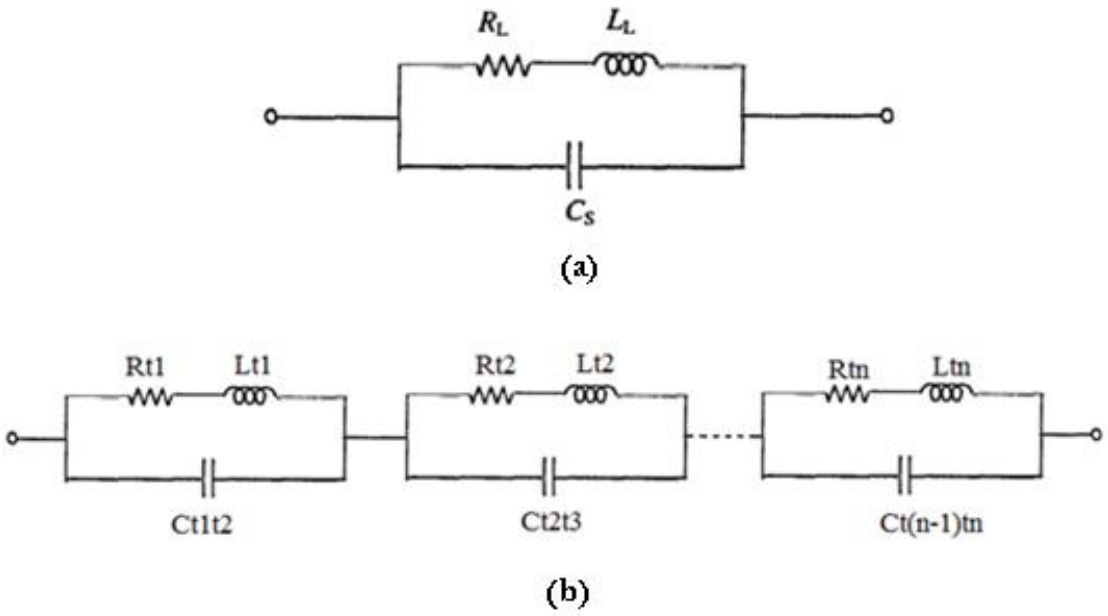

Figure 4.2- (a) The simplified lumped parameter equivalent circuit of an inductor. (b) A network of lumped equivalent circuits for n turn of the inductor[109].

The equivalent impedance of the model shown in Figure 4.2 is given by Bartoli [109]:

$$|Z| = \sqrt{r^2 + x^2} \quad \text{EQ 4.2}$$

And

$$\varphi = arctan\left(\frac{x}{r}\right) \quad \text{EQ 4.3}$$

The series reactance x:

$$x = \frac{j\omega L_S(1 - \omega^2 L_S C_S - {R_S}^2 C_S/L_S)}{(1 - \omega^2 L_S C_S)^2 + (\omega C_S R_S)^2} \quad \text{EQ 4.4}$$

$$r = R_S \frac{1}{(1 - \omega^2 L_S C_S)^2 + \ \omega^2 {C_S}^2 \ {R_S}^2} \quad \text{EQ 4.5}$$

The series resistance r and the series reactance x can be measured with a network analyser and they are in general, frequency dependent. Figure 4.3 shows the magnitude and phase of impedance for the inductor at high-frequency. The reactance x is zero when the inductor is operated at the self-resonant frequencyF_r:

We can find R_S and L_S as following

$$R_S = \frac{1 - \sqrt{1 - 4r^2\omega^2 {C_S}^2 (1 - (\omega^2 L_S C_S)^2}}{2r\omega^2 {C_S}^2} \quad \text{EQ 4.6}$$

$$L_S = \frac{1 + \sqrt{\frac{R_S}{r} - (\omega C_S R_S)^2}}{\omega^2 C_S} \quad \text{EQ 4.7}$$

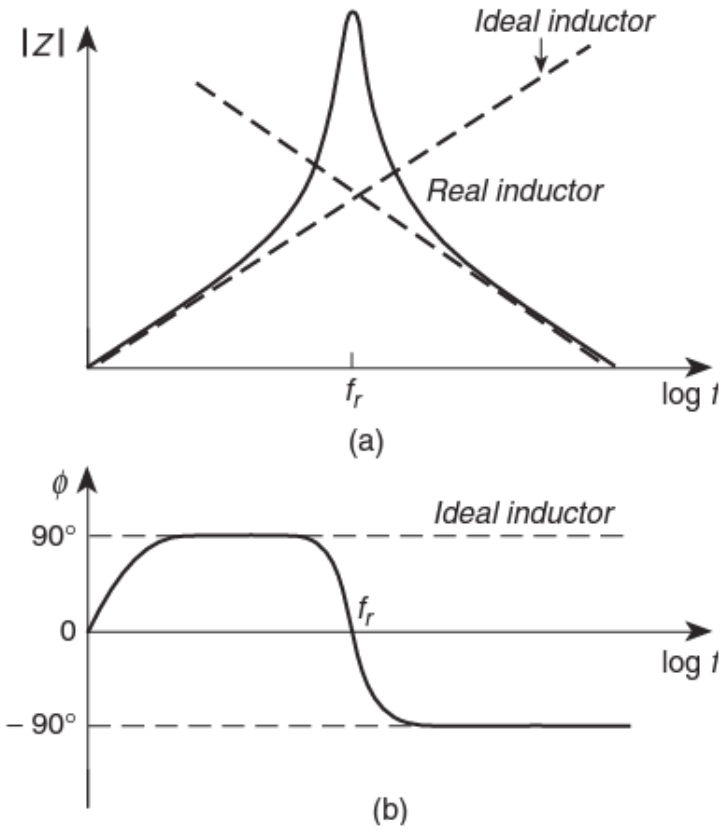

Figure 4.3-Impedance of the high-frequency inductor model. (a) | Z | versus frequency. (b) Φ versus frequency [54].

The self-capacitance of an inductor can be experimentally determined by measuring the self-resonant frequency f_r and the inductance L with a network analyser. The self-resonant frequency can be detected by the maximum magnitude or the zero phase of the inductor impedance [54].

The self-capacitance can be calculated from the equation:

$$C_s = \frac{1}{4\pi^2 L {f_r}^2} \qquad \text{EQ 4.8}$$

A network of lumped equivalent circuits for n turns of the inductor similar to the one shown in Figure 4.4, but with a square cross section conductor, will be proposed later in this chapter and will be solved in order to find the equivalent impedance and consequently the parasitic capacitance of the inductor.

Figure 4.4 shows a solenoid inductor with a conductor having a resistivity ρ and therefore a series resistance R_s. Insulated turns of conductors form turn-to-turn capacitances C_{tt}. Therefore, an electric field exists between the turns with different potentials and stores electric energy. At high frequencies, the displacement current flows through the capacitors and bypasses the inductive and resistive conductors [54].

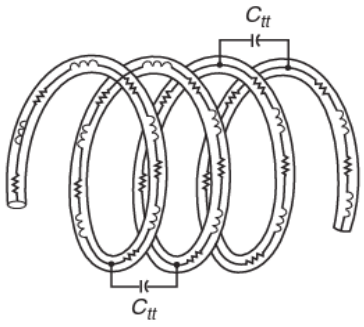

Figure 4.4- Distributed inductance, resistance, and capacitance of an inductor [54].

4.1.2 Parasitic Capacitance

The capacitance of a parallel-plate capacitor, which consists of two conductive plates insulated from each other as shown in Figure 4.5, is equal to the ratio of the charge stored on one plate to the voltage difference between the two plates [54].

C=Q/V EQ 4.9

The capacitance is a function only of the geometry of the design (e.g. area of the plates and the distance between them) and the permittivity of the dielectric material between the plates of the capacitor. For a capacitor constructed of the two parallel plates in Figure 4.5, both of area A separated by a distance d, if d is sufficiently small with respect to the smallest dimension of A, the capacitance C is [54]:

$$C = \varepsilon_r \varepsilon_0 \frac{A}{d} \quad \text{EQ 4.10}$$

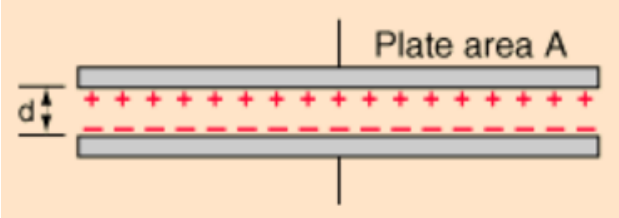

Figure 4.5- Parallel-plate capacitor.

Where

C is the capacitance, in farads F.

A is the area of overlap of the two plates, in square meters m^2.

ε_r is the relative static permittivity (sometimes called the dielectric constant) of the material between the plates (for a vacuum, ε_r = 1).

ε_0 is the di-electric constant ($\varepsilon_0 \approx 8.854 \times 10^{-12}$ F · m^{-1}).

d is the separation between the plates, in meters *m*.

In a solenoid inductor any two adjacent turns can function as a capacitor, though the results parasitic capacitance is small unless the turns are close together for long distances or over a large area. The geometrical structures of solenoid inductors are much more complex than those of the parallel plate capacitor, which makes deriving a formula for the parasitic capacitance complicated. Some analytical methods to calculate the parasitic capacitance for simple geometries of inductors will be explained below.

4.1.2.1 Analytical Expressions for Parasitic Capacitance

In previous studies [112][113][114][115][116] a high-frequency model of inductors is developed. The impedance of inductors is studied as a function of frequency. Physics-based analytical expressions for self-capacitances of foil winding inductors, single-layer, and multilayer round wire inductors are derived using geometrical methods.

Researchers [54] [116][117] discussed various analytical methods to calculate the parasitic capacitance for simple geometries of inductors and transformers, many of which are based on empirical formula.

In [117] an analytical method is used to determine the self-capacitance of a single-layer inductor as is shown in Figure 4.6. It is assumed that the capacitances between nonadjacent turns are much lower than those between adjacent turns and can be neglected. The formula EQ 4.11 for the capacitance between two parallel round bare conductors placed in a homogeneous medium has been derived for the turn-to-turn capacitance of a single-layer inductor without or with a nonconductive core.

$$C_{tt} = \frac{\pi \epsilon l_T}{\cosh^{-1}(\frac{p}{2a})} = \frac{\pi \epsilon l_T}{ln\left[\frac{p}{2a} + \sqrt{\left(\frac{p}{2a}\right)^2 - 1}\right]} = \frac{\pi^2 \epsilon D_T}{ln\left[\frac{p}{2a} + \sqrt{\left(\frac{p}{2a}\right)^2 - 1}\right]} \quad for\ t \ll p - 2a \qquad \text{EQ 4.11}$$

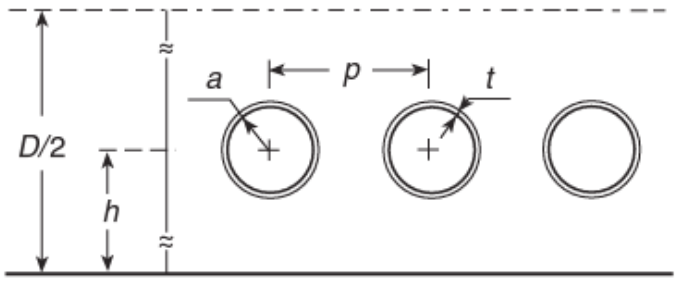

Figure 4.6- Cross-sectional view of a single- layer inductor with a core of a shield [117].

Where $l_T = \pi\ D_T$ is the length of a single turn, D_T is the coil diameter, 'a' is the bare wire radius, *t* is the thickness of the insulating coating, and *p* is the distance between the centrelines of two adjacent turns.

Methods for calculating self-capacitance of a multilayer inductor and a multilayer inductor with conductive core have been also presented previously; Massarini and Kazimierczuk [118] have used the delta Δ-to- star Y transformation to determine the stray capacitance of inductors with many turns as shown in EQ 4.12.

$$C_{1,N} = C_{tt} + \frac{C_{1,(N-2)}C_{tt}}{2C_{1,(N-2)} + C_{tt}} = C_{tt} + \frac{C_{tt}}{\frac{C_{tt}}{C_{1,(N-2)}} + 2} = C_{tt}\left[\frac{C_{tt} + 3C_{1,(N-1)}}{C_{tt} + 2C_{1,(N-1)}}\right] \quad for\ N \gg 4 \qquad \text{EQ 4.12}$$

4.1.2.2 Finite-Element Analysis (FEA) Method for Parasitic Capacitance

Unlike these analytical methodologies finite-element analysis (FEA) method has the ability to accurately determine the parasitic capacitances of complicated magnetic geometries while taking into consideration the physical properties of the materials.

Techniques and methods to quantitatively predict the parasitic capacitance of coils and cores at high-frequency by the usage of finite-element analysis (FEA) have been presented previously [119][120] where the turn-to-turn capacitance was found in order to obtain the equivalent self-capacitance of a single-layer coil consisting of n turns wound on a conductive core.

A Finite-element simulator such as MAXWELL from ANSOFT can solve the lumped capacitor network by giving a capacitance matrix represents the charge coupling within a group of conductors next to each other, which means the relationship between charges and voltages for the conductors. Consider for example a 3-conductor case with the outside boundary taken as a reference as shown in Figure 4.7. According to the Maxwell capacitance matrix [121][122] the net charge Q on each object will be given by the following equations:

$$Q_1 = C_{11}V_1 + C_{12}(V_1 - V_2) + C_{13}(V_1 - V_3) \qquad \text{EQ 4.13}$$

$$Q_2 = C_{22}V_2 + C_{12}(V_2 - V_1) + C_{23}(V_2 - V_3) \qquad \text{EQ 4.14}$$

$$Q_3 = C_{33}V_3 + C_{13}(V_3 - V_1) + C_{23}(V_3 - V_2) \qquad \text{EQ 4.15}$$

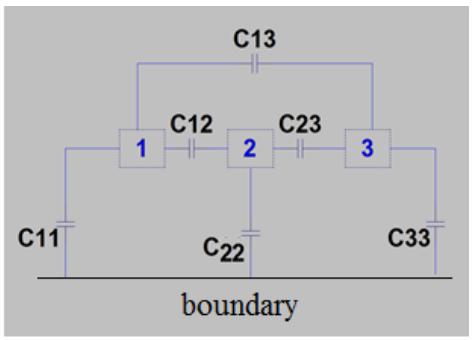

Figure 4.7-Capacitances between three conductors.

This can be expressed in matrix form as:

$$\begin{bmatrix} Q_1 \\ Q_2 \\ Q_3 \end{bmatrix} = \begin{bmatrix} C11 + C12 + C13 & -C12 & -C13 \\ -C12 & C12 + C22 + C23 & -C23 \\ -C13 & -C23 & C13 + C23 + C33 \end{bmatrix} \begin{bmatrix} V_1 \\ V_2 \\ V_3 \end{bmatrix} \quad \text{EQ 4.16}$$

The C matrix is:

$$C = \begin{bmatrix} C11 + C12 + C13 & -C12 & -C13 \\ -C12 & C12 + C22 + C23 & -C23 \\ -C13 & -C23 & C13 + C23 + C33 \end{bmatrix} \quad \text{EQ 4.17}$$

Extending to the general case, the Maxwell capacitance matrix has the form:

$$\begin{bmatrix} C11 + C12 + \cdots + C1n & -C12 & \cdots & -C1n \\ -C12 & C12 + C22 + C23 & \cdots & -C2n \\ \cdots & \cdots & \cdots & \cdots \\ -C1n & -C2n & \cdots & C1n + C2n + \cdots + Cnn \end{bmatrix}$$

EQ 4.18

For 3 conductors with voltage applied to one conductor $V_1 = 1$ and zero volts applied to the other two conductors $V_2 = 0$ & $V_3 = 0$, the capacitance matrix from EQ 4.17 will be as follow:

$$C = \begin{bmatrix} C11 + C12 + C13 \\ -C12 \\ -C13 \end{bmatrix} \quad \text{EQ 4.19}$$

4.1.3 Flow Chart of the Methodology

In this chapter, a method of obtaining the impedance curve and analysing the equivalent circuit of the inductor is presented and validated experimentally. Both inductance and capacitance matrices are obtained using Maxwell 16 software (Magneto-static and Electrostatic solvers). An equivalent electrical circuit of the inductor is proposed and solved in LTSPICE, and the impedance curve is obtained. The method will be validated experimentally using the Impedance Analyser KEYSIGHT E4990A. The flow chart of the method is shown in Figure 4.8 below.

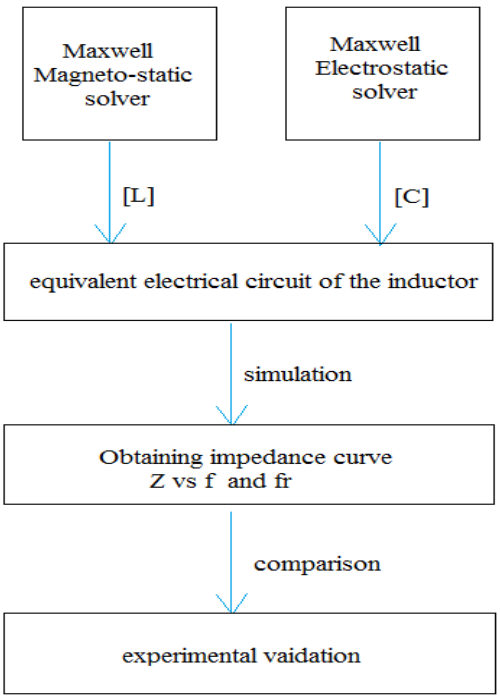

Figure 4.8-The flow chart of the method.

Each stage of obtaining the impedance cure in frequency domain will be explained in the following sections.

4.2 Electrostatic Simulation, Capacitive parameters

The capacitance matrices of the arrangements shown in Figure 4.9 have been obtained using Maxwell 16 (electrostatic solver) giving the values of capacitance as in between adjacent turns ($C_{t1t2}, C_{t2t3}\ldots C_{t25t26}$) and non-adjacent turns (C_{t1t3}, C_{t2t4}, $C_{t3t5}\ldots C_{t24t26}$). While Cm is the capacitance between the turns of both inductors as shown in Figure 4.9-(b) and C_{ts} is the capacitance between the bottom copper substrate and the inductor as shown in Figure 4.9-(c). The values of the capacitance are arranged in Table 4.4. Since the ferrite of the core is a very low conductivity material, the parasitic capacitances between the inductor and the core have been ignored. The inductor's geometry and dimensions are shown in Appendix A, Figure 7.3.

The element in the matrix C_{t1t1} are the sum of all capacitances from one conductor to all other conductors (C_{t1t1}=C_{t1t3}+ C_{t2t4}+$C_{t3t5}\ldots$+Ct_{24t26}). These terms represent the self-capacitance of the conductors. Each is numerically equal to the charge on a

conductor when one volt is applied to that conductor and the other conductors (including ground) are set to zero volts.

The turns were separated into individual rings in order to obtain the capacitance between them. A natural boundary is considered, where the normal component of the electric flux density D changes by the amount of surface charge density, and the tangent component of the electric field E is continuous. No special conditions are imposed. A region of air with size 100% bigger than the inductor size is encompassing the inductor but no voltage distribution has been applied between the inductor and the region.

Figure 7.9 in Appendix C shows the capacitance matrix of the inductor as in arrangement in Figure 4.9-(c). The stray capacitance between non-adjacent turns will be ignored since it is small comparing to the capacitance between adjacent turns.

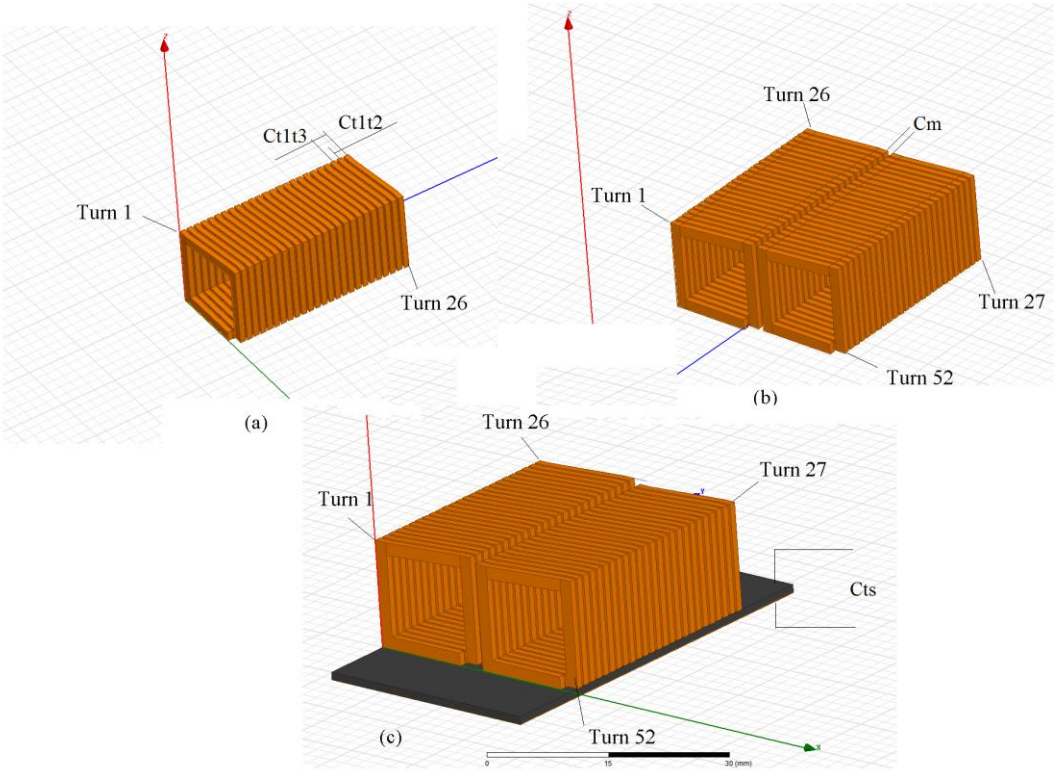

Figure 4.9- Different arrangement of the inductor in order to obtain the stray capacitance.

4.3 Magneto-static Simulation, Inductive Parameters

In order to evaluate the inductance for each turn in Figure 4.9-(a) & (b) considering also the coupling inductance between turns, the inductance matrix has been obtained from Maxwell (Magneto-static solver).

4.3.1 Grouping Inductance Matrix Elements

The matrix with the inductance of each turn and the mutual inductance between the turns has been obtained using Maxwell software (Electro-magnetic software), a current has been be applied across the inductor.

The inductance matrix calculation is processed using the grouping function [121] which considers the coupling between the turns. The inductances of the coils can be calculated as follows:

$$L_{series\ group} = \sum_{i=1}^{m} L_{coil_i} + \sum_{i=1}^{m}\sum_{j=1}^{m} M_{ij} \times n_i \times n_j \quad , i \neq j \qquad \text{EQ 4.20}$$

Where:

• m is the number of source entries being grouped.

• $Lcoil_i$ represents the self-inductance term of the coil

• Mij the mutual inductance terms between the turns of the inductors.

• n_i ,n_j are the number of turns for each coil in the group.

Figure 7.10 in Appendix C shows the inductance matrix of the inductor as in the arrangement in Figure 4.9-(b).

4.4 The Equivalent Circuit of the Inductor

After computing the capacitance and inductance matrices for the inductor using Maxwell Electro-statics and Magneto-static simulation a proposed equivalent circuit will be solved using these values in order to obtain the impedance curve of the inductor in frequency domain.

An equivalent circuit (the classic lumped model of an inductor), as shown in Figure 4.2-(b), of an inductor has been explained previously [54][56][119][123], where the parasitic capacitance turn to turn, turn to substrate and turn to core were analysed.

This method is referred in this chapter as notion1 and is explained below analytically using standard derivation considering 3 turns, as shown in Figure 4.10, assuming R1=R2=R3=0 in order to simplify the formulas.

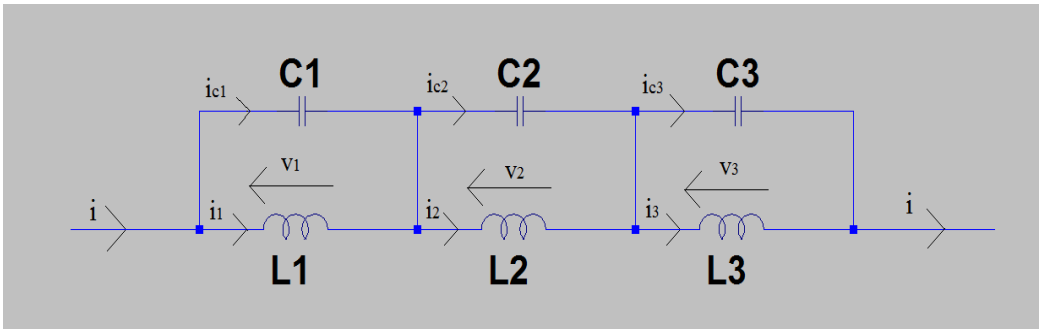

Figure 4.10- Lumped model of three adjacent turns of an inductor, notion 1.

4.4.1 The Equivalent Circuit of the Inductor Notion 1

From Figure 4.10 the input current is split through the inductor's turns i_1, i_2 & i_3 and the parasitic capacitors i_{C1}, i_{C2} &i_{C3}. While v is the voltage drop across each turn and its parasitic capacitance.

$$\begin{Bmatrix} i = i_1 + i_{C1} \\ i = i_2 + i_{C2} \\ i = i_3 + i_{C3} \end{Bmatrix} \quad \& \quad v = v_1 + v_2 + v_3 \qquad \text{EQ 4.21}$$

The instantaneous voltage across each turn of the inductor is equal to total inductance of the turn multiplying by the instantaneous rate of current change (amps per second). For a constant amplitude, sinusoidal current through the three turns the voltage vector is given by:

$$\begin{bmatrix} v_1 \\ v_2 \\ v_3 \end{bmatrix} = \begin{bmatrix} L_1 & M_{12} & M_{13} \\ M_{21} & L_2 & M_{23} \\ M_{31} & M_{32} & L_3 \end{bmatrix} \times \begin{bmatrix} d_{i1}/d_{t1} \\ d_{i2}/d_{t2} \\ d_{i3}/d_{t3} \end{bmatrix} = j\omega[L] \times \begin{bmatrix} i_1 \\ i_2 \\ i_3 \end{bmatrix} \qquad \text{EQ 4.22}$$

While, the instantaneous current through each parasitic capacitors is equal to capacitance of the turn multiplying by the instantaneous rate of voltage change (volts per second). For constant voltage across the three turns the current vector is given by:

$$j\omega \times \begin{bmatrix} C_1 & 0 & 0 \\ 0 & C_2 & 0 \\ 0 & 0 & C_3 \end{bmatrix} \times \begin{bmatrix} v_1 \\ v_2 \\ v_3 \end{bmatrix} = \begin{bmatrix} i_{C1} \\ i_{C2} \\ i_{C3} \end{bmatrix} \qquad \text{EQ 4.23}$$

Using EQ 4.21 in EQ 4.22

$$\frac{1}{j\omega} \times [L]^{-1} \times \begin{bmatrix} v_1 \\ v_2 \\ v_3 \end{bmatrix} = \begin{bmatrix} i_1 \\ i_2 \\ i_3 \end{bmatrix} = \begin{bmatrix} i - i_{C1} \\ i - i_{C2} \\ i - i_{C3} \end{bmatrix} \quad \text{EQ 4.24}$$

Using EQ 4.23 in EQ 4.24

$$\left\{\frac{1}{j\omega} \times [L]^{-1} + j\omega[C_M]\right\} \times \begin{bmatrix} v_1 \\ v_2 \\ v_3 \end{bmatrix} = \begin{bmatrix} i \\ i \\ i \end{bmatrix} \quad \text{EQ 4.25}$$

Thus, the admittance Y and the impedance Z of the inductor with 3 turns are:

$$\text{Y} = \left\{\frac{1}{j\omega} \times [L]^{-1} + j\omega[C_M]\right\} \quad \text{EQ 4.26}$$

$$\text{Z} = (Y)^{-1} = \left\{\frac{1}{j\omega} \times (L)^{-1} + j\omega(C_M)\right\}^{-1} \quad \text{EQ 4.27}$$

While the capacitance matrix and the inductance matrix of the three turns are:

$$[C_M] = \begin{bmatrix} C_1 & 0 & 0 \\ 0 & C_2 & 0 \\ 0 & 0 & C_3 \end{bmatrix} \text{ \& } [L] = \begin{bmatrix} L_1 & M_{12} & M_{13} \\ M_{21} & L_2 & M_{23} \\ M_{31} & M_{32} & L_3 \end{bmatrix}$$

This method has been validated experimentally, first the impedance curve of the inductor in Figure 4.9(a) has been obtained from solving notion 1 in MATLAB using both inductance and the capacitance matrices from the MAXWELL Software. A Ferrite N95 core has been used in order to increase the inductance value, thus the resonance frequency is decreased and the impedance curve with its maximum value can be captured with the analyser frequency range [20 Hz-120 MHz].

The impedance curve of the inductor has been obtained by the KEYSIGHT E4990A impedance analyser. Both curves are compared as shown in Figure 4.11, where there is a significant difference between both simulation and experiment. For the resonance frequency, there is a difference of 63 MHz which means that resonance frequency's value from measurements is around 58% below that from simulation. This difference can't be justified only by the measurement errors and the difference in the inductor geometry between the designed and the real inductor. This means that this studied equivalent circuit (notion1) is not accurate for the inductor of this study. For the difference of the magnitude at resonant frequency this is due to the fact that the resistive component in the equivalent circuit has been ignored in order to simplify the simulation.

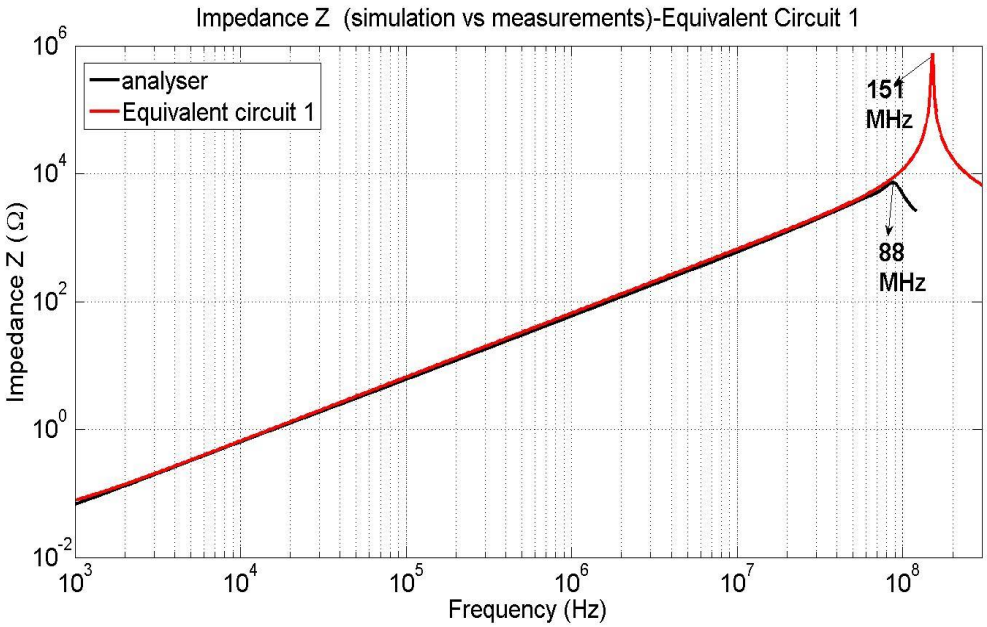

Figure 4.11-Impedance Z of inductor with 26 turns and N95 ferrite core-simulation vs measurements using equivalent circuit 1(notion 1).

From the comparison between the computed parasitic capacitance from both simulation and measurements in Table 4.1 an important difference is noticed that the simulation capacitance's value is around 3 times smaller than it is in measurements, the effects of parasitic capacitance are not accurately reflected in the model. Therefore a more precise equivalent circuit is needed. This equivalent circuit of the inductor is proposed and called Notion 2.

Table 4.1- Total parasitic capacitance C (pF) for the inductor with 26 turns and N95 ferrite core, notion1 vs measurements

Total parasitic capacitance C (pF)	
Simulation	Measurements
0.1	0.33

4.4.2 Distributed Model

In this section, a new approach, regarding the turn to turn parasitic capacitance will be presented and will be explained using two turn model as shown in Figure 4.12.

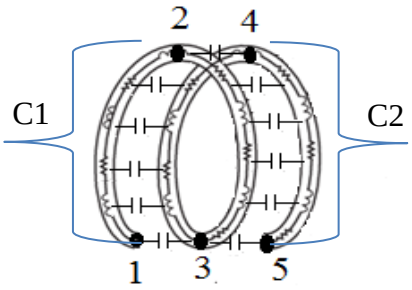

Figure 4.12- Proposed analyses method for parasitic capacitance between two turns.

Each turn has been divided into two partial inductance, (1, 2, 3) for first turn and (3, 4, 5) for second turn as shown in Figure 4.12. When the current enter point 1 it divides and part of it passes through the parasitic capacitance c_1 and arrives at point 4 after the point 3 which means to the second turn as it is explained more in Figure 4.13. Similarly, when the current enter point 2, part of it passes through the parasitic capacitance c_1 and arrives at point 5 after the point 4. Thus each turn to turn capacitance c_{tt} is the sum of capacitors c_1 and c_2, also each turn inductance Lt is the sum of inductors L1and L2.

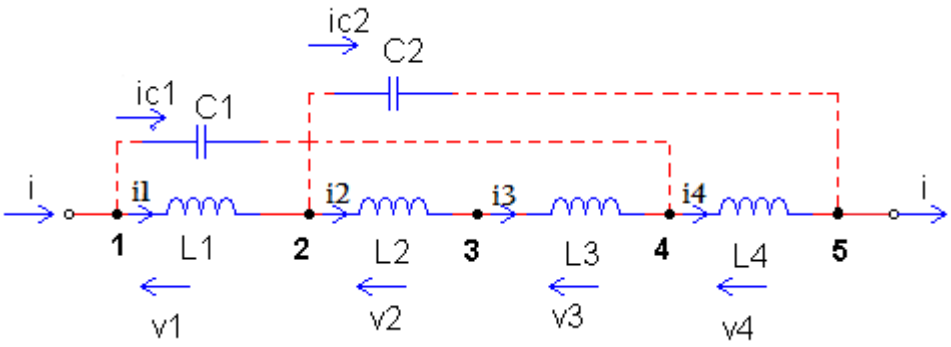

Figure 4.13- Electric circuit representation of the proposed analysis method for parasitic capacitance between two turns.

From Figure 4.13 the input current is split through the inductor's partial turns (i_1, i_2, i_3 & i_4) and also through the parasitic capacitance i_{C1} (between 1&4) and i_{C2} (between 2&5). v is the voltage drop across each turn and its parasitic capacitance. Thus, the current and the voltage drop in the circuit are as in the following equations:

$$\begin{Bmatrix} i_1 = i - i_{c1} \\ i_2 = i_3 = i - i_{c1} - i_{c2} \\ i_4 = i - i_{c2} \\ i_5 = i \end{Bmatrix} \quad \begin{matrix} v_{c1} = v_1 + v_2 + v_3 \\ v_{c2} = v_2 + v_3 + v_4 \end{matrix} \quad \begin{Bmatrix} v = v_1 + v_2 + v_3 + v_4 \end{Bmatrix} \qquad \text{EQ 4.28}$$

The instantaneous voltage across each partial turn of the inductor is equal to inductance of that part multiplied by the instantaneous rate of current change (amps per second). For constant amplitude sinusoidal current through the two turns as shown in Figure 4.13 the voltage matrix of the voltage of each partial inductance (ignoring mutual coupling) is giving in the equation:

$$\begin{bmatrix} v_1 \\ v_2 \\ v_3 \\ v_4 \end{bmatrix} = j\omega \times \begin{bmatrix} L_1 & 0 & 0 & 0 \\ 0 & L_2 & 0 & 0 \\ 0 & 0 & L_3 & 0 \\ 0 & 0 & 0 & L_4 \end{bmatrix} \begin{bmatrix} i_1 \\ i_2 \\ i_3 \\ i_4 \end{bmatrix} \qquad \text{EQ 4.29}$$

The instantaneous current through each parasitic capacitors is equal to capacitance of the turn multiplied by the instantaneous rate of voltage change (volts per second). For constant voltage across the two turns the current matrix giving:

$$\begin{bmatrix} i_{c1} \\ i_{c2} \end{bmatrix} = J\omega \times \begin{bmatrix} c_1 & 0 \\ 0 & c_2 \end{bmatrix} \times \begin{bmatrix} v_{c1} \\ v_{c2} \end{bmatrix} : \begin{Bmatrix} i_{c_1} = J\omega c_1 v_{c_1} \\ i_{c_2} = J\omega c_2 v_{c_2} \end{Bmatrix} \qquad \text{EQ 4.30}$$

Considering $i_1, i_2, i_3 \; and \; i_4$ from EQ 4.28 in EQ 4.29:

$$\begin{bmatrix} v_1 \\ v_2 \\ v_3 \\ v_4 \end{bmatrix} = j\omega \times \begin{bmatrix} L_1 & 0 & 0 & 0 \\ 0 & L_2 & 0 & 0 \\ 0 & 0 & L_3 & 0 \\ 0 & 0 & 0 & L_4 \end{bmatrix} \begin{bmatrix} i - i_{c_1} \\ i - i_{c1} - i_{c2} \\ i - i_{c1} - i_{c2} \\ i - i_{c2} \end{bmatrix} \qquad \text{EQ 4.31}$$

considering i_{c_1}&i_{c_2} from EQ 4.30 in EQ 4.31:

$$\begin{bmatrix} v_1 \\ v_2 \\ v_3 \\ v_4 \end{bmatrix} = j\omega \times \begin{bmatrix} L_1 & 0 & 0 & 0 \\ 0 & L_2 & 0 & 0 \\ 0 & 0 & L_3 & 0 \\ 0 & 0 & 0 & L_4 \end{bmatrix} \times \left(\begin{bmatrix} i \\ i \\ i \\ i \end{bmatrix} - j\omega \begin{bmatrix} c_1 v_{c_1} \\ c_1 v_{c_1} + c_2 v_{c_2} \\ c_1 v_{c_1} + c_2 v_{c_2} \\ c_2 v_{c_2} \end{bmatrix} \right) \qquad \text{EQ 4.32}$$

considering v_{c1}&v_{c2} from EQ 4.28 in EQ 4.33:

$$\begin{bmatrix} v_1 \\ v_2 \\ v_3 \\ v_4 \end{bmatrix} = j\omega \times \begin{bmatrix} L_1 & 0 & 0 & 0 \\ 0 & L_2 & 0 & 0 \\ 0 & 0 & L_3 & 0 \\ 0 & 0 & 0 & L_4 \end{bmatrix} \times \left(\begin{bmatrix} i \\ i \\ i \\ i \end{bmatrix} - j\omega \begin{bmatrix} c_1(v_1 + v_2 + v_3) \\ c_1(v_1 + v_2 + v_3) + c_2(v_2 + v_3 + v_4) \\ c_1(v_1 + v_2 + v_3) + (v_2 + v_3 + v_4) \\ c_2(v_2 + v_3 + v_4) \end{bmatrix} \right) \quad \text{EQ 4.33}$$

assuming that c_1=c_2=c_d :

$$\begin{bmatrix} v_1 \\ v_2 \\ v_3 \\ v_4 \end{bmatrix} = j\omega \times \begin{bmatrix} L_1 & 0 & 0 & 0 \\ 0 & L_2 & 0 & 0 \\ 0 & 0 & L_3 & 0 \\ 0 & 0 & 0 & L_4 \end{bmatrix} \times \left(\begin{bmatrix} i \\ i \\ i \\ i \end{bmatrix} - j\omega \begin{bmatrix} v_1 \\ v_2 \\ v_3 \\ v_4 \end{bmatrix} \times \begin{bmatrix} c_d & c_d & c_d & 0 \\ c_d & 2c_d & 2c_d & c_d \\ c_d & 2c_d & 2c_d & c_d \\ 0 & c_d & c_d & c_d \end{bmatrix} \right) \quad \text{EQ 4.34}$$

Thus:

$$\left\{ \frac{1}{j\omega} \times [L]^{-1} + j\omega[C_M] \right\} \times \begin{bmatrix} v_1 \\ v_2 \\ v_3 \\ v_4 \end{bmatrix} = \begin{bmatrix} i \\ i \\ i \\ i \end{bmatrix} \quad \text{EQ 4.35}$$

Where [L] = $\begin{bmatrix} L_1 & 0 & 0 & 0 \\ 0 & L_2 & 0 & 0 \\ 0 & 0 & L_3 & 0 \\ 0 & 0 & 0 & L_4 \end{bmatrix}$

and

$[C_M]$ = $\begin{bmatrix} c_d & c_d & c_d & 0 \\ c_d & 2c_d & 2c_d & c_d \\ c_d & 2c_d & 2c_d & c_d \\ 0 & c_d & c_d & c_d \end{bmatrix}$

And Figure 4.13 leads to:

$$v = v_1 + v_2 + v_3 + v_4 = (\sum_{i=1}^{4} \sum_{j=1}^{4} Z_{ij} \times i) \quad \text{EQ 4.36}$$

Thus, the admittance Y and the impedance Z of the inductor with 2 turns are:

$$\text{Y} = \left\{ \frac{1}{j\omega} \times [L]^{-1} + j\omega[C_M] \right\} \quad \text{EQ 4.37}$$

$$\text{Z} = (Y)^{-1} = \left\{ \frac{1}{j\omega} \times [\text{L}]^{-1} + j\omega\,[C_M] \right\}^{-1} = \begin{bmatrix} Z_{11} & Z_{12} & Z_{13} & Z_{14} \\ Z_{21} & Z_{22} & Z_{23} & Z_{24} \\ Z_{31} & Z_{32} & Z_{33} & Z_{34} \\ Z_{41} & Z_{42} & Z_{43} & Z_{44} \end{bmatrix} \quad \text{EQ 4.38}$$

Assuming that it is assumed that $c_d = c_1 = c_2$.

4.4.3 New Lumped Model of the Inductor Notion 2

A new lumped model for two adjacent turns of an inductor (notion 2) is proposed as shown in Figure 4.14.

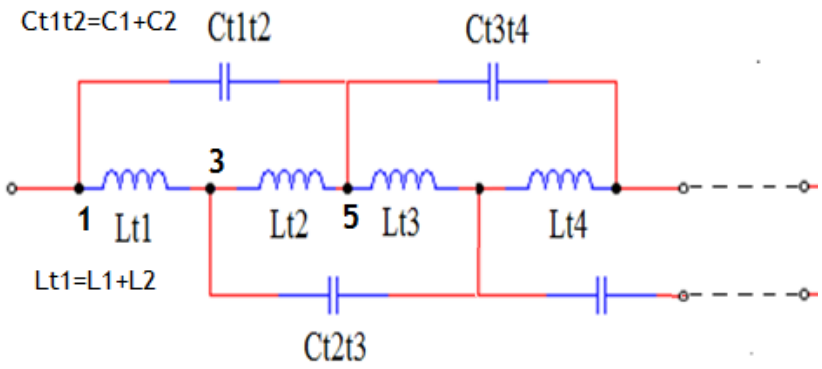

Figure 4.14- Proposed lumped model of two adjacent turns of an inductor (notion 2) for parasitic capacitance between two turns.

The equivalent impedance of this lumped model (notion 2) is

$$Z_{eq} = \frac{2jL_t\omega}{1-2LC_{tt}L_t\omega} \qquad \text{EQ 4.39}$$

c_{tt} is the turn to turn capacitance and it is the sum of capacitors c_1 and c_2, also each turn inductance Lt is the sum of inductors L1and L2.

The equivalent impedance of each of the three previous models, for two adjacent turns, (as in Figure 4.10, Figure 4.12 and Figure 4.14) are compared in Figure 4.15. In this comparison the distributed model (Figure 4.12) is extended to 32 partial inductance and the model have been solved numerically. Parameters for these calculations are:

- $L_t = L_{t1} = L_{t2} = L_1 + L_2 + L_3 + \cdots + L_{32} = L_{33} + L_{34} + L_{35} + \cdots + L_{64}$
- $L_1 = L_2 = L_3 = \cdots = L_{64} = L_t/32$
- $C_{tt} = C_1 + C_2 + C_2 + \cdots + C_{32}$
- $C_1 = C_2 = C_2 = \cdots = C_{32} = C_{tt}/32$
- Fixed values for $C_{tt} = 3\,pF$ *and* $L_t = 1\,nH$ have been considered in the calculation.

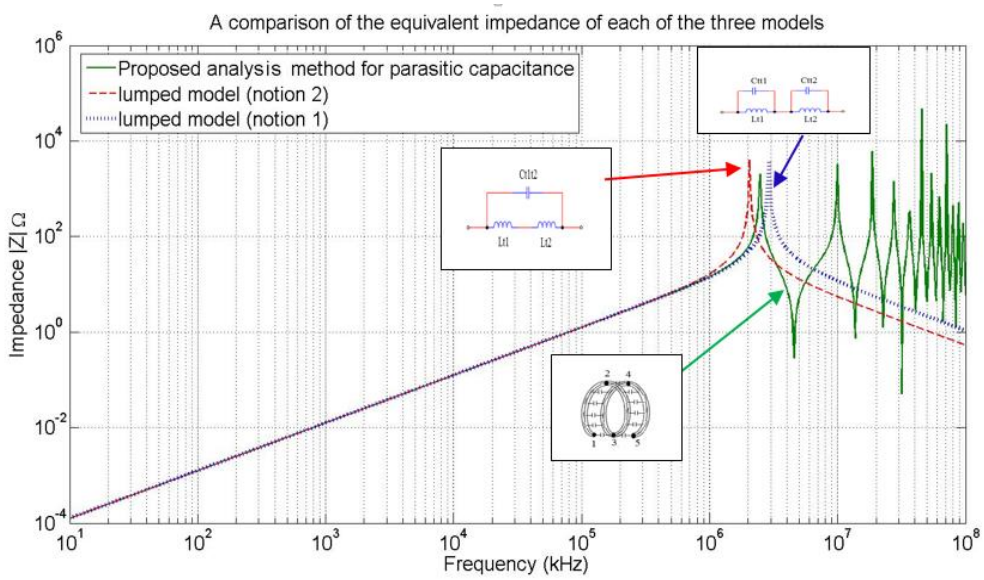

Figure 4.15-A comparison of the equivalent impedance of each of the three previous models.

The first resonant frequency of the distributed model is smaller than classical lumped model (notion 1) and higher than the proposed lumped model (notion 2). However, as the measurements showed in Figure 4.11, the resonance frequency of the inductor is over estimated by notion 1. This comparison (Figure 4.15) shows that notion 2 can better represent the frequency behaviour of the inductor, as it already predicts a smaller first resonant frequency comparing to the distributed model.

Here, the idea of notion 2 will be applied to a 26-turns inductor as shown in Figure 4.16 and compared with measurements.

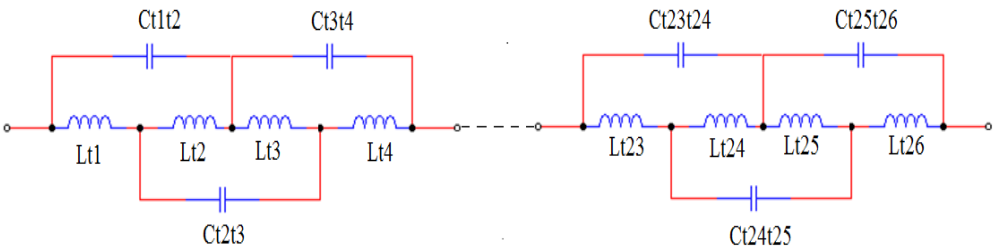

Figure 4.16- Proposed lumped model of 25 turns of an inductor (notion 2).

The experimental impedance curve of the inductor was obtained with the usage of Analyser KEYSIGHT E4990A while the theoretical impedance curve was obtained by solving the equivalent circuit equation from above for 26 turns in MATLAB R2012a using both inductance and the capacitance matrices from MAXWELL Software. The impedance curves are compared as shown in Figure 4.17.

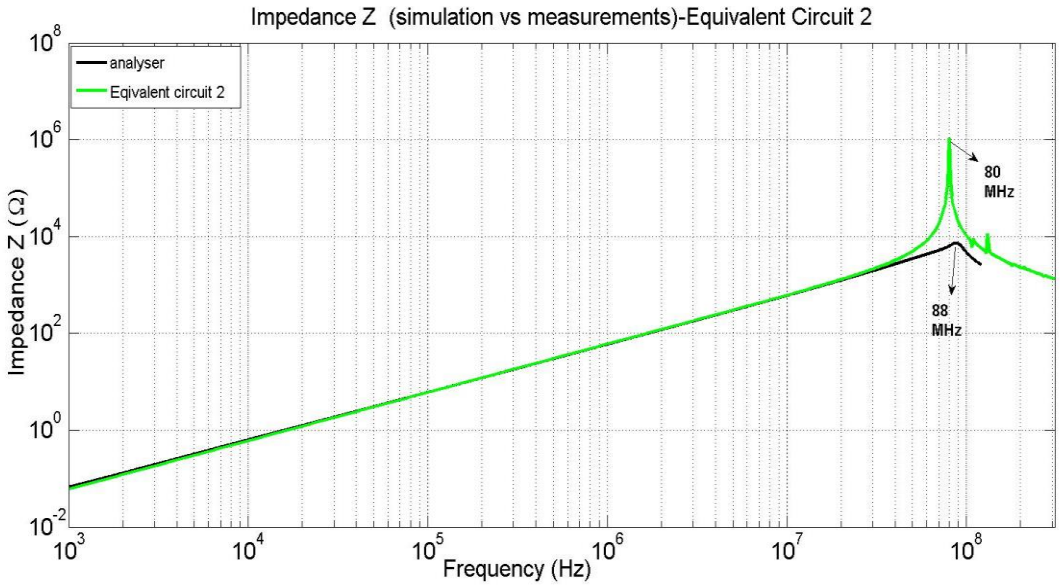

Figure 4.17- Impedance Z of inductor with 26 turns and N95 ferrite core- simulation vs measurements using equivalent circuit 2.

The comparison between the simulation using the proposed notion 2 and the measurements indicates a good agreement between them. For the resonance frequency, there is a difference of 8 MHz which means that resonance frequency's value from simulation is around 90% of that from measurements. This difference can be justified by:

1- Measurements error due to compensation and calibration in the impedance analyser.
2- The difference in the inductor geometry between simulation and reality which might cause slight differences in both inductance and parasitic values.
3- For the difference of the magnitude this is due to the fact that the resistive component in the equivalent circuit has been ignored in order to simplify solving the simulation.

Parasitic capacitances has been obtained from the impedance curves and compared in Table 4.2. It shows a reasnoble agreement between simulation and measurements.

Table 4.2- Total parasitic capacitance C (pF) for the inductor with 26 turns and N95 ferrite core, notion2 vs measurements

Total parasitic capacitance C (pF)	
Simulation	Measurements
0.39	0.32

4.4.4 Simplified Equivalent Circuit in Simulation

The simulation is done in both MATLAB and LTSPICE, where in MATLAB the inductance matrix, which was obtained by MAXWELL Electro-magnetic solver, is imported including the coupling between all turns. In LTSPICE a simplified method is applied and the total inductance value taken from MAXWELL is divided by the number of turns and called inductance per turn Lt. In this case coupling is ignored. It has been proved that both methods of computing the inductance have the same results regarding to the impedance curves up to the first resonance frequency as shown in Figure 4.18.

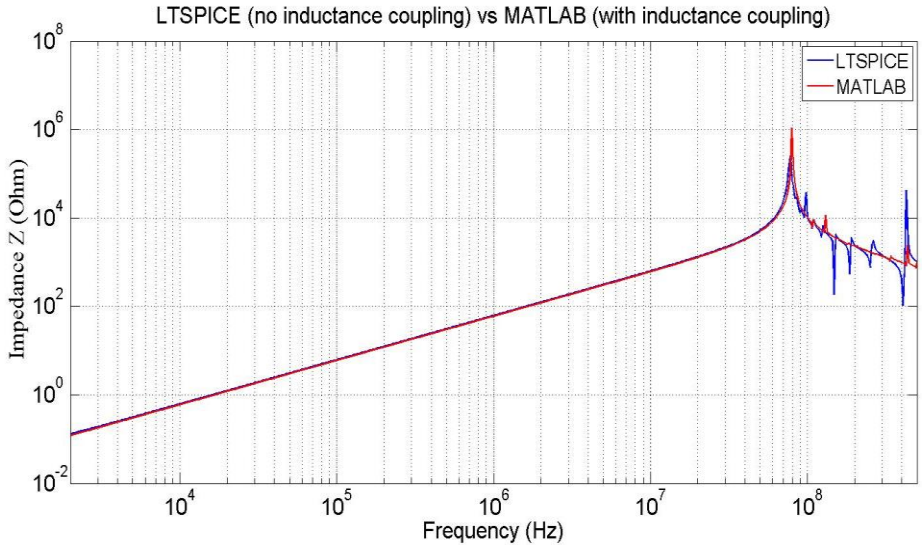

Figure 4.18- Impedance curve for one inductor with N95 ferrite core 26 turns. LTSPICE vs MATLAB

4.5 The Two Port Network Measurements

In this section the two port network measurements will be explained in order to obtain the transfer function from the output to the input with open output $I_2 = 0$ which will reflect the behaviour of the interturn parasitic capacitance of the proposed inductor and between the inductor and the bottom substrate. This kind of measurements is needed when the inductor is soldered on the substrate as shown in Figure 4.9-(c) and Figure 3.9.

A two port network is a four terminal circuit in which the terminals are paired to form an input port and an output port. The defining of port voltages and currents are shown in Figure 4.19. The linear circuit connecting the two ports is assumed to be in zero state and to be free of any independent sources, which means that there is no initial energy stored in the circuit and the box in the figure below contains only resistors, capacitors, inductors, mutual inductance, parasitic capacitance and dependent sources [124].

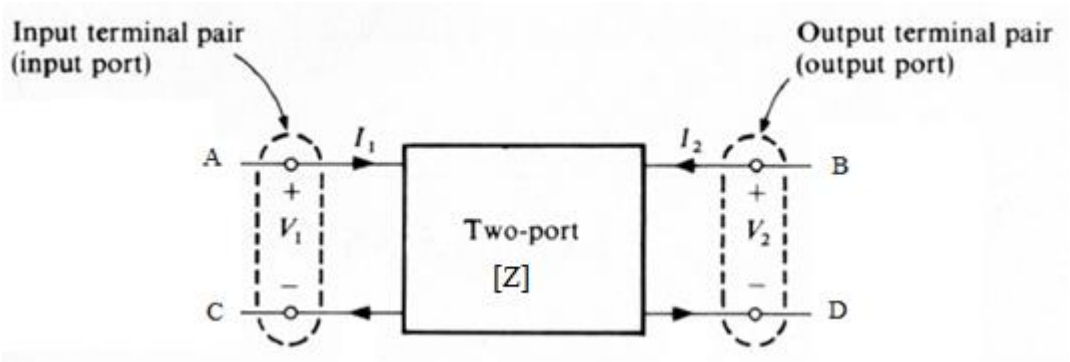

Figure 4.19- Two-port circuit [Z]impedance matrix [125].

In order to characterize a two-port circuit we should identify the circuit parameters. In this approach, port voltages $V_1$and V_2 and port currents $I_1$and I_2 are the only available variables. The circuit parameters are defined by expressing two of these four port variables in term of other two variables. The four matrices, which can be obtained by analysing the two port network, and their defining equations are organised in Table 4.3 below.

Table 4.3- The matrices which can be obtained by analysing the two port network [125].

Matrix	*Express*	*In terms of*	*Defining equations*
Impedance $\begin{bmatrix} z_{11} & z_{12} \\ z_{21} & z_{22} \end{bmatrix}$	V_1,V_2	I_1, I_2	$V_1 = z_{11}I_1 + z_{12}I_2$ *and* $V_2 = z_{21}I_1 + z_{22}I_2$
Admittance $\begin{bmatrix} y_{11} & y_{12} \\ y_{21} & y_{22} \end{bmatrix}$	I_1, I_2	V_1,V_2	$I_1 = y_{11}V_1 + y_{12}V_2$ *and* $I_2 = y_{21}V_1 + y_{22}V_2$
Hybrid $\begin{bmatrix} h_{11} & h_{12} \\ h_{21} & h_{22} \end{bmatrix}$	V_1,I_2	I_1,V_2	$V_1 = h_{11}I_1 + h_{12}V_2$ *and* $I_2 = h_{21}I_1 + h_{22}V_2$
Transmission $\begin{bmatrix} A & B \\ C & D \end{bmatrix}$	V_1,I_1	V_2, $-I_2$	$V_1 = AV_2 - BI_2$ *and* $V_2 = CV_2 - DI_2$

In order to obtain these matrices experimentally the two port network open /short measurements [126][127], should be done with the usage of impedance analyser. On the other hand, to obtain the impedance curves analytically the equivalent electric circuit of the inductor from notion2 will be simulated with the usage of LTSPICE.

To find the transfer function matrix [T], the impedance matrix [Z] has been found first analytically using standard derivations [125] and experimentally following the two port circuit measurements for the equivalent circuit of the passive components as shown in Figure 4.19 below.

The port voltage in terms of the port current [125]:

$$V_1 = Z_{11}I_1 + Z_{12}I_2 \qquad \text{EQ 4.40}$$

$$V_2 = Z_{21}I_1 + Z_{22}I_2 \qquad \text{EQ 4.41}$$

Both Z_{11}& Z_{22} are the driving points of the two port's impedance. While, Z_{12} is the forward transfer impedance and Z_{21} is the reverse transfer impedance.

For reciprocal networks $Z_{12} = Z_{21}$. For symmetrical networks $Z_{11} = Z_{22}$. For reciprocal lossless networks all the Z_{11}, Z_{22}, Z_{12} and Z_{21} are purely imaginary.

In order to find the impedance matrix the open/short circuits measurements between AC and BD in Figure 4.19 are done as in the following equations [125]:

1- Measurements between AC with BD open, $I_2 = 0$:

$$Z_1 = Z_{11} = \frac{V_1}{I_1} \qquad \text{EQ 4.42}$$

2- Measurements between AC with BD shorted, $V_2 = 0$:

$$Z_2 = Z_{11} - \frac{Z_{12}Z_{21}}{Z_{22}} = \frac{V_1}{I_1} \qquad \text{EQ 4.43}$$

3- Measurements between BD with AC open, $I_1 = 0$:

$$Z_3 = Z_{22} = \frac{V_2}{I_2} \qquad \text{EQ 4.44}$$

4- Measurements between BD with AC shorted, $V_1 = 0$:

$$Z_4 = Z_{22} - \frac{Z_{21}Z_{12}}{Z_{11}} = \frac{V_2}{I_2} \qquad \text{EQ 4.45}$$

The impedance matrix Z is found by solving these equations EQ 4.42 till EQ 4.45 :

$$Z = \begin{bmatrix} Z_1 & \sqrt{Z_1Z_3 - Z_2Z_3} = \sqrt{Z_3Z_1 - Z_4Z_1} \\ \sqrt{Z_1Z_3 - Z_2Z_3} = \sqrt{Z_3Z_1 - Z_4Z_1} & Z_3 \end{bmatrix} \qquad \text{EQ 4.46}$$

To find the transfer function matrix from [Z] to [T1], as shown in Figure 4.20,the input voltage and current are expressed in terms of output voltage and current:

$$V_1 = AV_2 + BI_2' \qquad \text{EQ 4.47}$$

$$I_1 = CV_2 + DI_2' : I_2' = -I_2 \qquad \text{EQ 4.48}$$

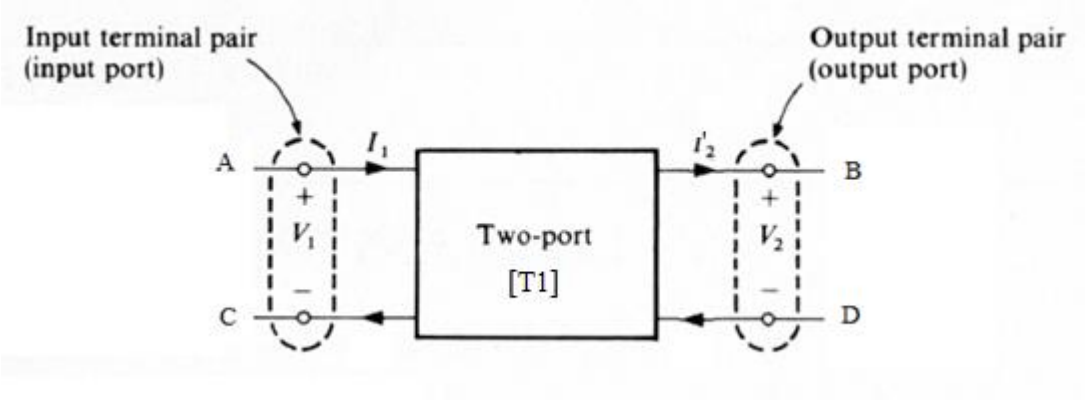

Figure 4.20- Two-port circuit [T1] Transmission matrix [125].

In order to find the transmission matrix the open/short circuit measurements between AC and BD in Figure 4.20 are done and by solving EQ 4.40, EQ 4.41, EQ 4.47 and EQ 4.48. the transmission matrix is :

$$[T_1] = \begin{bmatrix} A_1 & B_1 \\ C_1 & D_1 \end{bmatrix} = \begin{bmatrix} \frac{Z_{11}}{Z_{21}} & \frac{-Z_{12}Z_{21} + Z_{11}Z_{22}}{Z_{21}} \\ \frac{1}{Z_{21}} & \frac{Z_{22}}{Z_{21}} \end{bmatrix} \quad \text{EQ 4.49}$$

And the transfer function T which express the output voltage to the input voltage when the output is open circuit is:

$$Tr = \frac{V_2}{V_1} \text{ When } -I_2 = 0 = \frac{Z_{11}}{Z_{22}} \quad \text{EQ 4.50}$$

4.5.1 The Inductor in LC Filter

In order to study the performance of the inductors on the substrate (Figure 3.9) as a part of LC filter, the inductors on the PCB are associated with capacitors to achieve a complete LC filter. The inductor is connected to a capacitor Co of value 4 µF shown in Figure 4.21. The experimental result is presented in the experimental validation section below.

Figure 4.21- The output Capacitor Co (4 µF).

The transfer function matrix [T] for the cascaded circuits of the inductor and the capacitor, shown in Figure 4.22, will be found.

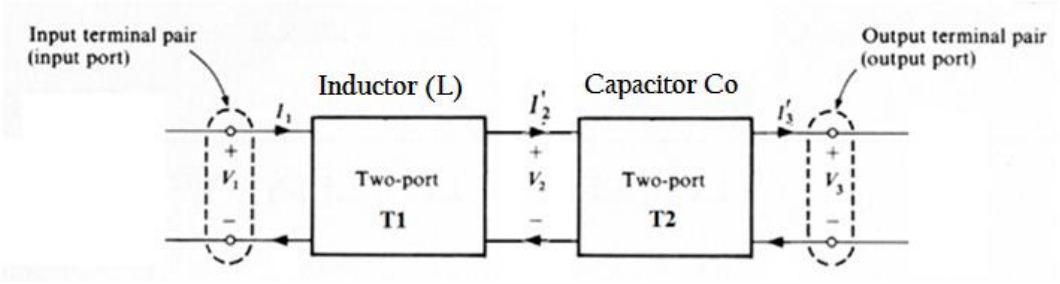

Figure 4.22- Tow-port circuit with output capacitor C.

The equations EQ 7.1 to EQ 7.16 in Appendix C explain how to cascade two two- port circuits. Thus, following the same method, the output port in terms of the input port is [125]:

$$\begin{bmatrix} V_1 \\ I_1 \end{bmatrix} = [T_1][T_2] \begin{bmatrix} V_3 \\ I_3{}' \end{bmatrix} \qquad \text{EQ 7.3}$$

$$\begin{bmatrix} V_1 \\ I_1 \end{bmatrix} = \begin{bmatrix} A_1 & B_1 \\ C_1 & D_1 \end{bmatrix} \begin{bmatrix} A_2 & B_2 \\ C_2 & D_2 \end{bmatrix} \begin{bmatrix} V_3 \\ I_3{}' \end{bmatrix} = \begin{bmatrix} A & B \\ C & D \end{bmatrix} \begin{bmatrix} V_3 \\ I_3{}' \end{bmatrix} \qquad \text{EQ 7.4}$$

And the equivalent transmission matrix of the two cascaded ones is [T]:

$$[\mathrm{T}] = \begin{bmatrix} A & B \\ C & D \end{bmatrix} \qquad \text{EQ 7.5}$$

A=$A_1A_2 + B_1C_2$

B=$A_1B_2 + B_1D_2$

C=$C_1A_2 + D_1C_2$

D=$C_1B_2 + D_1D_2$

The LC filter will be analysed later using the impedance analyser.

4.6 Simulation and Experimental Validation

With the usage of LTSPICE IV software and MATLAB R2012 the equivalent circuit will be solved in order to find the resonance frequency and the impedance curve. Ctt is the turn to turn parasitic capacitance, Cm is the parasitic capacitance between the two half-windings and Cts is the parasitic capacitance between the inductor windings and the bottom substrate. Figure 4.23 shows a two turns' equivalent circuit and a cross section showing the structure of the equivalent circuit of two inductor next to each other soldered on a copper substrate each of n and m turns. Component values are given in Table 4.4.

Table 4.4- Passive values of the inductor obtained by Maxwell software

Terms	Description	Value used in LTSPICE
C_{tt}	capacitance between adjacent turns	3.4 pF
C_m	capacitance between two adjacent turns, one in each half-winding (both inductors)	0.04 pF
C_{ts}	capacitance between the bottom copper substrate and the inductor	1.5 pF
$R_t(DC)$	dc resistance per turn	0.6mΩ
L_{total} (air cored)	Total inductance for 52 turns- air cored inductor obtained from Maxwell Electro-magnetic solver	6 µH

L_t (air cored) = L_{total} (air cored) /52 turns	Inductance per turn for air cored inductor	0.11µH
L_t (N95 core with distributed air gap) = L_{total} (N95 core with distributed air gap)/26 turns	Total inductance for 26 turns-Ferrite N95 core with distributed air gap 18/10-obtained from Maxwell Electro-magnetic solver	10µH
L_{total} (N95 core with distributed air gap)	Inductance per turn for N95 core with distributed air gap	0.38µH
L_{total} (N95 core with distributed air gap)	Total inductance for 52 turns-Ferrite N95 core with distributed air gap 18/10-obtained from Maxwell Electro-magnetic solver	24 µH
L_t (N95 core with distributed air gap) = L_{total} (N95 core with distributed air gap)/52 turns	Inductance per turn for N95 core with distributed air gap	0.45 µH

The accuracy of the suggested notion2 and equivalent circuit approach will be validated by comparing the simulation results to measurements which are done with the usage of the impedance Analyser KEYSIGHT E4990A.

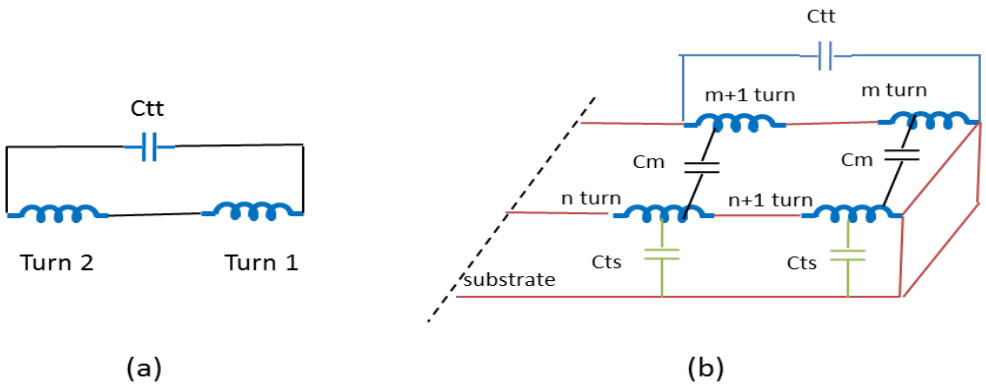

Figure 4.23 – (a) Two turns' equivalent circuit. (b) A cross section showing the structure of the equivalent circuit of two inductor next to each other soldered on a copper substrate each of n and m turns.

4.6.1 Pre Test Preparation; Calibration and Compensation of the Impedance Analyser KEYSIGHT E4990A 20Hz-120MHz.

In order to prepare the experimental set-up pre-test essential calibration and compensation steps have been done prior to the measurements of the inductor. The Oscillator Levels (Voltage or Current) are included in Table 4.5.

User calibration consists of two calibration data acquisition procedures: OPEN and SHORT circuit, these types of calibration data must be obtained when performing user calibration, as shown in Figure 4.24.

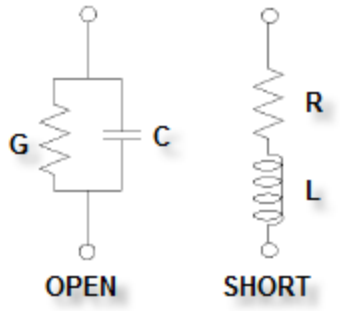

Figure 4.24- The circuit models of the fixture compensation kit used for the KEYSIGHT E4990A Impedance Analyser [128].

Table 4.5- The Oscillator (OSC) Level (Voltage or Current).

The Oscillator (OSC) Level (1 mV/20 μA resolution)	Min	Max
Voltage	-0.5 V	+0.5 V
Current	200 μA	20 mA

4.6.2 Experimental Validation Inductor Equivalent Circuit Notion 2

The equivalent circuit of both inductors on short substrate, as shown in Figure 4.9-c, has been simulated in LTSPICE using notion 2 as explained above and the values from Table 4.4 were used in order to find the transfer function.

The measurement in the lab has been done with the usage of the impedance Analyser KEYSIGHT E4990A, as shown in Figure 4.25 , where the impedance matrix [Z] has been obtained through the method of two port network measurements. The transfer matrix [T] has been obtained by solving the equations EQ 4.42 to EQ 4.49 in MATLAB and plotting the transfer function, as in EQ 7.16 Appendix C, $Tr = \frac{V_2}{V_1}$ when $(-I_2 = 0)$.

Figure 4.25- The two port network measurements of two inductors on short substrate

The comparison has been done for the inductors with an air cored and with ferrite N95. The impedance curves have been organised in Figure 4.26 and Figure 4.27.

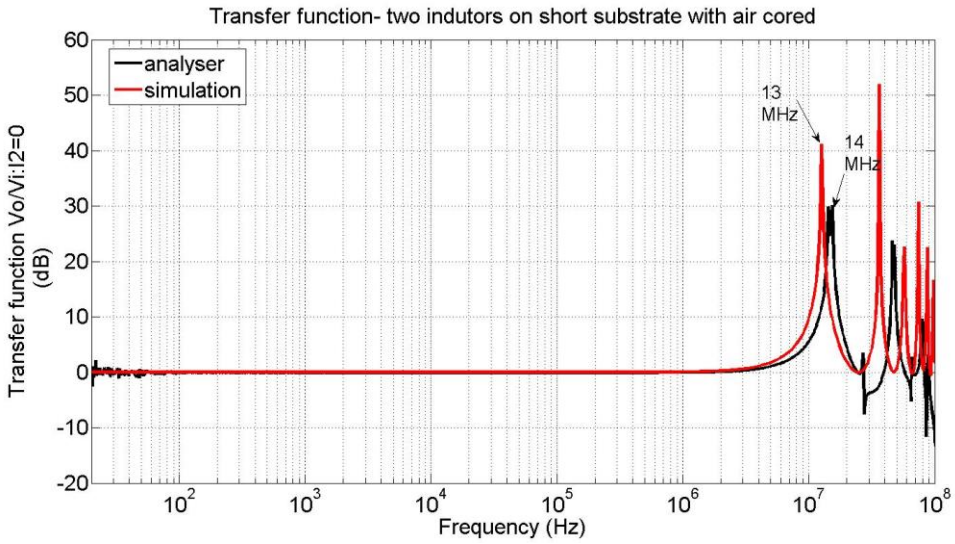

Figure 4.26- The transfer function of the two inductors on short substrate with air cored, simulation vs measurements (in power scale).

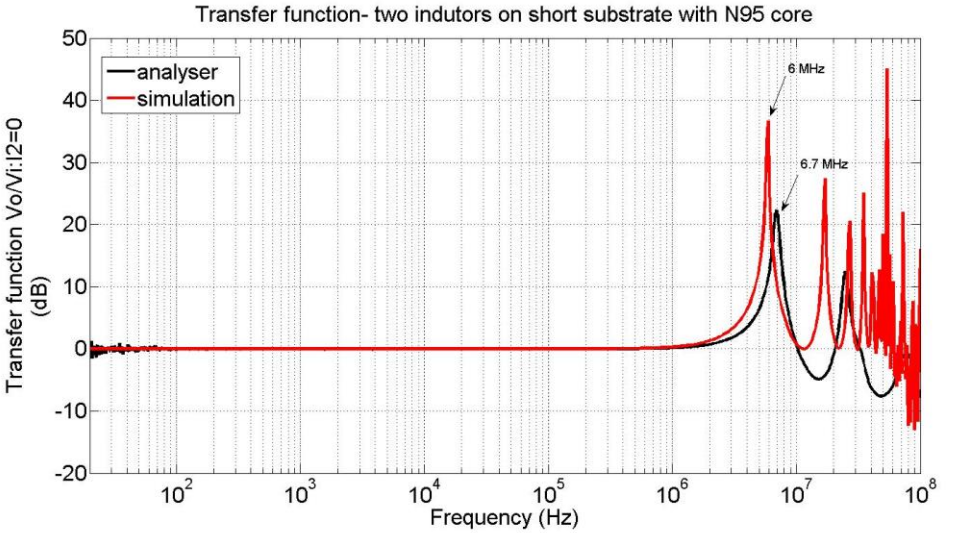

Figure 4.27- The transfer function of the two inductors on short substrate with ferrite N95 core, simulation vs measurements (in power scale).

As it is shown in Figure 4.26 and Figure 4.27, notion 2 with the equivalent circuit-2 has generated a transfer function almost matching the curves obtained by the measurements, although there is a difference in the magnitude due to the ac resistive

effect which has been ignored in the simulation. Resonance frequency's (f0) difference between measurements and simulation for air cored and N95 ferrite core is 10% and 7% respectively, an acceptable error and it can be justified by the measurements error due to calibration and compensation and the difference between the inductor geometry in simulation and reality.

4.6.2.1 Modelling the Inductor on the Substrate Level at High Frequency

The main aim is modelling the inductor on the substrate level in order to estimate the parasitic capacitance and its effect on the inductor performance and after the validation of the proposed equivalent circuit notion2, the accuracy of notion2 has been found to be satisfying.

Thus, in order to check the performance of both inductors on the substrate level, as shown in Figure 3.9 and Figure 4.28, the equivalent circuit is simulated in LTSPICE using notion 2 as has been explained above and using the values from Table 4.4 and Table 4.6 in order to find the transfer function.

The measurement in the lab is done with the usage of the impedance Analyser KEYSIGHT E4990A following the same method as before.

Figure 3.9 shows the substrate with the both inductors soldered on it, these two inductor, each is with 26 turns, are connected together from one side forming one inductor with 52 turns, while on the opposite side the current is passing through the first inductor and coming out from the ending of the second inductor. Dimensions of each inductor of 26 turns are shown in Appendix A, Figure 7.3. The main aim is to characterise the inductor and the copper substrates total parasitic capacitance.

As it is shown in Figure 4.28 there are 5 areas where the parasitic capacitances are to be computed. 2 and 4 present the equivalent circuits of the two inductors, while 1, 3 and 5 are the connected parts of the top copper substrate.

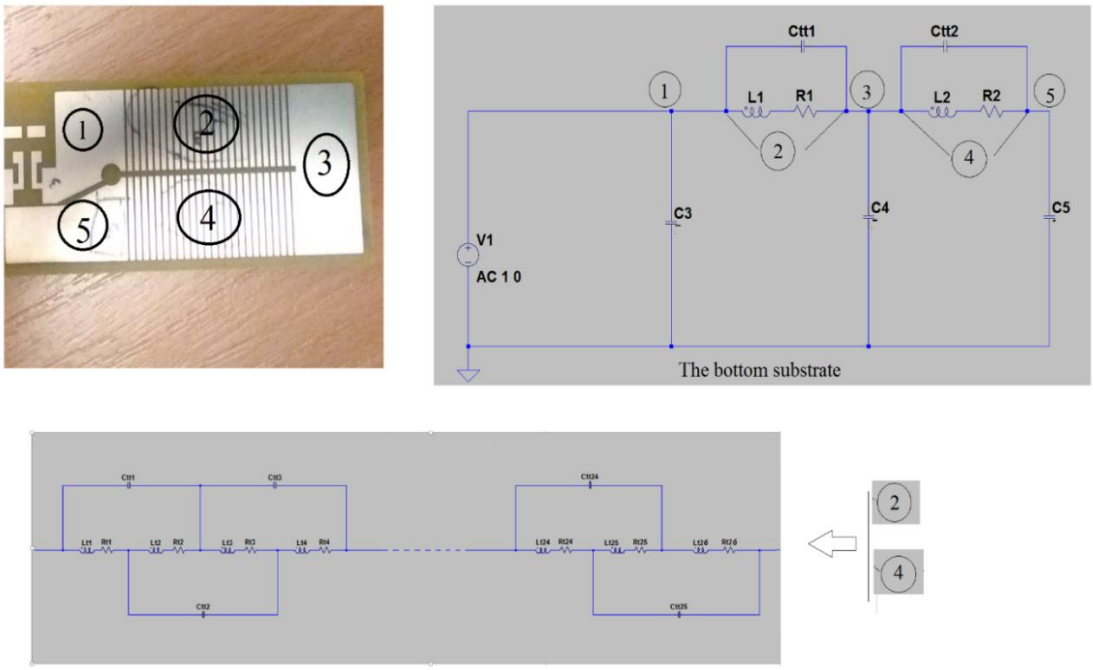

Figure 4.28- The equivalent circuit of the two inductors soldered on the substrate level with the parasitic capacitance of the inductor and the copper substrates top and bottom.

In order to include the effect of the copper substrate in the two port network measurements, the parasitic capacitances between the top substrate 1, 3 and 5 as shown in Figure 4.28 have been obtained from Maxwell and the values have been organised in Table 4.6. It shows that the copper substrate is contributing most to the parasitic capacitance, thus dominating the parasitic effect on the transfer function of both inductors and the substrate.

Table 4.6- Parasitic capacitance between the turns of the inductor on long substrate

Ctt	*3.4 pF*
Cm	*0.04 pF*
Cts	*1.5 pF*
C3	*53 pF*
C4	*50 pF*
C5	*25 pF*

As it is shown in Figure 4.29, the simulation has generated a transfer function curves almost matching the curves obtained by the measurements. The first resonance frequency's (f0) difference between measurements and simulation is around 5%, an acceptable error and it can be justified by the measurement error due to calibration and compensation and the difference between the inductor geometry in both simulation and reality.

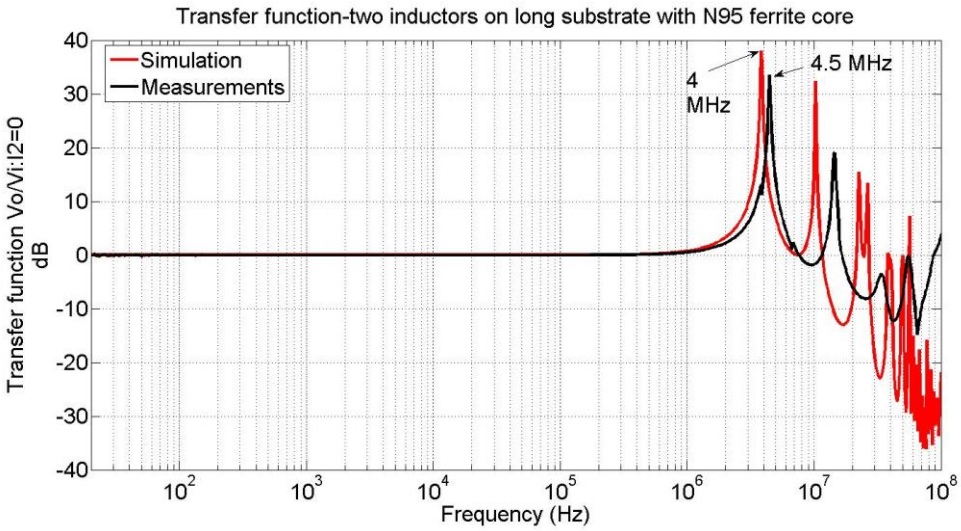

Figure 4.29- The transfer function of the two inductors on the long substrate with ferrite N95 core, simulation vs measurements (in power scale).

The transfer function which is reflecting the frequency response of the inductor has been studied through simulation in order to understand what parameters of the inductor and the substrate affecting the resonance and anti-resonance.

In LTSPICE simulation, the values of the inductance, capacitance and resistors from Figure 4.28 has been changed and the frequency response has been obtained and the effect on the resonance frequency has been noted as it is shown in Figure 4.30 below:

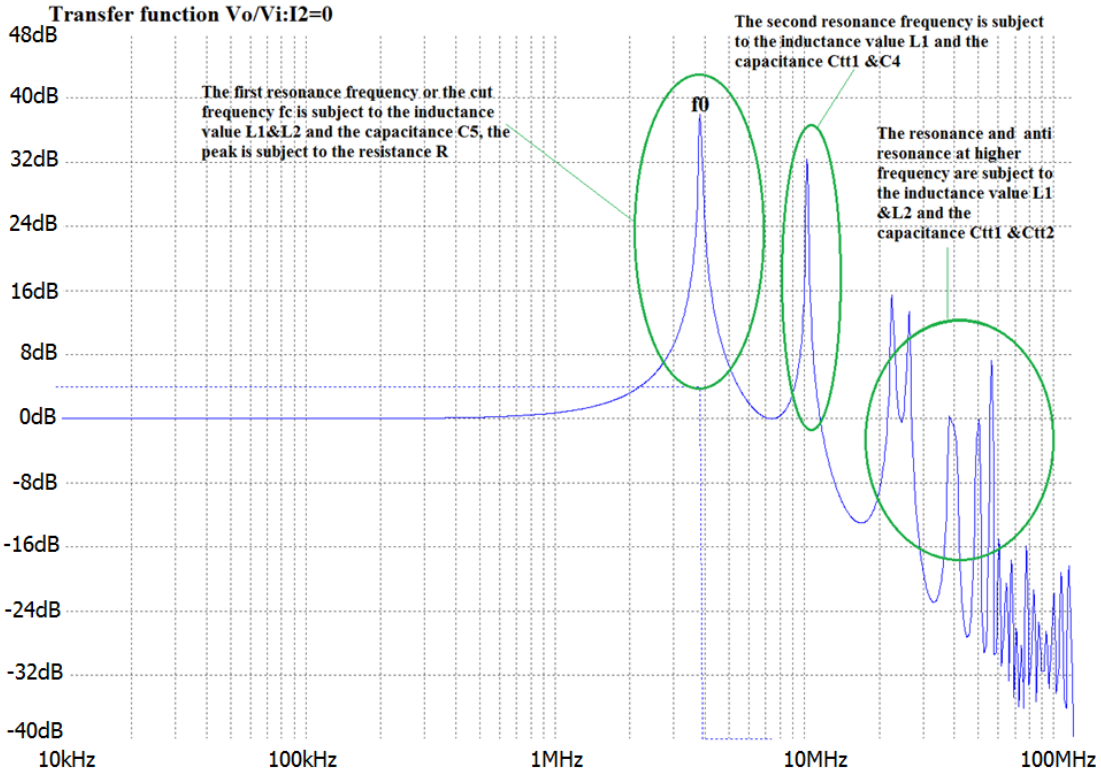

Figure 4.30- The Transfer function from the input to the output in frequency domain from simulation.

1- The first resonance frequency f_0 is subject to the inductance value L_1 and L_2 and also C_5, the parasitic capacitance of the copper substrate part (5), while the peak is subject to the resistor of R.
2- The second resonance frequency is subject to the inductance value of the first inductor L_1, the turn to turn capacitance C_{tt1} of the first inductor and C_4 the parasitic capacitance of the copper substrate part (3).
3- The anti-resonance frequency is subject to the inductance value L_1 and L_2 and the turn to turn capacitance C_{tt1} and Ctt_2.

An overlay of the result from Figure 4.27 (the inductor with ferrite on short substrate) and Figure 4.29 (the inductor with ferrite on long substrate) for comparison, with the consideration of the fact that the inductance value L_1 &L_2 also the inductor parasitic capacitance C_{tt}, C_m and C_{ts} are the same in both cases, shows that with the contribution of the extra copper part to the parasitic capacitance the resonance frequency has dropped almost 40%. Furthermore the peak of the first resonance

frequency has increased around three time due to the reduced resistance in the long substrate. Here the comparison was made between the results from the measurements only as for simulation the ac inductor resistance R_{AC} has been ignored. The second resonance frequency has dropped due to the existence of C_4 caused by the extra copper substrate, considering that both L_1 and C_{tt1} are the same in both substrates.

In simulation or measurement, the multiple resonances and anti-resonances from the model may be artefacts of the simulation model (C and L discretisation).

4.6.2.2 The confidence factor CF's validation

A confidence factor was introduced as a useful consistency test to check measurement reliability.

From EQ 4.46: $Z_2 Z_3 = Z_4 Z_1$

Thus, the confidence factor is defined as follow:

$$CF = |(Z_2 Z_3)/(Z_4 Z_1)| = |(Z_4 Z_1)/(Z_2 Z_3)| \quad \text{EQ 4.51}$$

If the condition in EQ 4.46 is met then the confidence factor CF is equal to 1. This condition has been explored with the usage of the analyser KEYSIGHT E4990A and CF for the both inductors on the long substrate has been compared as shown in Figure 4.31.

CF of the inductor with ferrite N95 core is equal to 1 up to 4 MHz then it deviates from 1, we are able to distinguish a maximum deviation of about 1.8 times at 5 MHz, while CF of the inductor with air cored core is equal to 1 up to 7 MHz after this it deviates from 1 about 1.6 times at 60MHz. and this because of the fact that the measurement accuracy changes with impedance, leading to large errors in one or more of the impedance matrix terms.

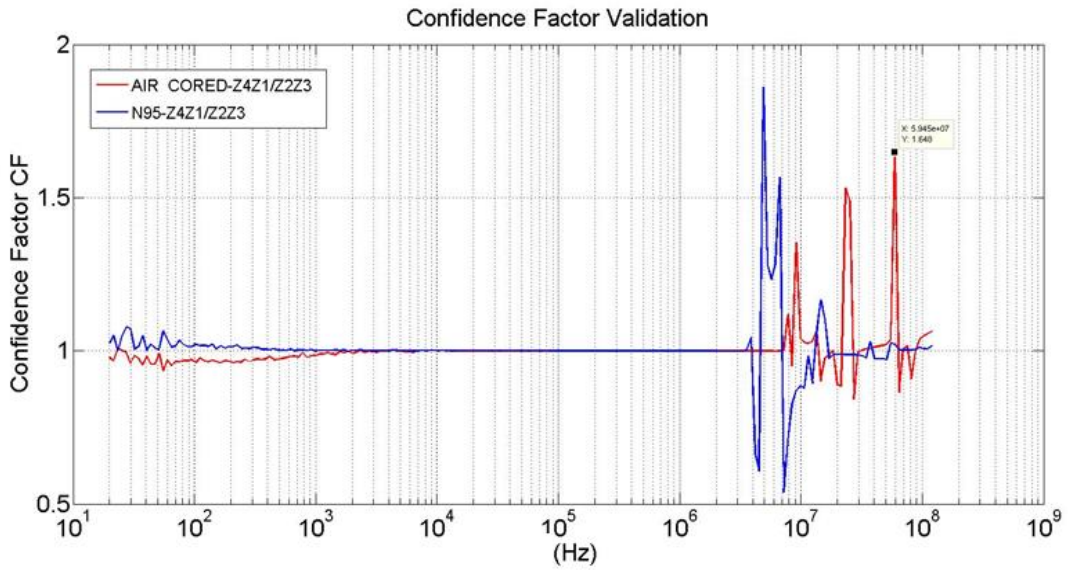

Figure 4.31- The confidence factor validation for the two inductors on the long substrate.

4.6.3 The Inductor in an LC Filter Application

The inductors on the PCB are associated with capacitors to achieve a complete LC filter. The capacitor consists of connected capacitors in parallel and series soldered on a PCB as shown in Figure 4.21. Schematic PCB details are given in Figure 7.12 and Figure 7.13 in Appendix C, while its impedance Z curve is shown in Figure 7.14.

The transfer function for the inductor and output capacitor (LC filter), as shown in Figure 4.32, has been obtained with the help of the impedance analyser (two transfer functions measured separately) and combined using cascading two of two- port circuit formula EQ 7.1 to EQ 7.16. It shows a resonance frequency of 17 kHz.

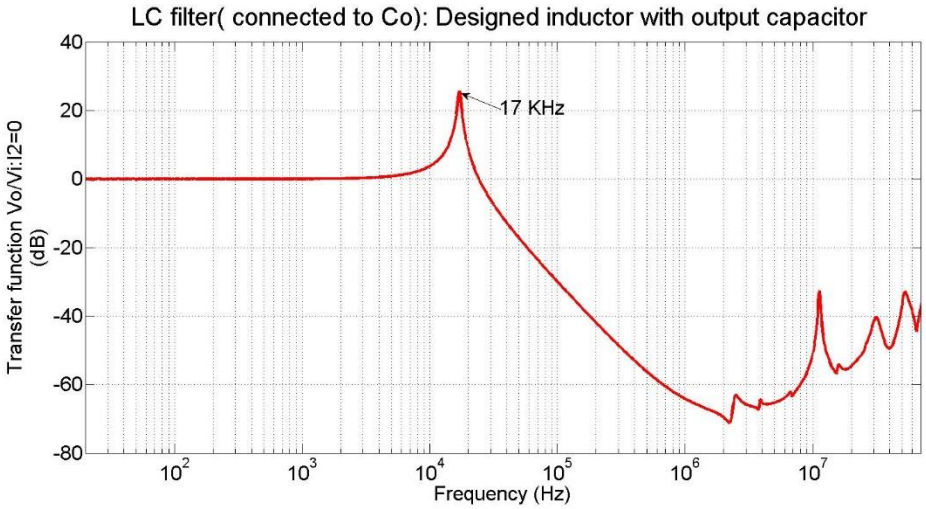

Figure 4.32- Transfer function-The designed inductor with N95 ferrite core-on PCB and the output capacitor Co.

4.6.4 Comparison with a Commercial Inductors

A comparison between the designed inductor and the high current commercial inductor (the same as used in the previous comparison) and has been done for the filtering perspective. The commercial inductor has an inductance of 30 µH and a self-resonance frequency around 6 MHz. The transfer function for each of them with the output capacitor Co is shown in Figure 4.33.

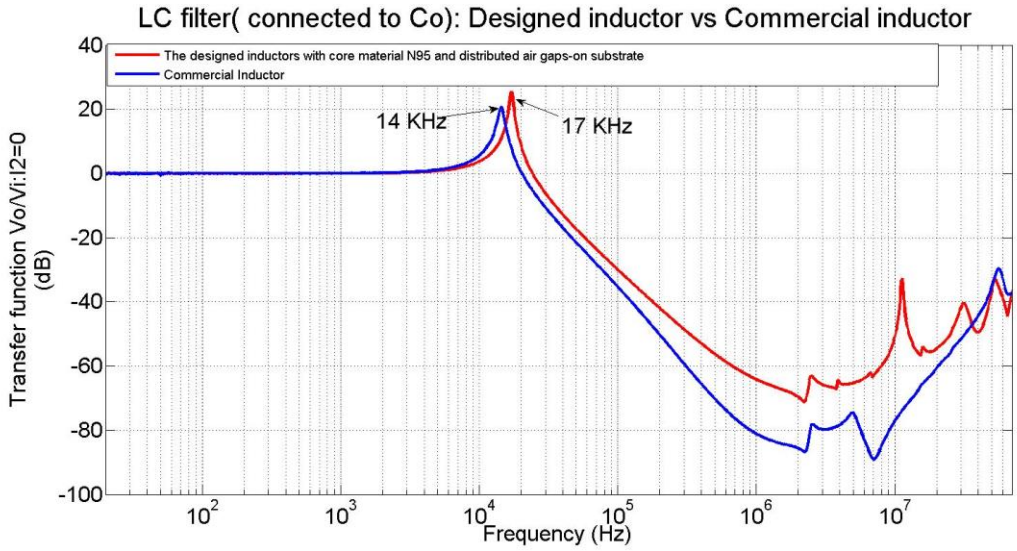

Figure 4.33- A comparison between the transfer function of the designed inductor and the commercial inductor with Co (in power scale).

It is shown from the results above that both inductors has almost the same performance in the LC filter at high frequency with a difference in the first resonance frequency of 3 kHz and a larger difference between the 3rd and the 4th resonance and anti-resonance frequencies due to the difference in the winding geometry of the both inductors which leads to a different parasitic capacitance between the both. Also the difference of the magnitude of both curves indicates a lower resistance in the designed inductor than in the commercial. In other words, both inductors have a close enough performance at high frequency, but the designed inductor is still more preferable for size and weight which suits the integration on the PCB substrate level. Please refer to the weight and size of the designed inductor in Chapter 3 section (3.5.3).

4.7 Conclusion

In this chapter, a characterisation of the magnetic components (the designed inductor and magnetic core) has been done. The classical approach (notion 1) has been found not suitable to model the proposed inductor at high frequency as it fails to predict the first resonance frequency of the inductor as shown in Figure 4.11, where that resonance frequency's value from measurements is around 58% of that from simulation. Thus another equivalent electric circuit of the inductor (notion 2) is proposed and solved in LTSPICE in order to predict the resonance frequency of the inductor. A comparison between the simulation and the measurements, as shown in Figure 4.17, indicates a good agreement between them. The resonance frequency's value from simulation is around 90%.

The proposed method has been validated experimentally using the Impedance Analyser KEYSIGHT E4990A by means of impedance measurements between the input and output of the inductor. Results have shown a good agreement between simulation and measurements. Thus, the proposed equivalent circuits is considered to be valid. The inductor with the core material on the DBC has shown a resonance frequency of 4 MHz.

A comparison between the designed inductor and a commercial off-the-shelf inductor from the shelf with a similar magnetic aspect has shown a similar performance for both inductors at high frequency but the designed inductor is still preferred due to its small size and weight which suits the integration on the PCB substrate level.

5 Chapter 5- Loss Measurements under DC bias and AC Ripple

5.1 Introduction

In this chapter the performance of the designed inductor, under realistic operating conditions is investigated. This magnetic component can be used as the output filter in a PWM inverter or a DC/DC converter. Figure 5.1 shows typical current waveforms which the windings of the inductor will be expected to conduct. In these waveforms, a high frequency AC ripple component is superimposed on a low frequency or a DC component.

Increasing the energy density of the magnetic components is achieved by increasing current densities through the inductor windings since energy is proportional to current squared. Thus, it is important to study the losses produced in this component and identify the magnitude of each source of loss. This will be accomplished by taking into account the performance of the component under the large signal AC ripple and instantaneous DC bias tests (part of a low frequency AC component).

After measuring the total energy loss in the magnetic component, the contributions of different sources of loss into that total loss, under an instantaneous DC bias and AC ripple, are investigated. These sources are: magnetic core loss, AC loss in the windings and the losses due to the DC component of the inductor (winding) current. Measurements are made using large signal rectangular voltage waveforms in order to provide more representative results for power electronic applications and provide a basis for validation of design simulations.

The magnetic losses and their dependency on the frequency and flux density will be examined in detail within this chapter. Large signal characterisation, unlike the small signal analysis, is limited to lower frequencies (some 250 kHz). However, they provide conditions which are closer to those which would be found in the real applications and therefore one can rely on the characterisation results to estimate the performance of the magnetic component. Operating within these conditions will produce different levels of losses in the core compared to losses that are given by the datasheet values and this will be compared below.

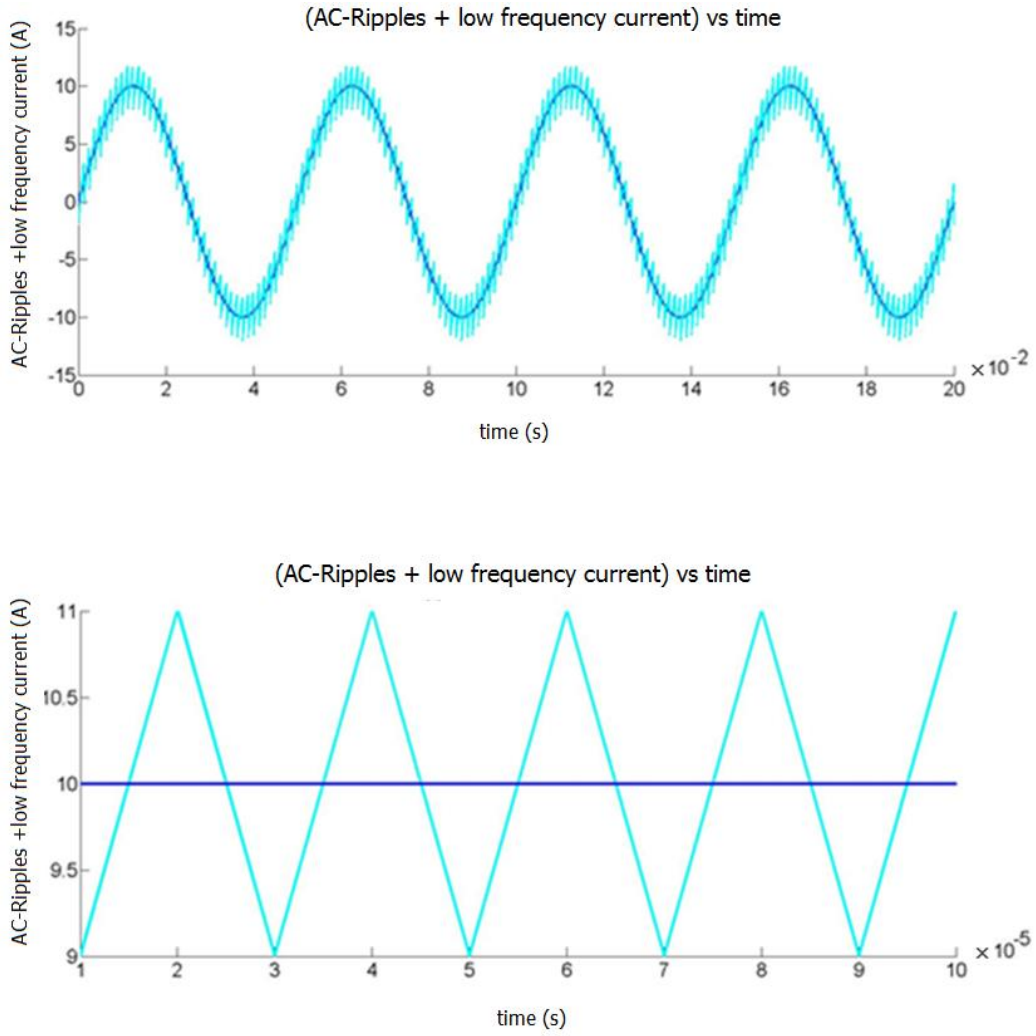

Figure 5.1- AC current ripple superimposed on an instantaneous DC component.

5.2 Winding and Magnetic Losses in Inductor

Inductor losses consists of winding losses and core losses. These losses are caused by DC and AC current.

1- Losses under DC current: The losses in a DC inductor are made up of copper losses due to the winding resistance.
2- Losses under AC current: The losses in an AC inductor are made up of copper losses (resistive, eddy current and proximity losses in the windings) and Magnetic losses in the core (due to hysteresis and eddy current if the core is conductive).

5.2.1 Winding Loss

In general, winding losses are subject to the shape and frequency of the current flowing through the inductor winding. For instance in applications such as PWM converters, the inductor current contains a DC component, a fundamental component and harmonics. Thus, the resulting winding loss depends on the DC current components as well as the DC and AC winding resistances R_{wDC} and R_{wAC} respectively. Studies have been done on AC resistance of windings at high frequencies including skin and proximity effects [87][129][130]. Analytical methods in calculating high frequency winding loss (in round wire) such as Dowell's method and Bessel-function methods require assumptions which severely reduce their accuracy [131]. Moreover, this method is valid only for non-gapped magnetic materials.

Thus some modification of Dowell's method [131] was proposed based on FEM simulation data and expressing the results in terms of normalized parameter. Thus they construct a model to determine proximity-effect loss for any round-wire winding. Such numerical methods are capable of calculating loss with errors less than 2% and as each individual conductor must be modelled, this drastically reduces the speed for designs with high conductor strand counts.

Studies on non-sinusoidal inductor current waveforms [132][133] and high-frequency effects on the winding losses [134] have also been presented previously. However, there is a lack of comprehensive approaches to inductor design with gapped cores taking both skin and proximity effects into account in the presence of a non-sinusoidal inductor current. Furthermore, the superimposed DC and AC current waveforms effect, which was ignored in [132], should be considered too. Thus, further methods for finding the losses under these conditions will be investigated.

5.2.2 Losses under High Frequency AC Ripple and DC Bias with an air-gapped core

The ideal choice for the magnetic material is one with high magnetic saturation and low magnetic loss, however when using an air-gapped core, applying high frequency ripple will introduce additional losses in the windings around the air gap, this is known as proximity losses. This is due to the magnetic fringing flux interacting with the windings around the airgap as shown in Figure 2.7 (the flux fringing has been explained previously in chapter 2). When the length of air gap increases, the proximity

effect also increases [135][56]. The reason is that when the gap dimension becomes too large, the fringing flux will interface with the copper winding and produce eddy currents within the winding, generating heat, just like an induction heater. The fringing flux will jump the gap and if the core is conductive, will also produce eddy currents in the core, as shown in Figure 2.7.

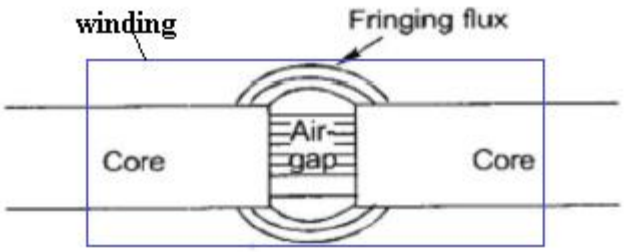

Figure 5.2-flux fringing at air gap [56].

Existing high-frequency winding loss calculation methods usually include skin effect [136], but ignore the fringing effect losses (proximity loss) caused by air-gap fringing fluxes, resulting in large errors for winding loss analysis and loss reduction designs . Hu and Sullivan [137] proposed a method to replace the air-gap effect with an equivalent winding in the air-gap location and to delete the winding window boundary effects of the core and set of current carrying conductors in a region of uniform permeability. However, with a large air-gap, the accuracy of this method will be poor, especially for the field distribution near the air-gap. Thus, another study [138] proposed a modification scheme which is suitable for larger air gaps by replacing the air-gap magnetic voltage drop with an equivalent surface current sheet with certain shape and certain current density distribution near the air-gap.

In general, the DC inductor winding resistance is given by:

$$R_{wDC} = \frac{\rho_w l_w}{A_w} \qquad \text{EQ 5.1}$$

Where $\rho_w$is the winding conductor resistivity, l_w is the winding conductor length, and A_w is the cross-sectional area of the winding conductor.

If the inductor is operated at DC or at a low frequency and the current density is uniform [54] then the winding power loss can be expressed by

$$P_{wDC} = R_{wDC} I_{DC}^2 \qquad \text{EQ 5.2}$$

Where I_{DC} is the RMS value of the current flowing in the conductor and R_{wDC} is the DC resistance of the winding.

When the operating frequency is high, the current density is not uniform anymore and the winding AC resistance R_{wAC} is higher than the DC resistance R_{wDC} due to the skin and proximity effects [54] and the AC winding resistance can be expressed by:

$$R_{wAC} = R_{wDC} + \Delta R_{wAC} = R_{wDC}\left(1 + \frac{\Delta R_{wAC}}{R_{wDC}}\right) = F_R R_{wDC} \qquad \text{EQ 5.3}$$

Where R_{wAC} is the AC winding resistance, F_R is the AC-to-DC resistance ratio or AC resistance factor, and it is defined as the AC-to-DC winding resistance ratio

$$F_R = \frac{R_{wAC}}{R_{wDC}} = 1 + \frac{\Delta R_{wAC}}{R_{wDC}} \qquad \text{EQ 5.4}$$

In applications where the inductor current is not a pure sinusoid, the harmonics associated with the inductor current waveform should be taken into account when calculating the winding power loss. In general, a periodic non-sinusoidal inductor current waveform consists of a DC component, a fundamental component and an infinite number of harmonics. If the DC component and the amplitudes or the RMS values of the current harmonics as well as the DC and AC winding resistances at the harmonic frequencies are known, the winding power loss at DC and each harmonic and therefore the total winding loss can be calculated. The inductor current i_L waveform can be expanded into a Fourier series as in EQ 5.5

$$i_L = I_L + \sum_{n=1}^{\infty} I_{mn} \cos(n\omega t + \varphi_n) = I_L + \sqrt{2} \sum_{n=1}^{\infty} I_n \cos(n\omega t + \varphi_n) \qquad \text{EQ 5.5}$$

Where I_L is the DC component of the inductor current, I_{mn} is the amplitude of the n^{th} harmonic of the inductor current, $I_n = I_{mn}/\sqrt{2}$ is the rms value of the

n^{th} harmonic of the inductor current, and φ_n is the phase of the n^{th} harmonic frequency.

Actually, Kondrath and Kazimierczuk, in their study [54] [139], proposed an expression for winding loss due to skin and proximity effects including harmonics in an inductor carrying periodic non-sinusoidal current. With the consideration of the formulas EQ 5.1 till EQ 5.5 the general expression for winding loss because of the DC current and all harmonics of the inductor current is [139].

$$
\begin{aligned}
P_w = \; & P_{wDC} + P_{wAC} = R_{wDC}I_L^2 + \sum_{n=1}^{\infty} R_{wACn}I_n^2 \\
& = R_{wDC}I_L^2 + R_{wAC1}I_1^2 + R_{wAC2}I_2^2 + \cdots \ldots . + R_{wACn}I_n^2 \\
& = R_{wDC}I_L^2 + \left[1 + \frac{R_{wAC1}}{R_{wDC}}\left(\frac{I_1}{I_L}\right)^2 + \frac{R_{wAC2}}{R_{wDC}}\left(\frac{I_2}{I_L}\right)^2 + \cdots + \frac{R_{wACn}}{R_{wDC}}\left(\frac{I_n}{I_L}\right)^2\right] \\
& = R_{wDC}[I_L^2 + \sum_{n=1}^{\infty} F_{Rn}I_n^2] = R_{wDC}I_L^2\left[1 + \sum_{n=1}^{\infty} F_{Rn}\left(\frac{I_n}{I_L}\right)^2\right] \\
& = P_{wDC}\left[1 + \sum_{n=1}^{\infty} F_{Rn}\left(\frac{I_n}{I_L}\right)^2\right] = P_{wDC}\left[1 + \frac{1}{2}\sum_{n=1}^{\infty} F_{Rn}\left(\frac{I_{mn}}{I_L}\right)^2\right]
\end{aligned}
$$

EQ 5.6

The AC winding loss is

$$
P_{wAC} = \sum_{n=1}^{\infty} R_{wACn}I_n^2 = R_{wDC}I_L^2 + R_{wAC1}I_1^2 + R_{wAC2}I_2^2 + \cdots + R_{wACn}I_n^2 \qquad \text{EQ 5.7}
$$

Where $R_{wDC}$is the DC winding resistance, R_{wACn} is the AC winding resistance at the n^{th} harmonic frequency ($R_{wAC1}, R_{wAC2}, R_{wAC3}, \ldots . at\ f_1, 2f_1, 3f_1 \ldots ..$) and $F_{Rn} = \frac{R_{wACn}}{R_{wDC}}$ is the AC-to-DC resistance ratio at the n^{th} harmonic frequency. Figure 5.3 shows the spectra of inductor current, inductor winding resistance, and winding power loss.

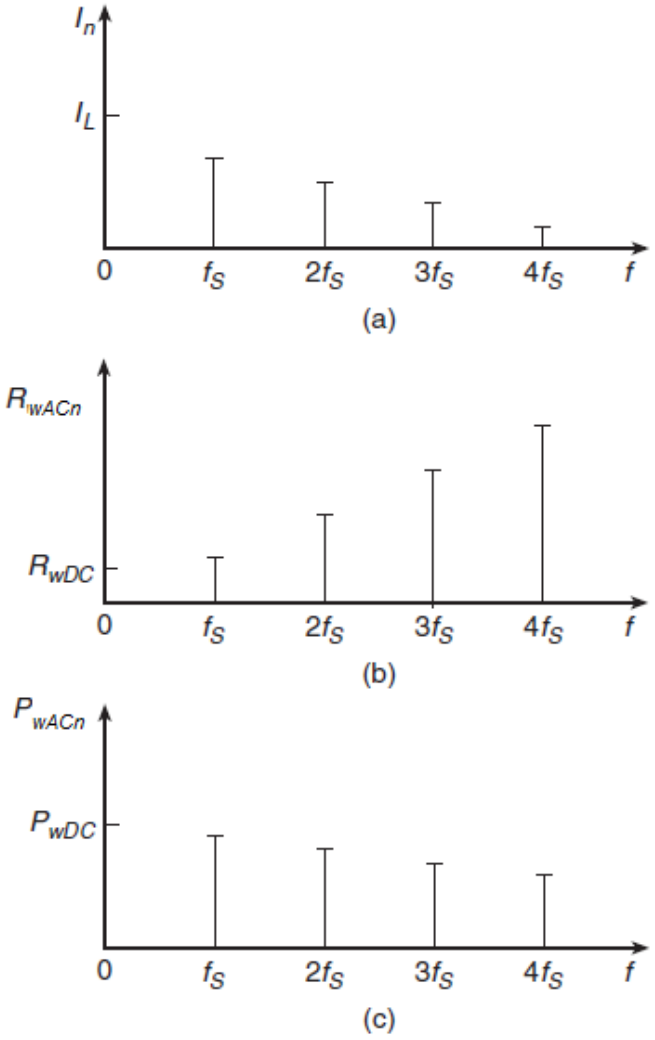

Figure 5.3 - Spectra of the inductor current, winding resistance, and winding power loss. (a) Spectrum of the inductor current. (b) Spectrum of the inductor winding resistance. (c) Spectrum of the inductor winding power loss [54].

5.2.3 Magnetic Losses under sinusoidal waveforms

Ferrite is a nonconductive magnetic material, thus it does not suffer from any eddy currents flowing inside the material and there is no ohmic loss or resistive loss inside a ferrite core. However, when magnetic materials such Ferrite, powdered iron or composite nano-crystaline cores are subject to biased magnetic field strength, then the magnetic losses increase with DC bias and AC flux amplitude causing a temperature rise in core materials which affects the performance of power electronic device and can potentially reduce the component life time. Therefore, the prediction of core loss

is extremely important and as such, a great deal of effort has been made into modelling core losses in magnetic components [140][141] [142] [143][144].

Typically, the equation that characterizes core losses is the power equation, known the Steinmetz equation [64] EQ 5.8 .

$$P_V = k f^{\alpha} \hat{B}^{\beta} \qquad \text{EQ 5.8}$$

Where $\hat{B}$ is the peak induction of a sinusoidal excitation with frequency f, P_V is the time-average power loss per unit volume, and k, α, β are material parameters, which are referred to as the Steinmetz parameters [145] and they are valid for a limited frequency and the flux density.

Unfortunately, this empirical equation is only valid for sinusoidal excitation, while in power electronics applications, the material is mostly exposed to non-sinusoidal flux waveforms. Therefore, different approaches [140] [141] [146] have been developed to overcome this limitation and determine losses for triangular flux waveforms.

5.2.4 Core Loss Measurements with non-Sinusoidal Waveforms under DC Bias Conditions

Improvements of the Steinmetz equation have been made [140] [141] [146] in order to estimate losses with non-sinusoidal waveforms. In [146] researchers studied the possibility of separating the flux waveform into major and minor loops, they measured the core loss using a toroidal ferrite core, and calculated the loss separately for the major loop and for each minor loop but with loss depending on peak-to peak flux density instead of instantaneous flux density. Although the improved method of the Generalised Steinmetz Equation (iGSE) overcame some of the problems with previous methods, it still faced some limitations due to the difficulties of choosing Steinmetz parameters with the variation of frequency and harmonic content over a wide frequency range [146]. Furthermore, the iGSE predicts loss independently of the dc bias while for example the loss in a ferrite core is known to vary with DC bias [142].

In [143] [147], calculation of the magnetic losses uses a loss map of the magnetic material on the basis of the dynamic minor loop, based on measurements is presented. Here researchers used the loss map in order to store the loss information for different

operating points, each described by the flux density ripple ΔB, the frequency f, the temperature T, and a dc bias H_{dc}.

In other studies [111] [148], methods to determine core losses were based on separating the total loss into loss components such as hysteresis losses, classical eddy current loss and excess eddy current loss. However, all of the approaches using loss separation also have a practical disadvantage in that they require extensive measurement and parameter extraction with a given material before they become useful.

Research in [149] presented the core losses, for air-gapless cores, under DC biased conditions for different materials including ferrite using the Steinmetz pre-magnetization graph (SPG). For a considered frequency range, results shows that the graph is independent of the frequency f with accuracy obtained ≤ ±15%. .

Nevertheless, the above proposed calculation models were tested and validated using toroidal cores with the assumption of a uniform flux density, without air gaps. Therefore, for alternative shaped cores or cores with air gaps, an improved model is needed.

Fiorillo and Novikov [150][151] have elaborated a precise iron loss prediction method under distorted flux density without the use of minor hysteresis loops. However, their formula requires a further knowledge of the amplitude, the phase and the harmonic number of the flux density harmonics. Also, for high frequency prediction (more than 1 kHz) additional tests are likely to be required.

In the following chapter a method of Loss separation is proposed in order to measure the losses of an inductor with air-gapped cores with high frequency ripple and DC bias using large signal rectangular voltage waveforms. AC, DC and core losses will be calculated and obtained separately.

5.3 Proposed Analysis Method of Losses Separation

The calculation of losses in magnetic components under AC ripple and DC bias requires extensive measurements as suitable data is rarely given on data sheets. Thus, in order to measure the losses of an inductor with air-gapped cores with high frequency ripple and DC bias using large signal rectangular voltage waveforms, a method of loss

separation is proposed. AC, DC and core losses will be calculated and obtained separately.

Total measured losses are obtained experimentally by applying rectangular voltage waveforms to the designed and manufactured inductor. The experimental test bench consists of a DC-DC boost converter with the Inductor Under Test (IUT) as the input inductor of the converter as shown in Figure 5.4. Current flowing through the inductor during operation of the circuit has a triangular shape. In this experimental setup, the DC level of the current as well as the amplitude of the AC ripple can be adjusted.

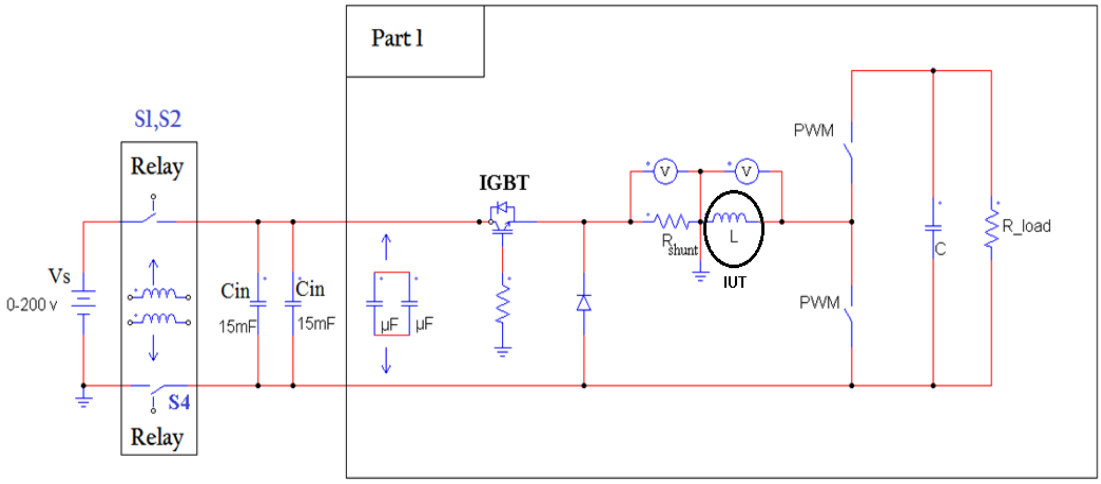

Figure 5.4- A basic schematic of DC-DC converter for losses measurements. (For details of the Connections to XMC Chipset and part 1 schematics please refer to Appendix D).

The total losses of the inductor and air-gapped core, operated with high frequency ripple and DC bias using large signal rectangular voltage waveforms, are separated into loss components which can be identified in three different categories:

1- DC losses: Applied current is decomposed into a DC component and high frequency ripple by Fourier series analysis. Losses due to the average value of the current are called DC losses.
2- Eddy current and proximity losses in the windings: This category includes the losses due to the interaction of the fringing magnetic fields with the windings

and skin effect in the conductor [152] [153] In this category only current ripple is considered.

3- Magnetic losses: Magnetic losses emanate from the core material and depend on the level of the DC magnetic field intensity and also on its variation around this average value.

Total losses are sum of these three components:

$$P_{tot} = P_{AC} + P_{DC} + P_{core} \qquad \text{EQ 5.9}$$

With the usage of suitable instruments such as four-terminal micro-ohm meters DC resistance can be directly measured and subtracted from the total resistance of the inductor $R_{measured}$ obtained by impedance measurement analysis, thus the AC resistance (AC winding losses R_{wAC} associated to Eddy current and proximity losses in the winding and Remnant resistance $R_{remnant}$ associated to the core losses) is the rest of the resistance. DC loss $P_{wDC}$is found using EQ 5.11.

Now, in order to calculate the Eddy current and proximity losses, we need to obtain the AC resistance R_{wAC} of the windings. This resistance is obtained by impedance measurement analysis. The impedance of the inductor is measured by progressively including increasing numbers of turns of the inductor windings in the measurement (N: 5- 52). Remnant resistance (which is associated to the core losses) is obtained by extrapolating the impedance curves to N = 0, at constant($N \times i$). Results presented in the following section show that the resistance due to core losses is negligible comparing to winding AC resistance in small signal measurements.

The phase current harmonics are used to compute the AC winding power loss using EQ 5.7. The first seven harmonics are considered (as the remaining harmonics are ignored due to their small values and their negligible effect on the AC winding loss). The power loss due to each harmonic is evaluated and then summed to find the total AC winding power loss. Estimation of winding AC losses are then obtained by applying Fourier analysis on the current waveform and using EQ 5.10:

$$P_{wAC} = \sum_{n=1}(I_n{}^2 \times R_{wAC\_n}) \qquad \text{EQ 5.10}$$

Where (I_n) is the RMS value of the nth harmonic of the current waveform and (R_{ac_n}) is the winding resistance at that frequency.

So called “DC losses” are obtained by using the average component (n = 0 in Fourier analysis or I_{ave}) and measuring the DC resistance of the windings, as EQ 5.11:

$$P_{wDC} = {I_{ave}}^2 \times R_{wDC} \qquad \text{EQ 5.11}$$

Winding DC resistance is measured by using a four-terminal micro-ohm meter, the resulting DC resistance of the inductor under test is: $R_{wDC} = 30m\Omega$

Total loss of the component, P_{tot} is obtained by measuring voltage across the inductor and the current following through it:

$$P_{tot} = \frac{1}{T}\int_{t_0}^{t_0+T} i_L . v_L . dt \qquad \text{EQ 5.12}$$

Core loss is then obtained using EQ 5.9 as all other components are measured and calculated.

5.3.1 Measuring R_{ac} with Impedance Analyser

In order to calculate AC losses P_{wAC} (Eddy current and proximity losses) for the inductors and the core, the AC resistance R_{wAC} of the windings is obtained by measurement with a KEYSIGHT E4990A impedance analyser. As previously mentioned, the impedance of the inductor is measured by progressively including an increasing number of turns of the inductor windings in the measurement (N: 5- 52). In order to fix the magnetic field H multiplied by the magnetic path l_m, the number of turns multiplied by the current has been fixed (N*I= 0.1 turn.A).). Remnant resistance $R_{remnant}$ (which is associated to the core losses only) is the resistance at number of turns N equal to zero and it is obtained by extrapolating the resistance curve shown in Figure 5.5 to the N = 0 point. It is proven from the curve in Figure 5.5 the resistance at N=0 is around 9 mΩ which is small enough to consider the core losses as negligible compared to winding AC resistance R_{wAC} for small signal measurements. A linear interpolation of the data shows the relationship between the AC resistance R_{wAC}, which is defined by EQ 5.13, and the number of turns as shown in Figure 5.5 and EQ 5.14.

$$R_{wAC} = R_{measured} - R_{wDC} \qquad \text{EQ 5.13}$$

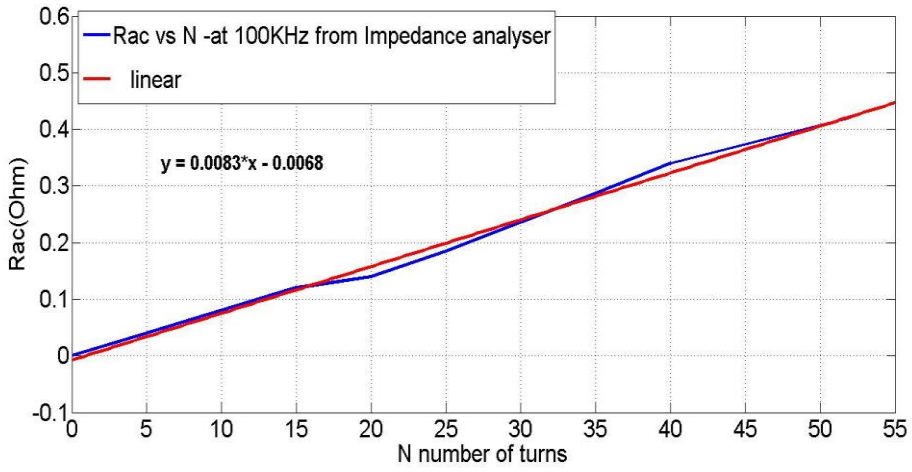

Figure 5.5- The AC resistance R_{wAC} of the windings vs numbers of turns of the windings in small signal measurements at 100 KHz.

$$R_{wAC} = 0.0083N - 0.0068 \qquad \text{EQ 5.14}$$

The measurements organised in Table 5.2 have been done taking the current and voltage limit of the impedance analyser into consideration whose parameters (the maximum and minimum current and voltage's allowable level) are shown in Table 5.1. Thus, with the usage of EQ 5.15 it has been ensured that the voltage and the current level inside the impedance analyser doesn't exceed the allowable limits.

$$v = (jwL + R_{DC}) \times i \qquad \text{EQ 5.15}$$

Table 5.1- The maximum and minimum current and voltage's allowable level of the impedance analyser

$i_{min} = 200\mu A$ $i_{max} = 20mA$	$v_{min} = 5\ mV$ $v_{max} = 500\ mV$
$f = 1MHz$	

Table 5.2- Measurements in order to find R_{wAC}(at 100 kHz) vs N (number of turns)

N	***L (μH)***	***R_dc(Ω)***	***R_measured (Ω)-at 100 kHz***	***i(A)***	***v (volts)***	***N*i***
5	*1.00*	*3.071E-03*	*4.30E-02*	*2.00000E-02*	*1.26E-01*	*0.1*
15	*4.20*	*9.213E-03*	*1.29E-01*	*6.66666E-03*	*1.76E-01*	*0.1*
20	*3.89*	*1.228E-02*	*1.52E-01*	*5.00000E-03*	*1.22E-01*	*0.1*
25	*6.07*	*1.535E-02*	*1.95E-01*	*4.00000E-03*	*1.53E-01*	*0.1*
35	*1.19*	*2.150E-02*	*3.00E-01*	*2.86000E-03*	*2.14E-01*	*0.1*
40	*1.55*	*2.457E-02*	*3.70E-01*	*2.50000E-03*	*2.44E-01*	*0.1*
52	*2.63*	*3.194E-02*	*4.50E-01*	*2.00000E-03*	*3.30E-01*	*0.1*

Thus, it has been proven from EQ 5.14 and Figure 5.5 that the AC resistance measured by the impedance analyser with small signal is only AC resistance in the winding and the core is neglected at this condition (operating at such a low ampere turn level of 0.1 that is difficult to conclude anything for core losses), as R_{wAC} goes to zero when number of turn is zero.

5.4 Experimental Set up Describing the DC-DC Convertor

By using a DC-DC converter and the test bench set shown in Figure 5.6 the magnetic losses are measured using the same rectangular voltage waveforms seen in power converter instead of the more typical low voltage sinusoids used in impedance analysers and as such, a more realistic set of measurements can be made. The inductor, constructed with an N95 ferrite core has been added to the converter circuit. A block diagram of the experiment is shown in Figure 5.8, in which the inductor is connected in series with a small shunt resistor [154], (0.1 Ω) in order to measure the current through the inductor. This circuit also allows the inductor terminal voltage to be measured with a secondary winding of six turns has been used to measure the flux density in one part of the core, as shown in Figure 5.7. The voltage and peak to peak flux density were observed by using an oscilloscope.

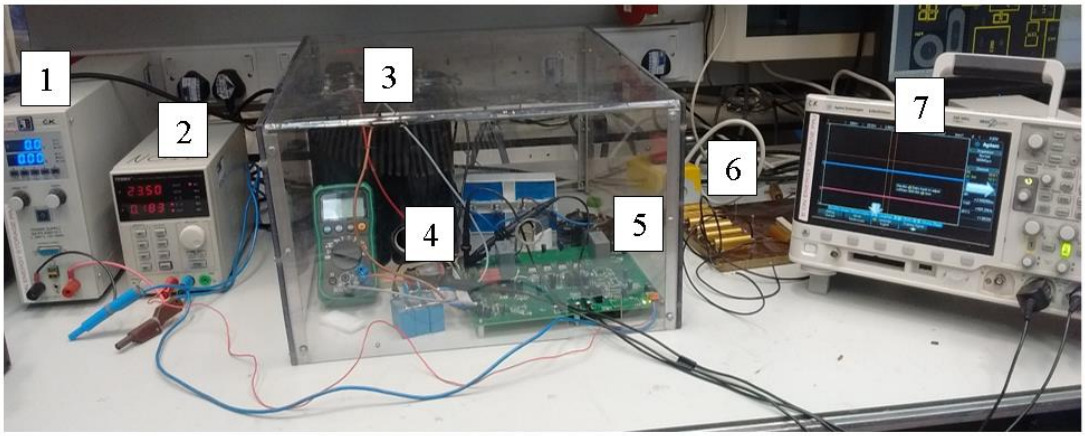

Figure 5.6- The test bench for losses measurements. 1- High voltage supply to charge the input capacitors, 2-power supply for the converter circuit board, 3-input capacitors, 4-Tested inductors with N95 ferrite core, 5-the converter with the control circuit board, 6-variable load, 7-Osciloscope.

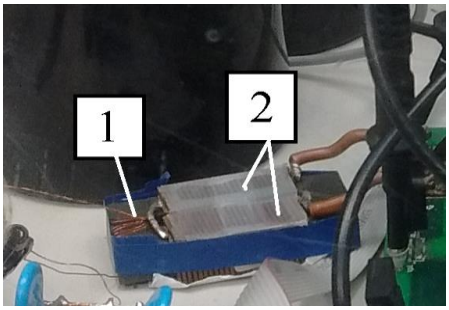

Figure 5.7- The design and fabricated inductor with the core material used in the losses measurements 1- the secondary winding N=6 in one leg of the core. 2- The inductor winding.

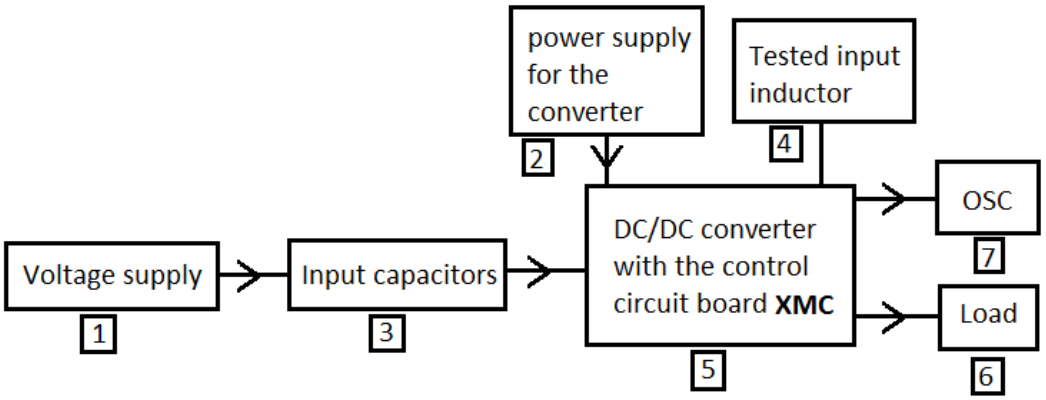

Figure 5.8- A block diagram of the experiment:1- High voltage supply to charge the input capacitors, 2-power supply for the converter circuit board, 3-input capacitors, 4-Tested inductors with N95 ferrite core, 5-the converter with the control circuit board, 6-variable load, 7-Osciloscope

Measurement sets have been done for fixed levels of ripple and different values of DC current and each set has been repeated for different frequencies [50-250 kHz] and different peak to peak flux densities [12-41 mT].

A basic schematic of DC-DC converter is shown in Figure 5.4. The converter is fed from a DC supply Vs. First, the IGBT is off and input capacitors Cin (with 15 mF capacitance each capacitors) are charged. The switch S2 is responsible for connecting and charging the capacitors from the power supply, while switch S1 is responsible for disconnecting the capacitors from the power supply and switch off the relay. Once the capacitors Cin are charged switch S4 will switch off the relay and disconnect the DC supply Vs from the system. At the same moment switch S4 will turn the timer on and after 1.8 ms the IGBT will be turned on for 3.5 ms and a square wave signal will be applied to the inductor using the PWM output stage. Within this time there is a possibility to change the duty cycle of the PWM stage, if this is needed, as the Micro-controller XMC1300 (For details refer to Figure 7.15 and Figure 7.16 Appendix D) provides the PWM with variable duty cycle. The PWM will send a rectangular signal (-4v till +15v) for each gate of the four SiC MOSFET [155]. The rise and fall times in the inductor current waveform should be considered by changing the duty cycle as

needed. During this short period the voltage drop across the shunt resistor R-shunt, which has the same current of the inductor, can be measured and i(t) determined. Also the voltage on both inductor and secondary winding is captured. After this the IGBT will be turned off. For each different measurement this procedure must be repeated as the capacitors will discharge automatically.

The measurement sequence is short, as the full time range of the output signal is around 3500 µs with a delay of 1.35 ms and sampling frequency 1GHz while, the waveform have been obtained within a time scale around 75 µs as shown in Figure 5.9.

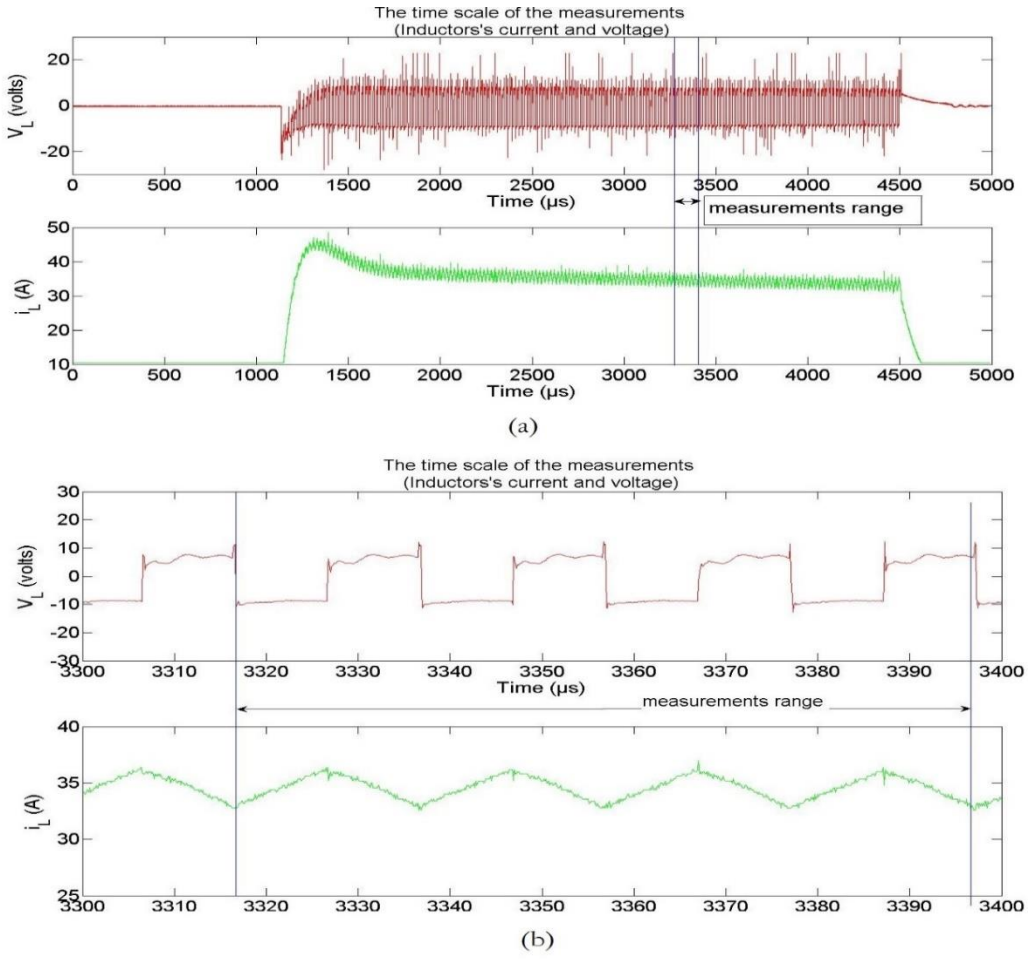

Figure 5.9- (a)-Graph to show both voltage and current of the inductor during test showing the full test time period. (b)-Graph to show a zoomed version of the voltage and current for the inductor during test.

5.4.1 Precision of the Measurements

This section will discuss the precision of the measurements made together with the individual sources of error in the system.

5.4.1.1 Shunt Resistor

A 100 W Thick Film Power Resistor (100 mΩ ±5%) [154], specifically designed for high frequency usage was used in the DC-DC convertor circuit as a shunt resistor in order to measure the inductor current.

The high frequency equivalent circuit of the resistor has been measured with the impedance analyser KEYSIGHT E4990A, and the series resistance and inductance of the measured impedance are shown in Figure 5.10

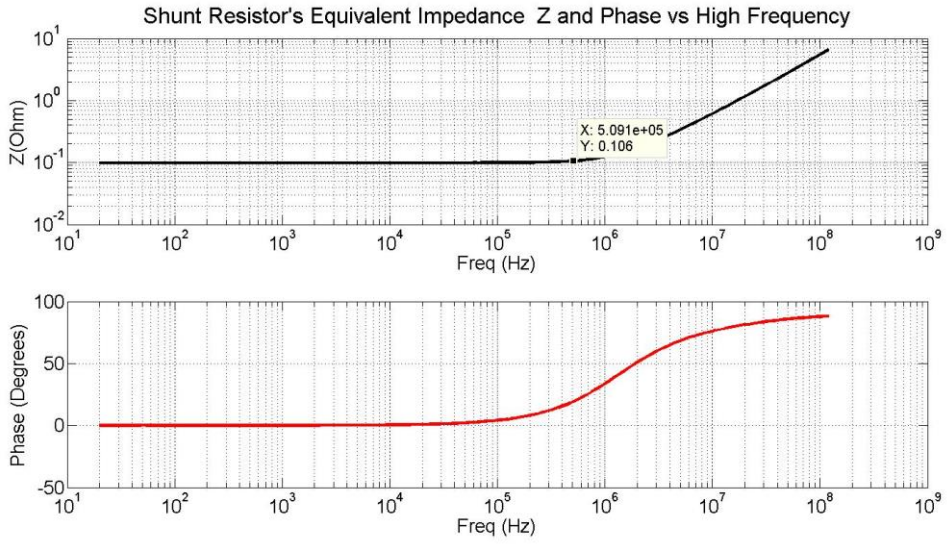

Figure 5.10- Shunt measurement resistor's equivalent impedance Z and Phase vs frequency.

One observation of the measurement results of the shunt resistor impedance is that the influence of frequency remains insignificant up to almost 500 kHz, with error less than 5%, note that the error is <1% for the frequency range used 50 kHz -250kHz, then the shunt impedance increases linearly with frequency, at 1 MHz, the shunt resistance error is around 20%, as shown in Figure 5.10.

5.4.1.2 Digital Quantisation Error

The digital quantisation error can become a significant part of any high precision measurement activity. This section will address the quantisation error (8 bit) when looking at the specific application challenges.

Figure 5.11 shows the current and voltage of the inductor at 50% duty cycle, 100 kHz, 49 A and 41 mT.

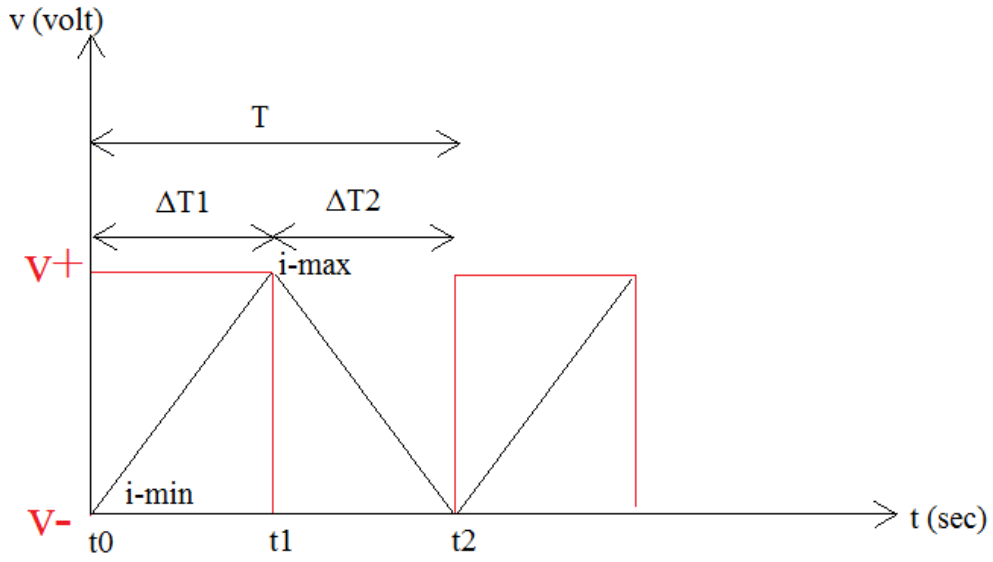

Figure 5.11- The current and voltage waves of the inductor at 50% duty cycle, 100 kHz, 49 A and 41 mT.

The total loss is found from Figure 5.11 with the usage of EQ 5.16.

$$P = \frac{1}{T}\left(v^{+}\left(\frac{i_{max}+i_{min}}{2}\right)\times(t_1-t_0) + \left(v^{-}\left(\frac{i_{max}+i_{min}}{2}\right)\times(t_2-t_1)\right.\right. \qquad \text{EQ 5.16}$$

Where, P is the total losses, v^{+} v^{-} are the maximum and minimum inductor voltage, i_{max}&i_{min} are the maximum and minimum inductor currents and T is the time period.

Considering a duty cycle D=50%, $(t_1 - t_0) = (t_2 - t_1) = \frac{T}{2}$. Thus:

$$P = \frac{1}{4}\left(v^{+} + v^{-}\right)(i_{max}+i_{min}) \qquad \text{EQ 5.17}$$

Considering that the current of the inductor i : $i = \frac{v_{sh}}{R_{sh}}$: R_{sh} is shunt resistance

Thus the total losses is

$$P = \frac{1}{4}\,(\,v^{+} + v^{-})(v_{sh-max} + v_{sh-min}) \times \frac{1}{R_{sh}} \qquad \text{EQ 5.18}$$

The precision of the measurement due to the digital quantisation error in the reading of the total losses $\frac{\Delta P}{P}$ can be indicated by following:

$$\Delta P = \frac{1}{4}\left[(v_{sh-max} + v_{sh-min}) \times \frac{1}{R_{sh}} \times \Delta v + (\,v^{+} + v^{-}) \times \frac{1}{R_{sh}} \times \Delta v_{sh} + (\,v^{+} + v^{-})(v_{sh-max} + v_{sh-min}) \times \frac{\Delta R}{R_{sh}^{2}}\right]$$

Thus,

$$\frac{\Delta P}{P} = \frac{\Delta v}{(\,v^{+} + v^{-})} + \frac{\Delta v_{sh}}{(v_{sh-max} + v_{sh-min})} + \frac{\Delta R_{sh}}{R_{sh}} \qquad \text{EQ 5.19}$$

Where:

ΔP is the absolute error of the total losses.

$\Delta v = 0.804\,V$ is the inductor voltage corresponding to the minimum digital level.

$\Delta v_{sh} = 0.008\,V$ is the voltage drop in the shunt resistor corresponding to the minimum digital level.

$\Delta R_{sh} = \pm 5\%$ is the shunt resistance error for the frequency range used.

Giving an example for the waveforms seen in Figure 5.11 from the measurements:

R_{sh} =0.1Ω, ΔR_{sh} = 0.001 at 1%, Δv=0.804, Δv_{sh}=0.008, $v_{sh-max} = 5.7\ volt$, $v_{sh-min} = 4.0\ volt$, $v^{+} = 74.95\ volt$, $v^{-} = -64.95\ volt$.

Using EQ 5.19

$$\frac{\Delta P}{P} = \frac{0.804}{10} + \frac{0.008}{9.7} + \frac{0.001}{0.1} = 0.081 + 0.0008 + 0.01 \cong 0.09$$

Where the error in the inductor voltage is (0.081) around 8% and the error in the inductor current is (0.0008 + 0.01) around 1.08%.

Thus, the precision of the measurement due to the digital quantisation error is around 9 % including an 8% error in the inductor voltage and a 1% the error in the inductor current.

5.4.1.3 Probe Calibration

The current and voltage waveforms of the inductor have been obtained with the use of InfiniiVision MSO-X-2024A Oscilloscopes which has an analogue bandwidth of 200 MHz. In order to ensure a precise reading the waveform shape must of a high quality. Thus, the 10X probes used have been calibrated using a high quality square wave signal source which contains a frequency content from several hundred Hz to several kHz and amplitude from below 1 volt to several volts.

The steps listed below have been followed to complete the calibration:

1. The probe is connected to signal source, the ground clip to the ground, and the probe tip to the signal output.
2. Adjust the trimming cap on the probe handle is adjusted until a straight-edged square wave is obtained, as shown in Figure 5.12 (middle picture).

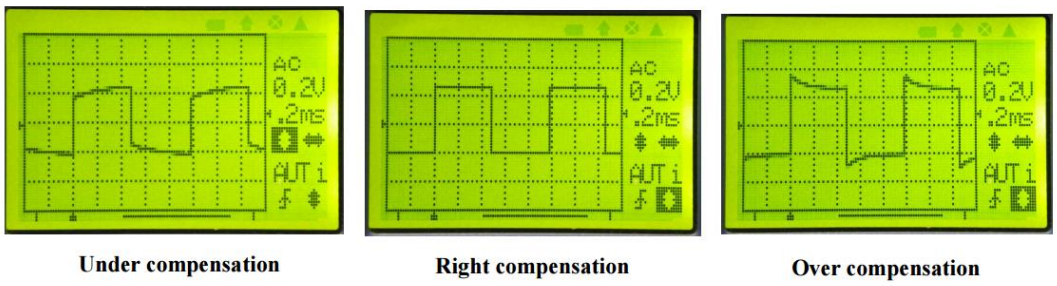

Figure 5.12- Steps for probe calibration.

When a signal passes through a circuit some frequency components incur a loss (or gain) more than others and as a result, we will see its shape distorted at the output. It is therefore important that the calibrated waveform shape must be good. It should have nice and sharp right angles at its corners.

5.4.1.4 Temperature

The current has been applied through the inductor during a very short time period (milliseconds) and as such, the temperature of the inductor could be considered to be fixed for the duration of the test.

5.5 Experimental Results

Measurement sets have been done for fixed levels of AC ripple and different values of DC current in order to fully characterise the inductor using realistic power converter waveforms. The AC ripple has been set by fixing the peak to peak flux density ΔB and this is done by adjusting both supply voltage and the resistive load. Each set has been repeated for different frequencies [50 – 250 kHz] and different peak to peak flux densities [12 - 41 mT], thus different AC ripple magnitudes.

5.5.1 MATLAB acquisition program

Software has been developed within MATLAB in order to acquire the measured data and to save it in a data file, which can be used for further analysis. The waveforms are acquired by this program via a USB connection. The inductor's current and voltage, the voltage on the secondary winding and ΔB curve are plotted immediately on the screen. The total losses and core losses are then calculated for each measurement at different DC bias values. Figure 5.13 shows the inductor's current and voltage waveform, at 150 kHz, 40A.

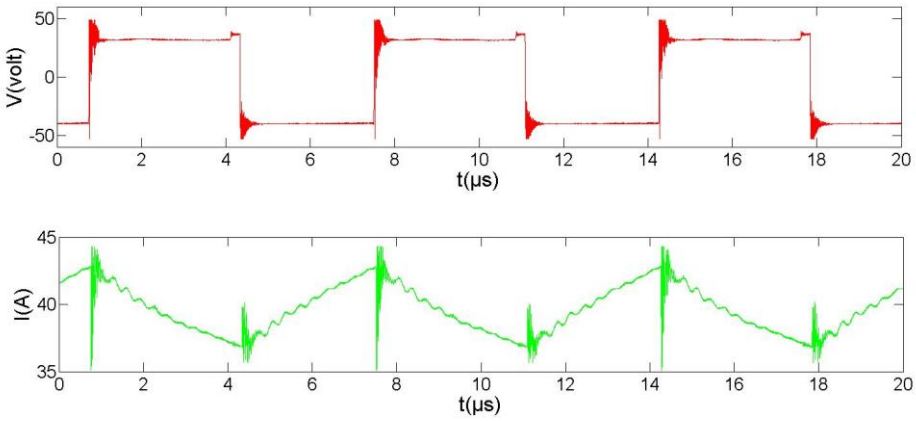

Figure 5.13- Inductor's current and voltage waveform as measured for N95 ferrite core under rectangular waveforms. At 150 kHz, 12 mT and40A mean.

5.5.2 Harmonic Spectrum

The harmonics of the signal $I(t)$were composed in Fourier series as in EQ 5.20

$$I(t) = \sum_m \left[a_m \times \cos\left(\frac{2m\pi}{T} \times t\right) + b_m \times \sin\left(\frac{2m\pi}{T} \times t\right)\right] + a_0 \quad \text{EQ 5.20}$$

T is the period (s).

t is the time (s).

a_m & b_m are the Fourier series coefficients.

a_0 is the DC value of the signal (A)

The Fourier series coefficient can be obtained from EQ 5.21and EQ 5.22 in order to find the magnitude of each harmonics at different orders from EQ 5.23.

$$a_m = \frac{2}{NT}\int_0^{NT} \cos(\frac{2m\pi t}{T}). \quad \text{EQ 5.21}$$

$$b_m = \frac{2}{NT}\int_0^{NT} \sin(\frac{2m\pi t}{T}). \quad \text{EQ 5.22}$$

$$I_m = \sqrt{a_m^2 + b_m^2} \quad \text{EQ 5.23}$$

where:

I_m is the magnitude of harmonics at order m (A).

Figure 5.14 shows both the measured signal and recomposed Fourier series of the current with good agreement between them up to m =20.

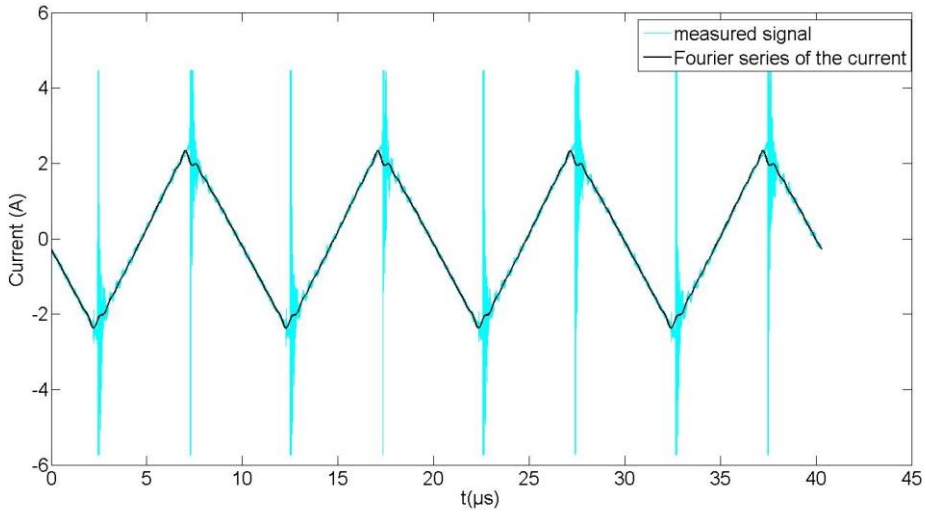

Figure 5.14- The measured signal and the Fourier series of the current (at 100 kHz, 26A and 12mT)

The magnitude of harmonics at orders m= [1-7] (at 100 kHz, 26A and 12mT) are organised in Table 5.3.

Table 5.3- The magnitude of harmonics at order m.

m	1	2	3	4	5	6	7
I_m(A)	1.9395	0.0706	0.1843	0.0365	0.0547	0.0218	0.0225

5.5.3 Measurements Results

In this section, measurement results are presented and a new approach is introduced to describe core loss calculation under DC bias conditions and it can be seen that the core losses change for different frequencies. This approach is based on a graph that shows equations obtained by curve fitting which defines the relationship between the core losses and the DC bias. This is done on the core material ferrite N95 from EPCOS [156] with ten distributed air gaps with a total air gap length of 18 *mm*.

5.5.3.1 Core Losses under DC Bias Conditions

In order to measure the flux density in the core, a secondary winding with 6 turns was added on one leg of the core as shown in Figure 5.7. Maxwell simulation was used to obtain the flux density in the core. Figure 5.15 shows non-homogeneity of the flux density at different points of the core, thus an average flux density is assumed to be fixed for each test of the core at each current value.

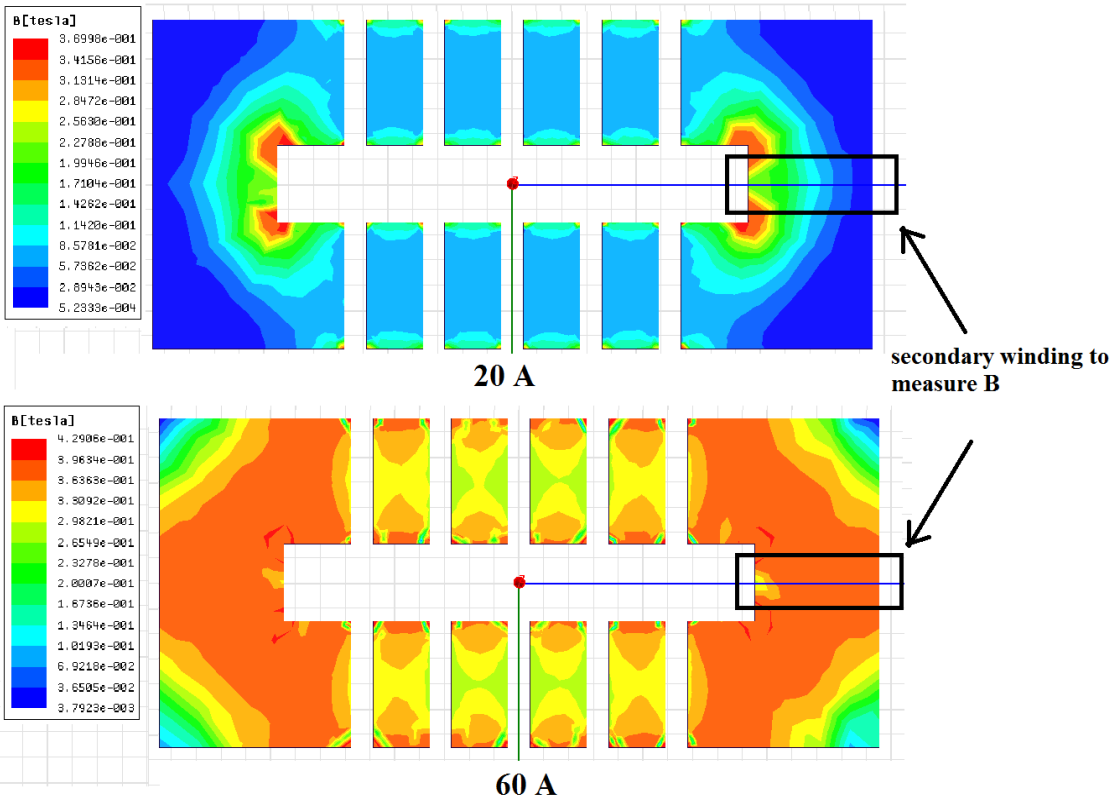

Figure 5.15- Flux density in the core at I=20 and 60 A.

The flux density has been calculated by measuring the voltage drop on the secondary winding v_2 and using EQ 5.24.

$$B = \frac{1}{N \times A_c} \int v_2 . dt \qquad \text{EQ 5.24}$$

Where N is number of turns in the secondary winding N=6, A_c is the cross section of the core m^2 and $v_2$is the voltage drop on the secondary winding.

Losses from different sources at 150 kHz with a peak-to-peak flux density ΔB=12 mT and for different DC bias values are found as shown in In Figure 5.16, and Table 5.4 .

Winding losses (DC and AC) were calculated depending on the formulas EQ 5.1 to EQ 5.7, while the total losses where measured and computed using EQ 5.12. The core loss is calculated using EQ 5.9.

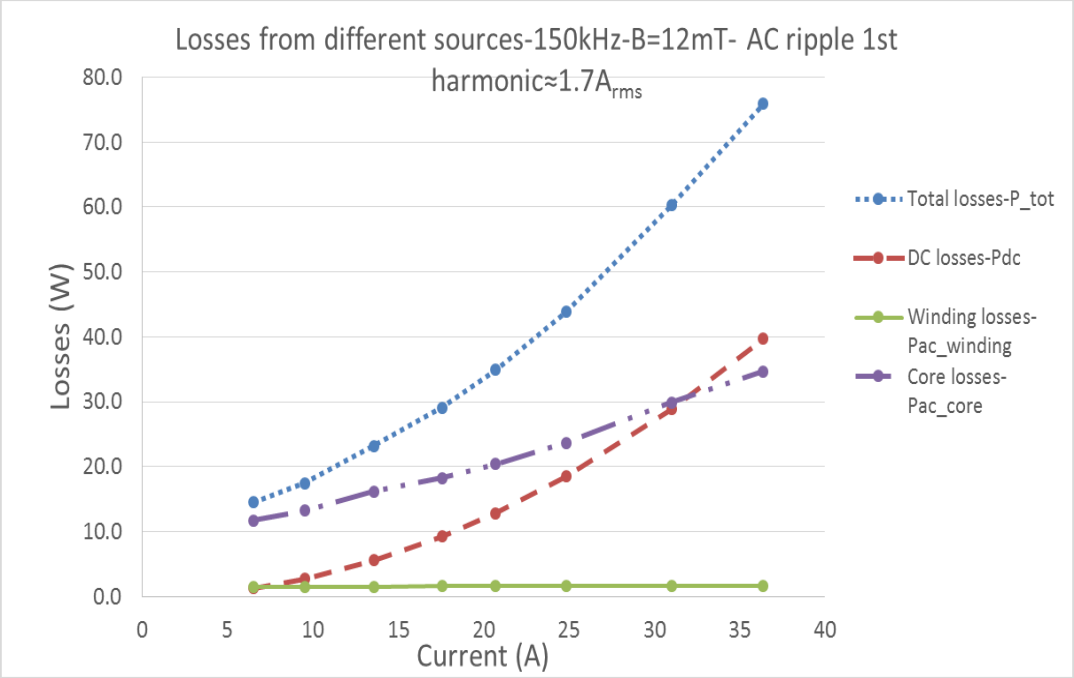

Figure 5.16- Separated losses from different sources vs DC bias current.

Figure 5.16 shows how both DC losses and core losses increase as the DC bias increases while AC winding losses are nearly constant. This is due to the fact that the value of AC ripple injected into the inductor during the tests is constant.

Table 5.4- Separated losses from different sources vs dc bias current at 150 kHz, B=12mT.

$I(A)$	$P_{tot}(W)$	$P_{dc}\ (W)$	$P_{ac}(W)$	$P_{core}(W)$
7	14.5	1.3	1.49	11.7
10	17.5	2.7	1.50	13.3
14	23.2	5.5	1.50	16.2
18	29.1	9.3	1.58	18.3
21	34.9	12.9	1.61	20.4
25	43.8	18.5	1.63	23.7
31	60.3	28.8	1.60	29.9
36	75.9	39.7	1.59	34.6

In order to identify the dependency of the AC winding loss on the frequency, the AC losses were plotted against frequency for two values of peak-to-peak flux density ΔB (12 & 22 mT) and the curves were fitted as shown in Figure 5.17 and EQ 5.25.

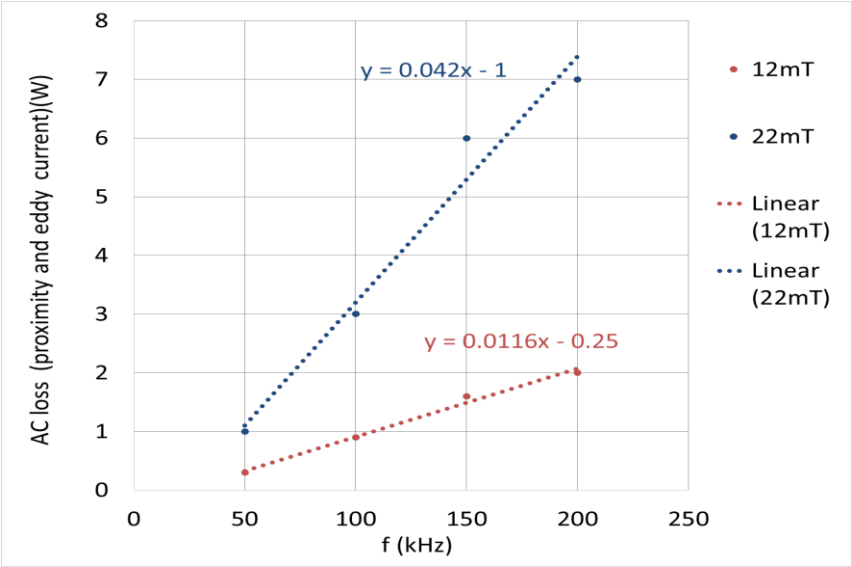

Figure 5.17- The AC winding loss under different ripple values as a function of frequency for two values of peak-to-peak flux density ΔB 12 & 22 mT.

$$P_{AC} = af \pm b \qquad \text{EQ 5.25}$$

It is clear from the results above that the AC winding loss shows a linear relationship with frequency.

In order to analyse the core loss and find its dependency on both flux density and frequency, first the core losses with different DC bias values are plotted as a function of the peak-to-peak flux density ΔB, as shown in Figure 5.18.

The first harmonic of the current ripple is fixed at $I_{n=1} \approx 1.7\ A_{rms}$ and the blue curve is the total measured losses in the inductor at 150 kHz, as shown in Figure 5.16, where it can be seen that the core loss increases as the average current is increased to higher values. Again, the 1st harmonic of the current is kept constant for all measurements, the increase in the core loss can then be related to two factors: a) increasing the harmonic contents of the current and b) behaviour of the material for minor high frequency hysteresis loops [144].

The obtained core losses as a function of DC bias values are plotted for different peak-to-peak flux density ΔB for a fixed frequency of 100 kHz and a curve fitted as shown in Figure 5.18.

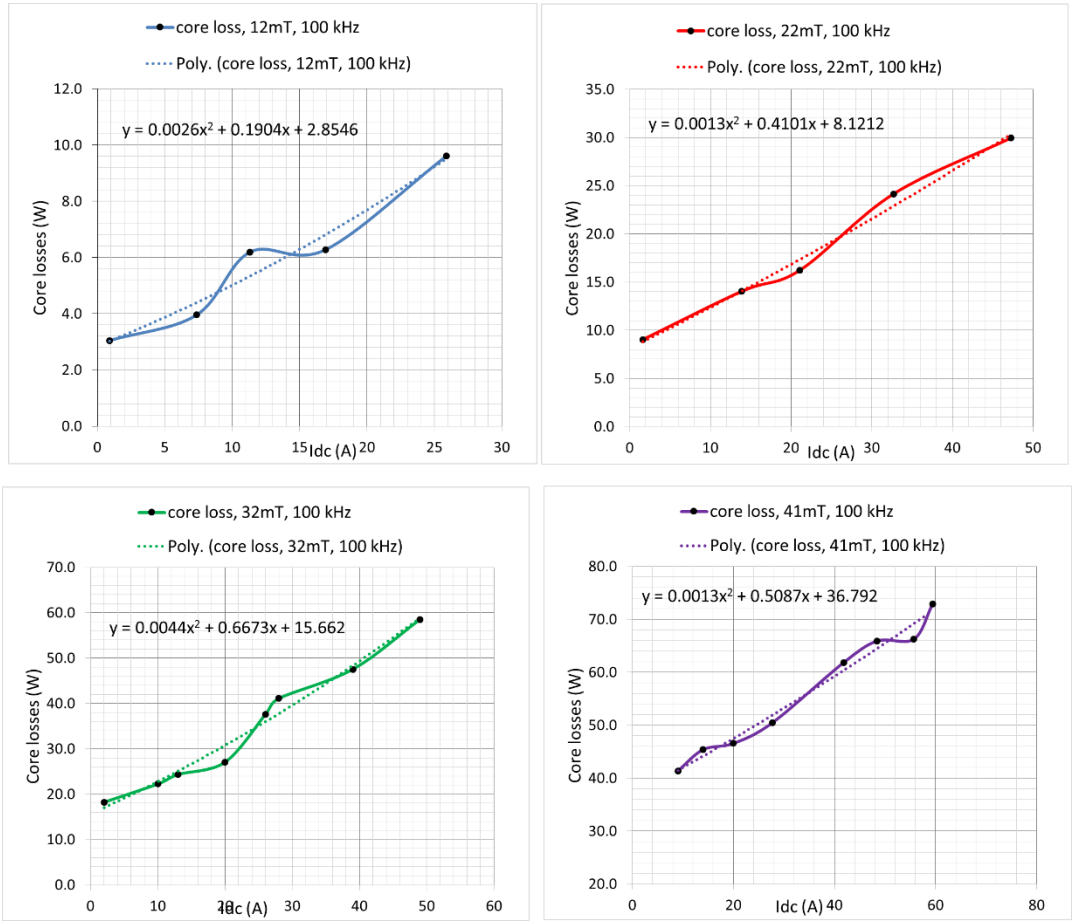

Figure 5.18- The core losses under different DC bias values as a function of the peak-to-peak flux density ΔB Where: f=100 kHz.

The equations defining the relationship between the core loss and the DC bias were obtained by curve fitting the measurments results and used to find the core losses against peak-to-peak flux density ΔB for different values of DC bias at 100 kHz. EQ 5.26 obtained from the curve fitting shown in Figure 5.19 was analysed and the constants α_1 and $\alpha_2$were found and these are organised in Table 5.5 and Figure 5.20

$$P_{core} = \alpha_1 \Delta B^2 \pm \alpha_2 \Delta B \qquad \text{EQ 5.26}$$

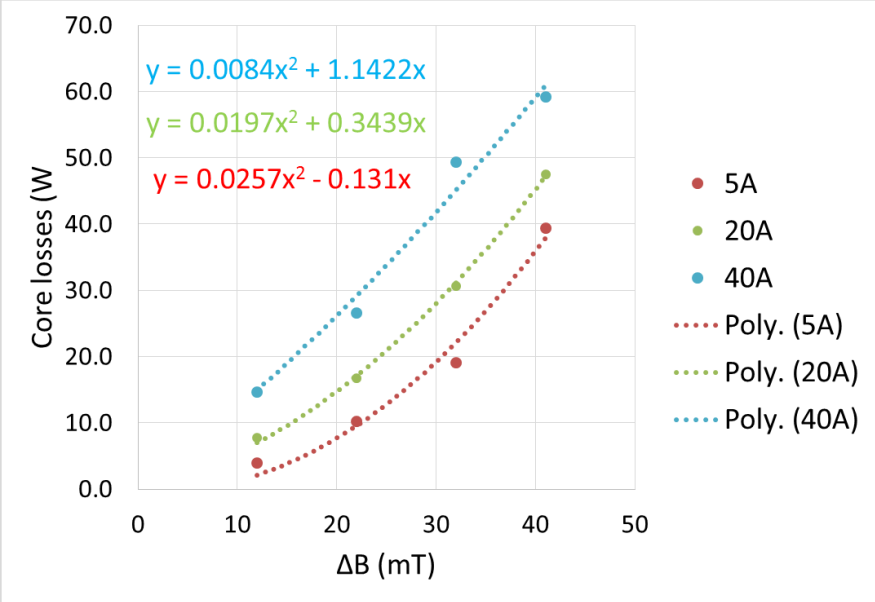

Figure 5.19- The core losses against peak-to-peak flux density ΔB for different values of DC bias at 100 kHz.

Table 5.5- Constants α_1 and α_2 for different DC bias

I_dc (A)	*α_1(W, mT)*	*α_2(W, mT)*
5	*0.0257*	*0.131*
20	*0.0197*	*0.3439*
30	*0.0144*	*0.7236*
40	*0.0084*	*1.1422*
50	*0.0014*	*1.6128*

The constants α_1 and α_2 were plotted against the DC bias and curve fitting defined a second order relationship between the constants and the current, as shown in Figure 5.20 and from EQ 5.27 & EQ 5.28.

$$\alpha_1 = -5E-06{I_{dc}}^2 - 0.0003I_{dc} + 0.0273 \qquad \text{EQ 5.27}$$

$$\alpha_2 = 0.0005{I_{dc}}^2 - 0.0054I_{dc} + 0.0763 \qquad \text{EQ 5.28}$$

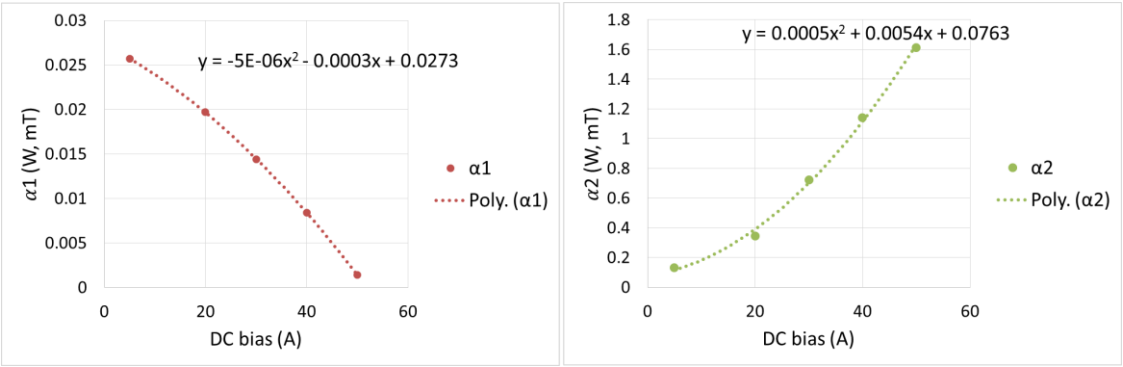

Figure 5.20- The constants α_1 and α_2 vs the DC bias, at 100 kHz.

Thus the core losses are

$$P_{core} = \alpha_1(I_{DC})\Delta B^2 \pm \alpha_2(I_{DC})\Delta B \qquad \text{EQ 5.29}$$

The core loss is a function of both DC bias and peak to peak flux density $P_{core}(I_{DC}, \Delta B^2)$.

5.5.3.2 Core losses Dependency on the Frequency

In order to outline the dependency of the core losses on the frequency, first, core losses under different DC bias values are plotted as a function of frequency for a fixed peak-to-peak flux density ΔB of 12 mT and curves are fitted as shown in Figure 5.21.

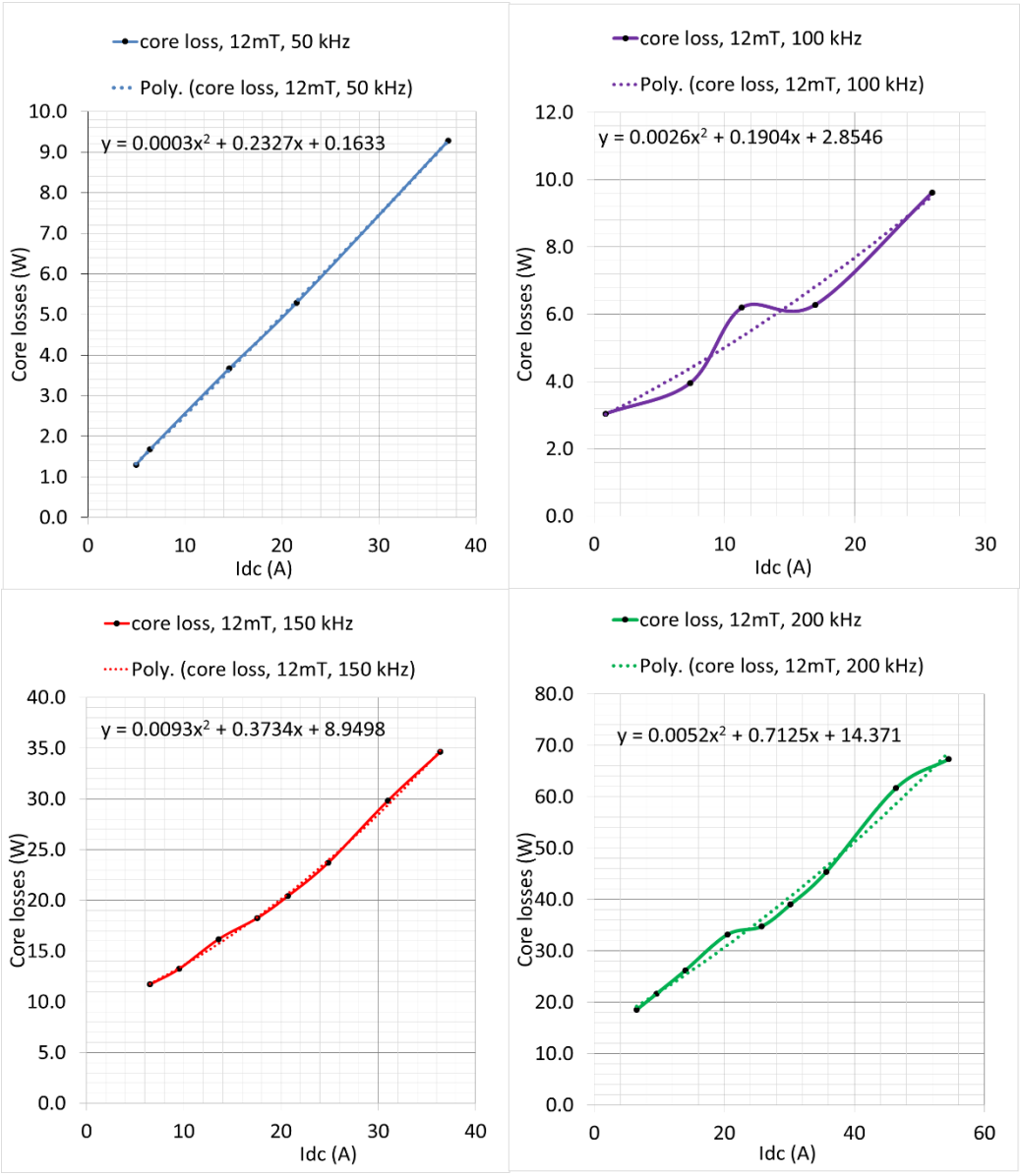

Figure 5.21- The core losses under different DC bias values as a function of frequency for fixed peak-to-peak flux density ΔB of 12 mT.

The equations defining the relationship between the core losses and the DC bias were obtained from the measurements and used in order to find the core losses against frequency for different values of DC bias at ΔB =12 mT. EQ 5.30 has been obtained from the curve fitting as it is shown in Figure 5.21. These were analysed and the constants β_1 and $\beta_2$were found and organised in Table 5.6 and Figure 5.22.

$$P_{core} = \beta_1 f^2 \pm \beta_2 f \qquad \text{EQ 5.30}$$

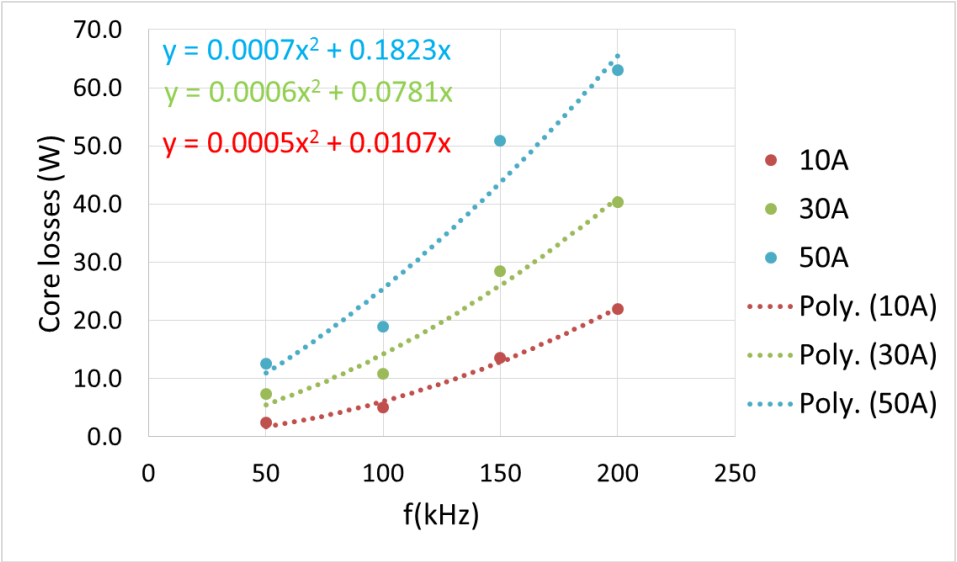

Figure 5.22- The core losses against frequency for different values of DC bias at ΔB=12 mT.

Table 5.6- Constants β_1 and β_2 for different DC bias level.

I_dc (A)	*β_1(W, kHz)*	*β_2(W, kHz)*
10	*0.0005*	*0.0107*
20	*0.0006*	*0.0.0395*
30	*0.0006*	*0.0781*
40	*0.0007*	*0.1259*
50	*0.0007*	*0.1823*

The constants β_1 and β_2 were plotted against the DC bias and curve fitting defined a second order relationship between the constants and the current, as it shown in Figure 5.23 and from EQ 5.31 & EQ 5.32.

$$\beta_1 = 5\mathrm{E}-06 I_{dc} + 0.0005 \qquad \text{EQ 5.31}$$

$$\beta_2 = 5\mathrm{E}-05 {I_{dc}}^2 + 0.00154 I_{dc} - 0.0092 \qquad \text{EQ 5.32}$$

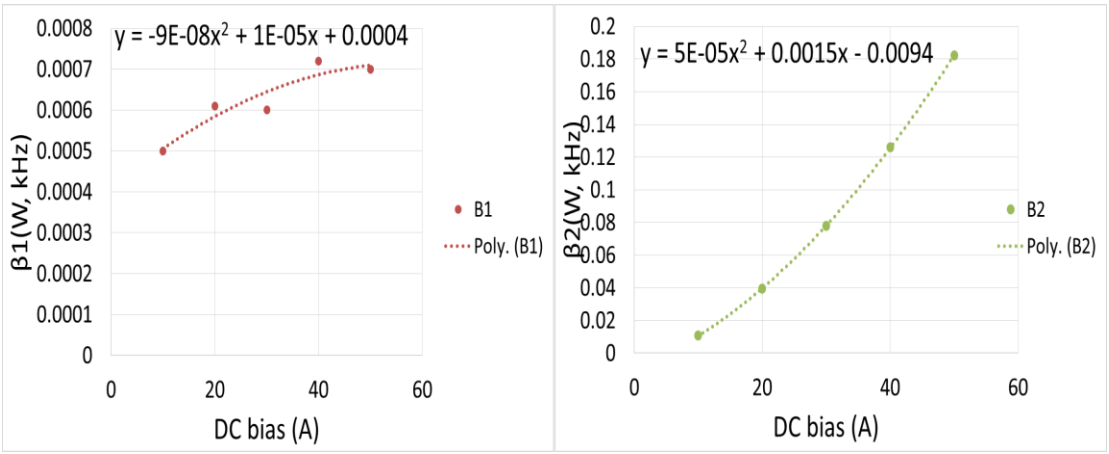

Figure 5.23- The constants α_1 and α_2 vs the dc bias, at 100 kHz.

Finding the core loss as a function of both DC bias and frequency $P_{core}(I_{DC}, f)$ as in EQ 5.33

$$P_{core} = \beta_1(I_{DC})f^2 \pm \beta_2(I_{DC})f \qquad \text{EQ 5.33}$$

As a result, a formula to calculate the losses in the air gapped core has been obtained and it is a function of the DC current, AC current presented by the AC component of the flux density and the frequency.

A comparison between the value of core losses taken from the data sheet for N95 ferrite and EQ 5.29 at 100 kHz and I_{DC}=0 is shown in Table 5.7, while a comparison between the value of core losses taken from the data sheet for N95 ferrite and EQ 5.33 at B=12 mT and I_{DC}=0 is shown in Table 5.8.

Table 5.7- A comparison between the value of core losses taken from data sheet for N95 ferrite and measurements. For a different flux density values at 100 kHz.

100 kHz, I_{DC}=0, α_1 = 0.0273, α_2 = 0.0763		
ΔB (mT)	*P_{core} (kW /m3)- From EQ 5.29*	*P_{core} (kW/m3)- from data sheet for N95 ferrite*
25	*1721*	*3.5*
32	*2758*	*5.06*
41	*4448*	*10*

Table 5.8- A comparison between the value of core losses taken from data sheet for N95 ferrite and measurements, for a different frequency values at 12mT.

$12mT$, $I_{DC}=0$, $\beta_1 = 0.0004, \beta_2 = -0.0092$		
$f\ (kHz)$	$P_{core}\ (kW/m3)$- From EQ 5.29	$P_{core}\ (kW/m3)$- from data sheet for N95 ferrite
50	49	Not found
100	279	Not found
150	691	Not found
200	1284	Not found

It is clear from the results above that the data sheet reference for finding the core losses is not valid for all measurement conditions. This is possibly because the data sheet reference core loss curves were found by using a toroidal core with no airgap and excited with a sinusoidal flux waveforms. Also, the effect of the non-homogeneity of the flux density at different points of the core on the results, as shown in Figure 5.15.

Thus, in the case of an inductor with gapped core and different geometry there is a necessity of proposing a new method for finding the core losses considering the flux fringing effect, and this has been proposed and discussed previously. A formula to calculate the losses in the air gapped core has been obtained and it is a function of the DC current, AC current presented by the AC component of the flux density and the frequency.

5.5.4 A Comparison with a Commercial Inductors

The same commercial inductor (high current, helical inductor-30uH-180A) was used in order to compare it with the designed inductor from a size, weight and thermal point of view and to determine, performance at high frequencies and its losses. In this section the comparison of the total losses, between the designed inductor and the commercial inductor are presented. A comparison of energy density and size implications of the use of the standard inductor is discussed in Chapter 3

The loss measurements have been performed using the same test bench explained previously. At a frequency of 200 kHz the total loss has been found for two AC ripple

values 3 A & 5 A. Neither the flux density nor the core losses have been obtained neither as the structure of the inductor prevented the necessary measurements so the comparison between both inductors is with respect to the total loss. The sum of AC winding loss and the core loss were found by subtracting the DC loss from the total losses. Results are organised in Table 5.9.

Table 5.9- Losses measurements for a high current helical inductor-30uH-180A at f=100 kHz,

Loss measurements for a high current helical inductor-30uH-180A, f=100 kHz, $RwDC = 1.5\ m\Omega$			
AC Ripple (A)	I_{DC} (A)	P_{TOTAL} *(W)*	$PwAC + P_{core}$ *(W)*
3	*19*	*15.3*	*14.8*
	35	*34.0*	*32.1*
	46	*57.7*	*54.6*
5	*28*	*36.4*	*35.2*
	46	*59.8*	*56.6*
	60	*66.9*	*61.5*

Figure 5.24 shows a comparison between the winding AC and core losses for both inductors at 200 kHz, 40 A DC, and AC ripple 3A & 5A. It is apparent that the designed inductor suffers from higher winding AC and core losses. This is mainly due to higher proximity and eddy current effects because of the distributed air gaps, while the commercial inductor has an aluminium metal enclosure with a powdered core including one small air gap of nearly 2 mm.

Furthermore, the inductor winding is smaller and shorter comparing to the designed inductor in this study; $R_{DC-designed} = 30\ m\Omega$ whereas, $R_{DC-commercial} = 1.5\ m\Omega$. This will lead to a much smaller DC loss in the commercial inductor than in the designed inductor. This is to be expected due to the physical size differences seen with the two inductor types. Also note that the commercial inductor is rated at 180A

rather than the nominal 80A of the designed inductor. A significantly lower resistance for the commercial inductor is thus to be expected.

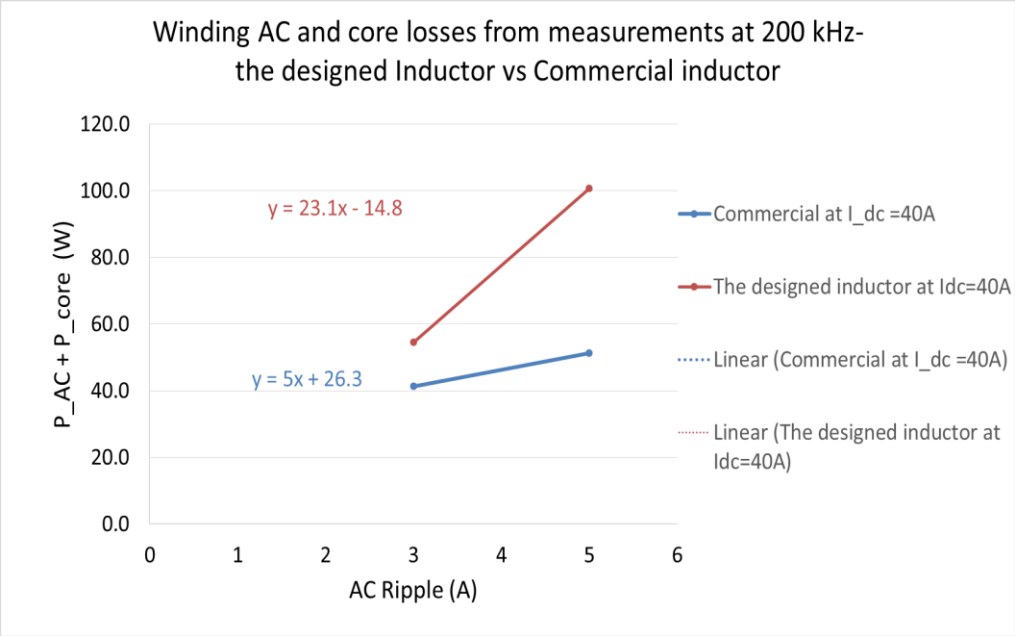

Figure 5.24- Winding AC and core losses from measurements at 200kHz- the designed Inductor vs Commercial inductor

5.6 Conclusion

This chapter has presented a method to evaluate and determine the distribution and source of losses in high energy density inductors. Fourier analysis of the current waveform, combined with impedance measurement and direct electrical loss measurement on the component, has been applied in order to decompose the losses into its different sources. The total losses have been measured by applying a rectangular voltage waveform to the inductor when used as the input of a DC-DC converter in order to apply a realistic flux duty to the magnetic material. The loss measurements have been repeated for different values of ripple current and frequency in order to complete the description of the overall loss as a function of the average current and the AC ripple. The total loss of the magnetic components has been found including DC winding loss, AC winding loss and core loss. A formula to calculate the losses in the air gapped as a function of the DC current, AC current presented by the AC component of the flux density and the frequency has been obtained.

6 Chapter 6- Conclusion and Further work

The main goal of this research was to improve the design of the inductor in order to achieve higher energy densities, specifically by utilising higher current densities in the winding, coupled with the ability to limit the temperature increase of the inductor through the usage of an effective cooling system. Studies have included the influence of the operating dc current, current ripple, airgap location and operating frequency on the inductor design and its resulting characteristics

6.1 Main contributions

The main contributions of this thesis are as follows:

- Improved design of high energy density inductor with a volume of $25.05 \times mm^3$ and a weight of 0.0935 kg, by applying high current densities, comparing to existing commercial inductors with a volume of $207.4 \times 10^3\ mm^3$ and a weight of 0.5 kg. A current density of 46 A/mm2 was shown to be sustainable yielding an energy storage density of 0.53 J/ kg. This is 5 times more than the energy storage density found in the commercial inductor (this comparison has not included the cooling system for the commercial inductor, while it has included the DBC and the cooling layer of the designed inductor excluding the pumps and the pipes.
- Evaluation of the use of a ferrite core with distributed air gap for high frequency and high current applications overcoming saturation and leakage effects associated with a single, lumped air-gap.
- A Novel lumped model in order to find the equivalent electric circuit of the winding for fast determination of the resonance frequency of the inductor is proposed.
- An inductor design methodology where the losses are calculated and a thermal heating is applied for minimum volume.
- Calculation and experimental determination of total loss of the magnetic components including DC winding loss, AC winding loss and obtaining a formula to calculate the losses in the air gapped core as a function of the DC

and AC current presented by the AC component of the flux density and the frequency.

6.2 Summary of the Chapters

In Chapter 2, the design of the inductor was improved for minimum volume and desired inductance L. With the aim of preventing saturation of the magnetic material at high current, a distributed air gap was introduced and improved to achieve the desired inductance in the available volume when operated at high current. Ferrite N95 was used as a core material. The saturation effect has been examined with the usage of Maxwell16.0 3D software (Magneto-static solver) and validated experimentally. The results have successfully avoided the saturation of the core at high current of 80 A by distributing the air gaps along the core.

In Chapter 3, the work has covered the thermal investigation of the cored inductors with its improved design for minimum volume. The inductor geometric model has been exported into ANSYS R15.0 where it has been analysed thermo-electrically under the effect of high current DC. The thermal management method has been validated experimentally by obtaining the temperature of the inductor when applying a high current across it, demonstrating that a high-current energy-dense inductor can be achieved by utilising a high current density in the winding coupled with the usage of an effective cooling system. It has been found that increasing the current up to 70 A, a current density of around 46A/mm^2 will increase the temperature of the inductor from the ambient temperature by 40 °C. A comparison between the temperature of a commercial inductor and the designed inductor from energy density perspective has shown that the proposed designed inductor with its light weight and smaller volume is more suitable for the purpose of the integration than bulky commercial inductor.

In Chapter 4 electrical characterisation of the magnetic components (the designed inductor and magnetic core) has been performed and an equivalent electric circuit of the inductor proposed and solved in LTSPICE in order to predict the resonance frequency and parasitic capacitance of the inductor at high frequencies. The proposed method has been validated experimentally using the Impedance Analyser KEYSIGHT E4990A by means of impedance measurements between the input and output of the inductor. Results showed good agreement between simulation and measurements.

Thus, the proposed equivalent circuits is considered to be valid. The inductor with the core material on the DBC has shown a resonance frequency of 4 MHz.

A comparison between the designed inductor and a commercial, off-the-shelf inductor with similar magnetic aspect has shown a similar performance for both inductors at high frequency. The commercial and designed inductors have a cut-off frequency of 14 and 17 kHz respectively when used in a LC filter. However, the designed inductor with its light weight and smaller volume is more suitable for the purpose of the integration than the bulky commercial inductor.

Chapter 5 presented a method to evaluate and determine the distribution and source of losses in high energy density inductors. Fourier analysis of the current waveform, combined with impedance measurement and direct electrical loss measurement on the component, has been applied in order to decompose the losses into their different sources. The total losses have been measured by using the inductor as the input of a DC-DC converter in order to apply a realistic flux waveform to the magnetic material. The losses have been measured for different values of ripple current and frequency in order to complete the description of the overall loss as a function of the average current and the AC ripple. A formula to calculate the losses in the air gapped core has been obtained as a function of the DC current, ripple current presented by the AC component of the flux density and the frequency.

6.3 Further Work

6.3.1 Improving the Contact Area between the Winding and the DBC

The assembly process used to create the inductor and mount it to the DBC was difficult to control, resulting in significant voiding in the mount-down solder layer and an increased thermal resistance. Investigation of alternative fabrication techniques is recommended in order to overcome these deficiencies.

6.3.2 Losses Measurements on a Toroidal N95 Core

It would be desired to carry out further work to investigate the accuracy of the formulae for the core losses obtained by the method proposed in Chapter 6. Measurements on toroidal N95 cores would be appropriate, facilitating direct comparison with the values in the datasheet of N95 ferrite material. As the magnetic

core losses determined in this study show relatively large values, it would be also interesting to employ the same methods to investigate different magnetic core material with less magnetic loss at high frequencies.

7 Appendices.

7.1 Appendix A

Application	Advantages	Disadvantages
Low Frequency (<1 kHz) High Flux Applications Generators Motors Power Transformers	• Ease of forming shapes allows possible use in inexpensive, high loss applications such as relays, small motors.	• Flux density low • Relative cost high • Limited size of parts
Medium Frequency (1-100 KHz) Non-Linear High Flux Applications Flyback Transformers Deflection Yokes Inverters Wide Band Transformers Recording Heads Pulse Transformers Memory Cores	• Cost much lower than Nickel-Iron alloys, especially thin tapes • Moderately high permeabilities available • Low losses, especially in upper half of this range • Inherent shielding in pot cores • Good wear resistance • Easily adapted to mass production	• Flux density lower than Nickel-Iron alloys • Permeabilities lower than Nickel-Iron alloys • Curie Temperature fairly low • Good mating surface necessary for high inductance • Smaller flux change than bobbin cores
Medium Frequency (1-100 KHz) Low Flux, Linear Applications Loading Coils Filter Cores Tuned Inductors Wide Band Transformers Antenna Rods	• Permeabilities higher than powdered iron or Permalloy cores • Gapped pot cores provide: 1. Adjustability 2. Stability - temperature, time, A. C. flux density, D.C. bias 3. Self-shielding • µQ Products higher than other materials • Wide choice of Inductance and Temperature Coefficient	• Low Curie point • Need precision grinding of air gap • Brittleness • Mounting hardware needed
Higher Frequencies (>200 KHz) Low Flux, Linear Applications Filters Inductors Tuning Slugs	• Low losses (especially eddy current) • Ferrites, powdered iron and moly-permalloy can operate at higher frequencies • Medium frequency advantages apply	• Permeabi lity decreases with frequency • Medium frequency disadvantages apply • Poor heat transfer
Microwave frequencies (>500 MHz)	• Low dielectric losses • Good gyromagnetic properties • Only bulk materials available	

Figure 7.1- Application considerations-Ferrite Advantages and Disadvantages [68].

Material	Initial Perm. μ_o	Bmax Kilogausses	Loss Coefficients e x 10^6	a x 10^3	c x 10^3	Curie Temp. °C	Resistivity (ohm-cm)	$\mu_o Q$ at 100 kHz	Operating Frequencies
Fe	250	22	-	-	-	770	$10x10^{-6}$	-	60-1000 Hz
Si-Fe (unoriented)	400	20	870	120	75	740	50 x 10^{-6}	-	60-1000 Hz
Si-Fe (oriented)	1500	20	-	-	-	740	$50x10^{-6}$	-	60-1000Hz
50-50 Ni Fe (grain-oriented)	2000	16	-	-	-	360	40 x 10^{-6}	-	60-1000Hz
79 Permalloy	12,000 to 100,000	8 to 11	173	-	-	450	55 x 10^{-6}	8000 to 12,000	1 kHz-75kHz
AMORPHOUS Alloy B	3000	15-16	-	-	-	370	$135x10^{-6}$	-	to 250 kHz
AMORPHOUS Alloy E	20,000	5-6.5	-	-	-	205	140 x 10^{-6}	-	to 250 kHz
Permalloypowder	14 to 550	3	.01 to .04	.002	.05 to .1	450	1.	10,000	10 kHz-1 MHz
High Flux powder	14 to 160	15	-	-	-	360	-	-	10 kHz to 1 MHz
Kool Mu®powder	26 to 125	10	-	-	-	740	-	-	to 10 MHz
Iron powder	5 to 80	10	.002 to .04	,002 to .4	.2 to 1.4	770	10^4	2000 to 30,000	100 kHz-100 MHz
Ferrite-MnZn	750 to 15,000	3 to 5	.001	.002	.01	100 to 300	10 to 100	100,000 to 500,000	10 kHz-2 MHz
Ferrite-NiZn	10 to 1500	3 to 5	-	-	-	150 to 450	10^6	30,000	200 kHz-100MHz
Co-Fe 50%	800	24	-	-	-	980	70 x 10^{-6}	-	-

Figure 7.2-Properties of soft magnetic materials [68].

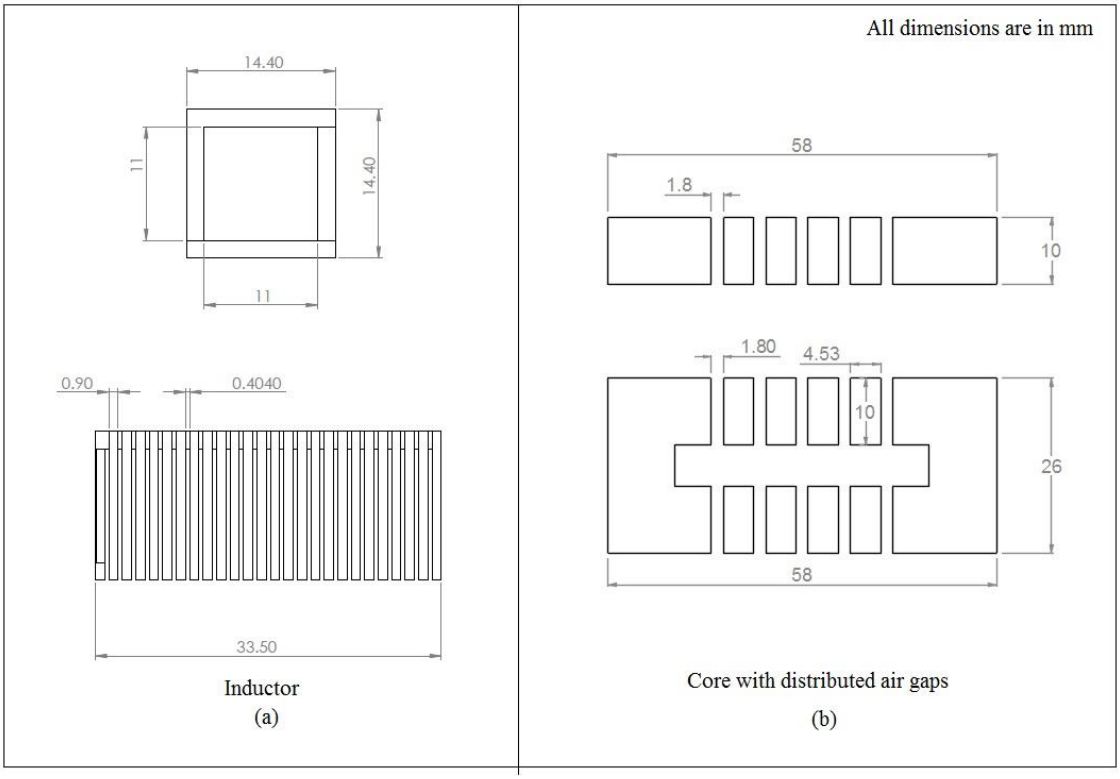

Figure 7.3- Winding and core's dimension.

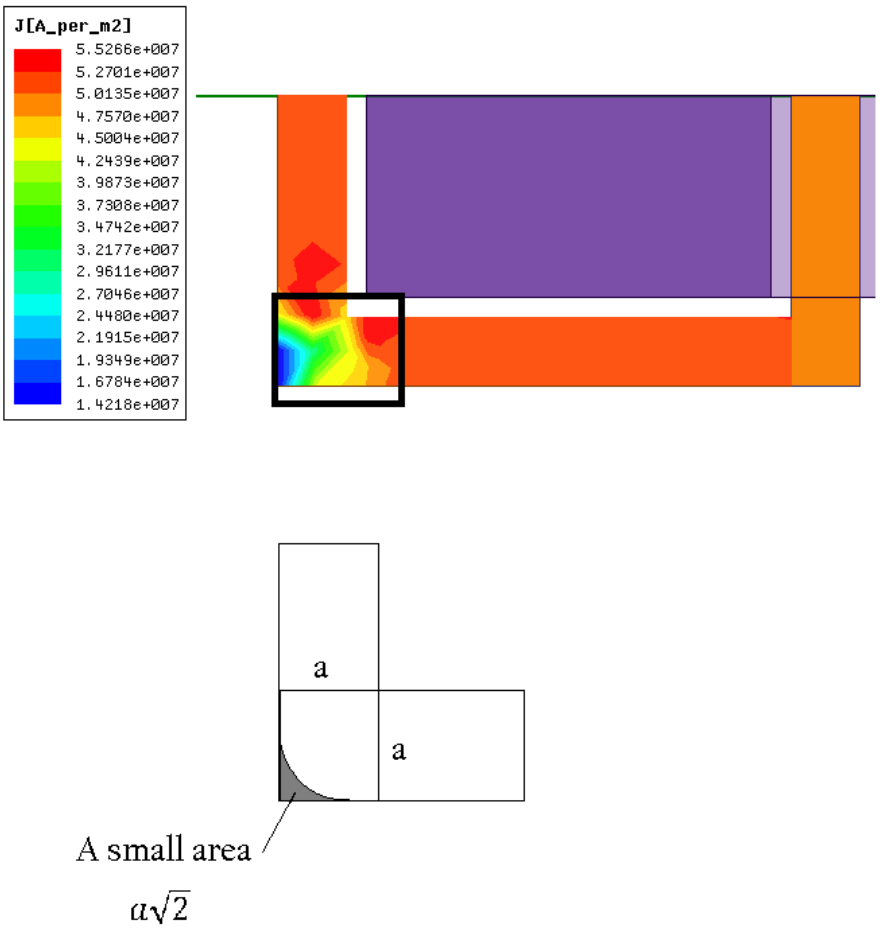

Figure 7.4- The flow of the current through the inductor in the corner area of the copper winding.

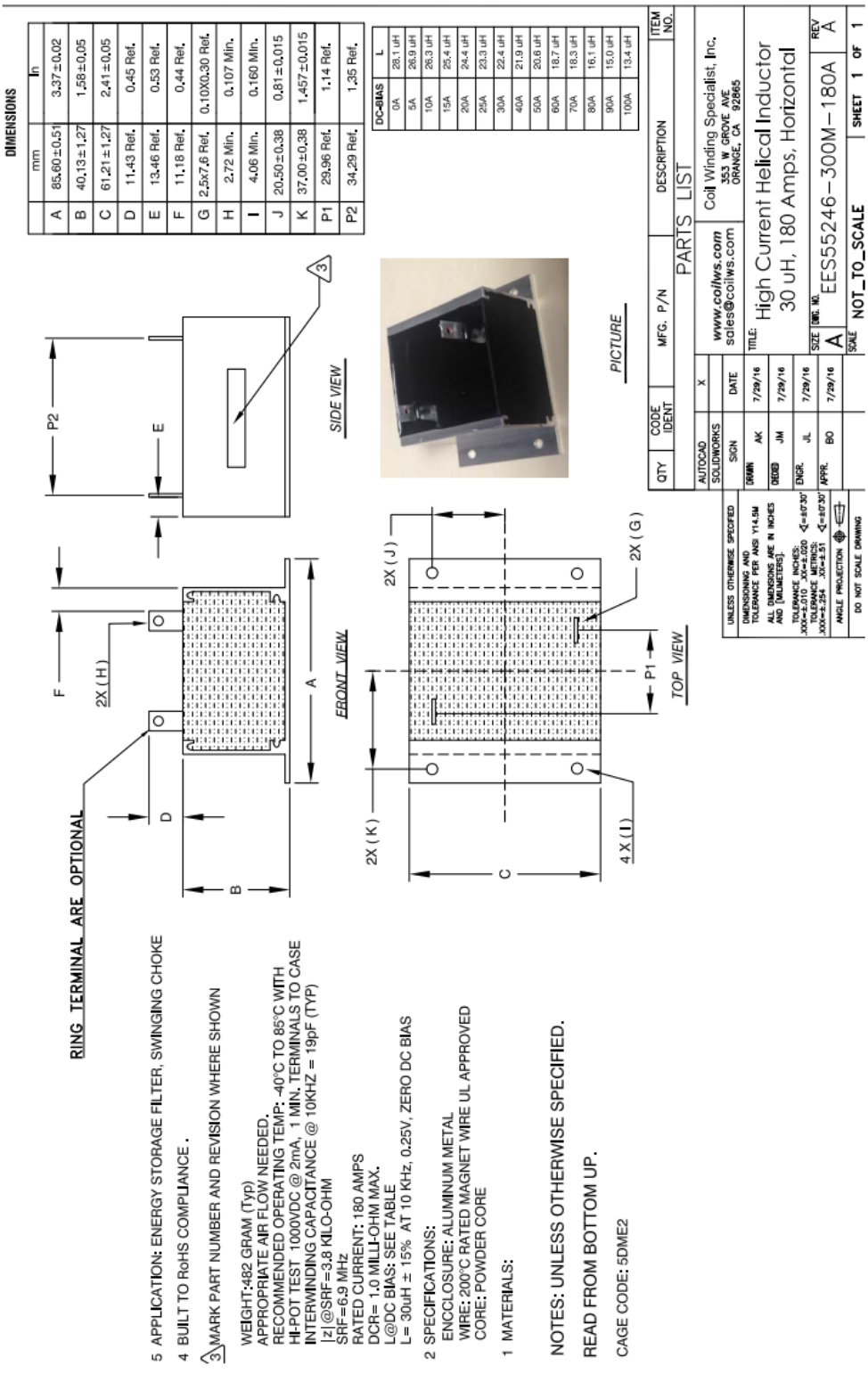

Figure 7.5- A high current helical inductor-30uH-180A.

7.2 Appendix B

Table 7.1 – Typical heat transfer coefficients for a number of commonly used power module cooling techniques [94]

Cooling Method	*Typical heat transfer coefficient (W/m^2K)*
Natural Convection (air)	*3 - 25*
Natural Convection (water)	*15 - 1000*
Forced Convection (air)	*10 – 200*
Forced Convection (water)	*Up to 10,000*
Condensing steam	*5,000 – 50,000*
Boiling Water	*Up to 50,000*
Microchannel	*Up to 50,000*
Jet Impingement	*Up to 50,000*
Spray cooling (water)	*Up to 500,000*
Ultra thin film evaporation	*10,000 to 500,000*

Table 7.2-properties of water at 25°C.

Properties of water at 25°C

ρ (kg/m^3)	998
C_p (J/kgK)	4182
μ (Ns/m^2)	0.001003
K (W/mK)	0.60
Pr	7.0

Table 7.3 – Materials, thicknesses, thermal conductivities and thermal resistances of the proposed package.

Layer name	*Material*	*Thickness (mm)*	*Thermal Conductivity (W/mK)at 26°C*
Inductor	*Cu*	*(1-14)*	*400*
Solder	*Sn-3.5Ag*	*0.1-0.2*	*33*
DBC Copper	*Cu*	*0.2*	*400*
Aluminium Nitride	*AlN*	*1*	*170*
DBC Copper	*Cu*	*0.2*	*393*

Table 7.4- Temperature vs current for one side cooling method

One side cooling-no core				
Ta=24.9 °C, water flow rate=0.0132 $kg.s^{-1}$ or Ls^{-1}				
I (A)	inductor T(°C)-Max	water T-inlet(°C)	water T-outlet(°C)	Δt (T-outlet)- (T-inlet)
20	28.85	25.30	26.51	1.21
30	32.69	25.40	25.88	0.48
40	38.33	25.42	26.22	0.80
50	45.92	25.40	26.59	1.20
60	55.89	25.47	27.26	1.79
70	68.65	25.48	28.04	2.56
80	84.8	25.61	28.93	3.32

Figure 7.6 shows the transient for the outlet temperature of the water till the stability value at 60A.

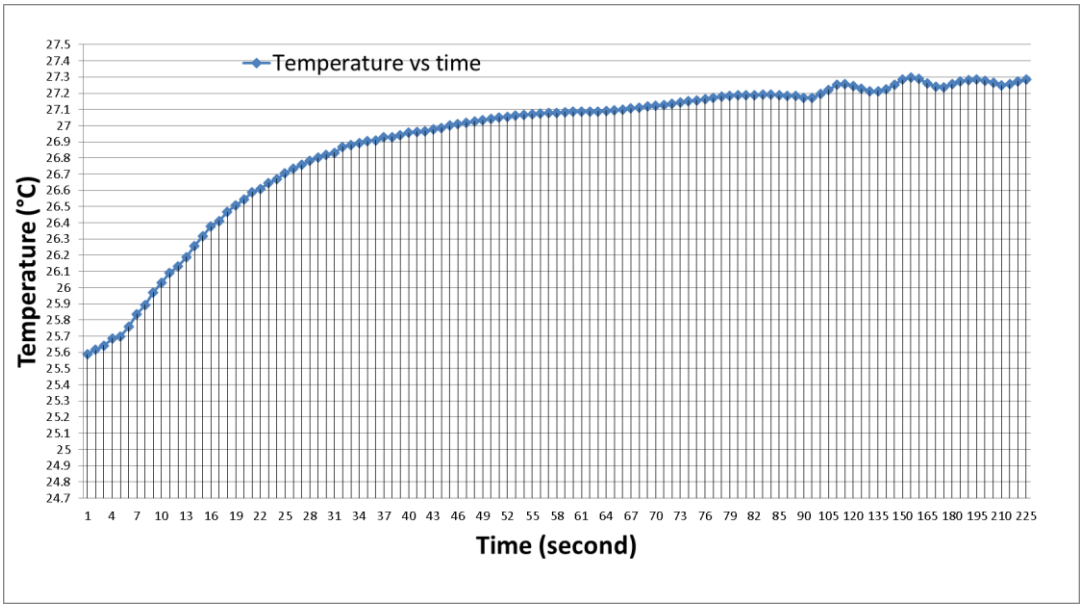

Figure 7.6-Outlet temperature of the water vs Time –at 60A.

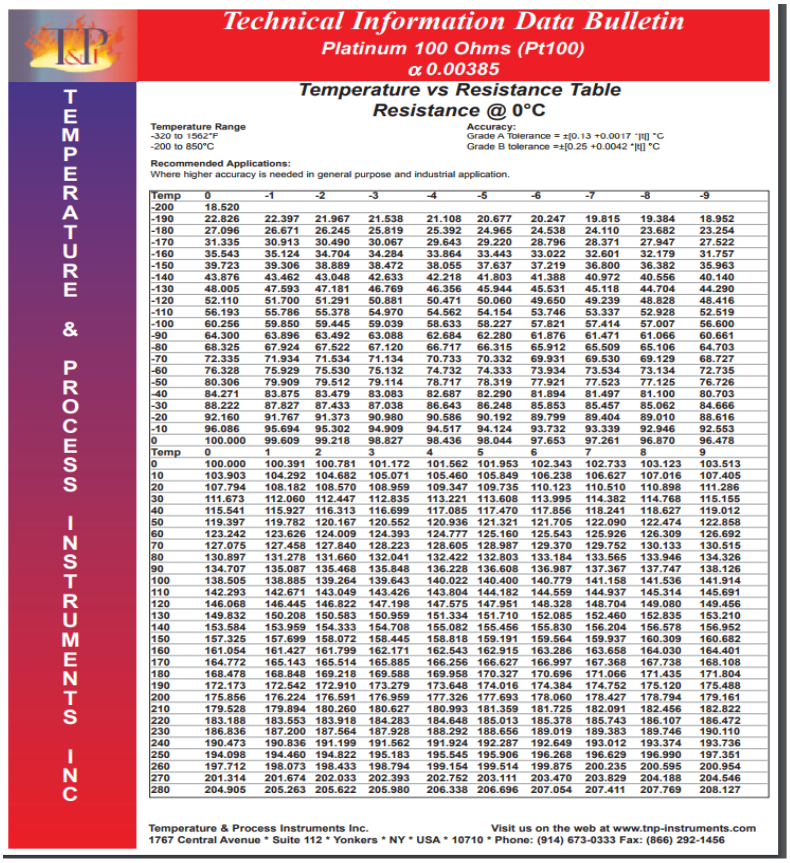

Technical Information Data Bulletin

Platinum 100 Ohms (Pt100)

α 0.00385

Temperature vs Resistance Table

Resistance @ 0°C

TEMPERATURE & PROCESS INSTRUMENTS INC

Temperature Range
-320 to 1562°F
-200 to 850°C

Accuracy:
Grade A Tolerance = ±[0.13 +0.0017 *|t|] °C
Grade B tolerance =±[0.25 +0.0042 *|t|] °C

Recommended Applications:
Where higher accuracy is needed in general purpose and industrial application.

Temp	0	-1	-2	-3	-4	-5	-6	-7	-8	-9
-200	18.520									
-190	22.826	22.397	21.967	21.538	21.108	20.677	20.247	19.815	19.384	18.952
-180	27.096	26.671	26.245	25.819	25.392	24.965	24.538	24.110	23.682	23.254
-170	31.335	30.913	30.490	30.067	29.643	29.220	28.796	28.371	27.947	27.522
-160	35.543	35.124	34.704	34.284	33.864	33.443	33.022	32.601	32.179	31.757
-150	39.723	39.306	38.889	38.472	38.055	37.637	37.219	36.800	36.382	35.963
-140	43.876	43.462	43.048	42.633	42.218	41.803	41.388	40.972	40.556	40.140
-130	48.005	47.593	47.181	46.769	46.356	45.944	45.531	45.118	44.704	44.290
-120	52.110	51.700	51.291	50.881	50.471	50.060	49.650	49.239	48.828	48.416
-110	56.193	55.786	55.378	54.970	54.562	54.154	53.746	53.337	52.928	52.519
-100	60.256	59.850	59.445	59.039	58.633	58.227	57.821	57.414	57.007	56.600
-90	64.300	63.896	63.492	63.088	62.684	62.280	61.876	61.471	61.066	60.661
-80	68.325	67.924	67.522	67.120	66.717	66.315	65.912	65.509	65.106	64.703
-70	72.335	71.934	71.534	71.134	70.733	70.332	69.931	69.530	69.129	68.727
-60	76.328	75.929	75.530	75.132	74.732	74.333	73.934	73.534	73.134	72.735
-50	80.306	79.909	79.512	79.114	78.717	78.319	77.921	77.523	77.125	76.726
-40	84.271	83.875	83.479	83.083	82.687	82.290	81.894	81.497	81.100	80.703
-30	88.222	87.827	87.433	87.038	86.643	86.248	85.853	85.457	85.062	84.666
-20	92.160	91.767	91.373	90.980	90.586	90.192	89.799	89.404	89.010	88.616
-10	96.086	95.694	95.302	94.909	94.517	94.124	93.732	93.339	92.946	92.553
0	100.000	99.609	99.218	98.827	98.436	98.044	97.653	97.261	96.870	96.478
Temp	0	1	2	3	4	5	6	7	8	9
0	100.000	100.391	100.781	101.172	101.562	101.953	102.343	102.733	103.123	103.513
10	103.903	104.292	104.682	105.071	105.460	105.849	106.238	106.627	107.016	107.405
20	107.794	108.182	108.570	108.959	109.347	109.735	110.123	110.510	110.898	111.286
30	111.673	112.060	112.447	112.835	113.221	113.608	113.995	114.382	114.768	115.155
40	115.541	115.927	116.313	116.699	117.085	117.470	117.856	118.241	118.627	119.012
50	119.397	119.782	120.167	120.552	120.936	121.321	121.705	122.090	122.474	122.858
60	123.242	123.626	124.009	124.393	124.777	125.160	125.543	125.926	126.309	126.692
70	127.075	127.458	127.840	128.223	128.605	128.987	129.370	129.752	130.133	130.515
80	130.897	131.278	131.660	132.041	132.422	132.803	133.184	133.565	133.946	134.326
90	134.707	135.087	135.468	135.848	136.228	136.608	136.987	137.367	137.747	138.126
100	138.505	138.885	139.264	139.643	140.022	140.400	140.779	141.158	141.536	141.914
110	142.293	142.671	143.049	143.426	143.804	144.182	144.559	144.937	145.314	145.691
120	146.068	146.445	146.822	147.198	147.575	147.951	148.328	148.704	149.080	149.456
130	149.832	150.208	150.583	150.959	151.334	151.710	152.085	152.460	152.835	153.210
140	153.584	153.959	154.333	154.708	155.082	155.456	155.830	156.204	156.578	156.952
150	157.325	157.699	158.072	158.445	158.818	159.191	159.564	159.937	160.309	160.682
160	161.054	161.427	161.799	162.171	162.543	162.915	163.286	163.658	164.030	164.401
170	164.772	165.143	165.514	165.885	166.256	166.627	166.997	167.368	167.738	168.108
180	168.478	168.848	169.218	169.588	169.958	170.327	170.696	171.066	171.435	171.804
190	172.173	172.542	172.910	173.279	173.648	174.016	174.384	174.752	175.120	175.488
200	175.856	176.224	176.591	176.959	177.326	177.693	178.060	178.427	178.794	179.161
210	179.528	179.894	180.260	180.627	180.993	181.359	181.725	182.091	182.456	182.822
220	183.188	183.553	183.918	184.283	184.648	185.013	185.378	185.743	186.107	186.472
230	186.836	187.200	187.564	187.928	188.292	188.656	189.019	189.383	189.746	190.110
240	190.473	190.836	191.199	191.562	191.924	192.287	192.649	193.012	193.374	193.736
250	194.098	194.460	194.822	195.183	195.545	195.906	196.268	196.629	196.990	197.351
260	197.712	198.073	198.433	198.794	199.154	199.514	199.875	200.235	200.595	200.954
270	201.314	201.674	202.033	202.393	202.752	203.111	203.470	203.829	204.188	204.546
280	204.905	205.263	205.622	205.980	206.338	206.696	207.054	207.411	207.769	208.127

Temperature & Process Instruments Inc.
1767 Central Avenue * Suite 112 * Yonkers * NY * USA * 10710 * Phone: (914) 673-0333 Fax: (866) 292-1456
Visit us on the web at www.tnp-instruments.com

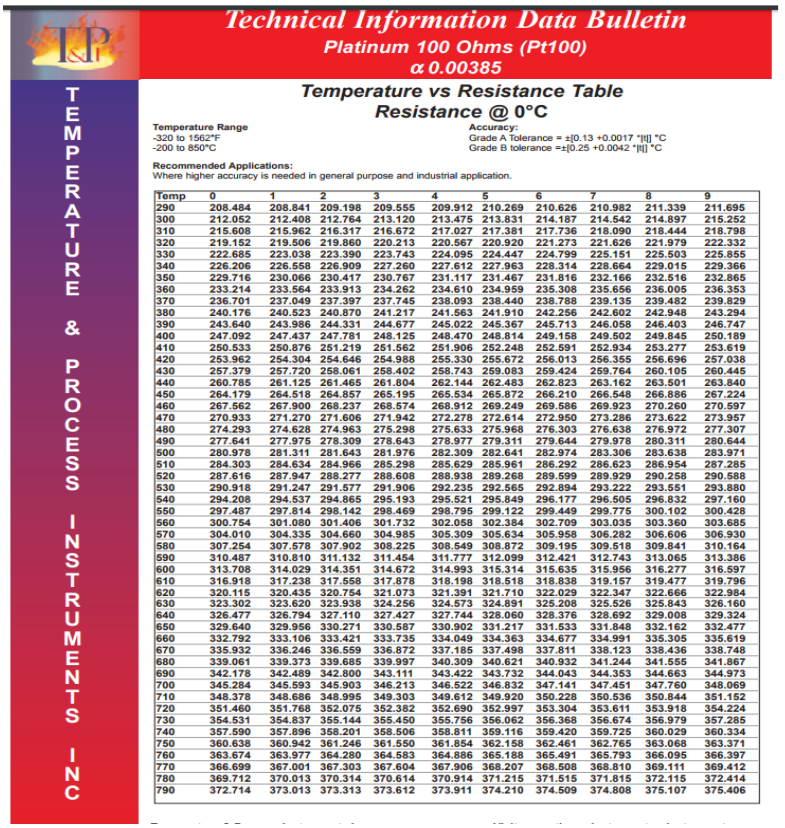

Technical Information Data Bulletin

Platinum 100 Ohms (Pt100)

α 0.00385

Temperature vs Resistance Table

Resistance @ 0°C

TEMPERATURE & PROCESS INSTRUMENTS INC

Temperature Range
-320 to 1562°F
-200 to 850°C

Accuracy:
Grade A Tolerance = ±[0.13 +0.0017 *|t|] °C
Grade B tolerance =±[0.25 +0.0042 *|t|] °C

Recommended Applications:
Where higher accuracy is needed in general purpose and industrial application.

Temp	0	1	2	3	4	5	6	7	8	9
290	208.484	208.841	209.198	209.555	209.912	210.269	210.626	210.982	211.339	211.695
300	212.052	212.408	212.764	213.120	213.475	213.831	214.187	214.542	214.897	215.252
310	215.608	215.962	216.317	216.672	217.027	217.381	217.736	218.090	218.444	218.798
320	219.152	219.506	219.860	220.213	220.567	220.920	221.273	221.626	221.979	222.332
330	222.685	223.038	223.390	223.743	224.095	224.447	224.799	225.151	225.503	225.855
340	226.206	226.558	226.909	227.260	227.612	227.963	228.314	228.664	229.015	229.366
350	229.716	230.066	230.417	230.767	231.117	231.467	231.816	232.166	232.516	232.865
360	233.214	233.564	233.913	234.262	234.610	234.959	235.308	235.656	236.005	236.353
370	236.701	237.049	237.397	237.745	238.093	238.440	238.788	239.135	239.482	239.829
380	240.176	240.523	240.870	241.217	241.563	241.910	242.256	242.602	242.948	243.294
390	243.640	243.986	244.331	244.677	245.022	245.367	245.713	246.058	246.403	246.747
400	247.092	247.437	247.781	248.125	248.470	248.814	249.158	249.502	249.845	250.189
410	250.533	250.876	251.219	251.562	251.906	252.248	252.591	252.934	253.277	253.619
420	253.962	254.304	254.646	254.988	255.330	255.672	256.013	256.355	256.696	257.038
430	257.379	257.720	258.061	258.402	258.743	259.083	259.424	259.764	260.105	260.445
440	260.785	261.125	261.465	261.804	262.144	262.483	262.823	263.162	263.501	263.840
450	264.179	264.518	264.857	265.195	265.534	265.872	266.210	266.548	266.886	267.224
460	267.562	267.900	268.237	268.574	268.912	269.249	269.586	269.923	270.260	270.597
470	270.933	271.270	271.606	271.942	272.278	272.614	272.950	273.286	273.622	273.957
480	274.293	274.628	274.963	275.298	275.633	275.968	276.303	276.638	276.972	277.307
490	277.641	277.975	278.309	278.643	278.977	279.311	279.644	279.978	280.311	280.644
500	280.978	281.311	281.643	281.976	282.309	282.641	282.974	283.306	283.638	283.971
510	284.303	284.634	284.966	285.298	285.629	285.961	286.292	286.623	286.954	287.285
520	287.616	287.947	288.277	288.608	288.938	289.268	289.599	289.929	290.258	290.588
530	290.918	291.247	291.577	291.906	292.235	292.565	292.894	293.222	293.551	293.880
540	294.208	294.537	294.865	295.193	295.521	295.849	296.177	296.505	296.832	297.160
550	297.487	297.814	298.142	298.469	298.795	299.122	299.449	299.775	300.102	300.428
560	300.754	301.080	301.406	301.732	302.058	302.384	302.709	303.035	303.360	303.685
570	304.010	304.335	304.660	304.985	305.309	305.634	305.958	306.282	306.606	306.930
580	307.254	307.578	307.902	308.225	308.549	308.872	309.195	309.518	309.841	310.164
590	310.487	310.810	311.132	311.454	311.777	312.099	312.421	312.743	313.065	313.386
600	313.708	314.029	314.351	314.672	314.993	315.314	315.635	315.956	316.277	316.597
610	316.918	317.238	317.558	317.878	318.198	318.518	318.838	319.157	319.477	319.796
620	320.115	320.435	320.754	321.073	321.391	321.710	322.029	322.347	322.666	322.984
630	323.302	323.620	323.938	324.256	324.573	324.891	325.208	325.526	325.843	326.160
640	326.477	326.794	327.110	327.427	327.744	328.060	328.376	328.692	329.008	329.324
650	329.640	329.956	330.271	330.587	330.902	331.217	331.533	331.848	332.162	332.477
660	332.792	333.106	333.421	333.735	334.049	334.363	334.677	334.991	335.305	335.619
670	335.932	336.246	336.559	336.872	337.185	337.498	337.811	338.123	338.436	338.748
680	339.061	339.373	339.685	339.997	340.309	340.621	340.932	341.244	341.555	341.867
690	342.178	342.489	342.800	343.111	343.422	343.732	344.043	344.353	344.663	344.973
700	345.284	345.593	345.903	346.213	346.522	346.832	347.141	347.451	347.760	348.069
710	348.378	348.686	348.995	349.303	349.612	349.920	350.228	350.536	350.844	351.152
720	351.460	351.768	352.075	352.382	352.690	352.997	353.304	353.611	353.918	354.224
730	354.531	354.837	355.144	355.450	355.756	356.062	356.368	356.674	356.979	357.285
740	357.590	357.896	358.201	358.506	358.811	359.116	359.420	359.725	360.029	360.334
750	360.638	360.942	361.246	361.550	361.854	362.158	362.461	362.765	363.068	363.371
760	363.674	363.977	364.280	364.583	364.886	365.188	365.491	365.793	366.095	366.397
770	366.699	367.001	367.303	367.604	367.906	368.207	368.508	368.810	369.111	369.412
780	369.712	370.013	370.314	370.614	370.914	371.215	371.515	371.815	372.115	372.414
790	372.714	373.013	373.313	373.612	373.911	374.210	374.509	374.808	375.107	375.406

Figure 7.7-PT100 Resistance Table, Temperature vs Resistance.

Figure 7.8 shows a comparison between the temperature of the commercial inductor at currents 80, 100 and 120 A. The temperature has been captured after 15 minutes, the rise in temperature at higher current is noticeable but small with an increasing from the ambient temperature around 30 °C at 80 A, 41 °C at 100 A and 50 °C at 120A.

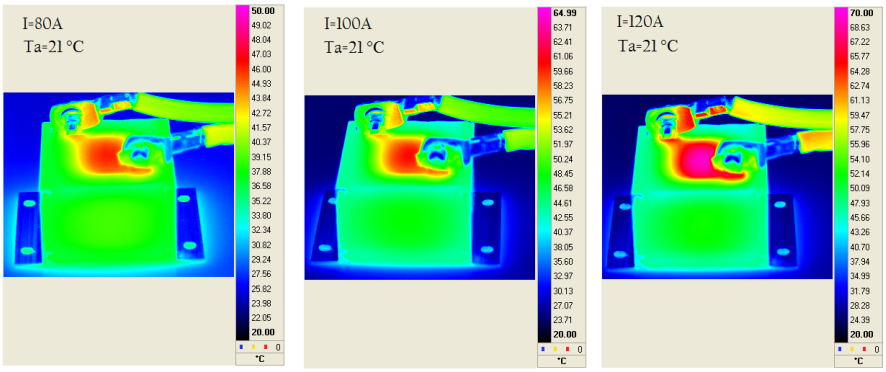

Figure 7.8- A comparison between the temperature of the commercial inductor at currents (a)-80 A, (b)-100 A and (c)-120 A.

7.2.1 High Current Density Air Cored Inductor for Direct Power Module Integration

High current density air cored Inductors for direct power module integration

Rasha Saeed, C. Mark Johnson, Lee Empringham, Liliana De Lillo

The University of Nottingham

Nottingham, UK

NG7 2RD

Tel.: +44 / (115) – 8468840.

E-Mail: eexrs12@nottingham.ac.uk

URL: http://www.nottingham.ac.uk

Acknowledgement

This work was supported by the UK Engineering and Physical Sciences Research Council; grant reference EP/I038543/1.

Keywords

« Packaging », « Passive component integration », « Thermal design »

Abstract

This paper presents an investigation into the integration of high current density inductors into a double side cooled sandwich power module package from the perspective of thermal management of the integrated inductors. The advantage of using this integration method with regards to using the converter thermal management system will be discussed in order to create a high speed optimised commutation circuit. The main aim is to allow the use of a high current density and hence obtain a high power density and high energy storage.

Introduction

Most of the recent studies [1] [2] into power electronic integrated systems have focused their attention on improving their performance in order to achieve higher power densities, reduced cost and size, increased efficiency and reliability. Passive components, mainly inductors, transformers and capacitors, are often the largest and most expensive components in a power electronic circuit. Furthermore, inductors are often responsible for the much of the power loss and volume of the converter [3]. However, there are significant limitations with present technology and significant challenges still need to be faced by researchers in this field.

The new generation of Silicon Carbide SiC and Gallium Nitride GaN [4] [5] power devices have the potential to offer significant improvements to power electronic concepts. These devices have the ability to operate at higher temperatures and higher switching frequencies, which, in turn, means increased performance, higher efficiencies and higher power densities. With higher current density chips compared to their silicon counterparts, smaller packages could be obtained, also if operating frequencies are increased, the physical size of the passive components can be reduced, while maintaining or improving efficiency [6]. The inclusion of Silicon Carbide (SiC) devices can have a dramatic effect on the converter. In a previous study [7], a comparison of an all silicon matrix converter switching at 8kHz had the same efficiency as a hybrid SiC Si (SiC schottky barrier diodes used instead of Si PN diodes) matrix converter operating at 19kHz. This could have a significant impact on the size and weight of the passive filter components. However, the advantageous features of these new devices cannot be presently fully utilised due to the packaging technologies being presently employed and there

are a significant number of issues which require consideration including the inter-component interactions of the power converter [8].

The work in this paper is based on a modular commutation circuit concept. Here, instead of the typical approach to creating high current converters where an increasing number of device die are bonded in parallel, requiring the use of paralleling gate resistors which then in turn slows the devices to such an extent that the advantages start to diminish, a smaller, optimized commutation cell is used in parallel with other commutation cells to create a larger power converter. This has the advantage that the commutation inductance can be optimised locally and the switching behaviour of the devices is then not compromised. This means however that an output inductor is needed for each commutation cell in order to be able to use these cells in parallel.

The specific purpose of this study is to investigate the integration of inductors at the power module substrate level. An added potential benefit of this would be that high speed power switching devices such as Silicon Carbide MOSFETs could be utilised the electro-magnetic interference emanating from the power module could be contained to some extent by creating internal filter configurations and ensuring that a clean, overshoot free commutation is possible. Integrated capacitances would also enable the stray inductances within the module commutation path to be further reduced compared to standard power modules, further enhancing performance.

Integrated inductances

The cooling of passive components, especially inductors is always challenging as the thermal management system needs to be designed to remove heat from the windings which are often buried or inaccessible. The advantage to having the inductors integrated into the power module is that the conductors could be constructed from the substrate materials and as such, will allow a direct conduction path from the winding to the outer surface and on to the thermal management system. This means that very good heat transfer will be possible out of the inductors and devices. One further possibility would be to use a double side cooled `sandwich structure' in order to further increase the thermal efficiency, allowing current densities which would normally not be possible in a standard inductor. High performance cooling technologies such as jet impingement cooling could also be used as the thermal management system which will reduce the temperature rise of the devices during operation. A schematic diagram of a jet impingement cooled sandwich module is shown in Figure 1-(a) [9] [10]. The concept for the power module containing a multitude of switching devices, each with its own output inductor

integrated into the substrate which is cooled by a liquid, jet impingement cooler is shown in figure 1-(b,c).

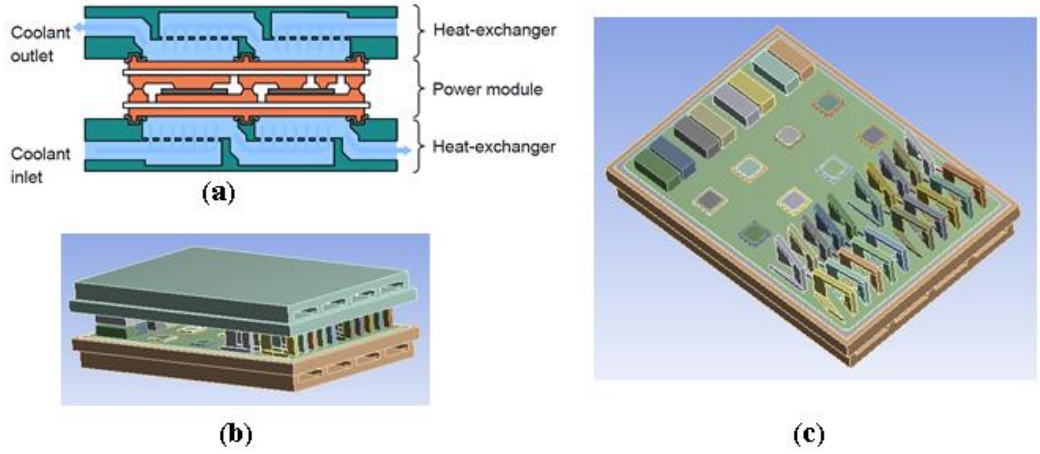

Figure 1: (a) A schematic diagram of a double side cooled sandwich module (b)(c) Expected integrated topology of power converter [10].

The inductors were integrated, in between the two DBC (direct copper bonding) ceramic substrates forming the 'sandwich module' [11]. This module is usually cooled on its top and bottom side, providing larger amount of cooling to the devices. By using the sandwich assembly, a light-weight and compact module can be achieved. A schematic diagram of a sandwich module is shown in Figure 1-(a) where two DBC ceramic substrate tiles are directly cooled using jet impingement [12].

The inductors were initially realised by cutting a spiral, solenoid from solid copper blocks and can be seen in Figure 2. Several test inductors have been constructed with a different numbers of turns and different inner hole dimensions but utilising the same total volume for each inductor. Inductances range varying 0.13 μ H-0.8 μ H were achieved. This shape chosen allows the inductors to be soldered or sintered directly onto the substrate in the sandwich package, as it is shown In Figures 2 & 3.

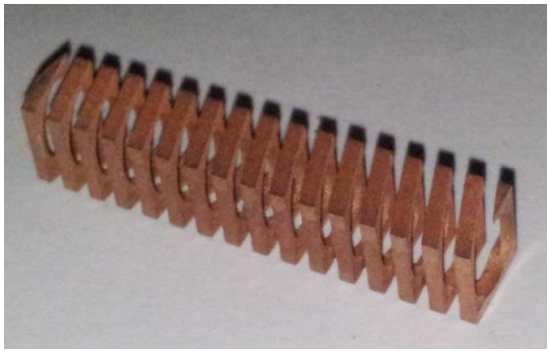

Figure 2: Example of an air cored inductor prior to integration

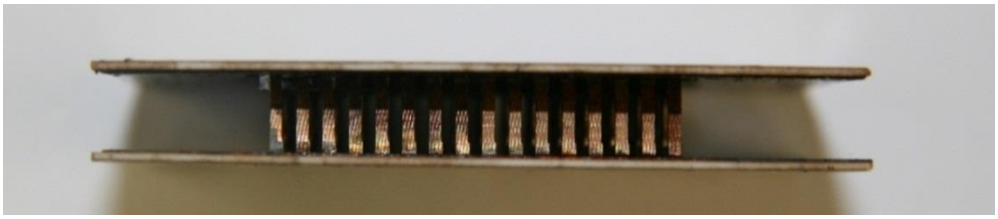

Figure 3: Air cored inductor soldered between two substrates prior to thermal testing

Thermal simulation and experimental results

In order to be able to model the complete package in the future, simulation models of the test inductors needed to be devised so that the experimental results could be used to fine tune and validate future simulations. ANSYS has been used to design the package and analyse the thermal characteristics.

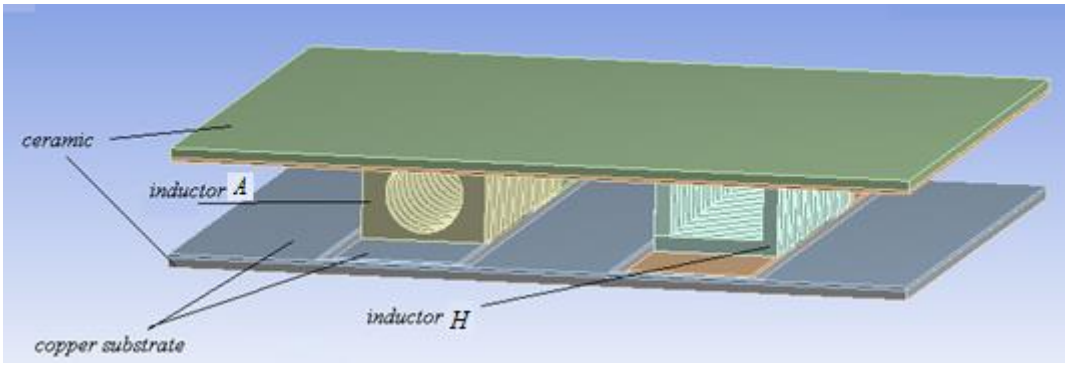

Figure 4: package sandwich structure, using air cored inductors A, H.

Figure 4 shows a sandwich structure consisting of two inductors. Inductor H (0.36 µH) has 16 turns and cross-section (8 mm x 6 mm) with square hole (6mmx4mm), while inductor A has 16 turns and cross-section (6 mm x 6 mm) with circle hole (D=6mm). The ceramic substrates are constructed from Al2O3.

A liquid cooling jacket was added to the package shown in Figure 1 in order to perform thermal tests on the inductors. An investigation of the thermal effects in the package, when different values of current, up to 100A, were applied through inductor H, while no current passed through inductor A was carried out in both the laboratory and in simulation. The tests have been done while the sandwich modules are cooled directly with the cooling fluid being sprayed onto the outside of the substrate to improve the heat extraction. Fig 5 shows the experiment in the lab which consists of the sandwich structure with top and bottom coolers, flow rate meter and thermal measurements for pre and post liquid temperature in order to calculate the calorimetric losses.

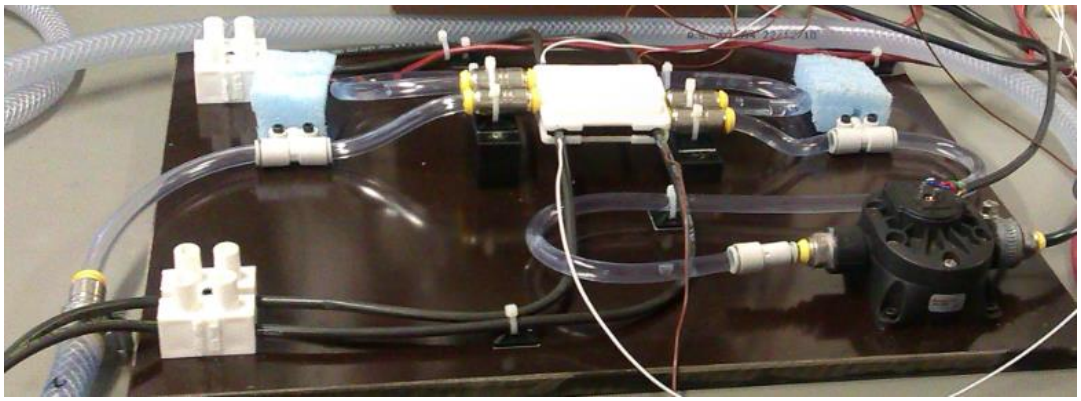

Figure 5: The lab experiment with the sandwich package and the cooling system.

The experiment was carried out at ambient temperature of 25C°. A current was applied through inductor H, and was increased from 0 up to 100A; the maximum temperature of the inductor was measured using a thermal camera. The temperature of both input and output water of the cooler was also measured together with the coolant flow rate. All experimental results have been organized in table I. Both the ANSYS simulation results and lab results were similar and can be seen in Figure 6. These results show that the temperature of the inductor increases proportionally to the current through the inductor. It should be noted that, a

conductor cross sectional area of 1mm squared was used to construct the inductors and as such, a current density of up to 100A/mm squared was achieved with only a 60 degree rise in temperature.

Table I: Maximum temperature of inductor H at various current's values

Inductor H (8 mm x 6 mm) with square hole (6mmx4mm)			
Water flow rate = 104 mL/min			
Current (A)	Water Tin C°	Water Tout C°	Inductor T C°
20	25.92	25.99	30
30	25.79	26.35	32.4
50	26.14	27.71	38
60	26.23	28.70	40.8
70	26.33	29.93	46.2
80	26.52	31.53	52.5
90	26.64	33.55	67
100	26.73	36.08	85.9

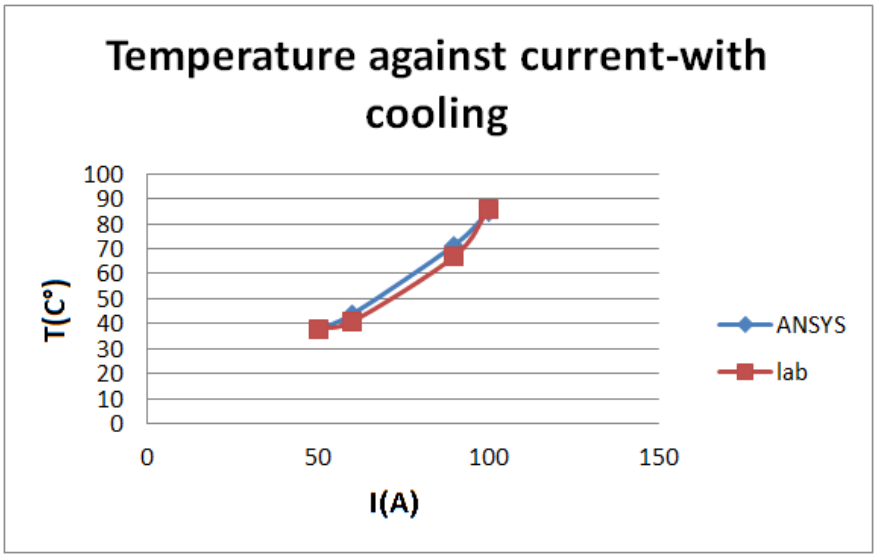

Figure 6- The hot-spot temperature of inductor against the current-with cooling in both lab and ANSYS.

While Figure 7 shows a comparisons of inductor's temperature A current 100A has been applied through inductor H, using Al2O3. It can be seen that the simulation matches the realistic experimental results.

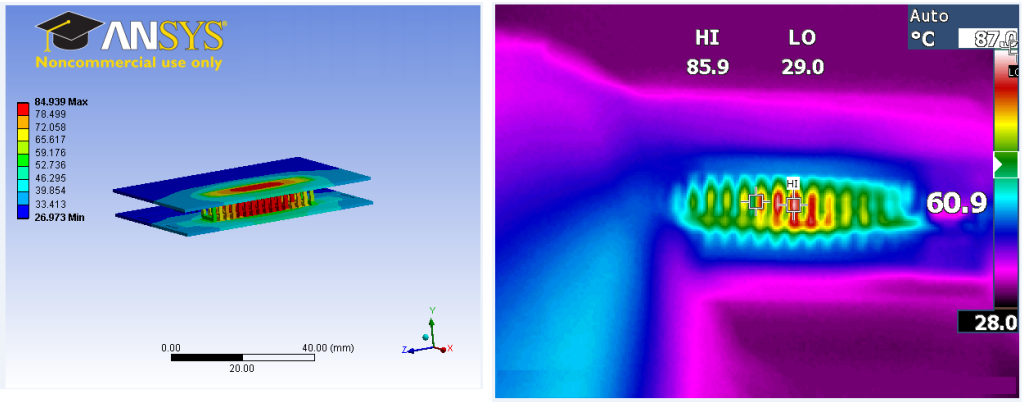

Figure 7: Inductor's temperature comparison between (a) ANSYS and (b) lab at 100A.

Conclusion

The concept of integrating inductance structures into power module substrates has been introduced. The thermal aspects of the integrated inductances have been simulated and then validated against with lab prototypes. The feasibility of using high current density thus high power density inductors has also been presented and shows that this method of integrating inductors into the substrate and with the efficient path of the heat to the thermal management system works well.

References

[1] B. Heinze, J. Lutz, R. Rupp, M. Holz, and M. Neumeister, "Surge Current Ruggedness of Silicon Carbide Schottky- and Merged-PiN-Schottky Diodes," in Power Semiconductor Devices and IC's, 2008. ISPSD '08. 20th International Symposium on, 2008, pp. 245-248.

[2] W. Zhimin, X. Ling, Z. Yang, L. Xiaobing, C. Mingxiang, C. Junjie, and L. Sheng, "Thermal analysis and improvement of high power electronic packages," in Electronic Packaging Technology and High Density Packaging (ICEPT-HDP), 2011 12th International Conference on, 2011, pp. 1-5.

[3] M. Araghchini, J. H. Lang, Y. Xuehong, K. Min Soo, F. Herrault, M. G. Allen, Q. Jizheng, and C. R. Sullivan, "Modeling and measured verification of stored energy and loss in MEMS toroidal inductors," in Energy Conversion Congress and Exposition (ECCE), 2012 IEEE, 2012, pp. 3293-3300

[4] N. Kaminski, "State of the art and the future of wide band-gap devices," in Power Electronics and Applications, 2009. EPE '09. 13th European Conference on, 2009, pp. 1-9.

[5] L. Coppola, D. Huff, F. Wang, R. Burgos, and D. Boroyevich, "Survey on High-Temperature Packaging Materials for SiC-Based Power Electronics Modules," in Power Electronics Specialists Conference, 2007. PESC 2007. IEEE, 2007, pp. 2234-2240.

[6] R. C. N. Pilawa-Podgurski, A. D. Sagneri, J. M. Rivas, D. I. Anderson, and D. J. Perreault, "Very High

Frequency Resonant Boost Converters," in Power Electronics Specialists Conference, 2007. PESC 2007. IEEE, 2007, pp. 2718-2724.

[7] L. Empringham, L. De Lillo, S. Khwan-On, C. Brunson, P. Wheeler, and J. C. Clare, "Enabling technologies for matrix converters in aerospace applications," in Compatibility and Power Electronics (CPE), 2011 7th International Conference-Workshop, 2011, pp. 451-456.

[8] C. M. Johnson, A. Castellazzi, R. Skuriat, P. Evans, L. Jianfeng, and P. Agyakwa, "Integrated High Power Modules," in Integrated Power Electronics Systems (CIPS), 2012 7th International Conference on, 2012, pp. 1-10.

[9] C. Buttay, J. Rashid, C. M. Johnson, F. Udrea, G. Amaratunga, P. Ireland, and R. K. Malhan, "Compact Inverter Designed for High-Temperature Operation," in Power Electronics Specialists Conference, 2007. PESC 2007. IEEE, 2007, pp. 2241-2247.

[10] Leslie, S.G., Cooling Options and Challenges of High Power Semiconductor Modules. Electronics Cooling, 2006. 12(4).

[11] Charboneau, B.C., et al., Double-Sided Liquid Cooling for Power Semiconductor Devices Using Embedded Power Packaging. Industry Applications, IEE Transactions on, 2008. 44(5): p. 1645-1655.

[12] Leslie, S.G., Cooling Options and Challenges of High Power Semiconductor Modules. Electronics Cooling, 2006. 12(4).

7.3 Appendix C

Figure 7.9 shows the parasitic capacitance matrix obtained by Maxwell Electro-Static Solver for the inductor (two winding in series next to each other each of 26 turns) and both are soldered on a copper DBC as is in Figure 4.9-(c) - no core material.

	turn 1	turn 2	turn 3	turn 4	turn 5	. . .	turn 48	turn 49	turn 50	turn 51	turn 52	bottom subtrate
turn 1	6.0922	-3.5036	-0.0983	-0.037	-0.021	. . .	-0.0032	-0.0075	-0.0265	-0.0571	-0.1002	-2.1555
turn 2	-3.5036	8.689	-3.4248	-0.0704	-0.0233	. . .	-0.005	-0.0205	-0.0384	-0.0215	-0.0126	-1.5227
turn 3	-0.0983	-3.4248	8.745	-3.4798	-0.0709	. . .	-0.0204	-0.038	-0.0206	-0.0054	-0.0055	-1.5124
turn 4	-0.037	-0.0704	-3.4798	8.8287	-3.5097	. . .	-0.0379	-0.0204	-0.005	-0.0017	-0.0035	-1.5073
turn 5	-0.021	-0.0233	-0.0709	-3.5097	9.016	. . .	-0.0203	-0.0048	-0.0014	-0.0009	-0.0026	-1.5048
.	.	.	.	.	.	. . .	.	.	.	.	.	.
.	.	.	.	.	.	. . .	.	.	.	.	.	.
.	.	.	.	.	.	. . .	.	.	.	.	.	.
turn 48	-0.0032	-0.005	-0.0204	-0.0379	-0.0203	. . .	8.5147	-3.3452	-0.0665	-0.0237	-0.0219	-1.4858
turn 49	-0.0075	-0.0205	-0.038	-0.0204	-0.0048	. . .	-3.3452	8.5123	-3.3453	-0.069	-0.0393	-1.4902
turn 50	-0.0265	-0.0384	-0.0206	-0.005	-0.0014	. . .	-0.0665	-3.3453	8.4634	-3.299	-0.0986	-1.4961
turn 51	-0.0571	-0.0215	-0.0054	-0.0017	-0.0009	. . .	-0.0237	-0.069	-3.299	8.4223	-3.382	-1.5152
turn 52	-0.1002	-0.0126	-0.0055	-0.0035	-0.0026	. . .	-0.0219	-0.0393	-0.0986	-3.382	5.8945	-2.1426
bottom substrate	-2.1555	-1.5227	-1.5124	-1.5073	-1.5048	. . .	-1.4858	-1.4902	-1.4961	-1.5152	-2.1426	80.074

	Ctntn (the self-capacitance of one turn); n is the number of turn=1,2,3,….52.
	Ctntn+1 (the turn to turn capacitance :between the turn and the adjutant turn);n and m =1,2,3,….52.
	CMnm (The mutual capacitance between the winding of the two inductors next to each other); n and m =1,2,3,….52
	Cstn (The capacitance between the turns of the inductor and the bottom of the substrate) ;n =1,2,3…52
	Ctntm (The capacitance between the turn and the non- adjutant turn); n and m =1,2,3,….52.

Figure 7.9 - The parasitic capacitance matrix of the inductor as in arrangement in Figure 4.9-(c). All values are in pF.

Figure 7.10 shows the inductance matrix of the inductor obtained by Maxwell Magneto-Static Solver for the inductor (two inductors in series next to each other each of 26 turns) as is in Figure 4.9-(b) at 5A-no core material. The total inductance is the sum of the self-inductance per turn and the mutual inductance for each turn with the other turns of the inductor winding. L-total is equal to 6 µH.

L(turn1) M1-2(mutual inductance between turn 1 & 2 L(turn2) M1-51(mutual inductance between turn 1 & 51

	turn 1	turn 2	turn 3	turn 4	turn 5	...	turn 48	turn 49	turn 50	turn 51	turn 52
turn 1	2.43E-02	1.11E-04	1.53E-02	6.93E-03	3.80E-03	...	-1.87E-05	1.13E-04	3.87E-04	8.76E-04	-5.10E-05
turn 2	1.11E-04	2.42E-02	1.24E-04	1.58E-04	2.04E-04	...	-8.50E-05	-7.57E-05	-6.64E-05	-5.80E-05	1.26E-03
turn 3	1.53E-02	1.24E-04	2.41E-02	9.85E-03	5.06E-03	...	3.55E-05	2.28E-04	6.06E-04	1.15E-03	-5.44E-05
turn 4	6.93E-03	1.58E-04	9.85E-03	2.41E-02	9.84E-03	...	2.30E-04	6.08E-04	1.15E-03	1.15E-03	-6.23E-05
turn 5	3.80E-03	2.04E-04	5.06E-03	9.84E-03	2.42E-02	...	6.06E-04	1.14E-03	1.14E-03	6.01E-04	-7.09E-05
.	.	.	.	.	.	...	.	.	.	.	.
.	.	.	.	.	.	...	.	.	.	.	.
.	.	.	.	.	.	...	.	.	.	.	.
turn 48	-1.87E-05	-8.50E-05	3.55E-05	2.30E-04	6.06E-04	...	0.02418	0.009801	0.005062	0.002909	0.000317
turn 49	1.13E-04	-7.57E-05	2.28E-04	6.08E-04	1.14E-03	...	0.009801	0.024192	0.00985	0.005068	0.000236
turn 50	3.87E-04	-6.64E-05	6.06E-04	1.15E-03	1.14E-03	...	0.005062	0.00985	0.023974	0.009888	0.000179
turn 51	8.76E-04	-5.80E-05	1.15E-03	1.15E-03	6.01E-04	...	0.002909	0.005068	0.009888	0.0239	0.000139
turn 52	-5.10E-05	1.26E-03	-5.44E-05	-6.23E-05	-7.09E-05	...	0.000317	0.000236	0.000179	0.000139	0.024374

L(turn52)

Figure 7.10- The inductance matrix of the inductor as in the arrangement in Figure 4.9-(b) at 5A-no core material, all values are in μH.

7.3.1 Cascade two of two- port circuit

Here the method of Cascade two of two- port circuit, [T1] & [T2] is explained as following:

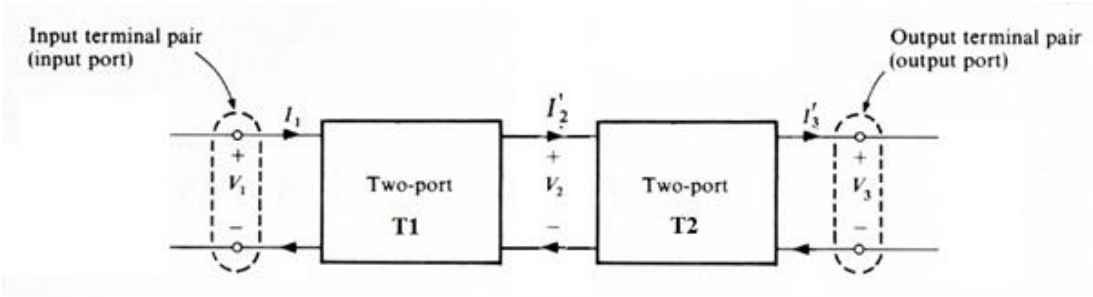

Figure 7.11- The Tow-port circuits in cascade.

From Figure 7.11:

$$\begin{bmatrix} V_1 \\ I_1 \end{bmatrix} = [T_1] \begin{bmatrix} V_2 \\ I_2{}' \end{bmatrix} \qquad \text{EQ 7.1}$$

$$\begin{bmatrix} V_2 \\ I_2{}' \end{bmatrix} = [T_2] \begin{bmatrix} V_3 \\ I_3{}' \end{bmatrix} \quad \text{EQ 7.2}$$

Thus

$$\begin{bmatrix} V_1 \\ I_1 \end{bmatrix} = [T_1][T_2] \begin{bmatrix} V_3 \\ I_3{}' \end{bmatrix} \quad \text{EQ 7.3}$$

$$\begin{bmatrix} V_1 \\ I_1 \end{bmatrix} = \begin{bmatrix} A_1 & B_1 \\ C_1 & D_1 \end{bmatrix} \begin{bmatrix} A_2 & B_2 \\ C_2 & D_2 \end{bmatrix} \begin{bmatrix} V_3 \\ I_3{}' \end{bmatrix} = \begin{bmatrix} A & B \\ C & D \end{bmatrix} \begin{bmatrix} V_3 \\ I_3{}' \end{bmatrix} \quad \text{EQ 7.4}$$

$$[\mathrm{T}] = \begin{bmatrix} A & B \\ C & D \end{bmatrix} \quad \text{EQ 7.5}$$

$$\mathrm{A} = A_1 A_2 + B_1 C_2 \quad \text{EQ 7.6}$$

$$\mathrm{B} = A_1 B_2 + B_1 D_2 \quad \text{EQ 7.7}$$

$$\mathrm{C} = C_1 A_2 + D_1 C_2 \quad \text{EQ 7.8}$$

$$\mathrm{D} = C_1 B_2 + D_1 D_2 \quad \text{EQ 7.9}$$

This is when the input is a function of the output. Now we will find the inverse matrix thus we find the output as a function of the input, as the following:

$$\begin{bmatrix} V_3 \\ I_3{}' \end{bmatrix} = \begin{bmatrix} A & B \\ C & D \end{bmatrix}^{-1} \begin{bmatrix} V_1 \\ I_1 \end{bmatrix} = \begin{bmatrix} A' & B' \\ C' & D' \end{bmatrix} \begin{bmatrix} V_1 \\ I_1 \end{bmatrix} \quad \text{EQ 7.10}$$

$$[T'] = \begin{bmatrix} A' & B' \\ C' & D' \end{bmatrix} = \frac{1}{AD-BC} \times \begin{bmatrix} D & -B \\ -C & A \end{bmatrix} \quad \text{EQ 7.11}$$

$$A' = \frac{D}{AD - BC} \quad \text{EQ 7.12}$$

$$B' = \frac{-B}{AD - BC} \quad \text{EQ 7.13}$$

$$C' = \frac{-C}{AD - BC} \quad \text{EQ 7.14}$$

$$D' = \frac{A}{AD - BC}$$ EQ 7.15

The transfer function:

$$Tr = \frac{V_2}{V_1} \text{ When } -I_2 = 0$$ EQ 7.16

Top Layer

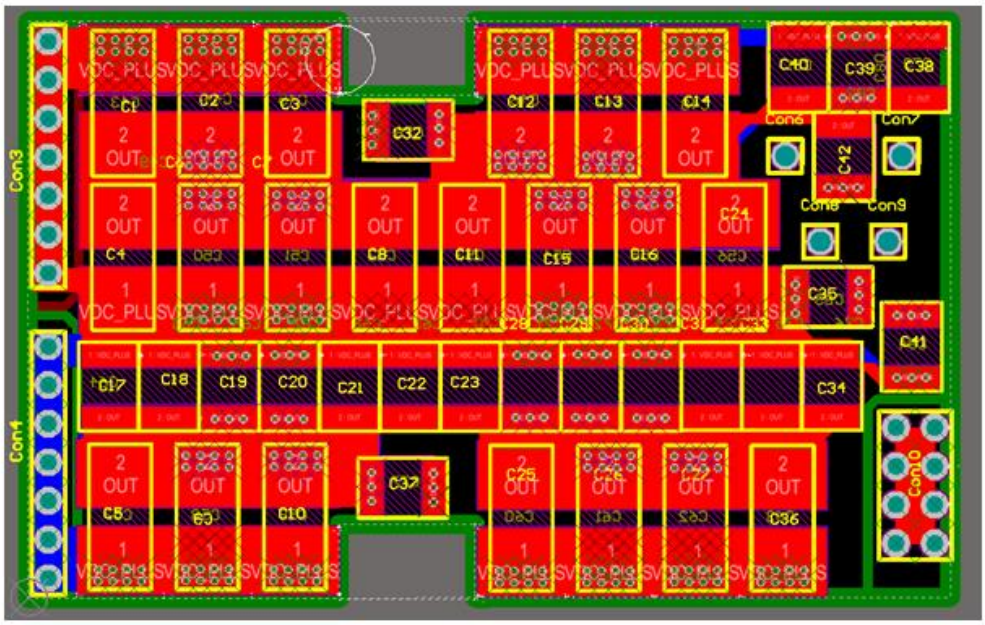

Bottom Layer

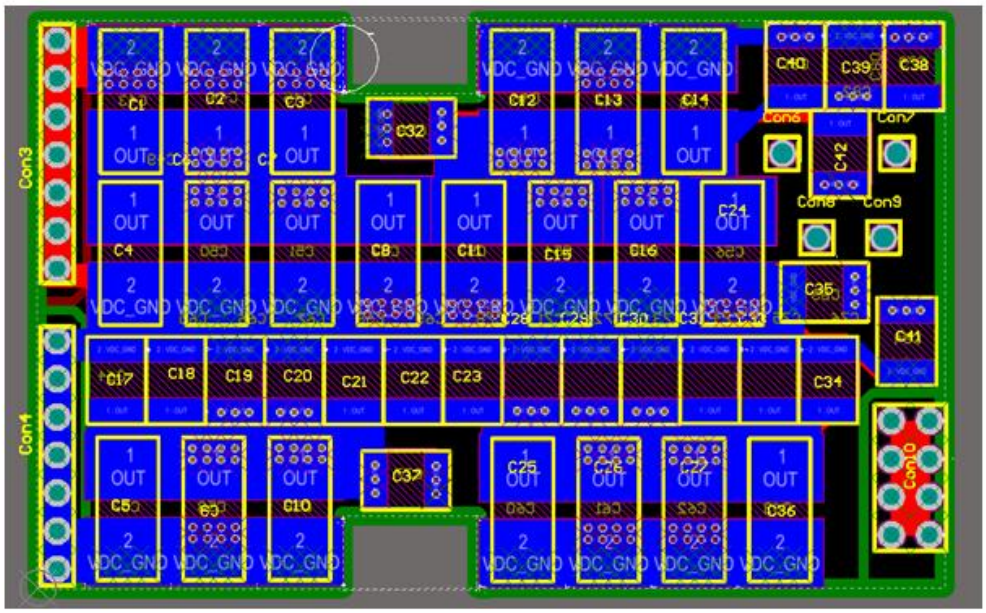

Figure 7.12- Capacitor Co PCB

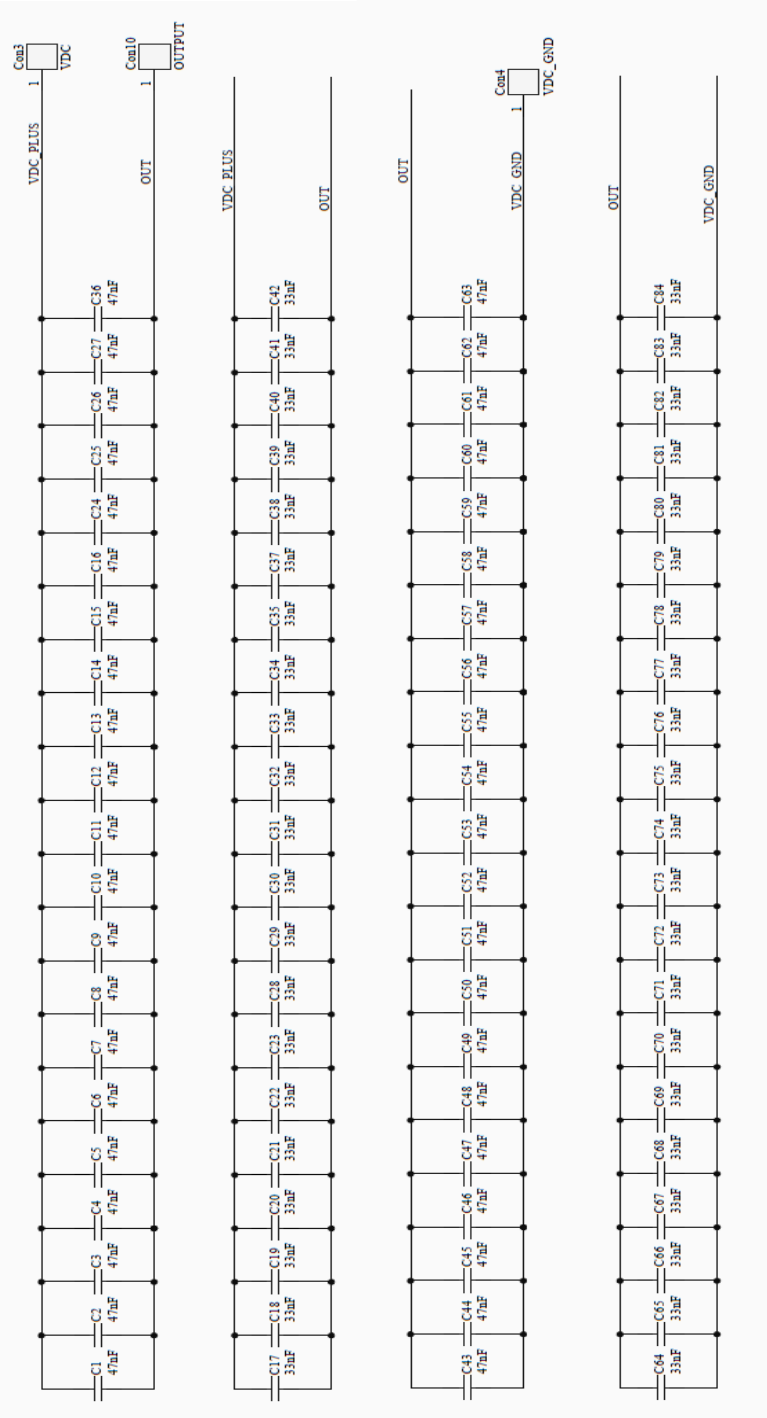

Figure 7.13- Schematic PCB – capacitor Co

The impedance of the capacitor is:

$$Z_C = \frac{1}{J\omega C} \qquad \text{EQ 7.17}$$

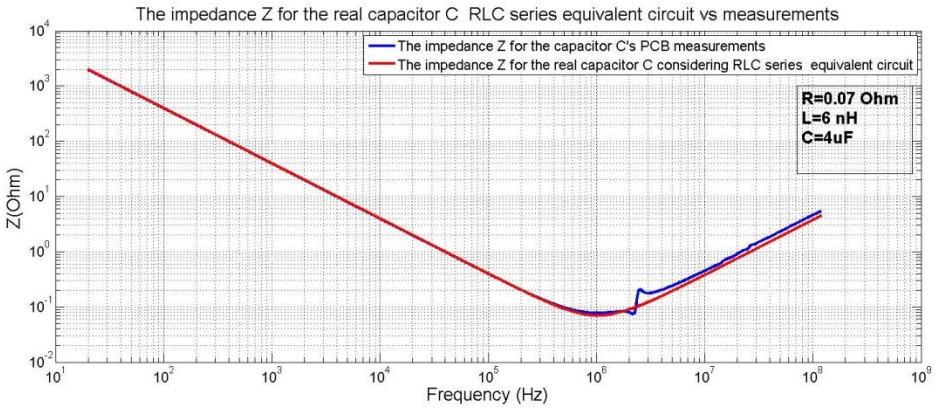

Figure 7.14- The impedance Z of the output capacitor Co.

7.4 Appendix D

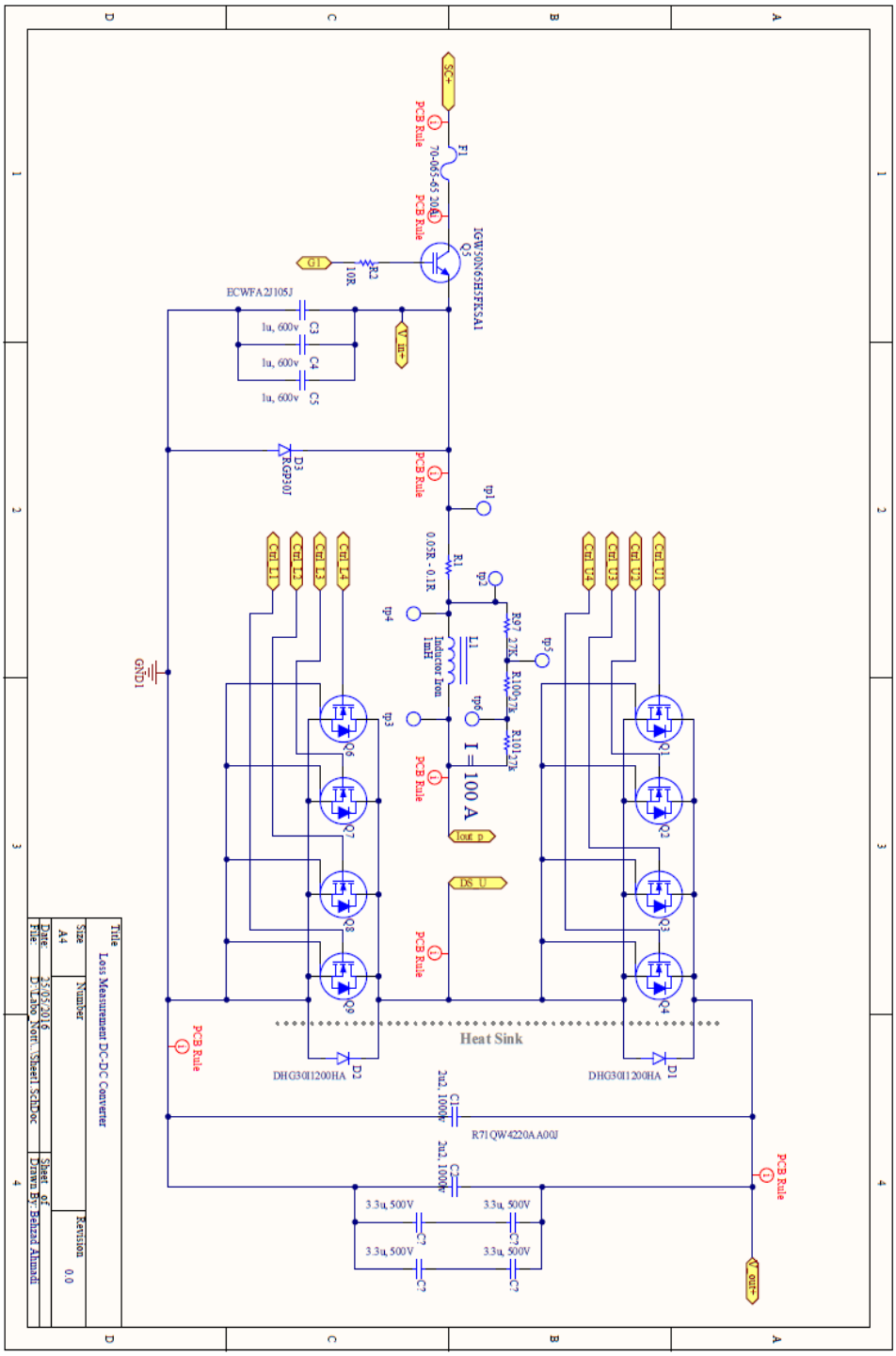

Figure 7.15- Losses measurements DC-DC converter- part 1 schematics

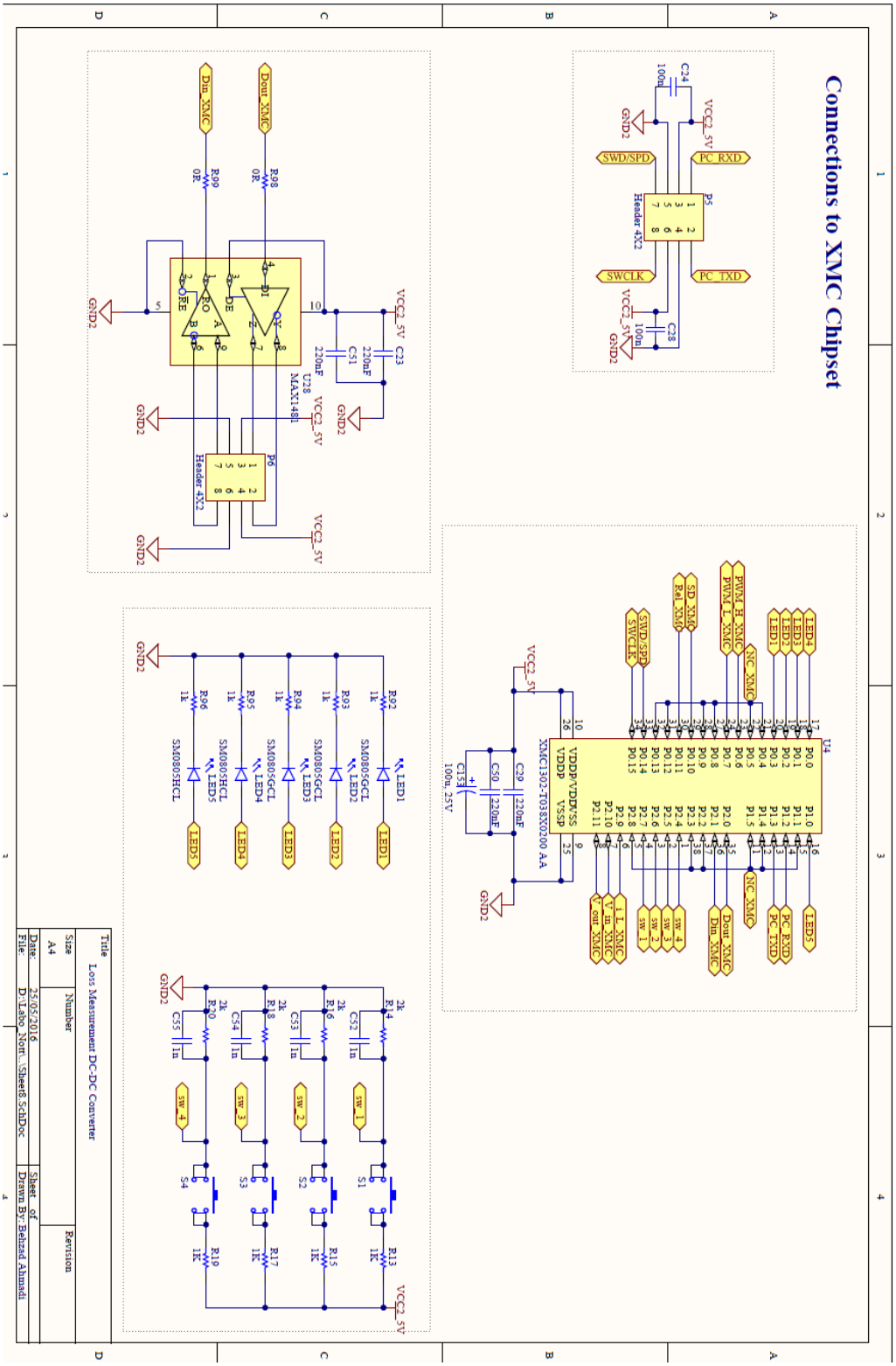

Figure 7.16- Losses measurements DC-DC converter- the Connections to XMC Chipset

8 References

[1] UK Transport and climate change data, UK Department of Transport Factsheets, pp.1-20, 2007.

[2] B. Heinze, J. Lutz, R. Rupp, M. Holz, and M. Neumeister, "Surge Current Ruggedness of Silicon Carbide Schottky- and Merged-PiN-Schottky Diodes," in Power Semiconductor Devices and IC's, 2008. ISPSD '08. 20th International Symposium on, 2008, pp. 245-248.

[3] W. Zhimin, X. Ling, Z. Yang, L. Xiaobing, C. Mingxiang, C. Junjie, and L. Sheng, "Thermal analysis and improvement of high power electronic packages," in Electronic Packaging Technology and High Density Packaging (ICEPT-HDP), 2011 12th International Conference on, 2011, pp. 1-5.

[4] M. Hirakawa, M. Nagano, Y. Watanabe, K. Andoh, S. Nakatomi and S. Hashino, T. Shimizu: "High Power Density interleaved DC/DC Converter using a 3-phase integrated Close-Coupled Inductor set aimed for electric vehicle", IEEE Energy Conversion Congress and Exposition (ECCE2010), pp.2451-2457, (2010).

[5] K. Hartnett, 1. Hayes, and M Egan: "Novel CCTT-Core Split Winding Integrated Magnetic for High-power DC-DC Converters", IEEE Energy Conversion Congress and Expo (ECCE20ll), pp. 598- 605, (2011).

[6] R. T. Naayagi, “A review of more electric aircraft technology”, IEEE International Conference on Energy Efficient Technologies for Sustainability (ICEETS), pp. 750-753, April, 2013.

[7] Z.C. Zhang, B.T. Ooi, "Multimodular Current-Source SPWM Converters for Superconducting Magnetic Storage System", IEEE Trans. on Power Electronics, Vol8, No.3, July 1993, pp.250-255.

[8] S.-Y Tseng, c.-L.Ou, S.-T. Peng and 1.-D.Lee, "Interleaved coupled-inductor Boost Converter with Boost Type Snubber for PV system", the 1st IEEE Energy Conversion Congress and Exposition (ECCE2009), pp.1860-1867, (2009).

[9] J. Imaoka, M. Yamamoto: "Novel integrated Magnetic core structure suitable for Transformer-Linked Interleaved Boost chopper circuit" IEEE Energy Conversion Congress and Expo (ECCE2012), pp. 3279- 3284,(2012).

[10] https://research.googleblog.com/2016/02/and-winner-of-1-million-little-box.html.

[11] F. J. Bryan and A. J. Forsyth, "A power dense DC-DC converter for a small electric vehicle," 6th IET International Conference on Power Electronics, Machines and Drives (PEMD 2012), Bristol, 2012, pp. 1-6.

[12] M. Araghchini, J. H. Lang, Y. Xuehong, K. Min Soo, F. Herrault, M. G. Allen, Q. Jizheng, and C. R. Sullivan, "Modeling and measured verification of stored energy and loss in MEMS toroidal inductors," in Energy Conversion Congress and Exposition (ECCE), 2012 IEEE, 2012, pp. 3293-3300.

[13] G. Shane and S. Sudhoff, "Design paradigm for permanent-magnetinductor-based power converters," Energy Conversion, IEEE Transactions on, vol. 28, no. 4, pp. 880–893, Dec 2013.

[14] R. C. N. Pilawa-Podgurski, A. D. Sagneri, J. M. Rivas, D. I. Anderson, and D. J. Perreault, "Very High Frequency Resonant Boost Converters," in Power Electronics Specialists Conference, 2007. PESC 2007. IEEE, 2007, pp. 2718-2724.

[15] J. W. Kolar, J Biela and J. Miniböck, "Exploring the Pareto Front of Multi-Objective Single-Phase PFC Rectifier Design Optimization -99.2% Efficiency vs. 7kW/dm3 Power Density", in Proc. IEEE 6th International Power Electron. And Motion Control Conf., (IPEMC) May. 2009. pp. 1- 21.

[16] N. Kaminski, "State of the art and the future of wide band-gap devices," in Power Electronics and Applications, 2009. EPE '09. 13th European Conference on, 2009, pp. 1-9.

[17] L. Coppola, D. Huff, F. Wang, R. Burgos, and D. Boroyevich, "Survey on High-Temperature Packaging Materials for SiC-Based Power Electronics Modules," in Power Electronics Specialists Conference, 2007. PESC 2007. IEEE, 2007, pp. 2234-2240.

[18] L. Empringham, L. De Lillo, S. Khwan-On, C. Brunson, P. Wheeler, and J. C. Clare, "Enabling technologies for matrix converters in aerospace applications," in Compatibility and Power Electronics (CPE), 2011 7th International Conference-Workshop, 2011, pp. 451-456.

[19] C. M. Johnson, A. Castellazzi, R. Skuriat, P. Evans, L. Jianfeng, and P. Agyakwa, "Integrated High Power Modules," in Integrated Power Electronics Systems (CIPS), 2012 7th International Conference on, 2012, pp. 1- 10.

[20] J. Imaoka; K. Okamoto; S. Kimura; M. Noah; W. Martinez; M. Yamamoto; M. Shoyama, "A Magnetic Design Method Considering DC- Biased Magnetization for Integrated Magnetic Components Used in Multi-Phase Boost Converters," in IEEE Transactions on Power Electronics , vol.PP, no.99, pp.1-1. doi: 10.1109/TPEL. 2017.2707385

[21] S. Chandrasekaran and L.U. Gokdere, "Integrated magnetics for interleaved DC-DC boost converter for fuel cell powered vehicles", Power Electronics Specialists Conference 2004, IEEE 35th Annual, Vol. 1, pp. 356-361, June 2004.

[22] N. Simpson, R. Wrobel and P. H. Mellor, "Multi-physics design of high-energy-density wound components," *2015 IEEE Energy Conversion Congress and Exposition (ECCE)*, Montreal, QC, 2015, pp. 3857-3864.

[23] J. Abu Qahouq V. Arikatla "Online Closed-Loop Auto-Tuning Digital Controller For Switching Power Converters" IEEE Transaction on Industrial Electronics. vol. 60 no. 5 pp. 1747-1758 May 2013.

[24] C. Deng D. Xu P. Chen C. Hu W. Zhang Z. Wen X. Wu "Integration of Both EMI Filter and Boost Inductor for 1-kW PFC Converter" IEEE Transaction on Power Electronics. vol. 29 no. 11 pp. 5823-5834 Nov. 2014.

[25] H. Wu J. Zhang Y. Xing "A Family of Multiport Buck-Boost Converters Based on DC-Link-Inductors (DLIs)" IEEE Transaction on Power Electronics. vol. 30 no. 2 pp. 735-746 Feb. 2015.

[26] H. Wu T. Mu Y. Xing "Full-Range Soft-Switching-Isolated Buck-Boost Converters with Integrated Interleaved Boost Converter and Phase-Shifted Control" IEEE Transaction on Power Electronics. vol. 31 no. 2 pp. 987-999 Feb. 2016.

[27] P. Malcovati M. Belloni F. Gozzini C. Bazzani A. Baschirotto "A 0.18-μm CMOS 91%-Efficiency 2-A Scalable Buck-Boost DC-DC Converter for LED Drivers" IEEE Transaction on Power Electronics. vol. 29 no. 10 pp. 5392-5398 Oct. 2014.

[28] X. Xie J. Li K. Peng C. Zhao Q. Lu "Study on the Single-Stage Forward-Flyback PFC Converter with QR Control" IEEE Transaction on Power Electronics. vol. 31 no. 1 pp. 430-442 Jan. 2016.

[29] J. Lee J. K. Kim J. H. Kim J. Baek G. Moon "A High-Efficiency PFM Half-Bridge Converter Utilizing a Half-Bridge LLC Converter under Light Load Conditions" IEEE Transaction on Power Electronics. vol. 30 no. 9 pp. 4931-4942 Sept. 2015.

[30] R. W. Erickson D. Maksimovic Fundamentals of Power Electronics Springer 2000.

[31] J. D. van Wyk F. C. Lee "On a Future for Power Electronics" IEEE J. of Emerging and Selected Topics in Power Electron. vol. 1 no. 2 pp. 59-72 June 2013.

[32] Z. Dang J. Abu Qahouq "Evaluation of High-Current Toroid Power Inductor with NdFeB Magnet for DC-DC Power Converters" IEEE Transaction on Industrial Electronics. vol. 62 no. 11 pp. 6868-6876 Nov. 2015.

[33] H. Jia J. Lu X. Wang K. Padmanabhan Z. J. Shen "Integration of a Monolithic Buck Converter Power IC and Bondwire Inductors with Ferrite Epoxy Glob Cores" IEEE Transaction on Power Electronics. vol. 26 no. 6 pp. 1627-1630 June 2011.

[34] P. Herget N. Wang E. J. O'Sullivan B. C. Webb L. T. Romankiw R. Fontana X. Hu G. Decad W. J. Gallagher "A Study of Current Density Limits Due to Saturation in Thin Film Magnetic Inductors for On-Chip Power Conversion" IEEE Transaction on magnetics. vol. 48 no. 11 pp. 4119-4122 Nov. 2012.

[35] M. S. Perdigao J. Trovao J. M. Alonso E. S. Saraiva "Large-Signal Characterization of Power Inductors in EV Bidirectional DC-DC Converters Focused on Core Size Optimization" IEEE Transaction on Industrial Electronics. vol. 62 no. 5 pp. 3042-3051 May 2015.

[36] L. Wang Z. Hu Y. Liu Y. Pei X. Yang "Multipermeability Inductors for Increasing the Inductance and Improving the Efficiency of High-Frequency DC/DC Converters" IEEE Transaction on Power Electronicsvol. 28 no. 9 pp. 4402-4413 Sept. 2013.

[37] Y. Su Q. Li F. C. Lee D. Hou S. She "Planar inductor structure with variable flux distribution - A benefit or impediment?" The 2015 IEEE Applied Power Electronics Conference and Exposition APEC'2015. pp. 1169-1176 Mar. 2015.

[38] X. FAng R. Wu Lu Peng J. Sin "A Novel Integrated Power Inductor with Vertical Laminated Core for Improved L/R Ratios" IEEE Electron Device Letters. vol. 35 no. 12 Dec. 2014.

[39] T. Tera H. Taki T. Shimizu "Loss Reduction of Laminated Core Inductor used in On-board Charger for EVs" 2014 International Power Electronics Conference (IPEC-Hiroshima 2014 - ECCE - Asia). pp. 876-882 2014.

[40] A. Stadler "The Optimization of High Frequency Inductors with Litz-Wire Windings" 8th International Conference on Compatibility and Power Electronics (CPE). pp. 209-213 2013.

[41] V. Sung W. G. Odendaal "Litz Wire Pulsed Power Air Core Coupled Inductor" IEEE Transactions on Industry Applications. vol. 51 no. 4 pp. 3385-3393 July/Aug. 2015.

[42] B. J. Lyons, J. G. Hayes and M. G. Egan, "Magnetic Material Comparisons for High-Current Inductors in Low-Medium Frequency DC-DC Converters," APEC 07 - Twenty-Second Annual IEEE Applied Power Electronics Conference and Exposition, Anaheim, CA, USA, 2007, pp. 71-77.

[43] A. Hilal and B. Cougo, "Optimal inductor design and material selection for high power density inverters used in aircraft applications," 2016 International Conference

on Electrical Systems for Aircraft, Railway, Ship Propulsion and Road Vehicles & International Transportation Electrification Conference (ESARS-ITEC), Toulouse, 2016, pp. 1-6.

[44] K. Nakamura, H. Yoshida, and O. Ichinokura, “Electromagnetic and thermal coupled analysis of ferrite orthogonal-core based on three dimensional reluctance and thermal-resistance network model,” Magnetics, IEEE Transactions on, vol. 40, no. 4, pp. 2050–2052, July 2004.

[45] B. J. Lyons, J. G. Hayes, and M. G. Egan, “Magnetic material comparisons for high-current inductors in low-medium frequency dc-dc converters,” in Proc. IEEE Appl. Power Electron. Conf., 2007, pp. 71–77.

[46] B. J. Lyons, J. G. Hayes, and M. G. Egan, “Experimental investigation of iron-based amorphous metal and 6.5% silicon steel for high-current inductors in low-medium frequency dc-dc converters,” in Proc. IEEE Ind. Appl. Conf., 2007, pp. 1781–1786.

[47] M. S. Rylko, B. J. Lyons, K. J. Hartnett, J. G. Hayes, and M. G. Egan, “Magnetic material comparisons for high-current gapped and gapless foil wound inductors in high frequency dc-dc converters,” in Proc. IEEE Power Electron. Motion Control Conf., 2008, pp. 1249–1256.

[48] M. S. Rylko, J. G. Hayes and M. G. Egan, "Experimental investigation of high-flux density magnetic materials for high-current inductors in hybrid-electric vehicle DC-DC converters," 2010 IEEE Vehicle Power and Propulsion Conference, Lille, 2010, pp. 1-7.

[49] R. Saeed, C. M. Johnson, L. Empringham and L. De Lillo, "High current density air cored Inductors for direct power module integration," 2014 16th European Conference on Power Electronics and Applications, Lappeenranta, 2014, pp. 1-6.

[50] M. Gerber, J.A. Ferreira, I.W. Hofsajer and N. Seliger, “A very high density, heatsink mounted inductor for automotive applications,” IEEE Industry Applications Conference, 2002, pp. 948-954.

[51] J. Espina, B. Ahmadi, L. Empringham, L. De Lillo and M. Johnson, "Highly-integrated power cell for high-power wide band-gap power converters," 2017 IEEE 3rd International Future Energy Electronics Conference and ECCE Asia (IFEEC 2017 - ECCE Asia), Kaohsiung, 2017, pp. 146-150.

[52] https://en.tdk.eu/download/528866/07b76833cf9a9f064109a5b937e959ba/pdf-n95.pdf.

[53] Y. Liu *et al*., "Multi-domain design of inverter-side inductor for LCL filter with 50kW 60 kHz high power density converter," 2017 IEEE Applied Power Electronics Conference and Exposition (APEC), Tampa, FL, USA, 2017, pp. 2527-2533.

[54] M. K. Kazimierczuk, High-Frequency Magnetic Components. A John Wiley and Sons, Ltd., Publication, 2009.

[55] A. Balakrishnan, W. T. Joines, and T. G. Wilson, "Air-gap reluctance and inductance calculations for magnetic circuits using a schwarzchristoffel transformation," IEEE Transactions on Power Electronics, vol. 12, pp. 654–663, July 1997.

[56] C. McLyman, Transformer and inductor design handbook, 1.21 – 1.26, Marcel Dekker Inc., (2004).

[57] Hanson, A., Belk, J., Seungbum, L., David J, P. and Charles R., S. (2015). Measurements and performance factor comparisons of magnetic materials at high frequency. [Online] 2015 IEEE Energy Conversion Congress and Exposition (ECCE): IEEE, pp.5657 - 5666.

[58] D. Perreault, J. Hu, J. Rivas, Y. Han, O. Leitermann, R. Pilawa-Podgurski, A. Sagneri, and C. Sullivan, "Opportunities and challenges in very high frequency power conversion," 24th Annu. IEEE Applied Power Electronics Conf. and Expo, pp. 1–14, Feb. 2009.

[59] Y. Han, G. Cheung, A. Li, C. Sullivan, and D. Perreault, "Evaluation of magnetic materials for very high frequency power applications," 39th IEEE Power Electronics Specialists Conf., pp. 4270–4276, Jun. 2008.

[60] R. Erickson and D. Maksimovic,´ Fundamentals of Power Electronics, 2nd ed. Springer Science and Business Media Inc., 2001, ch. 14 and 15.

[61] Y. Han and D. J. Perreault, "Inductor Design Methods With Low-Permeability RF Core Materials," in IEEE Transactions on Industry Applications, vol. 48, no. 5, pp. 1616-1627, Sept.-Oct. 2012.

[62] https://www.mag-inc.com/Products/Powder-Cores/Kool-Mu-Cores.

[63] http://www.coilws.com/index.php?main_page=page&id=41.

[64] E. C. Snelling, Soft Ferrites-Properties and Applications, Buttenvorths, London, 1988.

[65] https://en.tdk.eu/ferrites.

[66] K. D. T. Ngo and M. H. Kuo, "Effects of air gaps on winding loss in high- frequency planar magnetics," in Power Electronics Specialists Conference, 1988. PESC '88 Record, 19th Annual IEEE, 1988, pp. 1112-1119 vol.2.

[67]

http://www.coilws.com/index.php?main_page=208_212_229_395&cPath=208_212_229_395&main_page=index.

[68] http://www.lodestonepacific.com/distrib/pdfs/Magnetics/cg-01.pdf.

[69] G. F. Volpi, "Integrating Power Electronic System in Space Application: Limitation due to a Harsh Environment," in Integrated Power Systems (CIPS), 2006 4th International Conference on, 2006, pp. 1-6.

[70] R. Khazaka, L. Mendizabal, D. Henry and R. Hanna, "Survey of High-Temperature Reliability of Power Electronics Packaging Components," in IEEE Transactions on Power Electronics, vol. 30, no. 5, pp. 2456-2464, May 2015.

[71] M. H. Pooch, K. J. Dittmer, and D. Gabisch, “Investigations on the damage mechanism of aluminium wire bonds used for high power applications,” in Proc. Eur. Conf. Electr. Packaging Technol., 1996, pp. 128–131.

[72] Y. Yoshino, H. Ohtsu, and T. Shibata, “Thermally induced failure of copper-bonded alumina substrates for electronic packaging,” J. Amer. Ceramic Soc., vol. 75, no. 12, pp. 3353–3357, Dec. 1992.

[73] Skuriat, R., Johnson, C.M., Dietl, K., Vasel, J., Schmitz, G., 2009, “Thermal Management of Power Electronics in the More Electric Aircraft”, Moet forum, Barcelona, Spain.

[74] Rizvi, M. J., Skuriat, R., Tilford, T., Bailey, C., Johnson, C. M., & Lu, H., “CFD Analysis of Water Jet Impingement Cooling System for Effective Cooling of IGBTs used in Power Electronics”, EuroSimE 2009, Delft, The Netherlands.

[75] Skuriat, R., Johnson, C.M., “Thermal Performance of Baseplate and Direct Substrate Cooled Power Modules”, 4th IET Conference on Power Electronics Power Electronics, PEMD 2008, York.

[76] R. Skuriat and C. M. Johnson, "Direct Substrate Cooling of Power Electronics," 5th International Conference on Integrated Power Electronics Systems, Nuremberg, Germany, 2008, pp. 1-5.

[77] N. Mohan, T. Undeland and W. Robbins, Power Electronics: Converters Application and Design. New York, Wiley, 1996.

[78] Goodfellow Cambridge Ltd., "Metals, Alloys, Compounds, Ceramics, Polymers, Composites", Catalogue 1993/94.

[79] C. M. Johnson, A. Castellazzi, R. Skuriat, P. Evans, J. Li and P. Agyakwa, "Integrated High Power Modules," 2012 7th International Conference on Integrated Power Electronics Systems (CIPS), Nuremberg, 2012, pp. 1-10.

[80] C. M. Johnson, et al. “Compact Double-Side Liquid-Impingement-Cooled Integrated Power Electronic Module”, ISPSD '07. pg. 53-56.

[81] B. A. Jasperson, Y. Jeon, K. T. Turner, F. E. Pfefferkorn and W. Qu, "Comparison of Micro-Pin-Fin and Microchannel Heat Sinks Considering Thermal-Hydraulic Performance and Manufacturability," in IEEE Transactions on Components and Packaging Technologies, vol. 33, no. 1, pp. 148-160, March 2010.

[82] Robert Skuriat, “Direct impingement cooling of power electronics”, PhD thesis, University of Nottingham. 2011.

[83] Charboneau, B.C., et al., Double-Sided Liquid Cooling for Power Semiconductor Devices Using Embedded Power Packaging. Industry Applications, IEE Transactions on, 2008. 44(5): p. 1645 1655.

[84] C. Buttay, J. Rashid, C. M. Johnson, F. Udrea, G. Amaratunga, P. Ireland, and R. K. Malhan, "Compact Inverter Designed for High-Temperature Operation," in Power Electronics Specialists Conference, 2007. PESC 2007. IEEE, 2007, pp. 2241-2247.

[85] Glynn, C., O'Donovan, T. S., and Murray, D. B., Jet Impingement Cooling, 9th UK National Heat Transfer Conference, Manchester, 2005.

[86] Johnson, C.M, Thermal Management in Power Electronics. 2010: University of Nottingham, School of EEE.

[87] P. I. Dowell, "Effects of Eddy Current in Transformer Windings," Proc. of IEEE, Vol. 113, No. 8, August, 1966.

[88] A. Bejan, Heat Transfer, John Wiley and Sons, 1993.

[89] http://docs-europe.electrocomponents.com/webdocs/139e/0900766b8139eb8f.pdf.

[90] http://docs-europe.electrocomponents.com/webdocs/1408/0900766b814089d0.pdf.

[91]http://www.deltaww.com/Products/CategoryListT1.aspx?CID=0304&PID=485&hl=en-US&Name=FHS-A6025B02.

[92] http://www.tek.com/sites/tek.com/files/media/media/resources/Integra_Series_Data.PDF.

[93] http://www.kayelaby.npl.co.uk/general_physics/2_3/2_3_7.html.

[94] Zhibin Yan, Rui Zhao, Fei Duan, Teck Neng Wong, Kok Chuan Toh, Kok Fah Choo, Poh Keong Chan and Yong Sheng Chua (2011). Spray Cooling, Two Phase Flow, Phase Change and Numerical Modeling, Dr. Amimul Ahsan (Ed.), ISBN: 978-953-307-584-6.

[95] N. Tang et al., "Fully Integrated Buck Converter With Fourth-Order Low-Pass Filter," in IEEE Transactions on Power Electronics, vol. 32, no. 5, pp. 3700-3707, May 2017.

[96] J. Fang, X. Li and Y. Tang, "A review of passive power filters for voltage-source converters," 2016 Asian Conference on Energy, Power and Transportation Electrification (ACEPT), Singapore, 2016, pp. 1-6.

[97] H. Chen, Z. Qian, Z. Zeng, and C. Wolf, “Modeling of parasitic inductive couplings in a Pi shaped common mode EMI filters,” IEEE Trans. Electromagn. Compat. vol. 50, no. 1, pp. 71–79, Feb. 2008.

[98] A. R. Jr Hefner, “Analytical modeling of device-circuit interactions for the power insulated gate bipolar transistor (IGBT),” IEEE Trans. Ind. Appl., vol. 26, no. 6, pp. 995–1005, Nov. 1990.

[99] H. Zhu, J. S. Lai, A. R. Hefner, Y. Tang, and C. Chen, “Analysis of conducted EMI emissions from PWM inverter based on empirical models and comparative experiments,” in Proc. IEEE PESC’99, 1999, vol. 2, pp. 861–867.

[100]W. Dong, “Analysis and evaluation of soft-switching inverter techniques in electric vehicle applications,” Ph.D. dissertation, Virginia Tech, Blacksburg, 2003.

[101] J. L. Kotny, X. Margueron and N. Idir, "High-Frequency Model of the Coupled Inductors Used in EMI Filters," in *IEEE Transactions on Power Electronics*, vol. 27, no. 6, pp. 2805-2812, June 2012.

[102] H. Yun, Y. Kim, C. Won, Y. Kim, Y. Kim, and A. Choi, “A study on inverter and motor winding for conducted EMI prediction,” in Proc. IEEE Int. Symp. Ind. Electron., 2001, vol. 2, pp. 752–758.

[103] X. Huang, J. S. Lai, and E. Pepa, “Analytical evaluation of modulation effect on three-phase inverter differential mode noise prediction,” in Proc. IEEE APEC’04, 2004, vol. 2, pp. 681–687.

[104] Q. Liu, F. Wang and D. Boroyevich, "Modular-Terminal-Behavioral (MTB) Model for Characterizing Switching Module Conducted EMI Generation in Converter Systems," in *IEEE Transactions on Power Electronics*, vol. 21, no. 6, pp. 1804-1814, Nov. 2006.

[105] J. E. Bridges and W. Emberson, "Determination of Filter Performance for Any Arbitrary Source or Load Impedance Based on Experimental Measurements," 1975

IEEE International Symposium on Electromagnetic Compatibility, San Antonio, Texas, 1975, pp. 1-5.

[106] J.C. Snowdon, Mechanical four-pole parameters and their application, Journal of Sound and Vibration, Volume 15, Issue 3, 8 April 1971, Pages 307-323, ISSN 0022-460X, http://dx.doi.org/10.1016/0022-460X(71)90427-5.

[107] M.L. Munjal, A.G. Doige, Symmetry of one-dimensional dynamical systems in terms of transfer matrix parameters, Journal of Sound and Vibration, Volume 136, Issue 3, 8 February 1990, Pages 467-475, ISSN 0022-460X.

[108] V. Easwaran, V.H. Gupta, M.L. Munjal, Relationship Between The Impedance Matrix And The Transfer Matrix With Specific Reference To Symmetrical, Reciprocal And Conservative Systems, Journal of Sound and Vibration, Volume 161, Issue 3, 8 March 1993, Pages 515-525, ISSN 0022-460X.

[109] M.Bartoli,A.Reatti,and M.K.Kazimierczuk,"High-frequency models of ferrite inductors", Proceedings of the IEEE International Conference on Industrial Electronics, Controls, and Instrumentation (IECON'94), Bologna, Italy, September 5–9, 1994, pp. 1670–1675.

[110] C.-M. Ong, Dynamic Simulation of Electric Machinery, Reading, MA: Prentice-Hall, 1998, pp. 38–40, 45–46, and 87–90.

[111] G.Bertotti, Hysteresis of Magnetism, San Diego, CA: Academic Press, 1998.

[112] R. G. Medhurst, "HF resistance and self-capacitance of single-layer solenoids," Wireless Engineers, pp. 35–43, February 1947, and pp. 80–92, March 1947.

[113] W.B.Boast, Principles of Electric and Magnetic Fields, New York: Harper & Brothers, 1956.

[114] R. J. Kemp, P. N. Mugatroyd, and N. J. Walkers, "Self-resonance in foil inductors," Electronics Letters, vol. 11, no. 15, pp. 337–338, July 1975.

[115] W.H.HaytJr., Engineering Electromagnetics, 4th Ed., New York: McGraw-Hill, 1981.

[116] A.Massarini and M.K.Kazimierczuk,“Modeling the parasitic capacitances of inductors,”Proceedingsofthe Capacitors and Resistors Technology Symposium (CARTS’96), New Orleans, LA, March 1996, pp. 78–85.

[117] G. Grandi, M. K. Kazimierczuk, A. Massarini, and U. Reggiani, “Stray capacitance of single-layer solenoid air-core inductors,” IEEE Transactions on Industry Applications , vol. 35, no. 5, pp. 1162–1168, September 1999.

[118] A.Massarini and M.K.Kazimierczuk,“Self-capacitance of inductors,” IEEE Transactions on Power Electronics , vol. 12, no. 4, pp. 671–676, July 1997.

[119] Qin Yu and T. W. Holmes, "A study on stray capacitance modelling of inductors by using the finite element method," in IEEE Transactions on Electromagnetic Compatibility, vol. 43, no. 1, pp. 88-93, Feb 2001.

[120] M. B. Shadmand and R. S. Balog, "A finite-element analysis approach to determine the parasitic capacitances of high-frequency multiwinding transformers for photovoltaic inverters," Power and Energy Conference at Illinois (PECI), 2013 IEEE, Champaign, IL, 2013, pp. 114-119.

[121] http://www.ansys.com/Products/Electronics/ANSYS-Maxwell.

[122] E. Di Lorenzo, “The Maxwell Capacitance Matrix”, White Paper WP110301, Fast Field Solvers, March 2011.

[123] N. Saxena, Electrical Engineering, 191 – 194, University Science Press New Delhi, (2010).

[124] J.Ebert,“ Four terminal parameters of HF inductors,” Bulletin de l’Acad’emie Polonaise des Sciences, S’erie des Sciences Techniques , no. 5, 1968.

[125] H. B.Gatland,“ Electronic Engineering Applications of Two-Port Networks ” Elsevier Ltd, 1976.

[126] X. Margueron, J. P. Keradec, “Identifying the Magnetic Part of the Equivalent Circuit of n-Winding Transformers,” Instrumentation and Measurement, IEEE Transactions on, vol. 56, n°. 1, p. 146-152, 2007.

[127] X. Margueron, J. P. Keradec, “Design of Equivalent Circuits and Characterization Strategy for n-Input Coupled Inductors,” Industry Applications, IEEE Transactions on, vol. 43, n°. 1, p. 14-22, 2007.

[128] http://ena.support.keysight.com/e4990a/manuals/webhelp/eng/

[129] M. K. Kazimierczuk, G. Sancineto, G. Grandi, U. Reggiani and A. Massarini, "High-frequency small-signal model of ferrite core inductors," in IEEE Transactions on Magnetics, vol. 35, no. 5, pp. 4185-4191, Sep 1999.

[130] A. Reatti and M. K. Kazimierczuk, "Comparison of various methods for calculating the AC resistance of inductors," in IEEE Transactions on Magnetics, vol. 38, no. 3, pp. 1512-1518, May 2002.

[131] Xi Nan and C. R. Sullivan, "An improved calculation of proximity-effect loss in high-frequency windings of round conductors," Power Electronics Specialist Conference, 2003. PESC '03. 2003 IEEE 34th Annual, 2003, pp. 853-860 vol.2.

[132] A. Ohri, T. Wilson and H. Owen, "Design of air-gapped magnetic-core inductors for superimposed direct and alternating currents," in IEEE Transactions on Magnetics, vol. 12, no. 5, pp. 564-574, Sep 1976.

[133] P.S. Venkatraman.: ‘Winding eddy current losses in switch mode power transformers due to rectangular wave currents’. Proc. Powercon 11, Section A-1, 1984, pp. 1–11.

[134] A. M. Urling, V. A. Niemela, G. R. Skutt and T. G. Wilson, "Characterizing high-frequency effects in transformer windings-a guide to several significant articles," Proceedings, Fourth Annual IEEE Applied Power Electronics Conference and Exposition, Baltimore, MD, 1989, pp. 373-385.

[135] Valchev, V.C. and Van den Bossche, A., 2005. Inductors and transformers for power electronics. CRC press.

[136] COONROD N.R.: ‘Transformer computer design aid for higher frequency switching power supplies’. IEEE Power Electronics Specialists Conf. Record, 84CH2000-8, 1984, pp. 257–267.

[137] Jiankun Hu, Charles R. Sullivan. Optimization of Shapes for Round Wire High Frequency Gapped Inductor Windings. Proceedings of IEEE Industry Application Society, IAS'98, 1998.

[138] W. Chen, X. Huang and J. Zheng, "Improved winding loss theoretical calculation of magnetic component with air-gap," Proceedings of The 7th International Power Electronics and Motion Control Conference, Harbin, China, 2012, pp. 471-475.

[139] N. Kondrath and M. K. Kazimierczuk, "Inductor winding loss owing to skin and proximity effects including harmonics in non-isolated pulse-width modulated dc-dc converters operating in continuous conduction mode," in IET Power Electronics, vol. 3, no. 6, pp. 989-1000, Nov. 2010.

[140] J. Reinert, A. Brockmeyer, and R. De Doncker, "Calculation of losses in ferro- and ferromagnetic materials based on the modified Steinmetz equation," IEEE Trans. Ind. Appl., vol. 37, no. 4, pp. 1055–1061, Jul./Aug. 2001.

[141] Jieli Li, T. Abdallah and C. R. Sullivan, "Improved calculation of core loss with non-sinusoidal waveforms," Conference Record of the 2001 IEEE Industry Applications Conference. 36th IAS Annual Meeting (Cat. No.01CH37248), Chicago, IL, USA, 2001, pp. 2203-2210 vol.4.

[142] A. Brockmeyer, "Experimental evaluation of the influence of DC-premagnetization on the properties of power electronic ferrites," Applied Power Electronics Conference and Exposition, 1996. APEC '96. Conference Proceedings 1996., Eleventh Annual, San Jose, CA, 1996, pp. 454-460 vol.1.

[143] S. Iyasu, T. Shimizu, and K. Ishii, "A novel iron loss calculation method on power converters based on dynamic minor loop," in Proc. Eur. Conf. Power Electron. Appl., 2005, pp. 2016–2022.

[144] C. A. Baguley, B. Carsten, and U. K. Madawala, 'The Effect of DC Bias Conditions on Ferrite Core Losses', Magnetics, IEEE Transactions on, vol. 44, no. 2, pp. 246–252, 2008.

[145] C. P. Steinmetz, “On the law of hysteresis,” Proc. IEEE, vol. 72, no. 2, pp. 197–221, Feb. 1984.

[146] K. Venkatachalam, C. R. Sullivan, T. Abdallah, and H. Tacca, “Accurate prediction of ferrite core loss with non-sinusoidal waveforms using only Steinmetz parameters,” in Proc. IEEE Workshop Comput. Power Electron. 2002, pp. 36–41.

[147] T. Shimizu and K. Ishii, “An iron loss calculating method for AC filter inductors used on PWM inverters,” in Proc. 37th IEEE Power Electron. Spec. Conf., 2006, pp. 1–7.

[148] W. A. Roshen, “A practical, accurate and very general core loss model for nonsinusoidal waveforms,” IEEE Trans. Power Electron., vol. 22, no. 1, pp. 30–40, Jan. 2007.

[149] J. Muhlethaler, J. Biela, J. W. Kolar and A. Ecklebe, "Core Losses Under the DC Bias Condition Based on Steinmetz Parameters," in *IEEE Transactions on Power Electronics*, vol. 27, no. 2, pp. 953-963, Feb. 2012.

[150] F. Fiorillo and A. Novikov, “An improved approach to power losses in magnetic laminations under nonsinusoidal induction waveform,” IEEE Trans. Magn., vol. 26, no. 5, pp. 2904-2910, 1990.

[151] F. Fiorillo and A. Novikov, “Power losses under sinusoidal, trapezoidal and distorted induction waveform,” IEEE Trans. Magn., vol. 26, no. 5, pp. __ 2559-2561, 1990.

[152] Jiankun Hu and C. R. Sullivan, ‘AC resistance of planar power inductors and the quasi-distributed gap technique’, IEEE Transactions on Power Electronics, vol. 16, no. 4, pp. 558–567, Jul. 2001.

[153] A. Van den Bossche and V. C. Valchev, ‘Improved calculation of winding losses in gapped inductors’, Journal of Applied Physics, vol. 97, no. 10, p. 10Q703, 2005.

[154] http://www.vishay.com/docs/50051/lto100.pdf.

[155] http://www.wolfspeed.com/c3m0120090j.

[156] https://en.tdk.eu/download/528866/f41b4c91d03b93ec92d9d5db65741d50/pdf-n95.pdf.